

Sheffield Hallam University

Si-DLC coatings optimized for low wear and low friction applications.

HOFMANN, Dieter.

Available from the Sheffield Hallam University Research Archive (SHURA) at:

<http://shura.shu.ac.uk/19805/>

A Sheffield Hallam University thesis

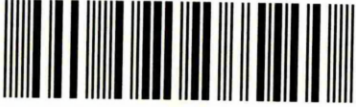
This thesis is protected by copyright which belongs to the author.

The content must not be changed in any way or sold commercially in any format or medium without the formal permission of the author.

When referring to this work, full bibliographic details including the author, title, awarding institution and date of the thesis must be given.

Please visit <http://shura.shu.ac.uk/19805/> and <http://shura.shu.ac.uk/information.html> for further details about copyright and re-use permissions.

Learning and Information Services
Adsetts Centre, City Campus
Sheffield S1 1WD

102 038 080 2


Sheffield Hallam University
Learning and Information Services
Adsetts Centre, City Campus
Sheffield S1 1WD

REFERENCE

ProQuest Number: 10697107

All rights reserved

INFORMATION TO ALL USERS

The quality of this reproduction is dependent upon the quality of the copy submitted.

In the unlikely event that the author did not send a complete manuscript and there are missing pages, these will be noted. Also, if material had to be removed, a note will indicate the deletion.



ProQuest 10697107

Published by ProQuest LLC (2017). Copyright of the Dissertation is held by the Author.

All rights reserved.

This work is protected against unauthorized copying under Title 17, United States Code
Microform Edition © ProQuest LLC.

ProQuest LLC.
789 East Eisenhower Parkway
P.O. Box 1346
Ann Arbor, MI 48106 – 1346

Si-DLC coatings optimized for low wear and low friction applications

Dieter Hofmann

A thesis submitted in partial fulfilment of the requirements of
Sheffield Hallam University
for the degree of Doctor of Philosophy

July 2014
PhD Thesis

Abstract

Diamond-like carbon (DLC) has excellent properties for the use as tribological coating such as high hardness, high wear resistance and a low friction coefficient. Nanolayer systems of hydrogenated diamond-like carbon (a-C:H) and silicon doped hydrogenated diamond-like carbon (Si-DLC or a-C:H:Si) have been studied. The objectives of this work are to develop layer combinations which allow combining low abrasive wear, low friction properties, and improved temperature stability for the coatings.

A literature survey on sputtering, plasma enhanced chemical vapor deposition (PECVD) and carbon based materials with a focus on a-C:H and Si-DLC coatings is given. This survey includes a brief overview of the 60 years history of DLC coating.

In the second part of the thesis, the experimental set up for the layer preparation by a magnetron based deposition method and a basic description of the process are presented. Using sputtering from a solid SiC target as a source of the Si for the Si-DLC instead of the commonly used PECVD process with Si-containing precursors Si-DLC/a-C:H nanolayers were deposited at high deposition rates.

For the coatings, the influence of the acetylene gas flow, the bias voltage, and the hydrogen and silicon concentration are discussed. Undoped a-C:H coatings with high indentation hardness above 40 GPa and very low abrasive wear rates of $0.6 \times 10^{-15} \text{ m}^3/(\text{Nm})$ and low hydrogen content of about 11 at.% were deposited. Si-DLC/a-C:H nanolayer coatings with high hardness of 20 to 30 GPa and a high temperature stability up to 500 °C were prepared. For these nanolayer films low friction coefficients of 0.06 to 0.11 and high abrasive wear rates of $>2.5 \times 10^{-15} \text{ m}^3/(\text{Nm})$ were achieved at high silicon contents above 15 at.%. On the other hand nanolayer coatings with low silicon contents of less than 10 at.% showed low wear rates below $1.7 \times 10^{-15} \text{ m}^3/(\text{Nm})$ combined with higher friction coefficients of 0.12 to 0.15. In order to combine the low abrasive wear rate and the low friction coefficient at first a Si-DLC/a-C:H layer with low Si-concentration followed by a second layer with high Si-concentration was deposited. Due to the low surface free energy of Si-DLC coatings of 30 to 35 mN/m the wetting behavior for some lubricants may deteriorate. In this case a further optimization of the nanolayer system is required.

Acknowledgments

Looking back to a longstanding history in PVD coating technology and in DLC coating I wish to express thanks to many colleagues in the industry and the research society for the great help they have given to better understand such coatings and the related technology.

First of all, I would like to thank my director of study in Sheffield Hallam University Prof. Dr. Papken Hovsepien and my supervisors Prof. Dr. Guenter Braeuer and Dr. Klaus Bewilogua of the Fraunhofer IST research institute for the opportunity to complete a part-time PhD program and their guidance and help during this time.

I have to give special thanks to Dr. Klaus Bewilogua for numerous fruitful discussions which allowed me to benefit from the experience of his long research career in the field of diamond-like carbon.

As managing director of AMG Coating Technologies it was important that the supervisory board supported my PhD program which was strongly initiated by the chairman of the supervisory board Dr. Jan Peter Osing. For this I am very grateful.

I would especially like to thank Mr. Stefan Kunkel of AMG Coating Technologies and Mr. Ralf Wittorf of Fraunhofer-IST for the very careful execution of the experimental work and the provision and discussion of the experimental data.

Finally, I would like to thank Dr. Peter Willich, Dr. Kirsten Schiffmann, Dr. Jan Petersen and Mrs. Meylia Lutansiето of Fraunhofer IST for the careful analyses (SIMS, SEM, XRD, and XRR) and for the tribological characterization of the coatings.

Conferences/ Seminars/ Publications

Presentations and publications during the time of the PhD program:

December 2011, Si-DLC based layer systems with application-optimized properties, EFDS Seminar, Dresden (Germany)

April 2012, From DLC to Si-DLC based layer systems with optimized properties for tribological applications, ICMCTF 2012, San Diego (USA)

September 2012, Deposition and properties of DLC, Si-DLC, Me-DLC coatings and DLC based nanolayer systems, keynote presentation at PSE 2012, Garmisch-Partenkirchen (Germany)

September 2012, Diamond-like carbon films – preparation techniques, properties and applications, presentation of Dr. Bewilogua at PSE 2012, Garmisch-Partenkirchen (Germany) D. Hofmann as coauthor

November 2012, Deposition and properties of DLC, Si-DLC coatings and DLC based nanolayer layer systems, presentation at scientific colloquium Fraunhofer-IST, Braunschweig (Germany)

January 2013, D. Hofmann, K. Bewilogua, S. Kunkel and R. Wittorf, From DLC to Si-DLC based layer systems with optimized properties for tribological applications, Surf. Coat. Technol. 215 (2013) 357-363, paper publication

August 2013, DLC coating: 60 years history of R&D and applications to recent results, plenary presentation at AEPSE 2013, Jeju (Korea)

January 2014, K. Bewilogua and D. Hofmann, Diamond-like carbon films – from first experiments to worldwide applications, Surf. Coat. Technol. 242 (2014) 214-225 (invited review paper)

Table of contents

1. Motivation for the work	7
2. Literature survey	12
2.1 Fundamentals of the sputtering technology	12
2.1.1 History of sputtering	12
2.1.2 Sputtering of elemental targets	13
2.1.3 Sputtering of multi component targets	16
2.1.4 Magnetron sputtering	18
2.1.5 Reactive sputtering	22
2.1.6 The unbalanced magnetron	23
2.1.7 Structure zone models for PVD coatings	26
2.2 Chemical vapor deposition	30
2.2.1 History of chemical vapor deposition	30
2.2.2 Deposition of carbon-based coatings	31
2.2.3 Deposition of silicon based coatings	34
2.3 Overview on carbon based materials	35
2.3.1 History of DLC coating	35
2.3.2 Comparison of properties for carbon-based materials	38
2.3.3 Classification, structure models and the subplantation model for DLC	41
2.3.4 Basic friction mechanisms for carbon-based coatings	44
2.3.5 Properties of hard and soft amorphous hydrogenated carbon (a-C:H) coatings	46
2.3.6 Friction of amorphous hydrogenated carbon (a-C:H) coatings	47
2.3.7 Wear of amorphous hydrogenated carbon (a-C:H) coatings	55
2.3.8 Friction and wear of a-C:H:Si (Si-DLC) coatings	64
3. Analytical and tribological methods for characterization of coatings	73
3.1 Adhesion evaluation using the scratch test	73
3.2 Adhesion evaluation using the Rockwell C indentation test	74
3.3 Indentation hardness and reduced indentation modulus evaluation	76

3.4 Abrasive wear rate and film thickness evaluation using the ball cratering test	78
3.5 Friction coefficient and adhesive wear coefficient determination using ball-on-disk test	80
3.6 Structural evaluation using X-Ray diffraction	82
3.7 Mass density evaluation using X-Ray reflectometry	83
3.8 Secondary Ion Mass Spectroscopy (SIMS) for the analysis of the layer composition	85
3.9 Scanning Electron Microscope (SEM)	87
3.10 Electron Probe Microanalysis (EPMA)	88
4. Experimental	89
4.1 Ion assisted a-C:H deposition using industrial system concepts	89
4.2 Coating system, parts to be coated and basic process sequence	91
4.3 Process data for a-C:H and Si-DLC deposition	96
5. Results and discussion	99
5.1 Reactive deposition using graphite, SiC/C and WC targets	99
5.2 Plasma Booster effect	102
5.3 Layer systems and deposition rates for a-C:H and Si-DLC	103
5.4 Results achieved for a-C:H coatings	108
5.5 Results achieved for Si-DLC/a-C:H nanolayer coatings	120
5.6 Layer combinations combining low-wear and low-friction properties	131
5.7 Properties of a-C:H and Si-DLC/a-C:H nanolayer coatings after tempering	134
5.8 Improvement of frictional and wear behavior under lubricated conditions	142
6. Conclusions and summary	145
References	149

1. Motivation for the work

Diamond-like carbon (DLC) based coatings are well known for tribological applications e.g. on automotive engine components in order to increase the wear resistance and to reduce the frictional forces in tribological contacts with and without lubrication. The coatings are typically used under critical conditions characterized by high specific loads and/or mixed friction to direct unlubricated material contact situations.

DLC is a coating material which is widely used in the automotive industry. The scenario of limited fossil fuel resources and the need to lower CO₂ emissions is the driving force to continuously improve the internal combustion engine and the automotive powertrain components. Therefore the aspects of the reduction of fuel consumption and CO₂ emission from the automobile create the need to minimize friction.

Holmberg et al. [1] estimated for the year 2009 that the worldwide fuel consumption (gasoline and diesel) which was required to compensate friction in passenger cars was 2.08×10^{11} liters, which corresponds to a combustion energy of 7.3×10^6 Terajoules. This study shows only for the friction losses an average fuel consumption of 340 liters per year for one passenger car having an average driving distance of 13000 km. Such friction losses in passenger cars could be reduced by 18% in 5 to 10 years which would reduce the CO₂ emission by 2.8×10^8 tonnes per year. It was estimated that in 15 to 25 years the CO₂ emission could be reduced by 61% which corresponds to 9.6×10^8 tonnes per year.

Tung and McMillan [2] of GM reported that a reduction of friction and wear in engine and drive train components could save only in the U.S. 120 billion US\$ per year.

Affenzeller et al. give a relationship between the reduction of engine friction of an internal combustion engine (ICE) and the fuel saving potential for an automobile [3]. In Figure 1.1 the energy conversion of the potential combustion energy of the fuel to mechanical energy and finally to the propulsion of a passenger car are given according to data from the GM research center and own research. It is shown that the engine friction has a significant influence on the energy remaining for propulsion because only a small fraction of about 30 to

40% of the fuel energy is converted to mechanical energy [4, 5]. Therefore the fuel consumption is significantly influenced by the engine friction which consumes about 5% related to the fuel energy but 12 to 17% of the mechanical energy of the engine. The relationship between the reduction of engine friction and the fuel saving potential is shown in Figure 1.1 according to [3].

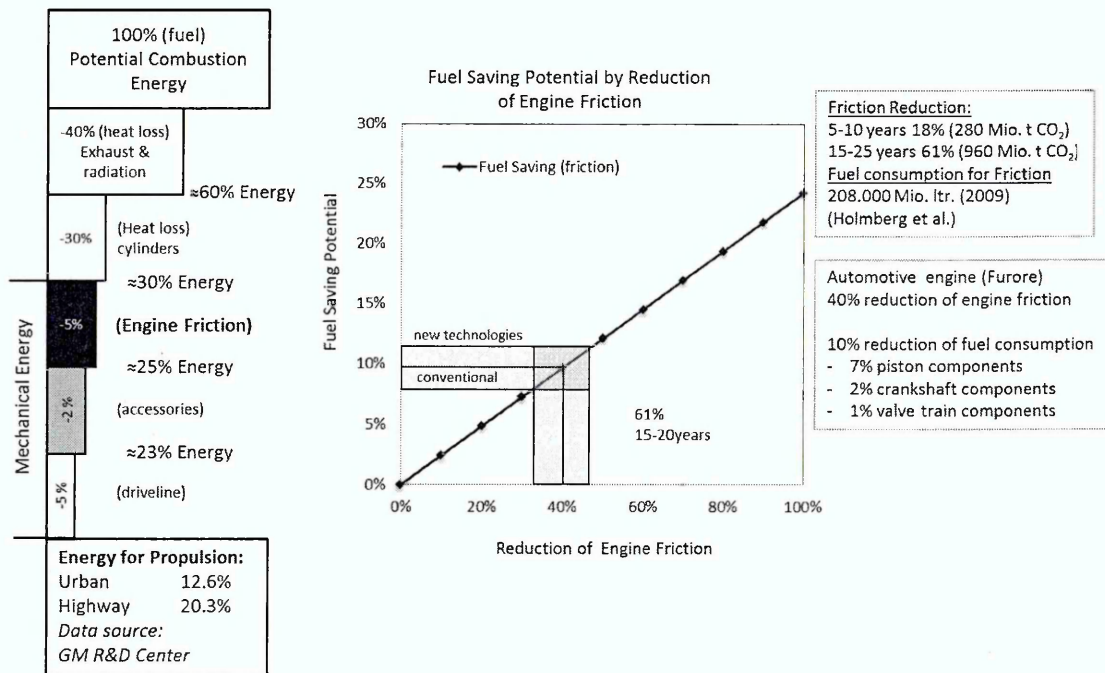


Figure 1.1 : Friction reduction and fuel saving potential for automobiles with combustion engines, according to Affenzeller et al. [3] and Holmberg et al.[1]

Using today's measures, around 40% friction reduction was estimated which would offer a fuel saving potential of about 10%. In a 10% reduction of fuel consumption resulting from a homogenous reduction of friction on the engine parts which are relevant for the friction losses the piston components would contribute 7%, the crankshaft components 2% and the valve train components 1%.

In order to reduce friction by applying a DLC coating it has to be considered that a direct material contact has to be present to achieve a benefit from the coated surface. This would be always the case under dry contact conditions but is also the case in fuel lubricated and oil lubricated systems under the conditions in a reciprocating internal combustion piston engine (ICE). In the reciprocating ICE

the engine strokes periodically move the pistons, the connecting rod, the crankshaft, the camshaft and the valves which includes periods of small and zero velocity. In this velocity region insufficient lubrication, boundary or mixed friction and solid contacts are present. There are new observations which show that at high speed conditions in the tribocontact - where under normal conditions a complete oil film is expected - several solid contacts can occur on critical components of a highly loaded downsized engine. The different contact situations for the applications of DLC coatings are shown in Figure 1.2.

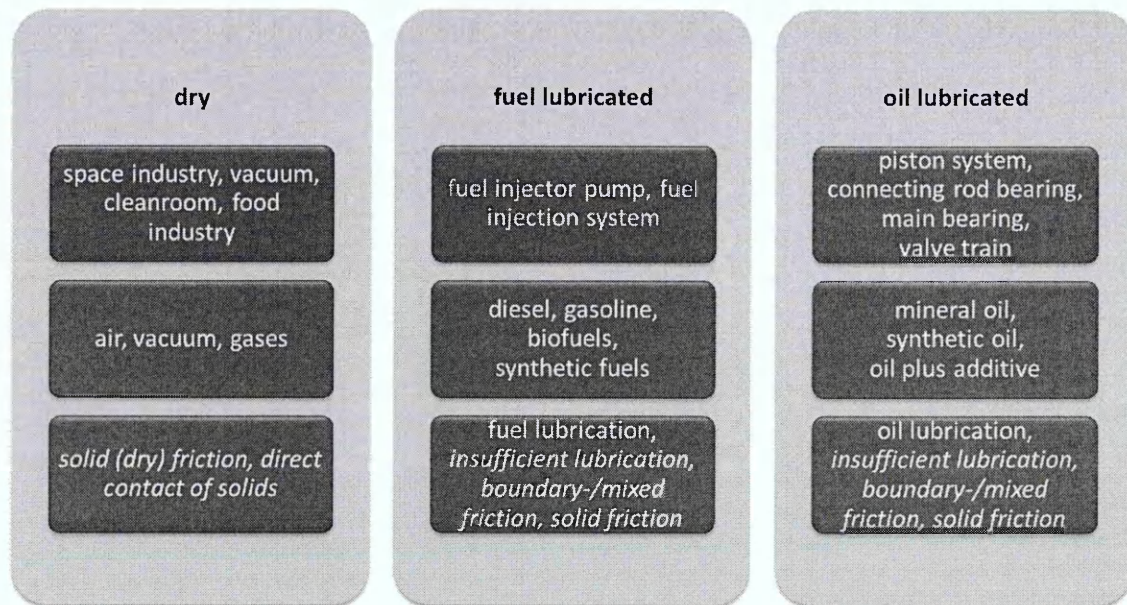


Figure 1.2 Application of DLC based coatings under dry, fuel- and oil- lubricated conditions

With PVD (physical vapor deposition) coatings significant reductions of engine friction can be achieved. The most important coating is highly durable DLC (diamond-like carbon) which offers low friction coefficients and high layer hardness. DLC coated components allow a significant reduction of wear and friction in automotive engine and drive train component groups.

In Europe the most important measure to reduce the fuel consumption of combustion engines is downsizing, which creates high specific loads on the engine components. This generates the need to further improve the durability of the surfaces in highly loaded contacts and therefore the application of PVD coatings which offer a fuel and CO₂ reduction potential of up to 20%.

For powertrain components like piston components, crankshaft components and valve train components the potential of engine friction reduction has been already mentioned.

The application of high-pressure direct fuel injection systems has significantly contributed to the reduction of fuel consumption and the CO₂ emission. The injector components need DLC coating in order to reduce friction and wear and to withstand high pressure which is presently 2000 bar and expected to increase to 3000 bar [6]. In this application DLC coatings allow smaller clearances of the injector needle sleeve which results in smaller leakages and a reduction of the load on the high pressure fuel injection pump.

Most of the automotive applications need coatings which have to resist high specific loads and severe wear conditions. Therefore undoped amorphous hydrogenated diamond-like carbon (a-C:H) coatings with high wear resistance are increasingly used. However, these a-C:H coatings have only a low temperature stability if used in oxidizing atmospheres and the increase of friction at increasing relative humidity is reported (see chapters 2.3.6 and 2.3.7). In order to further reduce the friction losses the application of silicon doped amorphous hydrogenated diamond-like carbon (Si-DLC or a-C:H:Si) would offer a solution but for these coatings much higher wear rates have been shown (see chapter 2.3.8). A solution for this problem could be found in combining properties of a-C:H and Si-DLC.

The main aim of the project was therefore the preparation of a-C:H-based coatings with low friction properties, high hardness and high wear resistance.

The following objectives for the research have to be considered in order to achieve coatings which can be used in industrial applications in the fields which are described above:

- Deposition of silicon doped a-C:H coatings (Si-DLC or a-C:H:Si) with high temperature stability in air and very low friction coefficients using the PVD method for deposition of silicon in order to achieve coatings with low hydrogen content.

- Development of Si-DLC/a-C:H nanolayer coatings and layer designs with high wear resistance, low friction coefficient and high temperature stability up to 500°C
- The friction coefficient of the a-C:H and the a-C:H/Si-DLC nanolayer coatings should not increase significantly with increasing relative humidity (RH) in humid air atmosphere in the range of 20 to 80% RH.

2. Literature survey

2.1 Fundamentals of the sputtering technology

2.1.1 History of sputtering

After the first discharge tube research by Faraday in 1838 the sputtering effect was first observed by Grove in 1852 [7] and Faraday in 1854 at studying glow discharges under vacuum conditions.

The first coating applications that applied the sputtering effect were reported by A. Wright in 1858 in the American Journal of Science and Arts on "mirror coatings" and a "Seed coat" on wax phonograph masters by Edison in 1892.

In 1910 the term sputtering was introduced by Thomson [8] which was later modified by Langmuir and Kingdon in their publications in the years 1920-1923 to sputtering.

The first sputtering theory which describes the influence of the ion energy was presented by Guenterschulze in 1930 [9].

The combination of a magnetic field with the electrical field at the sputter cathode to confine the plasma at the cathode region was first reported by Penning in 1936 [10].

In 1954 and 1955 the work of Wehner [11, 12] gave a detailed view to the ejection of target material including preferred angles at sputtering of single crystal targets and presented a picture on the sputtering yields depending on the position of elements in the periodic table. The use of sputtering to clean surfaces prior to PVD coating was reported in the early 1950s. In 1964 Mattox [13] reported about a deposition using accelerated ions. Maissel and Schaible [14] discussed the first bias sputtering in 1965. Mattox received a patent for ion plating in 1967 [15].

Clarke applied for the first magnetron patent in 1968 which was granted in 1971 [16]. A patent application which included a planar magnetron configuration was made by Corbani in 1973 [17]. The first patent for a practically usable planar magnetron was filed by Chapin [18] which was granted in 1979. The unbalanced magnetron was discussed in 1986 by Windows and Savvides [19, 20, 21].

2.1.2 Sputtering of elemental targets

Improved theories for the calculation of sputter yields of elemental targets are presented starting with the model of Sigmund in 1969 [22] which is based on the Boltzmann transport theory and incorporates the nuclear stopping theory of Lindhard and Scharff [23]. In the Sigmund formula for low energies (< 1keV) the Born-Mayer potential is more important than the Thomas-Fermi potential. Sigmund's relationship is valid for amorphous and polycrystalline targets at normal incidence of ions. The formula of Sigmund (2.1) can be used for a wide range of ion energies. Sputter yields for the incidence of ions with low energies up to 1 keV can be calculated by a simplified formula of Sigmund (2.2).

Sigmund's formula of 1969:

$$\text{Sputter Yield} \quad Y(E) = \frac{0.042 \cdot \alpha (M_2/M_1)}{U_s} * Sn(E) \quad (2.1)$$

E= Energy of bombarding ion [eV]

Sn(E)= Nuclear stopping cross section [eV*Å²/atom]
details are discussed at equation (2.4)

U_s= Surface binding Energy [eV]

α= Proportion of energy from incident ions back-reflected
to be available for sputtering (dimensionless factor)

α= 0.2 at low energy and M₂/M₁ <1

α= 0.15 + 0.13*(M₂/M₁) approx. according to Zalm [24]

Sigmund's formula simplified for low ion energies <1keV:

$$\text{Sputter Yield} \quad Y(E) = \frac{3 \cdot \alpha (M_2/ M_1)}{4\pi^2} * \frac{4 \cdot M_1 \cdot M_2}{(M_1 + M_2)^2} * \frac{E}{U_s} \quad (2.2)$$

E= Energy of bombarding ion [eV]

M₁= Mass of projectile - bombarding ion [a.m.u.]

M₂= Mass of target atom [a.m.u.]

U_s= Surface binding energy [eV]

α= Dimensionless factor (explanation in formula (2.1))

α= 0.2 at low energy and M₂/M₁ <1

α= 0.15 + 0.13*(M₂/M₁) approx. according to Zalm [24]

In 1980 Matsunami [25] published a first improvement of the Sigmund formula (2.1). A further improved semi-empirical sputter yield calculation of 1984 from Matsunami [26] includes the threshold energy and the inelastic stopping cross section from the Yamamura equation published in 1982 [27]. This semi-empirical equation of Matsunami is shown as equation (2.3).

Matsunami's semi-empiric formula of 1984:

$$\text{Sputter Yield } Y(E) = \frac{0.42 \cdot \alpha (M_2/M_1) \cdot Q \cdot K \cdot s_n(\epsilon)}{U_s [1 + 0.35 \cdot U_s \cdot s_e(\epsilon)]} \cdot [1 - (E_{th}/E)^{1/2}]^{2.8} \quad (2.3)$$

Y(E)= Sputter Yield (sputtered atoms per incident ion)

E= Energy of bombarding Ion [eV]

M₁= Mass of projectile - bombarding ion [a.m.u.]

M₂= Mass of target atom [a.m.u.]

U_s= Surface binding Energy [eV]

Q= Tabulated parameter

s_n(ε)= Reduced nuclear stopping cross section
[eV/(10¹⁵ atoms/cm²)]

s_e(ε)= Inelastic reduced stopping cross section

E_{th}= Threshold energy [eV]

K= Conversion factor S_n(ε) to S_n(E) [eV*cm²/(10¹⁵ atoms)]

ε= Lindhard-Scharff-Schiott reduced energy

α= 0.08 + 0.164*(M₂/M₁)^{0.4} + 0.0145*(M₂/M₁)^{1.29}

The widely used further refined semi-empiric formula for sputter yield calculation of Yamamura et al. [28] from 1996 is shown as equation (2.4). In this publication a collection of tabulated data for monoatomic solids can be found e.g. surface binding energies, best fit values of Q(Z₂), W(Z₂) and s(Z₂).

In this chapter sputtering for normal incidence of the projectile atoms on the sputter target is discussed but the results can be used for a magnetron cathode at low target voltages of several hundred volts, high plasma densities and small dark space distances.

The dependency of the sputtering yield on the angle of incidence of the bombarding ions to the target is discussed by Yamamura et al. [29], Ono et al. [30] and Wei et al. [31].

The Monte Carlo method can be used to calculate the energies transferred from the bombarding particles to the target atoms which includes the evaluation of the stopping power of the target material for the projectiles. This method allows describing of ion bombardment related effects in more detail. Information about sputter yield calculation using the Monte Carlo method can be found in the publications of Ziegler et al. and Biersack et al. [32, 33, 34].

The elemental sputtering yields for carbon (graphite), silicon, tungsten and chromium were calculated using the semi-empiric formula of Yamamura (equation 2.4). The calculated yields have been used for first estimations about the deposition rates and to estimate sputtering yields of compounds.

Yamamura's semi-empiric formula of 1996:

$$\text{Sputter Yield } Y(E) = \frac{0.042 \cdot Q(Z_2) \cdot \alpha(M_2/M_1)}{U_s} * \frac{Sn(E)}{1 + \Gamma \cdot k_e \cdot \epsilon^{0.3}} * [1 - (E_{th}/E)^{1/2}]^s \quad (2.4)$$

Y(E)= Sputter Yield (sputtered atoms/ incident ion)

E= Energy of bombarding Ion [eV]

M₁= Mass of projectile - bombarding ion [a.m.u.]

M₂= Mass of target atom [a.m.u.]

U_s= Surface binding Energy [eV]

Q(Z₂)= Tabulated dimensionless parameter

Sn(E)= Nuclear stopping cross section [eV*Å²/atom]

E_{th}= Threshold energy [eV]

Γ= W(Z₂) / [1+(M₁/7)³]

W(Z₂)= Tabulated dimensionless parameter

k_e= Lindhard electronic stopping coefficient [eV*cm²/atom]

ε= Lindhard-Scharff-Schiott reduced energy

s= Tabulated dimensionless parameter

α= 0.249(M₂/M₁)^{0.56} + 0.0035(M₂/M₁)^{1.5} for M₁ ≥ M₂

α= 0.0875(M₂/M₁)^{-0.15} + 0.165(M₂/M₁) for M₁ ≤ M₂

with: E_{th}= 6.7*U_s/γ for M₁ ≥ M₂

E_{th}= [1 + 5.7*(M₁/M₂)]*U_s/γ for M₁ ≤ M₂

γ= 4*M₁*M₂ / (M₁+M₂)² (Energy transfer factor)

$$\text{with: } Sn(E) = \frac{84.78 \cdot Z_1 \cdot Z_2}{(Z_1^{2/3} + Z_2^{2/3})^{1/2}} * \frac{M_1}{(M_1 + M_2)} * S_n^{TF}(\epsilon)$$

Z₁= Atomic number of projectile - bombarding ion

Z₂= Atomic number of target atom

S_n^{TF}(ε)= Reduced nuclear stopping cross section
[eV/(10¹⁵ atoms/cm²)]

$$\text{where: } S_n^{TF}(\epsilon) = \frac{3.441 \cdot \epsilon^{1/2} \cdot \ln(\epsilon + 2.718)}{1 + 6.355 \cdot \epsilon^{1/2} + \epsilon \cdot (6.882 \cdot \epsilon^{1/2} - 1.708)}$$

ε= Lindhard-Scharff-Schiott reduced energy [eV]

$$\text{where: } \epsilon = \frac{0.03255}{Z_1 \cdot Z_2 \cdot (Z_1^{2/3} + Z_2^{2/3})^{1/2}} * \frac{M_2}{(M_1 + M_2)} * E$$

$$\text{with: } k_e = \frac{(Z_1)^{2/3} \cdot (Z_2)^{1/2}}{(Z_1^{2/3} + Z_2^{2/3})^{3/4}} * \frac{(M_1 + M_2)^{3/2}}{(M_1)^{3/2} \cdot (M_2)^{1/2}} * 0.079$$

k_e= Lindhard electronic stopping coefficient [eV*cm²/atom]

2.1.3 Sputtering of multi component targets

For sputtering of compounds or mixed targets it has to be considered that at steady state conditions the elemental components of the bulk composition in the target material have to be removed by sputtering from the surface by creating fluxes of sputtered material with elemental compositions equal to the elemental concentrations in the bulk. This allows removing the target material in its bulk composition.

In case of the target materials SiC and WC the sputtering yields of silicon and carbon as well as tungsten and carbon are significantly different. In order to be able to achieve material fluxes that are equal to the bulk concentrations the surface concentration of carbon which has the lowest sputter yield has to be increased until steady state conditions are reached as shown in Figure 2.1 for SiC.

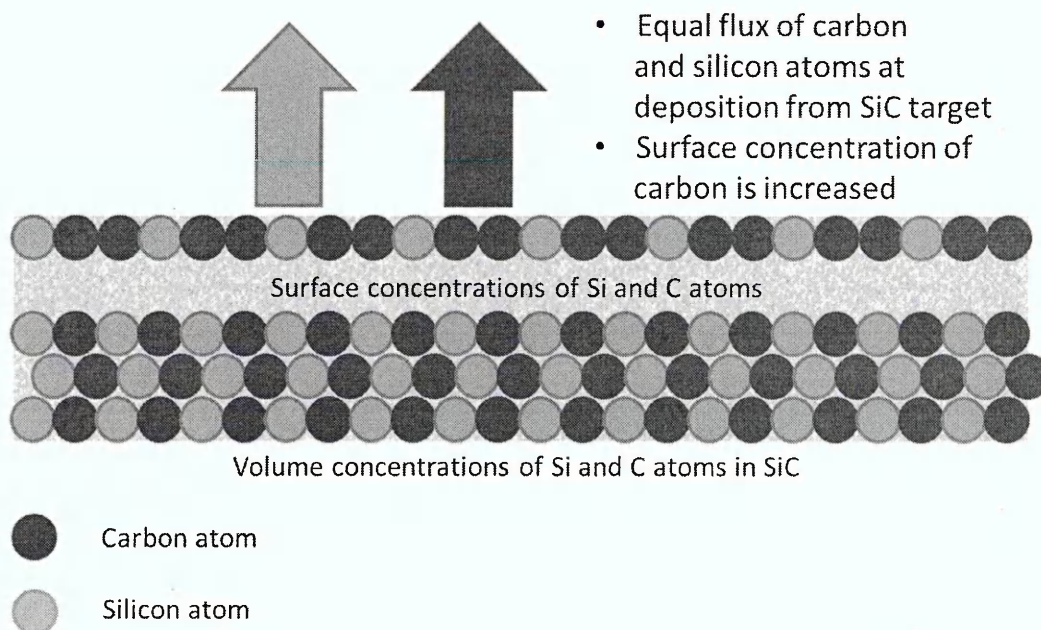


Figure 2.1 : Schematic view of surface and volume concentrations of carbon and silicon atoms at sputtering of SiC

In 1974 Andersen and Sigmund [35] described the sputtering of compounds by a simple linear cascade theory which can be found as equation (2.5).

Sputtering Yield ratio for a compound with two components, according to Andersen and Sigmund of 1974:

$$\frac{Y_c}{Y_{si}} \approx \frac{\alpha_c}{\alpha_{si}} * \left(\frac{M_{si}}{M_c} \right)^{2m} * \left(\frac{U_c}{U_{si}} \right)^{1-2m} \quad (2.5)$$

m = characterizes energy-loss section at low energy

Y_c = Partial sputter yield carbon

Y_{si} = Partial sputter yield silicon

α_c = concentration of carbon

α_{si} = concentration of silicon

U_c = surface binding energy carbon

U_{si} = surface binding energy silicon

M_c = atomic mass carbon

M_{si} = atomic mass silicon

A similar yield ratio can be calculated for W and C by exchanging the silicon related data for the values for tungsten.

An experimental sputtering yield of 0.5 for SiC at 500 eV Ar⁺ bombardment was reported by Comas and Cooper [36].

For more information about compound sputtering see the following references [37, 38, 39].

2.1.4 Magnetron sputtering

The sputtering technology achieved its industrial breakthrough through the introduction of the magnetron cathode which opened the field of high rate magnetron sputtering.

Magnetron sputtering uses a combination of electrical and magnetic fields. It took a long time to reach cathode hardware arrangements offering useful conditions for the practical application in the industry.

The history of the deposition technologies using combinations of electrical and magnetic fields starts with Penning [40] who submitted a patent application for a cylindrical post magnetron in 1935. The principle of the magnetron was discussed by Jepsen [41] in 1961 using crossed electrical and magnetic fields. Clarke applied for a patent for an inversed cylindrical magnetron [16] in 1968. A cylindrical magnetron was invented by Corbani [17] in 1973 which enabled only coating of cylindrical shapes. The final breakthrough for the industrially useable magnetron was the invention of the planar magnetron by Chapin [18] in 1974.

The first paper about the planar magnetron arrangement from Chapin was published in 1974 [42]. After the basic developments of Penning the magnetron technology needed a time period of ~35 years until its industrial application started. In this time period numerous improvements regarding the magnetron hardware and the magnetic field arrangements have been made.

The elements of sputtering with the planar magnetron cathode are presented in Figure 2.2.

For the magnetron cathode the sheath thickness of the darkspace at the target can be estimated using the Child-Langmuir equation (2.6). From the Child-Langmuir equation the thickness of the dark space was calculated by using equation (2.7). For a power density of 10 W/cm^2 and a potential difference between the plasma and the target of -500 V in an argon discharge a small sheath thickness of $d_{\text{sheath}} = 0.695 \text{ mm}$ is achieved. Under these conditions it is expected that the sheath geometry follows the contour of the erosion profile. This results in a normal impact of the argon ions and does not require considering sputter yields under angular conditions for smooth and non-structured target surface conditions. Therefore sputter yields calculated for normal incidence conditions can be used.

Magnetron Cathode; - Ucath. (0.4 -0.8 KV)

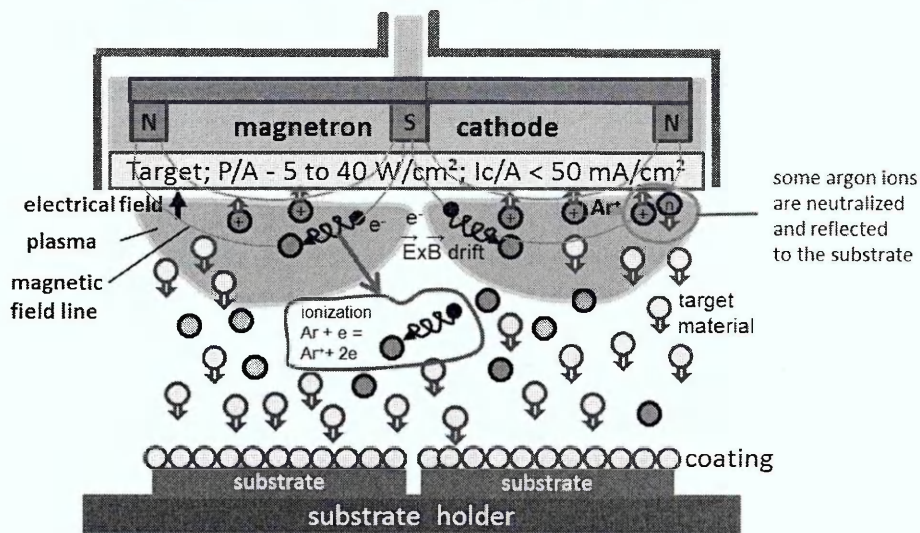


Figure 2.2 : Schematics of planar magnetron sputtering

Child-Langmuir-Equation used to estimate the dark space at the Magnetron cathode:

$$S^+ = \frac{4 \epsilon_0}{9} * \left(\frac{2e}{M} \right)^{1/2} * \frac{(U_{sheath})^{3/2}}{(d_{sheath})^2} \quad (2.6)$$

$$d_{sheath} = \left[\frac{4 \epsilon_0}{9} * \left(\frac{2e}{M} \right)^{1/2} * \frac{(U_{sheath})^{3/2}}{S^+} \right]^{1/2} \quad (2.7)$$

P/A =	10	W/cm ²	(typical power density)
P/A =	10 ⁵	W/m ²	(typical power density)
U _{sheath} =	500	V	(typical cathode voltage)
S ⁺ =	0.02	A/cm ²	(current density at cathode)
S ⁺ =	200	A/m ²	(current density at cathode)
ε ₀ =	8.854x10 ⁻¹²	As/V	(vacuum permittivity)
e =	1.602x10 ⁻¹⁹	As	(elementary charge)
u =	1.661x10 ⁻²⁷	kg	(unified atomic mass unit)
m _{Ar} =	39.95		(atomic mass of Argon)
M = u*m _{Ar} =	6.634x10 ⁻²⁶	kg	(mass of Argon ion)
d _{sheath} =			cathode dark space
d _{sheath} =	6.952x10 ⁻⁴	m	

Compared to the diode arrangement the magnetron cathode confines the electrons and therefore the glow discharge in front of the target. The interaction of the electron with a velocity which originates from the influence of the electrical field at the cathode and the parallel component of the magnetic field in front of the target that creates a Lorentz force on the electrons. The horizontal magnetic flux densities (B) in front of the target are in the range of 0.02 – 0.08 T which corresponds to 200 to 800 Gauss (often the magnetic field strength (H) is used in the publications in this case the range is from 15.9 to 63.7 kA/m which corresponds to 200 to 800 Oersteds) in front of the erosion profile at the line of maximum erosion. As a consequence the electrons follow the magnetic field lines having a gyration movement with a Larmor radius in the mm range and are confined in front of the target. The gyration movement of the electrons creates a longer travelling distance of the electrons through a unit volume in front of the target compared to a straight movement without the application of the magnetic field which results in more collisions with argon atoms and a higher charge density of the glow discharge plasma. This explains the higher ion current densities and deposition rates of more than one magnitude compared to the diode and the ability to use the magnetron cathodes at low pressures down to the 10^{-4} mbar range.

The magnetic field lines and a typical erosion profile in the target of a rectangular planar magnetron are shown in Figure 2.3. It is clearly seen that a magnetic tunnel is formed in front of the target. The trajectories of the electrons are shown at the target very schematically.

For magnetron sputtering typical rates of 1 to 10 nm/s were reported by Braeuer et al. [43]. For materials with high sputter yields like copper self-sustained sputtering is possible at high power densities of some tens W/cm². Under these conditions no process gas pressure is required for the discharge.

The plasma density and therefore the erosion in front of the target is influenced by the non-homogeneous horizontal component of the magnetic field. This results in an erosion profile in the target that reduces the target utilization to 20-30 %. By the use of special magnetic field and magnetic pole configurations such target utilizations can be improved by up to 50% without moving the magnetic field [44, 45].

A further step towards the improvement of the target utilization and the reduction of target poisoning at reactive sputtering was the use of a rotating cylindrical target in a rotatable magnetron arrangement. The rotating cylindrical magnetron, which was patented in 1982 by McKelvey [46], or the C-Mag™ magnetron [47] allow target utilizations of up to 90% to be achieved.

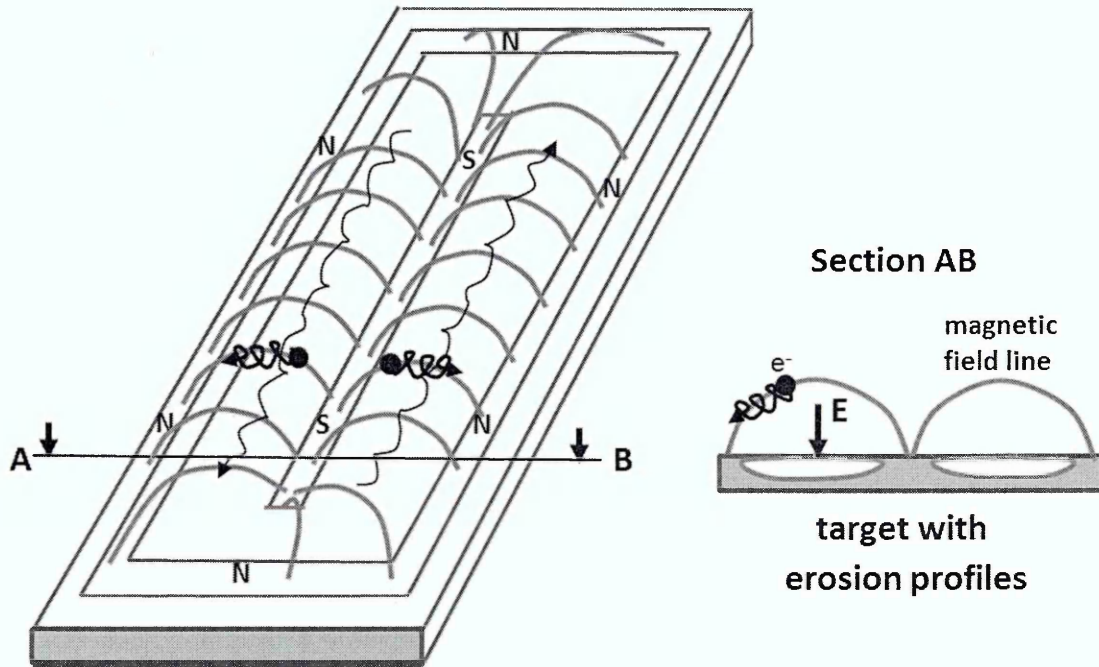


Figure 2.3 : Magnetic field lines, electron trajectories and a typical erosion profile for a rectangular planar magnetron

2.1.5 Reactive sputtering

The reactive sputtering process is used for the deposition of compound materials. Such compounds are achieved by the reaction of target material and the reactive gas. Typical reactive gases are e.g. N_2 , O_2 or carbon-bearing gases like e.g. methane or acetylene. As target materials metals, semiconductor materials like silicon or germanium are used in order to produce nitrides, oxides, carbonitrides or carbides. The plasma of the glow discharge supports the activation of the reactive species and therefore promotes the reactions and the formation of compounds. During reactive sputtering the target material also reacts with the reactive gas. Reaction products on the target, especially those with insufficient electrical conductivity, can cause target poisoning effects and hysteresis effects on the partial pressure, the deposition rate and the target voltage, depending on the mass flow of reactive gas. Under these conditions the reaction products on a poisoned target surface have a smaller sputtering yield compared to the "clean" target material which results in significantly reduced deposition rates. Measures to prevent target poisoning and to keep the deposition rates are important for the practice of reactive sputtering.

The target poisoning problem is more critical during reactive magnetron sputtering. Due to the non-uniform erosion of the target at specific locations of the sputter groove, like the groove edges, reaction products can be found.

The term reactive sputtering was already introduced by Veszi in 1953 [48].

But the first tools to control reactive sputtering were presented in the middle of the 1970s. Again it took a long time until reactive sputtering was used industrially which started in the early 1990s.

At the University of Uppsala reactive deposition of ZrN and TiN was systematically studied by Blom, Berg and Larson [49]. Berg presented a model for reactive sputtering [50, 51] which Larson used for reactive magnetron sputtering [52].

In the years 2003 and 2004 Depla et al. discussed the target poisoning during reactive magnetron sputtering in detail, by considering the influence of target poisoning through ion implantation on reactive sputtering processes [53, 54, 55]. The poisoning by ion implantation can be used as an extension of the Berg model [50].

A detailed review on modeling reactive sputtering processes was given by Berg and Nyberg in 2005 [56]. In this publication the role of the pumping speed in order to stabilize the reactive sputter deposition for a defined deposition rate, and the influence of the target reaction products to the “secondary” electron emission from the target at ion impact are discussed.

A more practice-oriented review on reactive sputtering was given by Musil et al. [57]. The dynamic behavior of the reactive sputter process was described by Kubart [58].

2.1.6 The unbalanced magnetron

Window and Savvides have studied the influence of the magnetic field on the substrate current for a circular planar magnetron [19] in 1986. The publication of Window and Savvides describes a dc magnetron with a magnetic field design for which the confinement of the electrons at the target region is broken up whilst maintaining a high ion flux to the target. For this special magnetron type the new name “Unbalanced Magnetron” was created by Window and Savvides [20]. The application of the unbalanced magnetron to ion assisted deposition and to modify the properties of the coatings was reported by Savvides and Window [21].

The principle of the planar unbalanced magnetron is shown in Figure 2.4. An unbalanced magnetron can be created from a normal magnetron by weakening of the magnetic field strength of the outer poles and strengthening the magnetic field strength of the inner pole(s) of the magnetic field array which would give a very small and focused plasma extension starting from the inner pole(s). The better procedure is to weaken the magnetic field of the inner pole(s) and strengthen the magnetic field of the outer poles of the magnetic field array which results in a wide zone of plasma extension starting from the outer poles as shown in Figure 2.4.

Unbalanced Magnetron Cathode; - Ucath. (0.4 -0.8 KV)

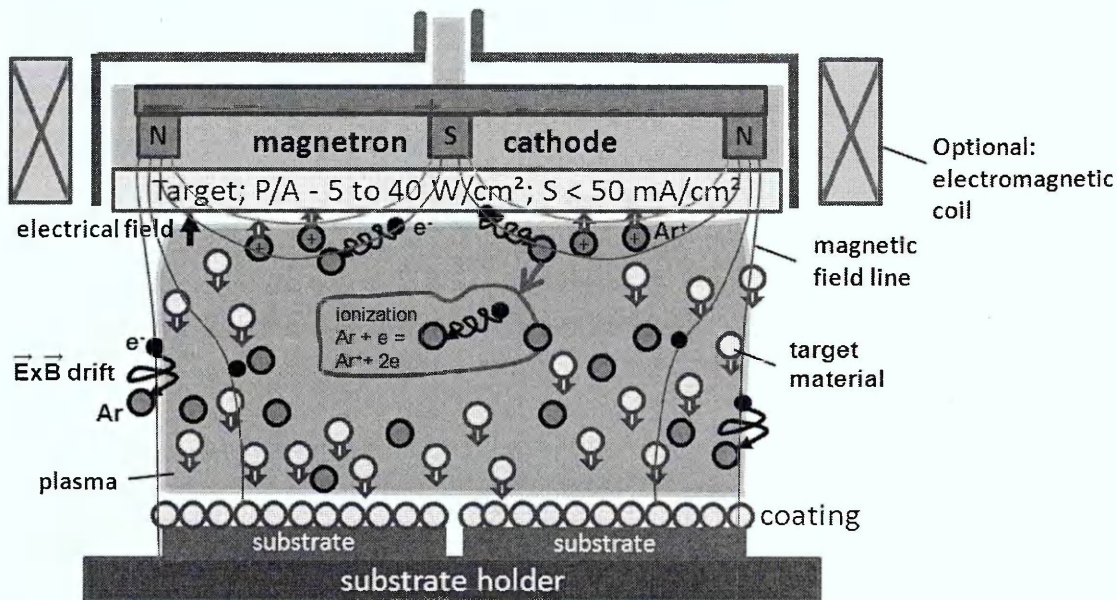


Figure 2.4 : Principle of the planar unbalanced magnetron cathode

Another method to achieve the unbalanced magnetron operation starts from a balanced magnetron cathode and is arranged with the use of an electromagnetic coil at the magnetron cathode. By operating the electromagnetic coil with direct current the magnetic field strengths of the outer poles of the magnetic field array are increased by the superposition of the magnetic fields of the coil and the magnet array of the magnetron. Under these conditions the magnetic field strength around the inner pole of the magnet array is weakened. This operation results in a controlled plasma extension as shown in Figure 2.4. Without the operation of the electromagnetic coil current, "normal" balanced magnetron operation conditions are present without the need of a change of hardware.

In the unbalanced operation mode of a magnetron cathode the plasma of the discharge is moved towards the substrate which offers at biasing of the substrate favorable conditions for ion plating. For well-designed unbalanced magnetron cathode arrangements high substrate current densities of some mA/cm^2 can be attained. For coating three-dimensional parts arrangements the use of a single unbalanced magnetron does not allow achievement of good tribological layer properties even if the parts are rotated. In order to overcome this problem unbalanced magnetron cathodes with changing magnetic polarities of the outer poles of the magnetic field arrays were used to form a magnetic

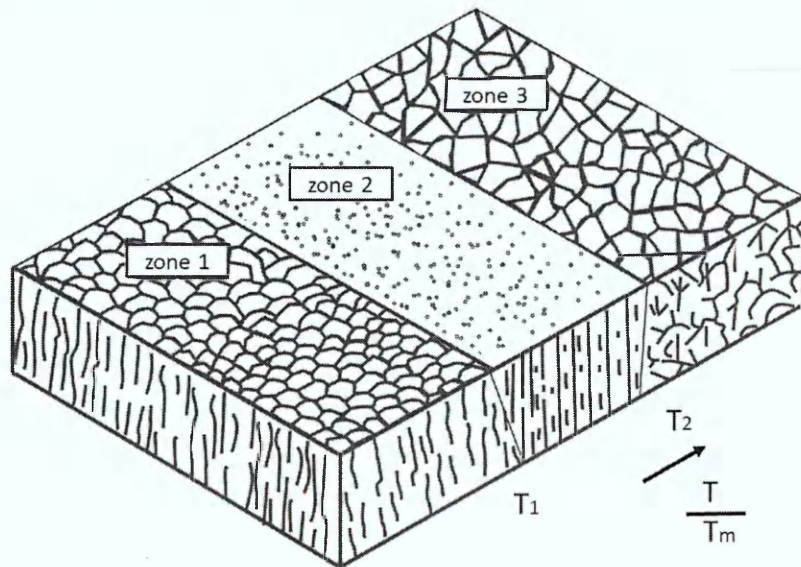
confinement for the electrons around region of three-dimensional parts. These conditions are present at the "Closed Field Arrangement" of Teer [59, 60, 61] which can be operated with two or more cathodes. Sproul [62] discussed multi-cathode arrangements of unbalanced magnetrons in 1991.

Hofmann et al. presented an unbalanced magnetron with opposing wide magnetic field array and anode [63, 64]. The opposing magnetic field array has opposite magnetic polarity of the outer poles compared to the outer magnetic poles of the magnetron. In this arrangement the effect of the unbalanced magnetron can be combined with the possibility of powering the anode in order to increase the plasma support. A good overview of the early status of the unbalanced magnetron can be found at Muenz [65]. Mapping of the plasma parameters of an unbalanced magnetron cathode was arranged by Kvasnica et al. [66] using a Langmuir probe technique. Characterization parameters for unbalanced magnetrons were presented by Svadkovski et al. [67]. Cathode current distributions on a circular unbalanced magnetron cathode target were evaluated by Clarke [68]. The plasma characteristic of the unbalanced magnetron has been investigated by Solov'ev [69].

2.1.7 Structure zone models for PVD coatings

The morphology of PVD coatings can be discussed using structure zone models which are very helpful in order to decide on necessary changes in coating or material strategies.

The first structure zone model was presented by Movchan and Demchishin in 1969 [70] for evaporated coatings based on studies on thick nickel, titanium, tungsten, aluminum oxide and zirconium dioxide films.



	zone 1	zone 2	zone 3
metals T/T_m	<0.3	0.3 - 0.45	>0.45
oxides T/T_m	<0.25	0.25- 0.45	>0.45

Figure 2.5 : Structure zone model for evaporated coatings, redrawn according to B. Movchan and A. Demchishin [70]

The structure zone model (SZM) of Movchan in Figure 2.5 shows the influence of the homologous temperature defined as absolute temperature T at deposition divided by the melting temperature T_m of the evaporated material on the microstructure of evaporated coatings.

In the case of evaporation the energy of the evaporated particles is low and is mainly defined by the temperature of the evaporation process. During the evaporation process at a temperature of 1500 K the average particle energy is 0.19 eV.

The SZM of Movchan can be used for all evaporation processes with particle energies in the range of 0.1 to 0.3 eV. The particles that stick on the surface,

the adatoms (adsorbed atoms) can be desorbed or reach nucleation after a surface diffusion process. At the time of the particle impact to the substrate the condensation energy and the kinetic energy are transferred to the substrate.

The structure zone 1 is present at low homologous temperatures of < 0.3 and is characterized by low adatom mobility conditions and self-shadowing effects. The surface mobility is not high enough to arrange compensation between different nucleation sites which results in tapered columns and open grain boundaries causing a porous microstructure.

In the range of homologous temperatures of 0.3 to 0.45 structure zone 2 is located which is characterized by increased adatom mobility, columnar grain structures and a dense grain boundary microstructure. This allows achieving dense coatings of high mass densities and low surface roughness. In structure zone 2 the grain size increases with increasing homologous temperature.

Zone 3 structure which is located at homologous temperatures above 0.45 is characterized by the effects of bulk diffusion and recrystallization with grain coarsening at increasing temperature. The result is a polycrystalline microstructure of high mass density. The temperature range of structure zone 3 can be used for epitaxial growth.

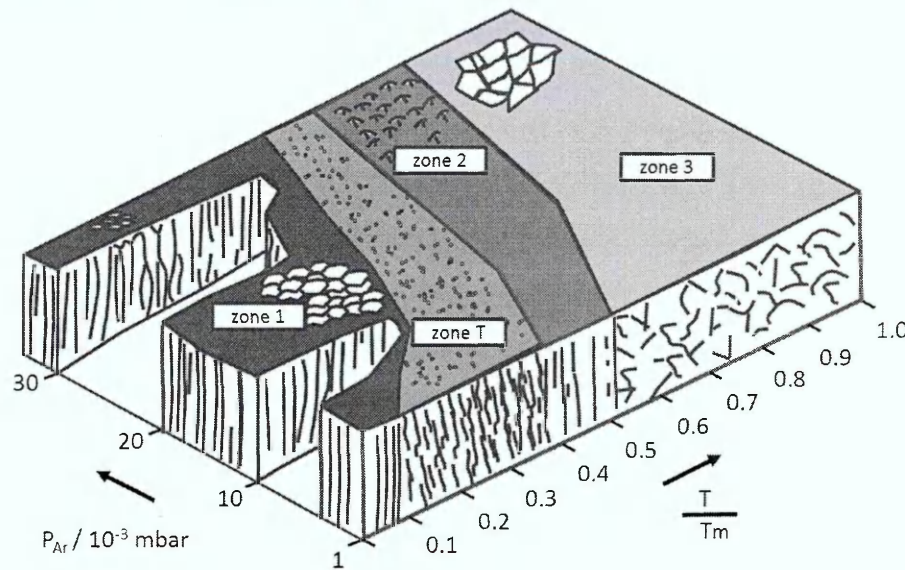


Figure 2.6 : Structure zone model for sputtered coatings, redrawn according to J. Thornton [71]

The structure zone model of Thornton [71] which was published in 1974 can be used for coatings deposited by the sputtering processes. The sputtering conditions are characterized by high particle energies of 4 to 40 eV compared to

the low energies at evaporation. The SZM of Thornton presented in Figure 2.6 shows the influence of the homologous temperature and the inert gas pressure (mainly argon is used) on the microstructure of sputtered coatings.

The higher energy of the sputtered particles results in a higher surface mobility which reduces the effect of self-shadowing in structure zone 1 at low pressure. With an increase in pressure the sputtered particles lose energy through collisions with the gas atoms of the process atmosphere in the vacuum chamber. This reduces the surface diffusion and increases porosity of the microstructure which results in tapered columns and voids similar to the zone 1 of Movchan's SZM.

At sputtering a transition zone T is observed which is characterized by a dense microstructure with fibrous grains, less voids and increased mass density compared to zone 1, due to increasing surface diffusion and nucleation during growth. Zone T moves to higher temperatures at increasing pressures.

In the Thornton SZM zone 2 and zone 3 can be explained in the same way as was discussed for the Movchan SZM.

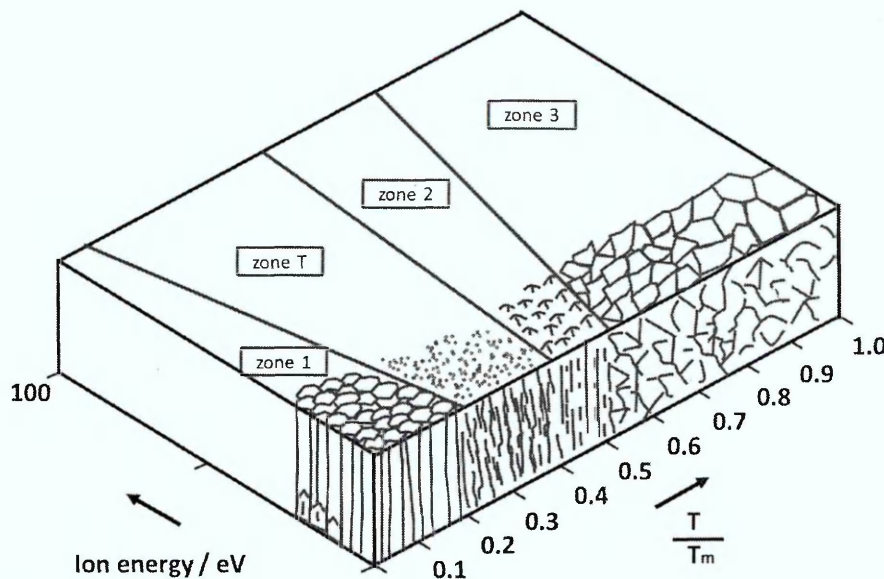


Figure 2.7 : Structure zone model for sputtered coatings, redrawn according to R. Messier [72]

The SZM of Messier and Giri [72] of 1984 can be used for ion plating conditions and shows the structure zones depending on homologous temperature and ion energy.

From Messier's SZM which is shown in Figure 2.7 it can be found that with increasing ion energy the transition from zone 1 to zone T is shifted to lower temperatures.

Messier's SZM does not include the effect of the ion current density which has a significant influence. Therefore Anders [73] presented in 2010 a structure zone model for plasma-based deposition and ion etching. In the SZM of Anders [73] a generalized temperature, a normalized energy flux and a thickness dependence of the structure are taken into account.

2.2 Chemical vapor deposition

2.2.1 History of chemical vapor deposition

Chemical vapor deposition (CVD) is a method that is used for the deposition of coatings on heated substrate surfaces. The coating procedure employs dissociation and/or chemical reactions. The temperatures for coating typically range from 200 to 1600 °C. Coatings with high density and high purity can be produced with controlled microstructure.

The CVD deposition is arranged starting from a gas or gas mixture which surrounds the substrates and is therefore capable to allow coating of complex substrate arrangements at non line of sight.

In one of the first CVD processes nickelcarbonyl $\{Ni(CO)_4\}$ was synthesized by Mond [74] in 1890 using the reaction of nickel with carbon monoxide. This was a pioneer step for the synthesis of carbonyl compounds of vanadium, chromium, manganese, iron and cobalt. By the end of the 19th century the carbonyl process of Mond was applied for the refining of nickel as one of the first industrial CVD processes [75]. For coating of carbon lamp filaments with tungsten the patented CVD process of De Lodyguine in 1893 [76] which based on the reduction of WCl_6 by H_2 was used. The production of other pure metals like Ti, Zr, and Ta followed using the Mond process, the van Arkel process and other methods.

In the early 1970s the use of the CVD process on semiconductors started successfully. The results from this field pushed the application of CVD in other industrial fields.

Plasma enhanced chemical vapor deposition (PECVD) has its roots in the works of Atl and Ing [77, 78, 79] published during the time 1963 to 1965. In the PECVD process the dissociation and chemical reactions are forced by the assistance of the plasma of a glow discharge where excitation and dissociation can be easily arranged at low temperatures by collisions with energetic electrons of the discharge. PECVD processes using radio frequency (13.56 MHz) with direct capacitively coupled or indirectly coupled plasma are widely used but also ECR, microwave (MW) and special direct current (DC) methods are used to supply the plasma with energy.

2.2.2 Deposition of carbon-based coatings

Deposition of diamond particles by a CVD process from CO, CO₂ and from hydrocarbon gases including CH₄ using seed crystals was filed by Eversole in 1958 [80]. Only very low growth rates for the diamond material were achieved having a simultaneous deposition of graphitic material.

Angus et al. [81] deposited in 1968 diamond at a temperature of 1050°C at 0.4 mbar pressure using methane gas. Improved diamond growth rates were achieved by Derjaguin et al. [82] with mixtures of hydrocarbon gases and hydrogen at high hydrogen contents.

During diamond deposition the addition of hydrogen offers the capability of etching off graphitic impurities.

Industrial deposition conditions were reached by a Japanese research group using the hot filament method (see Matsumoto et al. [83]) in 1982 and using a microwave plasma (see Kamo et al. [84]) in 1983.

For applications that required optimized diamond properties and a fine grained nanocrystalline microstructure with a smoother surface of the coating, the conventional diamond deposition process using 1% CH₄ + 99% H₂ according to Celi and Butler [85] was not sufficient. In order to achieve nanocrystalline diamond (NCD) Angus and Hayman [86] and other researchers used mixtures of methane and argon but only small quantities of diamond were received in the films.

A special solution was found in MW discharges at about 750°C with fullerene C₆₀ as precursor in C₆₀/Ar mixtures making use of the fragmentation process of C₆₀ which was discovered by Gruen [87]. NCD coatings with <100 nm crystallite size are achieved compared to μm grain sizes of conventional diamond coatings. NCD coatings have electrical conductivity due to the existence of π-bonds at the grain boundaries which quantitatively increase at decreasing grain size.

With the hot filament method Haubner et al. [88] produced NCD in 1993.

A better understanding of the mechanisms for diamond deposition was achieved by using the results obtained from the fullerene-based technology.

This enabled, after further research, the deposition of NCD using 1% CH₄ + 99% Ar as reported by Zhou et al. [89] in 1998. In this publication the transition from μ c-diamond to NCD is discussed. Ultrananocrystalline diamond films (UNCD) with crystallite sizes < 10 nm were prepared at temperatures down to 500 °C by McCauley et al. [90] and at 400 °C by Sumant et al. [91].

In the last decade intensive research work has been carried out on carbon nanotubes (CNTs) which are grown by the PECVD method by Meyyappan [92, 93].

The deposition of DLC coatings by the PECVD process using different C_xH_y precursors was studied in a joint research program of Fraunhofer IST and the University of Chemnitz (both located in Germany) between 2007 and 2009. The final report of the AIF research project IGF 15221 BG can be downloaded over the web [94]. The data and references [95, 96, 97, 98, 99, 100, 101, 102, 103, 104, 105, 106, 107] for Table 2.1 have been taken from this report.

Ref.	Method	Energy for the plasma discharge	Type of substrate bias	Gases	Rate [$\mu\text{m/h}$]	Hardness [GPa]
[95]	ECWR ion source	ICP 27 MHz + magn. field	DC	$\text{CH}_4 + \text{Ar}$	1.3	24
[96]	ECR	ECR microwave	MF, asymmetric bipolar pulsed	$\text{C}_2\text{H}_2 + \text{Ar}$	3.2	31
[97]	ECR	ECR microwave	DC	$\text{CH}_4 + \text{Ar}$	0,6	18
[98]	RF HCD - RF	Planar 13.56 MHz hollow cathode discharge	RF self-bias	$\text{Ar} + \text{He} + \text{C}_2\text{H}_2$	6.6	17.5
[99]	Dual DC/RF	13.56 MHz RF	DC	$\text{H}_2 + \text{CH}_4$	0.2	14
[100]	ECR	ECR microwave	RF self-bias	$\text{CH}_4 + \text{Ar}$	1.6	
[101]	bipolar DC PACVD	-	20 kHz bipolar pulsed	$\text{CH}_4 + \text{Ar} + \text{H}_2$	2.5	20
[102]	Plasma based Ion implantation	-	Bipolar HV pulses	C_2H_2	0.4	18
[103]	MEPCVD	CC RF + magnetic field	RF self-bias	CH_4	0.8	19
[104]	Plasma based Ion Implantation	Microwave	- 2kV pulses (1% dutyc.) + -200V DC	CH_4	1.1	12
[105]	ECWR (COPRA) ion source	ICP 13.56 MHz + magnetic field	RF powered extraction electrode	C_2H_2	5.8	about 60
[106]	ECR	ECR microwave	DC	$\text{H}_2 + \text{CH}_4$	0.2	16
[107]	expanding thermal plasma	DC plasma arc		$\text{Ar} + \text{C}_2\text{H}_2$	252	13

Table 2.1 : Published DLC coating combinations of plasma, substrate bias and used gas species on the deposition rate and the microhardness DLC coatings using data and references of the joint research program of the Fraunhofer IST Institute and the University of Chemnitz [94]

2.2.3 Deposition of silicon based coatings

A typical application of PECVD is the deposition of hydrogenated silicon nitride layers as antireflective and passivation layer on crystalline silicon solar cells [108, 109]. For the Si_3N_4 deposition silane or mixtures of silane and ammonia are used at substrate temperatures of 50 to 450°C. Another example for the solar cell application is the coating with silicon dioxide using nitrogen, silane and nitrous oxide (N_2O) mixtures [110]. SiO_2 or silicon-oxide based wear protective films were deposited on polycarbonate by a special arc plasma torch starting from oxygen and organosiloxane [111] precursors. These SiO_2 coatings contain a small content of hydrogen. Fahland of Fraunhofer FEP [112] reported on the application of microwave and high-frequency PECVD for the deposition of silicon-based polymer coatings. Such polymers show higher density, hardness and better barrier properties compared to chemically cross-linked polymers.

For electronic and microelectronic applications thermal CVD processes are used to deposit poly-silicon, silicon dioxide and silicon nitride. The types of precursors and temperatures for the following examples of thermal CVD deposition were taken from Ohring [113]. Si is deposited from SiCl_2 , SiCl_3 (1050-1200 °C) or SiCl_4/H_2 (600-700 °C). For SiC coating at 1100°C a mixture of SiCl_4 , toluene and H_2 can be used. SiO_2 can be deposited at 450 °C starting from SiH_4 and O_2 as precursors. For Si_3N_4 deposition at 750 °C SiCl_2H_2 and N_2O are reported. Using the PEVCD process and a mixture of SiH_4 and H_2 amorphous silicon can be deposited at 300 °C and polycrystalline silicon at 400°C. Fraunhofer IST reported on a special thermal hot wire activated CVD process developed for the deposition of a-Si:H/ $\mu\text{c-Si:H}$ coatings on a large substrate area of 500 mm x 600 mm using an inline coating system with silane and hydrogen as precursors [114]. The SiC deposition was arranged by CVD at 1500 to 1700 °C using SiH_4 and C_3H_8 or monomethylsilane (SiH_3CH_3) at < 850 °C. If the PECVD process is used for SiC coating from a mixture of silane and methane the substrate temperature is reduced to a range of 250 to 800 °C. Details on the SiC deposition process with monomethylsilane precursor are discussed by Habuka [115].

The PECVD deposition and the properties of silicon doped DLC (Si-DLC) coatings will be discussed in the following chapters.

2.3 Overview on carbon based materials

2.3.1 History of DLC coating

During carburizing experiments in a DC glow discharge Schmellenmeier [116] achieved under the condition of a low discharge current, using a mixture of argon and acetylene (C_2H_2), shiny black amorphous deposits of high hardness. These coatings, which were discussed in 1953, are expected to be the first DLC coatings. In 1956 the morphology of the deposited carbon-based coatings were more carefully analyzed by Schmellenmeier [117] using X-ray diffraction. Two strong diamond lines were found in the Debye-Scherrer-diagram. In the absence of strong graphite lines amorphous and crystalline regions were found showing a diamond-like structure.

Aisenberg and Chabot [118] used an ion beam deposition method to deposit diamond-like carbon. A low-pressure deposition chamber which contains a biased substrate in combination with a source chamber with a high-pressure arc is used. The carbon ions from the source chamber are used for DLC deposition and the discharge in the deposition chamber can act as a source of carbon ions. Using magnetic field assistance for the discharge, low-pressure operation and more ionization are achieved in the deposition chamber. The carbon ions are accelerated to a negatively biased substrate which can be powered by AC or RF at the deposition of insulating films. Amorphous and crystalline diamond-like carbon coatings were deposited. Insulating DLC films with resistivities of up to $10^{11} \Omega\text{cm}$ or more were achieved.

Whitmell and Williamson [119] used a DC glow discharge in a $\frac{1}{2}$ inch diameter pipe using ethylene as hydrocarbon gas. In front of the substrate, which was positioned on the cathode, a domed aperture was used to arrange a charge compensation at DLC coated substrates by electrons emitted from the dome edges. Hard, black-colored diamond-like carbon coatings were achieved on titanium alloy substrates.

Holland and Ojha [120] circumvented the discharge problems with insulating substrates by using RF plasma with a π -matching network having the substrates positioned on the RF powered cathode. DLC was deposited using butane (C_4H_{10}) as hydrocarbon gas in the RF diode glow discharge. At target

bias voltages of -430 to -750 V resistivities of 5×10^9 to $3.6 \times 10^{11} \Omega/\square$ were achieved.

Weissmantel et al. [121] deposited DLC using a dual ion beam configuration. Carbon was sputter deposited from a graphite target and the ion bombardment of the growing film was arranged from the second ion source using argon and methane ions.

Enke et al. [122] used an RF diode arrangement to deposit tribological hard DLC coatings in an argon acetylene mixture. The DLC coatings which were tested in nitrogen atmospheres at different relative humidities (RH) showed extremely low friction coefficients of 0.01 to 0.02 up to $RH < 1\%$.

In 1981 Andersson [123] reviewed the existing DLC deposition techniques and discussed DLC-like coatings from hydrocarbon gases in his publication from 1979 [124]. McKenzie et al. [125] used reactive post cathode magnetron sputtering with acetylene as a hydrocarbon gas in order to achieve amorphous carbon films for solar absorbers.

DC sputtering from cylindrical and planar magnetrons in argon and acetylene was used by Craig and Harding [126] in order to deposit a-C:H coatings from a metal cathode that was overcoated with carbon. The DLC layers were used as antireflective coatings on selective solar absorber cermet coatings.

Hofmann [127] filed a patent in 1984 for a combination of a planar magnetron with an opposing RF biased substrate to deposit DLC starting from metal targets using hydrocarbon gas. The patent that was granted in 1992 describes coating of molded parts using opposing magnetron cathodes. Using this method the deposition of DLC starting from a titanium target in an argon acetylene mixture was discussed at the IPAT conference 1985 [128]. Metal-free DLC coatings of high hardness were achieved at high acetylene mass flows having the active target surface completely covered with carbon from the discharge.

Various Me-DLC (a-C:H:Me) coatings including W-DLC were presented by Dimigen [129] in which the wear rates, the friction coefficients and electrical conductivity were discussed.

W-DLC layers were deposited on molded parts [130] using a planetary substrate arrangement and unbalanced magnetron cathodes with opposing magnetic field array in 1991. This plasma booster arrangement allows coating of large volumes [131]. Details on the plasma booster technology will be discussed in chapter 4. More information about the history of DLC coating are found in the publications of Hofmann et al. [132] and Bewilogua and Hofmann [133].

2.3.2 Comparison of properties for carbon-based materials

The properties of different crystalline and amorphous carbon-based materials are compared in Table 2.2. In order to classify the tetrahedral carbon (ta-C) and the hydrogenated diamond-like carbon-based coatings (a-C:H-based) the properties of crystalline graphite and crystalline diamond are provided. Depending on the manufacturing conditions ta-C and the a-C:H based coatings show significant differences in the diamond-like character which is mainly characterized by the number density of sp^3 - diamond bonds. In pure diamond, which is shown in Figure 2.8 according to Pierson [134], we see as gray shaded areas the three dimensional sp^3 covalent bonds located in the diamond structure. These sp^3 bonds are characterized by 4-fold coordination of carbon atoms and a characteristic angle of 109.5° between the orbitals.

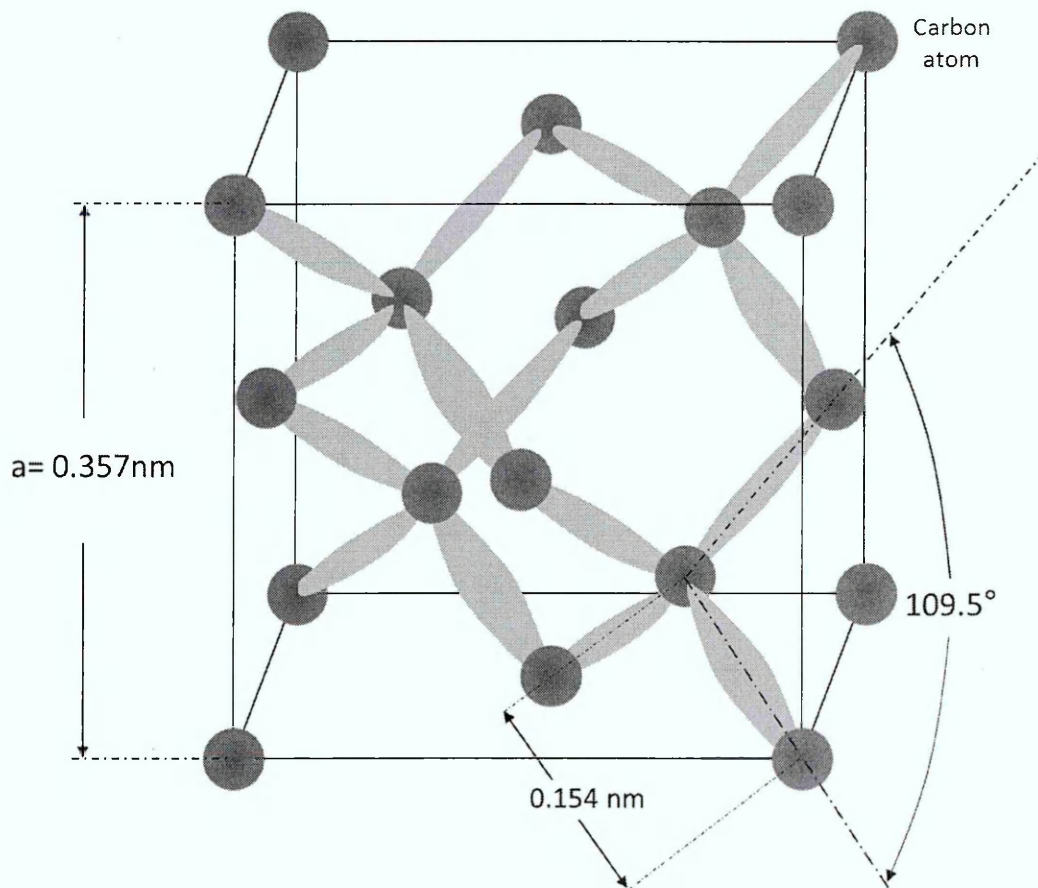


Figure 2.8 : Three dimensional sp^3 covalent bonds in a diamond structure as gray shaded areas (regions of high electron density), redrawn according to Pierson [134]

At the deposition of a-C:H hydrocarbon gases are commonly used which results in the incorporation of hydrogen into the a-C:H. If high quantities of hydrogen are present in the a-C:H polymeric hydrocarbon can be found in the coating. For these polymeric deposits sp^3 hybridization can be observed at C-H bonds e.g. in the methane molecule (C-H hybrid bond length 0.109 nm). Therefore these sp^3 bonds do not increase the diamond character of the a-C:H but promote the reduction of the hardness and the wear resistance.

The a-C:H also contains graphitic sp^2 bonded carbon. In the graphite lattice of the ABAB...-type which is shown in Figure 2.9 we see polyhedrons of 6 carbon atoms which are combined in planes with a distance of 0.335 nm between the planes. The carbon atoms in the polyhedrons create a stable network of 3-fold coordinated sp^2 bonded carbon (sigma bonds at a binding length of 0.142 nm). Between the planes weak π -bonds of carbon (van der Waals forces) are located.

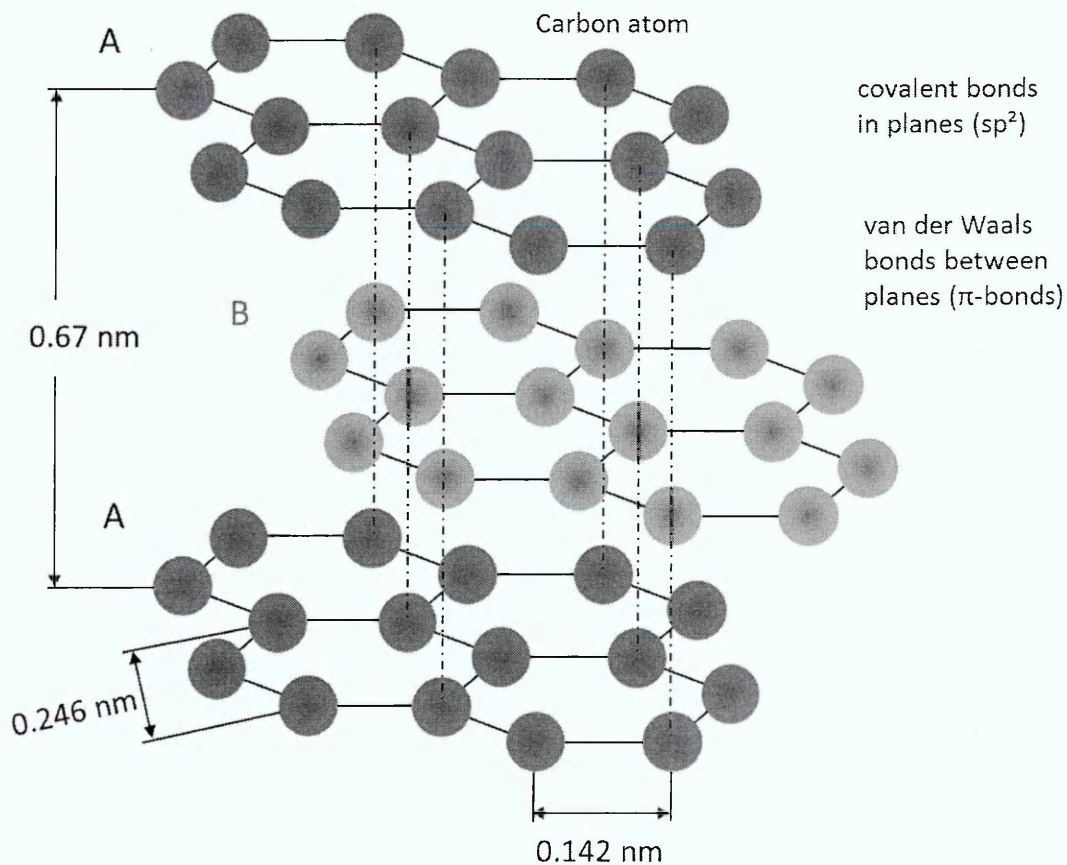


Figure 2.9 : Crystal structure of graphite

The bond strength of the sp^3 bond in diamond is very high with about 7.02 eV but the bond strength of the sp^2 bond in graphite is slightly higher with about 7.03 eV as discussed by Neuville [135].

	Diamond crystalline	ta-C tetrahedral carbon	a-C:H-based	Graphite crystalline
Mass density [g/cm ³]	3.515	1.9 – 3.1	0.9 – 2.4	2.267
sp^3 content	100%	40 – 90%	10 – 70%	0
Hydrogen content	0	< 1 at. %	7 – 65 at. %	0
Compressive stress [GPa]		2 – 6	0.1 – 2.5	
Hardness $H_{U_{PL}}$ [GPa]	100	50 – 80	10 – 45	< 5
Young's Modulus [GPa]	910-1150	200 – 600	100 – 250	9 – 15
Friction Coefficient (dry in air)	< 0.2	0.15 – 0.2	0.05 – 0.2	0.2 – 0.1
Band Gap [eV]	5.45	1.0 – 2.5	0.4 – 1.7	- 0.04
Max. operating temperature [°C]	600 – 1200	450 – 600	350 – 500	400 - 600

Table 2.2 : The properties of technically-used carbon-based material compared to hydrogenated diamond-like carbon-based coatings (extremely high and low values are not included in this table)

The data in Table 2.2 is taken from the references [136, 137, 138, 139, 140, 141, 142, 143, 144, 145, 146, 147, 148, 149, 150, 151, 152, 153, 154, 155, 156, 157, 158], own research results and data from the Fraunhofer IST research institute. The DLC based coatings include “pure” a-C:H, Si-DLC (a-C:H:Si) and industrially used Me-DLCs (a-C:H:Me) like W-DLC (a-C:H:W) and Ti-DLC (a-C:H:Ti)

Review papers which contain data regarding the properties of carbon-based materials as shown in Table 2.2 are found in references [159, 160, 161, 162, 163, 164].

2.3.3 Classification, structure models and the subplantation model for DLC

The first ternary diagrams for DLC coatings were presented from the group Moeller [165, 166] but in these diagrams the zones for the different types of DLC are not presented. In the first diagram of Robertson [167] ta-C:H, a-C:H, a-C and ta-C are indicated. A ternary diagram that shows the different DLC types in marked zones was presented by Ferrari and Robertson in 1994 [168]. In this diagram only a small region of sputtered a-C can be found which is marked as sputtered coating. The widely used diagram that was presented by Robertson in 2002 [161], shown in Figure 2.10, was extended by a new wide region of sputtered a-C(:H) which includes a-C and a-C:H with hydrogen contents of up to 30%. This region is overlapping with a-C:H produced by other methods of which PECVD is most commonly used. The overlapping of the regions indicates a combination of sputtered a-C:H and PECVD deposited a-C:H which has been used in the experiments described in chapter 4.

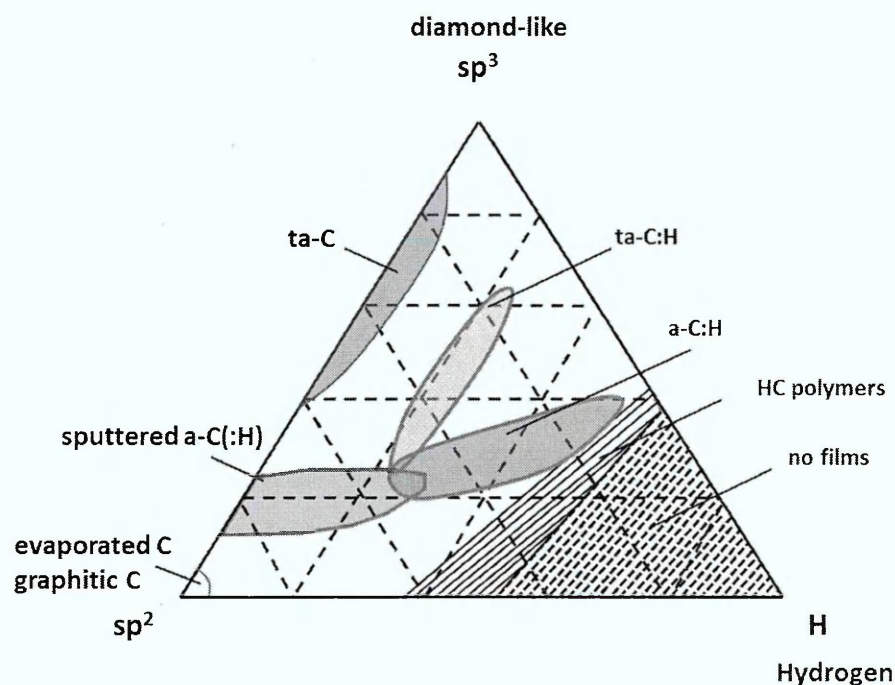


Figure 2.10 : Ternary phase diagram of diamond-like carbon types, redrawn according to Robertson [161]

Diamond (crystalline carbon) and amorphous diamond-like carbons are classified in order to assist the industrial application of such coatings by the

German VDI 2840 standard [169] of 2012 which divides the amorphous diamond-like carbons into hydrogen-free and hydrogenated films.

Phillips presented first structural models for amorphous materials in 1979 [170] and 1981 [171]. In these models a constraint counting method for random covalent networks was used. Mechanical constraint is achieved for 3 degrees of freedom therefore a ta-C coating with 80% sp^3 hybridized 4-fold coordinated carbon bonds is highly overconstrained which is combined with a high stress level of the coating. Whereas an a-C:H coating with a high atomic concentration of hydrogen with non-rigid networks tends to be underconstrained.

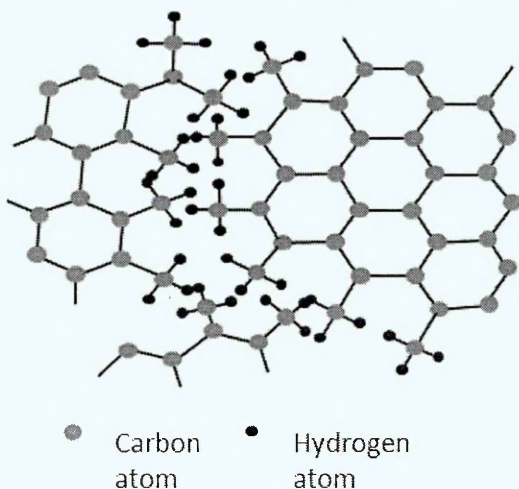


Figure 2.11 : 2-D structure model of a-C:H (1981), redrawn according to McKenzie and Briggs [125]

Figure 2.11 shows one of the first two-dimensional network models for a-C:H which was presented by McKenzie and Briggs [125] in 1981. Thorpe [172], classified in his theory for random networks of 1983, the covalent networks into polymeric glasses and amorphous solids with rigid networks. Using electron diffraction Bewilogua et al. [173] showed that for amorphous carbon preferentially five and six-fold carbon rings appeared. In 1984 the random network model was specifically discussed by Beeman [174]. Robertson [175] presented in 1987 sp^2 sites organized in compact clusters of fused six-fold rings. In a random covalent network model Angus and Jansen [176] showed that a fully constrained carbon network is achieved for hydrogen concentrations in the range of 16.7 to 61.5 at.%. The “Defected Graphite Model” of Tamor [32] of 1990 predicted a stable range at 20 to 60 at.% hydrogen for a-C:H with graphitic six-fold carbon rings as matrix. In 1991 Angus and Wang [177]

discussed 2-D network models for a-C:H which include sp^3 and sp^2 hybridization of carbon and the saturation of dangling bonds with hydrogen atoms which is shown in Figure 2.12.

Frauenheim et al. [178] used in 1995 density-functional-based (DF) molecular dynamic (MD) modeling to present the electronic and three dimensional structural properties of a-C:H and ta-C.

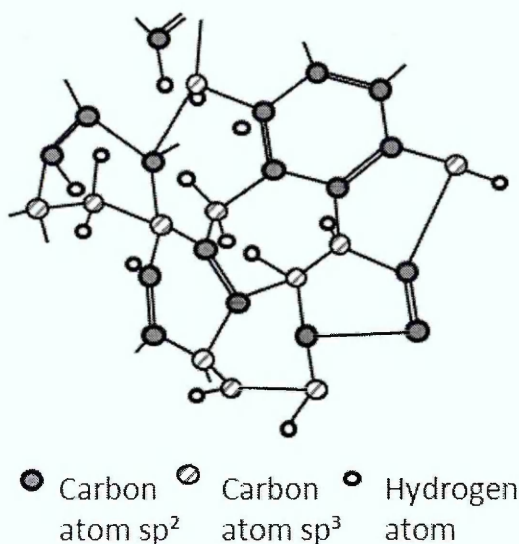


Figure 2.12 : 2-D structure model of a-C:H (1991), redrawn according to Angus and Wang [177]

The subplantation model which was first presented by Lifshitz et al. [179] in 1989 is used to describe the formation of sp^3 hybridized C-C bonds during the growth of DLC films under the presence of ion bombardment. During carbon ion bombardment the penetration of C atoms into the subsurface zone can be expected to cause increasing stress and density for the coatings. In the subplantation model the impact of “hyperthermal” incident ions which can be described as “thermal spike” is followed by a relaxation process. At too high ion energies graphitization is observed.

In 1993 Robertson [180] discussed the subplantation for ta-C coatings and showed that the increase of density correlates with the change of sp^2 into sp^3 hybridized carbon. Schwan et al. [181] showed in 1996 direct subplantation with carbon ions and indirect subplantation arranged by knock-on penetration with argon ions for magnetron sputtering. By Hofsaess et al. [182] the subplantation models which were present until 1998 were critically discussed.

The subplantation model of Miyagawa et al. [183] describes subplantation during the deposition of a-C:H using a methane-based plasma. At the hydrogenated surface region hydrogen and carbon are released by sputtering effects. From the subsurface region atomic hydrogen is released by collision cascades, knock-on hydrogen atoms are released by forming H₂-molecules and subplanted carbon atoms arrange the formation of sp³ hybridized C-C bonds. Both the subplantation and the release of hydrogen, which are a consequence of the ion bombardment, increase the mass density of the deposited a-C:H as well as the sp³ content.

2.3.4 Basic friction mechanisms for carbon-based coatings

Table 2.3 shows the friction mechanisms under dry (non-lubricated) conditions for various types of carbon-based coatings according to Erdemir and Donnet [184]. It is visible that the environment for interaction combined with the coating composition influences the coefficient of friction significantly. It can also be found that the friction coefficient increases with higher bond energies at the sliding contact where hydrogen from the coating passivates the dangling bonds at the surface and the humidity of the atmosphere plays an important role.

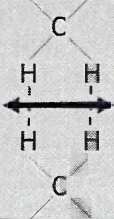
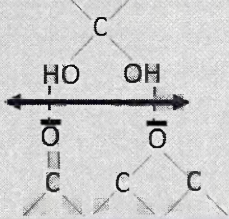
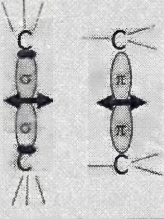
Type of DLC	a-C:H	a-C:H or a-C	ta-C and a-C
Friction coefficient	<0.02	0.1 – 0.2	>0.5
Nature of interaction	Van der Waals	Hydrogen	σ- or π-bond
Energy [eV/bond]	0.08	0.2	0.4 – 0.8
Type of interaction			
Environment for interaction	Inert gas or UHV	Humid atmosphere	UHV

Table 2.3 : Friction of carbon-based coatings in various atmospheres, redrawn according to Erdemir and Donnet [184]

For the Si-DLC (a-C:H:Si) Oguri and Arai [185, 186] reported that hydrated silica created by wear can act as a lubricant under humid conditions and Hioki [187] showed that the SiO bonds play an important role in friction reduction at high humidity.

Today friction can be simulated on an atomic or molecular scale, more information can be found in the review and guide of Dong et al. [188] from 2013. Another current field of application is the use of the DLC coatings under lubricated conditions.

In such applications the combination of coatings and lubricants and the use of additives have to be carefully evaluated for the present range of operational conditions. For these applications the surface free energy of the coating material has a significant influence on the frictional behavior [189, 190, 191]. In publications [192, 193, 194, 195, 196, 197, 198, 199, 200, 201, 202] the effect of the type of lubricant on the friction for DLC coated parts with or without the use of additives is discussed. Dry to lubricated conditions are compared for the DLC application on valvetrain components by Gangopadhyay et al. [203] in 2011.

2.3.5 Properties of hard and soft amorphous hydrogenated carbon (a-C:H) coatings

The basic layer properties of a-C:H-based coatings have already been discussed in chapter 2.3.2. The a-C:H coatings can be divided into hard and soft coatings depending on the hydrogen content in the films. Coatings with less than 40 at.% hydrogen show increasing hardness with decreasing hydrogen content caused by an increasing fraction of sp^3 type C-C bonds. For hydrogen contents above 40 at.% the polymeric character of the coatings increases with increasing hydrogen concentration and the sp^3 content of the coatings increases as well. In this region the sp^3 bonds also originate from C-H bonds in the hydrocarbons which cause softening of the coatings.

A more detailed view to a-C:H properties divided into soft a-C:H and hard a-C:H is given Table 2.4. The data is taken from the references [159, 160, 161, 162, 163, 164, 184, 204, 205, 206, 207, 208, 209, 210], own research results and data of the Fraunhofer IST research institute.

	a-C:H soft	a-C:H hard
Mass density [g/cm ³]	0.9 – 1.6	1.6 – 2.4
Crystal structure	amorphous sp^1 , sp^2 , sp^3	amorphous sp^2 , sp^3
sp^3 content	10 – 70%	30 – 60%
Hydrogen content	40 – 65 at. %	10 – 40 at. %
Compressive stress [GPa]	0.5 – 1	1 – 2.5
Hardness HU_{PL} [GPa]	10 – 15	15 – 45
Young's modulus [GPa]	100 – 150	150 – 300
Friction coefficient		
μ in vacuum	<0.01 - 0.02	0.02 - 0.08
μ in dry N ₂	0.01 - 0.03	0.03 - 0.06
μ in air ~50% humidity	0.1 - 0.5	0.1 - 0.2
Band gap [eV]	1.7 – 4	1.1 – 1.7
Refractive index (λ : 400-500 nm)	1.2 - 1.8	1.8 - 2.6
Max. operating Temperature [°C]	200 - 350	350

Table 2.4 : Properties of hard and soft a-C:H coatings
(Extremely high and low values are not included in this table)

2.3.6 Friction of amorphous hydrogenated carbon (a-C:H) coatings

The friction and wear properties of a-C:H and a-C:H:Si coatings are most important in order to describe the tribological behavior of these coatings. These properties and the related explanations and hypotheses have been studied intensively and the results are shown in this section of the literature review. Other properties which influence friction and wear behavior such as hardness, elastic modulus and residual stress have been basically discussed in the previous chapters. Some further details are presented in the following chapter "results and discussion".

Hydrogenated amorphous diamond-like carbon is a mixture of amorphous diamond, graphite and, in some cases, polymeric carbon which typically contains 20 to 40 at.% of hydrogen. From the material itself the wear behavior of a-C:H is significantly influenced by the presence of graphite with sp^2 bonds, sp^3 C-C diamond bonds and sp^3 or sp^1 C-H polymer related bonds which define mechanical properties like hardness, elastic modulus etc.. Typically the friction coefficients and the wear rates are derived from sliding wear conditions using the "ball-on-disk" test or a "linear oscillation movement" relative to a mating ball in a defined atmosphere or under vacuum conditions. The friction and wear test results are influenced by the following conditions:

- Material properties and production conditions of the tested a-C:H coating
- Material of the wear counterpart (often used are steels, Si_3N_4 , WC, SiC, Al_2O_3 , ZrO_2 , sapphire, $TiAl_6V_4$). Sometimes the wear counterpart is also coated with a-C:H
- Ball diameter or tip radius of the wear counterpart (diameter range 3 to 8 mm)
- Normal force, load (range 0.5 to 40 N)
- Pressure at Hertzian contact (0.5 to 3 GPa)
- Temperature at testing or annealing temperature prior to testing
- Sliding speed (range 0.2 to 600 cm/s)
- Surface conditions like surface roughness (typically polished parts are used)

- Type of gas atmosphere (most used are air and nitrogen at various relative humidity) or alternatively vacuum conditions (sometimes with defined partial pressures of water vapor or oxygen etc.)
- Lubricants and lubricant additives are not discussed in the literature survey because our coatings were tested only under “dry” conditions without the use of lubricants. Basic information about lubricants and related additives can be found in the books of Ludema and Rudnick with information for lubricants, oil formulations, fuels, water, alcohols etc. [211, 212] and lubricant additives [213].

The basic friction mechanisms for a-C:H and a-C:H:Si coatings were described in chapter 2.3.3. The conditions and effects used to explain the different frictional behavior of a-C:H coatings are presented in more detail at the end of this chapter where the origin of the wear behaviors which also includes frictional effects are discussed.

For a-C:H the friction and wear properties are expected to change with the formation of a carbon-rich transfer layer from the a-C:H coating at the counterpart of a wear contact. Such carbon-rich transfer layers were observed on the wear counterpart for a-C:H at sliding in UHV by Memming et al. [214] and under dry conditions (no use of lubricants) by Hirvonen et al. [215]. For a-C:H a detailed characterization of carbon rich transfer layers formed by sliding in dry nitrogen was presented by Erdemir et al. [216]. The formation of the carbon-rich transfer layers originating from a-C:H coatings are expected to substantially change the friction and wear behavior in sliding wear processes.

Enke and Dimigen [122] have shown in 1980 that the friction of a-C:H is strongly influenced by the presence of water vapor pressure using a nitrogen atmosphere. The coatings showed in the ball-on-disk test very low friction coefficients of 0.01 - 0.02 at low water vapor pressures in the range of 10^{-8} to 10^{-1} mbar. Starting at a water vapor pressure of about 1 mbar (~8% relative humidity) the friction coefficient strongly increased up to a final value of 0.19 at 100% relative humidity (RH).

The dependency of the friction coefficient on the relative humidity in a nitrogen atmosphere is shown in Figure 2.13 using the data from Enke et al. [122], as a smoothed curve.

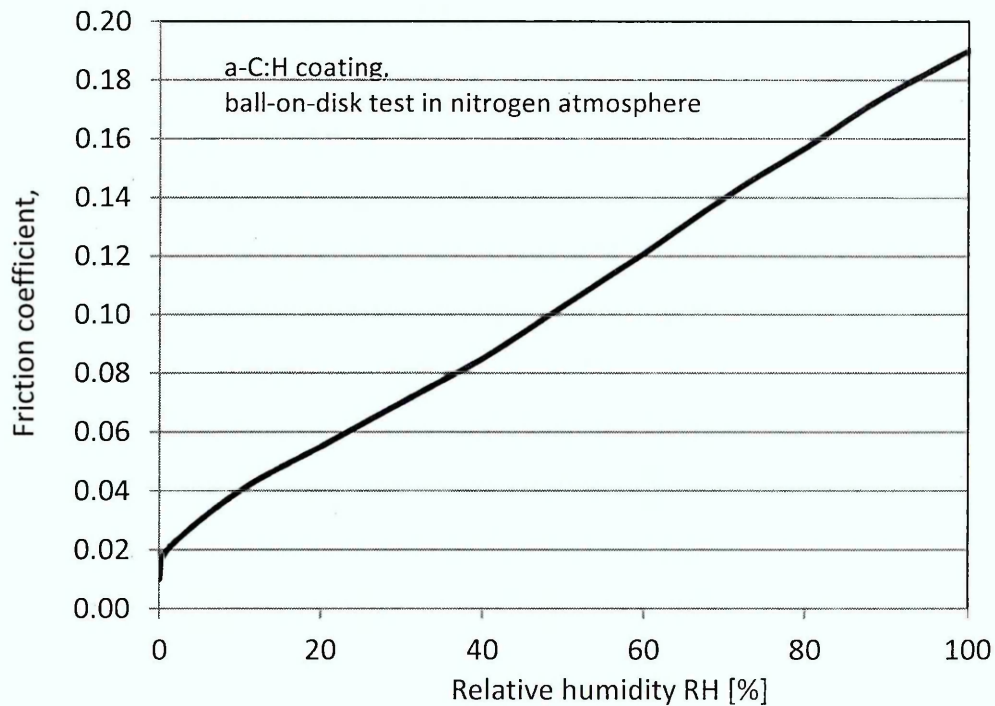


Figure 2.13 : Friction coefficient of a-C:H coatings in nitrogen depending on the relative humidity, redrawn according to Enke et al., [122] as a smoothed curve

The results of a literature survey on the friction of a-C:H depending on RH together with the related literature references are shown in Table 2.5 and Figure 2.14.

In order to allow a graphical presentation of the friction results as well as the wear results that were taken from the literature a classification of the results in classes of relative humidity was arranged.

The friction coefficients and the wear coefficients were taken over as numerical values, if available, or from diagrams which contain a certain degree of inaccuracy.

These friction coefficients were classified in RH classes in the following way:

Class	RH value range	Class	RH value range
0%RH	≥0 to <5% RH	60%RH	≥55% to <65% RH
10%RH	≥5% to <15% RH	70%RH	≥65% to <75% RH
20%RH	≥15% to <25% RH	80%RH	≥75% to <85% RH
30%RH	≥25% to <35% RH	90%RH	≥85% to <95% RH
40%RH	≥35% to <45% RH	100%RH	≥95% to ≤100% RH
50%RH	≥45% to <55% RH		

In most of the literature references a strong increase of the friction coefficient depending on increasing humidity can be observed.

Increasing friction coefficients from a range of 0.02 to 0.04 at low humidity to a range of 0.07 to 0.15 at high humidity were reported by Liu et al. against ZrO_2 [217], Tillmann et al. against WC [218]. Park et al. against steel [219, 220] and Li et al. against Si_3N_4 [221]. Compared to the coatings with ceramics as mating parts the highest friction coefficient of 0.2 is observed for the steel counterpart at high humidity. The a-C:H coatings which show this behavior are typically highly hydrogenated with hydrogen contents of 20 to 30%. This allows to achieve low friction conditions by high saturation of the dangling bonds with hydrogen at low humidity by the low-energy conditions of the H-H contact under the presence of a carbon-rich transfer layer. At higher humidities the contact conditions change with the existence of higher contact energy under the presence of water vapor which reduces the formation of a transfer layer according to Liu et al. [217] and Li et al. [221]. As reported by Freyman et al. [222] extremely low friction coefficients of 0.004 at 0% RH were achieved which increase to 0.01 at 10% RH. No further increase up to 50% RH was observed. These coatings have been produced by unbalanced magnetron sputtering from a graphite target using a mixture of argon and hydrogen.

Strongly increasing friction coefficients from a range of 0.05 to 0.1 at low humidity to a range of 0.2 to 0.5 at high humidities were shown by Sanchez-Lopez et al. [223] Suzuki et al. [224] and Gangopadhyay et al. [225] using steel as mating ball material for highly hydrogenated a-C:H coatings with 37 at.% hydrogen content.

Moderately increasing and almost stable friction coefficients from a range of 0.1 to 0.2 at low humidity to a range of 0.1 to 0.3 at high humidities were presented by Suzuki et al. against steel [224], Tanaka et al. against SiC [226] and Erdemir against Si₃N₄ [227] for coatings with hydrogen contents of 20 to 30 at. %.

Decreasing friction coefficients with the increase of relative humidity are shown by Waesche et al. against Si₃N₄, SiC and steel [228] but no coating properties are reported. Voevodin et al. [234] show for a-C:H coatings produced by PLD against sapphire a decrease of the friction coefficient from 0.06 at 10% RH to 0.04 at 90% RH and for steel from 0.23 at 10% RH to 0.12 at 90% RH. Sanchez-Lopez et al. [223] reported slightly decreasing friction coefficient from 0.25 to 0.21 when the humidity increased from 0% RH to 40% RH.

Generally one can say that for coatings with low or no hydrogen content, for a decrease in friction with an increase in humidity, water molecules change the strong interaction energy between carbon atoms to a weaker interaction force at the contact. For some materials lubricative films can be formed by the reaction of water molecules with the mating ball material which are also able to reduce friction at higher humidity. More detailed examples will be discussed in the following section where the wear of the a-C:H coatings under the influence of humidity is discussed.

Friction in Air at % RH	0	10	20	30	40	50	60	70	80	90	100	at.% H	Method Precursor	ball mat.; (a-C:H propert.)	Load; Speed
Miyoshi 1989 [229]					0.20								PECVD CH ₄	Si ₃ N ₄ ; (H=22 GPa)	1 N; 0.013cm/s
Kim 1991 [230]	0.16					0.08					0.19	55	PECVD CH ₄ +H ₂	Si ₃ N ₄	9.8 N; 1.87 cm/s
Erdemir 1991 [231]						0.15							PECVD CH ₄	Si ₃ N ₄	1 N; 2.6 cm/s
Erdemir 1991						0.13							PECVD CH ₄	Si ₃ N ₄	5 N; 2.6 cm/s
Erdemir 1991						0.12							PECVD CH ₄	Si ₃ N ₄	10 N; 2.6 cm/s
Erdemir 1991						0.16							PECVD CH ₄	Sapphire	1 N; 2.6 cm/s
Erdemir 1991						0.13							PECVD CH ₄	Sapphire	5 N; 2.6 cm/s
Erdemir 1991						0.11							PECVD CH ₄	Sapphire	10 N; 2.6 cm/s
Erdemir 1991						0.14							PECVD CH ₄	Sapphire	20 N; 2.6 cm/s
Erdemir 1991	0.07					0.16				0.16			PECVD CH ₄	Si ₃ N ₄	2 N; 2.6 cm/s
Paulmier 1993 [232]						0.10							PECVD C ₂ H ₂ +H ₂	steel	2 N; 5 cm/s
Donnet 1994 [233]					0.15							40	PECVD C ₂ H ₂	steel; (H=17GPa)	4 N; 0.17 cm/s
Voevodin 1995 [234]		0.06	0.06	0.06	0.05	0.05	0.05	0.04	0.04	0.04			PLD; PC target	sapphire; (H= 12 GPa)	1 N; 20 cm/s
Voevodin 1995		0.23	0.21	0.20	0.18	0.17	0.15	0.14	0.13	0.12			PLD; PC target	sapphire; (H= 12 GPa)	1 N; 20 cm/s
Liu 1996 [235]				0.04									IBD CH ₄	steel	5 N; 50 cm/s
Liu 1996				0.05									IBD CH ₄	steel	10 N; 50 cm/s
Liu 1996				0.09									IBD CH ₄	steel	20 N; 50 cm/s
Liu 1996* [236]					0.18								IBD CH ₄	ZrO ₂	1 N; 6 cm/s
Liu 1996*					0.06								IBD CH ₄	ZrO ₂	1 N; 160 cm/s
Liu 1996*					0.08								IBD CH ₄	ZrO ₂	10 N; 10 cm/s
Liu 1996*					0.05								IBD CH ₄	ZrO ₂	10 N; 160 cm/s
Erdemir 1996 [237]					0.06								IBD CH ₄	MgO-PSZ; (H= 12 GPa)	5 N; 100cm/s
Erdemir 1996					0.06								IBD CH ₄	MgO-PSZ; (H= 12 GPa)	5 N; 600cm/s
Liu 1997 [217]	0.02				0.08						0.10		IBD CH ₄	ZrO ₂	10 N; 50 cm/s
Liu 1997					0.30								IBD CH ₄	ZrO ₂	10 N; 6 cm/s
Gangopahyay 1997 [225]	0.09	0.10	0.15	0.18		0.29		0.48				37	PECVD	steel; (H=12 GPa)	4.4 N; 3.5 cm/s
Erdemir 1997 [227]					0.11								IBD CH ₄	steel	5 N; 10 cm/s
Erdemir 1997					0.16								IBD C ₂ H ₂	steel	5 N; 10 cm/s
Erdemir 1997					0.10								IBD CH ₄	steel	5 N; 60 cm/s
Yoon 1998 [238]	0.12					0.15							PECVD C ₆ H ₆	steel	5 N; 5 cm/s
Jiang 1998 [239]		0.13										20	PECVD UBM	WC	40 N; 5 cm/s
Ronkainen 2001 [240]						0.45						32	PECVD CH ₄	steel	5 N; 2 cm/s
Ronkainen 2001						0.4						32	PECVD CH ₄	steel	5 N; 150 cm/s
Ronkainen 2001						0.2						32	PECVD CH ₄	steel	40 N; 3 cm/s
Ronkainen 2001						0.15						32	PECVD CH ₄	steel	40 N; 150 cm/s
Ronkainen 2001						0.12						32	PECVD CH ₄	Al ₂ O ₃	5 N; 1 cm/s
Ronkainen 2001						0.1						32	PECVD CH ₄	Al ₂ O ₃	5 N; 300 cm/s
Ronkainen 2001						0.13						32	PECVD CH ₄	Al ₂ O ₃	22 N; 150 cm/s
Zhang 2002 [241]	0.07												PECVD C ₆ H ₆	SiC	1 N; 10 cm/s
Bewilogua 2002 [242]						0.2							PECVD C ₂ H ₂	steel	1 N; 4 cm/s
Gupta 2003 [243]						0.06						40	PECVD CH ₄	Al ₂ O ₃ ; (H= 28 GPa)	2.5 N; 10 cm/s
Gupta 2003						0.11						21	PECVD CH ₄	Al ₂ O ₃ ; (H= 39 GPa)	2.5 N; 10 cm/s
Suzuki 2003 [244]			0.06							0.11		24	PECVD hot filam.	steel; (H=11 GPa)	2 N; 1 cm/s
Suzuki 2003			0.07							0.14		37	PECVD ECR	steel; (H=10 GPa)	2 N; 1 cm/s
Suzuki 2003			0.1							0.11		31	RF PECVD CH ₄	steel; (H=18 GPa)	2 N; 1 cm/s

Table 2.5 part I of II : Friction of a-C:H in air depending on the relative humidity RH, data taken from references cited in this table

Friction in Air at %RH	0	10	20	30	40	50	60	70	80	90	100	at.% H	Method Precursor	ball mat.; (a-C:H propert.)	Load; Speed
Bremond 2003 [245]						0.15						10	PECVD	a-C:H; (H= 25 GPa)	3.4 N; 10 cm/s
Bremond 2003						0.15						10	PECVD	a-C:H; (H= 25 GPa)	3.4 N; 40 cm/s
Sanchez-Lopez 2003 [246]	0.05				0.28								PECVD H2+CH4	steel	10 N; 10 cm/s
Sanchez-Lopez 2003	0.25				0.21								PECVD CH4+H2	steel	10 N; 10 cm/s
Sanchez-Lopez 2003					0.23								PECVD CH4	steel	10 N; 10 cm/s
Sanchez-Lopez 2003	0.07				0.30								PECVD C2H2	steel	10 N; 10 cm/s
Tanaka 2003 [226]			0.13						0.24			22.5	PECVD IP C6H6	SiC; (H= 28 GPa)	0.64 N ;0.2 cm/s
Tanaka 2003			0.19						0.23			24	PECVD IP C7H8	SiC; (H=27 GPa)	0.64 N ;0.2 cm/s
Tanaka 2003			0.21						0.26			29	PECVD IP CH4	SiC; (H=18 GPa)	0.64 N ;0.2 cm/s
Tanaka 2003			0.15						0.21			22.5	PECVD IP C6H6	SiC; H= 28 GPa)	1.06 N ;0.2 cm/s
Tanaka 2003			0.21						0.23			24	PECVD IP C7H8	SiC; (H=27 GPa)	1.06 N ;0.2 cm/s
Tanaka 2003			0.20						0.20			29	PECVD IP CH4	SiC; (H=18 GPa)	1.06 N ;0.2 cm/s
Tanaka 2003			0.15						0.15			22.5	PECVD IP C6H6	SiC; H= 28 GPa)	0.64 N ;0.83 cm/s
Tanaka 2003			0.14						0.12			24	PECVD IP C7H8	SiC; (H=27 GPa)	0.64 N ;0.83 cm/s
Tanaka 2003			0.15						0.15			29	PECVD IP CH4	SiC; (H=18 GPa)	0.64 N ;0.83 cm/s
Tanaka 2003			0.13						0.14			22.5	PECVD IP C6H6	SiC; H= 28 GPa)	1.06 N ;0.83 cm/s
Tanaka 2003			0.11						0.12			24	PECVD IP C7H8	SiC; (H=27 GPa)	1.06 N ;0.83 cm/s
Tanaka 2003			0.15						0.15			29	PECVD IP CH4	SiC; (H=18 GPa)	1.06 N ;0.83 cm/s
Park 2003 [219]						0.08					0.2	30	PECVD C6H6	steel; (H= 11 GPa)	4 N ; 20 cm/s
Park 2004 [220]	0.03					0.10						25	PECVD IP C7H8	steel; (H=27 GPa)	10 N; 2 cm/s
Suzuki 2004 [224]						0.08						29	PECVD IP CH4	steel; (H=10 GPa)	10 N; 2 cm/s
Suzuki 2004						0.05						37	PECVD IP CH4	steel; (H=20 GPa)	10 N; 2 cm/s
Suzuki 2004						0.04						44	PECVD IP CH4+H2	steel; (H=6 GPa)	10 N; 2 cm/s
Li 2006 [221]		0.04	0.05	0.06		0.07		0.08		0.09			PECVD CH4	Si3N4; (H= 15 GPa)	2 N; 2 cm/s
Freyman 2006 [222]	0.004	0.01	0.02		0.02								UBM C-Targ. Ar+H2	a-C:H; (H= 13 GPa)	1 cm/s
Liu 2007 [247]			0.12		0.16			0.11	0.11			30	RF PECVD	corundum; (H=22 GPa)	2 N; 0.16 cm/s
Lawes 2007 [248]					0.15								PECVD	steel	40 N; 5 cm/s
Vanhulsel 2007 [249]					0.23							51	PECVD ICP CH4+H2	steel; (H= 9 GPa)	5 N; 1 cm/s
Vanhulsel 2007					0.25							49	PECVD ICP CH4+H2	steel; (H= 9 GPa)	5 N; 1 cm/s
Vanhulsel 2007					0.17							44	PECVD ICP CH4+H2	steel; (H= 14 GPa)	5 N; 1 cm/s
Ronkainen 2007 [250]					0.06								PECVD MS CH4	diamond; (H= 5 GPa)	5 N; 0.017 cm/s
Ronkainen 2007					0.11								PECVD MS CH4	diamond; (H= 5 GPa)	50 N; 0.017 cm/s
Ronkainen 2007					0.04								PECVD MS CH4	diamond; (H= 5 GPa)	5 N; 1 cm/s
Ronkainen 2007					0.04								PECVD MS CH4	diamond; (H= 5 GPa)	10 N; 1 cm/s
Wäsche 2008 [228]	0.14				0.08					0.06				steel	
Wäsche 2008					0.1					0.08				SiC	
Wäsche 2008					0.14					0.06				Si3N4	
Tillmann 2011 [218]		0.03								0.09		23.5	PECVD C2H2	WC; (H= 18 GPa)	10 N; 40 cm/s
Tillmann 2011		0.03								0.09		19.9	PECVD C2H2	WC; (H= 23 GPa)	10 N; 40 cm/s
Gant 2011 [251]					0.10								Balinit DLC Star	steel; (H= 19.6 GPa)	10 N; 10 cm/s
Gant 2011					0.05								Bekaert DLC	steel; (H= 17.6 to 25 GPa)	10 N; 10 cm/s
Gant 2011					0.25								Diamolith DLC	steel; (H= 44 GPa)	10 N; 10 cm/s
Santos 2013 [252]					0.10							19	RF PECVD	TiAl6V4	10 N; 10 cm/s

Table 2.5 part II of II : Friction of a-C:H in air depending on relative humidity, RH, data taken from references cited in this table

2.3.7 Wear of amorphous hydrogenated carbon (a-C:H) coatings

The ball-on-disk test, which is also called pin-on-disk test, and the reciprocating wear test with linear oscillation movement allow the determining of adhesive wear rates and friction coefficients under sliding conditions. In order to compare the wear rates presented in the literature the most common unit for the wear coefficient of $\text{mm}^3/(\text{Nm})$ is used.

Today an abrasive wear test, the ball cratering test, which is also known as CaloTest, is used with increasing frequency. In this test abrasive media are fed into the contact between the coating and the wear counterpart. The wear conditions of the ball cratering test are more independent of the friction properties of the coatings and the formation of transfer layers and characterize the abrasive wear resistance of the coating material itself. The ball cratering test method used for determining the wear rates of the produced a-C:H-based coatings is described in more detail in chapter 3.4 of this thesis.

According to Leyland and Matthews [253] the wear resistance achieved from the abrasive wear test are expected to follow the relationship of hardness to elastic modulus (H/E) which also appears in the “plasticity index” [254]. The hardness (H) of a coating can be estimated according to Kisly [255] as a product of the binding energy (E_b) and the covalency (a_c) divided by the square of the bond length (d) as $H \approx (E_b \times a_c)/d^2$. Charitidis et al. [256] considered that a coating needs to undergo a high proportion of elastic deformation and needs high resistance to plastic deformation which he called the “plastic resistance parameter”. The plastic resistance parameter (H^3/E^2) can be calculated from the equation (H^3/E^2): $P_y = K \times (H^3/E^2)$ for a load (P_y).

For a specific wear case the wear test has to be selected carefully in order to represent the dominant wear mechanism(s) of the practical application for which the a-C:H coated parts are used [257, 258].

The adhesive wear coefficients for a-C:H coatings in ambient air, depending on the relative humidity (RH), were taken from the “Ball-on-Disk” test or the “Linear oscillation Movement” test from various literature references. The wear coefficients of a-C:H coatings depending on RH in air and the related literature references are shown in Figure 2.15. In Table 2.6, the wear results and the

conditions of the wear test together with the literature references are given for ambient air depending on the relative humidity.

Figure 2.15 shows that for different a-C:H types and wear conditions the wear rate can increase or decrease with increasing RH. At high relative humidities above 90% RH for both types of wear behaviors the wear coefficients reach the same range of 2×10^{-8} to 1.7×10^{-7} mm³/(Nm).

For wear rates that increase with increasing relative humidity RH Liu et al. [217] observed a graphitized tribolayer. It was found that at low humidity under steady-state conditions only a small amount of graphitized coating material is needed to balance the generation and the consumption of tribofilm material which results in a low wear rate. Liu discussed that under dry conditions the graphitization of the coating material is promoted whereas at high humidity water molecules decelerate the graphitization process and no more graphitization was observed at 100% RH which meant that the coating was in direct contact with the ball material ZrO₂.

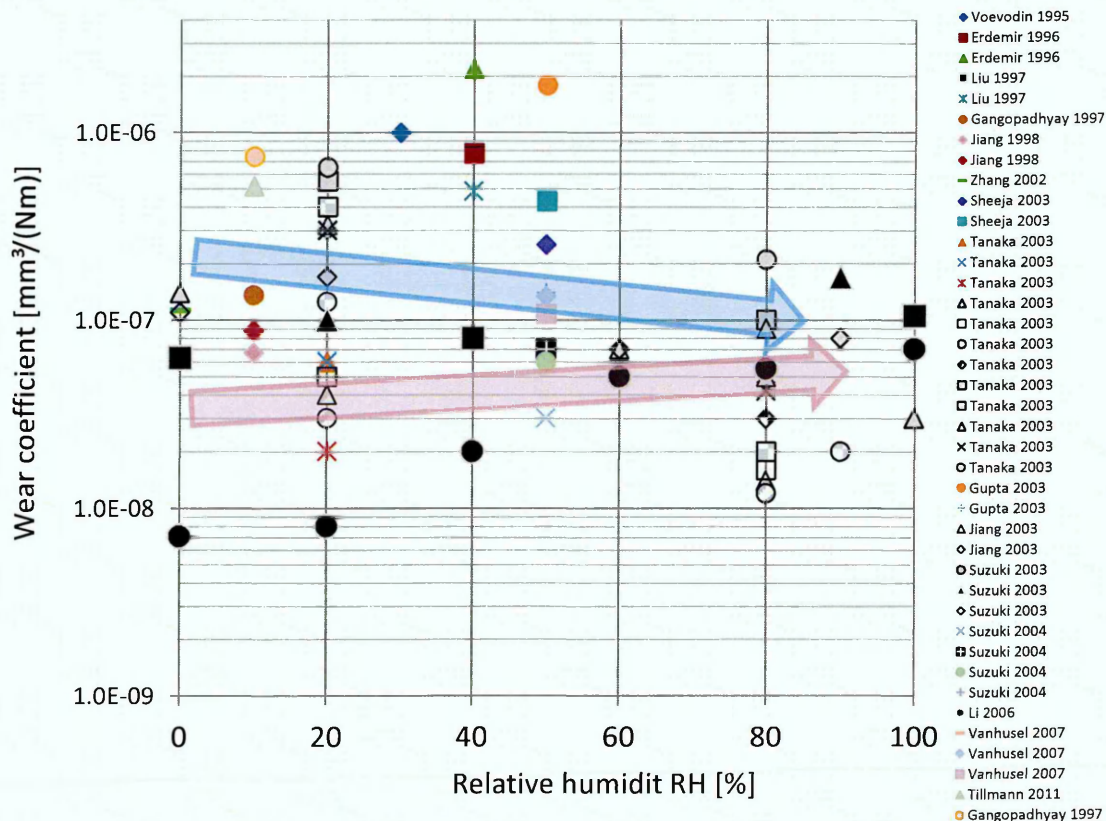


Figure 2.15 : Wear of a-C:H coated disks in air depending on the relative humidity, data taken from references cited in Table 2.6

Under direct contact conditions between ball material and the a-C:H coatings tribochemical reactions forming C=O bonds on the a-C:H coating were observed by Kim et al. [230] for humidity levels above 50% RH. The increasing oxidation of a-C:H with increasing humidity is combined with higher wear rates.

Increasing wear rates with higher humidity were also discussed by Li et al. [221] for a-C:H sliding against a Si₃N₄ ball. Again, the tribolayer formation on the Si₃N₄ under dry conditions and the oxidation of a-C:H at higher humidity are used to explain the wear behavior as a function of humidity in air and also in oxygen.

The higher bond strength of the oxidation products at the sliding contact of about 0.21 eV for C-O and C=O sites formed under highly humid conditions compared to the van der Waals bond in graphitic material of 0.08 eV under dry conditions was expected to cause the increase of the friction coefficients and the wear coefficients with increasing humidity.

Decreasing wear rates of a-C:H coatings were observed by Tanaka et al. [226] for a-C:H. For a-C:H coatings produced by PECVD using C₆H₆, C₇H₈ and CH₄ as precursors hydrogen contents of 22.5 at.%, 24 at.% and 29 at.% were achieved. The films were tested in air of 20% and 80% RH using a SiC ball as counterpart with sliding velocities of 0.2 and 0.83 cm/s and loads of 0.64 N and 1.06 N. In Table 2.6 it is shown that the wear rates increase with increasing load at high humidity. At low humidity only the wear coefficients of the CH₄ based coatings increased significantly, whereas the C₆H₆ and C₇H₈-based films show stable or decreasing wear. The wear increases at higher sliding speeds significantly for all types of a-C:H coatings at 20% and 80% RH. Tanaka suspects that reduction of wear with increasing humidity is related to the mild wear conditions and that was observed under both dry conditions with the existence of a transfer layer and highly humid conditions where the transfer layer disappears.

The reduction of friction at higher humidity could be explained by the oxidation of the a-C:H film and the SiC ball in a humid atmosphere. An oxidation process

similar to the oxidation of Si_3N_4 as discussed by Enomoto [259] is expected for SiC which can occur at the high temperatures on “hot spots” during sliding on the asperities when the SiC is not protected by a graphitic tribolayer. Under such conditions SiO_2 is formed and can react with water to form silicic acid ($\text{Si}(\text{OH})_4$) as described by Gao et al. [260]. At the tribocontact silicic acid can be accumulated and form a hydrated layer which can serve as a wear and friction reducing tribochemical film. Gao et al. [261] discusses this process in the presence of graphite which is necessary to accumulate the tribochemical film on the wear contact.

The low wear rates of SiC after oxidation in humid atmospheres were already discussed by Sasaki in 1989 [262]. According to Sasaki polar molecules like H_2O are adsorbed on the SiO_2 (oxidized surface of Si_3N_4 or SiC) forming protecting hydrated layers.

Jiang et al. [263] observed decreasing wear rates at increasing humidity in air for a-C coatings sliding against tungsten carbide balls. Under humid conditions adsorption of water at the dangling bonds reduces the energy in the surface contact and leads to finer wear debris and therefore smaller wear rates.

Suzuki et al. [244] found for a-C:H coatings produced with ECR PECVD an increase of wear with humidity whereas for coatings produced with RF PECVD and hot filament PECVD the wear rates decreased with humidity. The different tribological behavior was expected to result from the difference in microscopic film structure where the ECR PECVD based a-C:H coatings are characterized by larger crystallite sizes (L_C) which have been calculated from the I_D/I_G ratio using Raman spectroscopy.

The proportionality of $1/L_C$ with I_D/I_G for graphite was found by Tuinstra and Koenig [264] from systematic Raman and X-Ray diffraction studies and a general formula for the use of lasers in the visible range was presented by Cancado et al. [265] for nanographite.

Wear* in air at %RH	0	10	20	30	40	50	60	70	80	90	100	ball mat; (a-C:H propert.)	Load; Speed
Voevodin 1995 [234]				1.0E-06								sapphire; (H=12GPa)	P=0.8GPa;20cm/s
Erdemir 1996 [237]					7.8E-07							MgO-PSZ; (H=12GPa)	5N;100cm/s
Erdemir 1996					2.2E-06							MgO-PSZ; (H=12GPa)	5N;600cm/s
Liu 1997 [217]	6.3E-08				8.0E-08						1.1E-07	ZrO2	10N;50cm/s
Liu 1997					4.9E-07							ZrO2	10N;6cm/s
Gangopadhyay 1997 [225]		1.4E-07										steel;(H=12GPa;37at%H)	4.4N;3.5cm/s
Gangopadhyay 1997		7.5E-07										steel;(H=12GPa;37at%H)	4.4N;37cm/s
Jiang 1998 [239]		6.7E-08										WC; (~20at%H)	20N;5cm/s
Jiang 1998 [239]		8.8E-08										WC; (~20at%H)	40N;5cm/s
Zhang 2002 [241]	1.1E-07											SiC; (H=30.2GPa)	1N;10cm/s
Sheeja 2003 [266]						2.5E-07						ta-C coated steel	5N;3cm/s
Sheeja 2003						4.3E-07						steel	5N;3cm/s
Tanaka 2003 [226]			6.0E-08									SiC; -C6H6 used-	0.64N;0.2cm/s
Tanaka 2003			6.0E-08									SiC; -C7H8 used-	0.64N;0.2cm/s
Tanaka 2003			2.0E-08									SiC; -CH4 used-	0.64N;0.2cm/s
Tanaka 2003			4.0E-08						1.4E-08			SiC; -C6H6 used-	1.06N;0.2cm/s
Tanaka 2003			5.0E-08						1.6E-08			SiC; -C7H8 used-	1.06N;0.2cm/s
Tanaka 2003			3.0E-08						1.2E-08			SiC; -CH4 used-	1.06N;0.2cm/s
Tanaka 2003			3.0E-07						3.0E-08			SiC; -C6H6 used-	0.64N;0.83cm/s
Tanaka 2003			4.0E-07						2.0E-08			SiC; -C7H8 used-	0.64N;0.83cm/s
Tanaka 2003			5.5E-07						1.0E-07			SiC; -CH4 used-	0.64N;0.83cm/s
Tanaka 2003			3.2E-07						9.0E-08			SiC; -C6H6 used-	1.06N;0.83cm/s
Tanaka 2003			3.0E-07						4.2E-08			SiC; -C7H8 used-	1.06N;0.83cm/s
Tanaka 2003			6.5E-07						2.1E-07			SiC; -CH4 used-	1.06N;0.83cm/s
Gupta 2003 [243]						1.8E-06						Al ₂ O ₃ ; (H=28GPa;40at%H)	2.5N;10cm/s
Gupta 2003						1.4E-07						Al ₂ O ₃ ; (H=39GPa;21at%H)	2.5N;10cm/s
Jiang 2003 [267]	1.4E-07						7.0E-08		5.0E-08		3.0E-08	WC; (H=7GPa)	10N;25cm/s
Jiang 2003	1.1E-07						7.0E-08					WC; (H=7GPa)	10N;5cm/s
Suzuki 2003 [244]			1.3E-07							2.0E-08		steel; (H=11GPa)	2.05N;1cm/s
Suzuki 2003			1.0E-07							1.7E-07		steel; (H=10GPa)	2.05N;1cm/s
Suzuki 2003			1.7E-07							8.0E-08		steel; (H=18GPa)	2.05N;1cm/s
Suzuki 2004 [224]						3.0E-08						steel; (H=27GPa;25at%H)	10N;2cm/s
Suzuki 2004						7.0E-08						steel; (H=10GPa;29at%H)	10N;2cm/s
Suzuki 2004						6.0E-08						steel; (H=20GPa;37at%H)	10N;2cm/s
Suzuki 2004						1.2E-07						steel; (H=6GPa;44at%H)	10N;2cm/s
Li 2006 [221]	7.1E-09		8.0E-09		2.0E-08		5.0E-08		5.5E-08		7.0E-08	Si ₃ N ₄ ; (H=15GPa)	2N;2cm/s
Vanhusel 2007 [249]						1.1E-07						steel;(H=9GPa;51at%H)	5N;1cm/s
Vanhusel 2007						1.3E-07						steel;(H=9GPa;49at%H)	5N;1cm/s
Vanhusel 2007						1.1E-07						steel; (H=14GPa;44at%H)	5N;1cm/s
Tillmann 2011 [218]		5.2E-07										WC;(H=18GPa;24at%H)	10N;0.67cm/s

* Wear of a-C:H on disk expressed as wear coefficients in mm³/(Nm)

Table 2.6 : Wear of a-C:H coated disks in air depending on the relative humidity, data taken from references cited in this table

The wear rates of a-C:H in dry nitrogen are shown in Figure 2.16 depending on the relative humidity RH. The corresponding data for the wear rates given in Table 2.7 contains the type of coating processes, the wear test conditions and the literature references.

Li et al. [221] found for the a-C:H coatings in dry nitrogen a higher wear rate compared to the wear rates obtained in air which have been discussed above. At relative humidities above 40% RH the wear rates in nitrogen were significantly lower than in air but the friction coefficients were always lower in dry nitrogen than in dry air at the same relative humidities. Li observed that the a-C:H coating showed a flake-like peeling off in dry nitrogen combined with a large amount of wear debris around the contact region even with the existence of a carbon rich transfer layer on the Si₃N₄ ball. This indicates that a large mass transfer occurs in dry nitrogen to the Si₃N₄ ball. At 40% RH the worn surfaces of the a-C:H film are smooth and the contact area on the Si₃N₄ ball is covered with a compact and dense transfer layer. It was expected that water molecules passivate dangling bonds on the wear track on the a-C:H coating. The transfer layer became discontinuous at 100% RH and more wear debris together with severe wear of the Si₃N₄ ball were observed.

Vanhulsel et al. [249] observed for a highly hydrogenated film of about 9 GPa hardness with 49 at.% hydrogen content low wear rates in dry nitrogen. The wear rate decreased when the load increased from 10 to 20 N from 1×10^{-8} to 5×10^{-9} mm³/(Nm) respectively. The wear behavior could be explained by a high saturation of the dangling bonds with hydrogen and the related low friction and low wear effects. Decreasing wear at higher load is expected to result from increasing graphitization and improved transfer layer formation.

A very low a-C:H disk coating wear rate of 2.2×10^{-9} mm³/(Nm) in dry nitrogen was reported by Zhang et al. [241] for a coating with a high hardness of about 30 GPa which was produced by PECVD using benzene as precursor. The low wear rate and a low friction coefficient of 0.06 result from the formation of a lubricating carbon-based transfer layer on the SiC ball.

The wear rates at 100% RH for nitrogen atmosphere shown in Figure 2.16 depend on the ball material used and are comparable to the wear rates that have been observed for air at 100% RH.

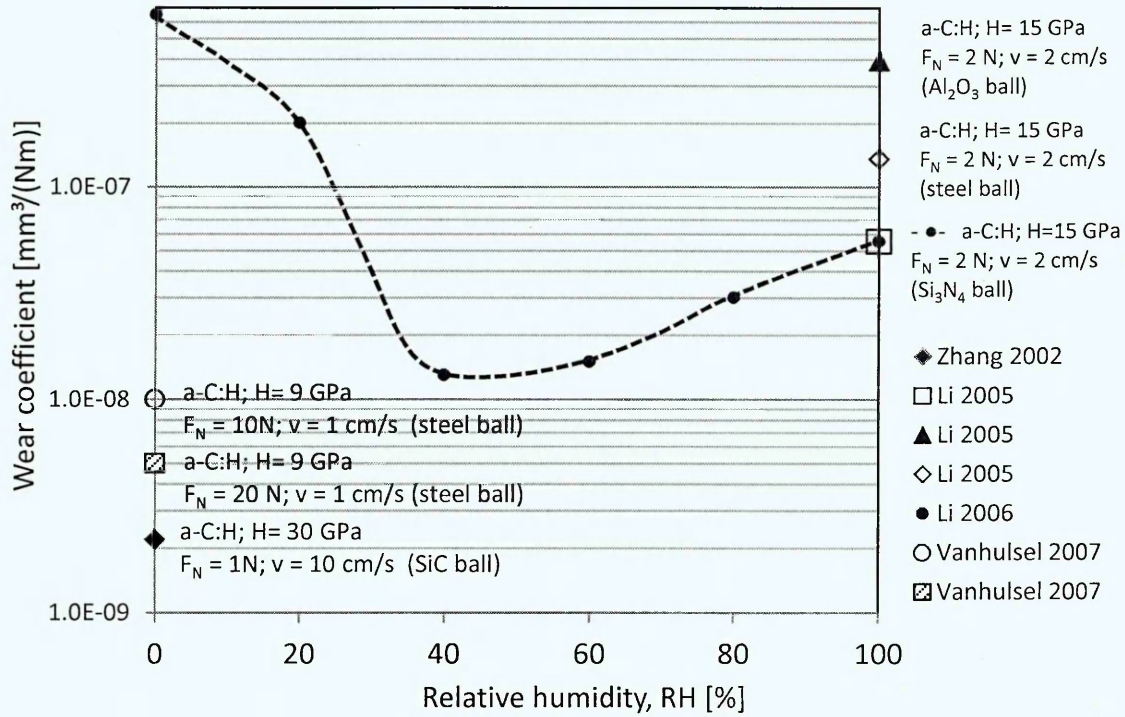


Figure 2.16 : Wear of a-C:H coated disks in nitrogen depending on humidity, RH, data taken from references cited in Table 2.7

Wear* in N ₂ at %RH	0	10	20	30	40	50	60	70	80	90	100	ball mat; (a-C:H propert.)	Load; Speed	Deposition
Zhang 2002 [241]	2.2E-09											SiC; (H=30.2GPa)	1N;10cm/s	a-C:H PECVD
Li 2005 [268]											5.5E-08	Si3N4; (H=15GPa)	2N;2cm/s	a-C:H PECVD
Li 2005											3.9E-07	Al2O3; (H=15GPa)	2N;2cm/s	a-C:H PECVD
Li 2005											1.4E-07	steel; (H=15GPa)	2N;2cm/s	a-C:H PECVD
Li 2006 [221]	6.5E-07		2.0E-07		1.3E-08		1.5E-08		3.0E-08		5.5E-08	Si3N4; (H=15GPa)	2N;2cm/s	a-C:H PECVD
Vanhusel 2007 [249]	1.0E-08											steel;(H=9GPa,49at%H)	10N;1cm/s	a-C:H PECVD CH ₄ +H ₂
Vanhusel 2007	5.0E-09											steel;(H=9GPa,49at%H)	20N;1cm/s	a-C:H PECVD CH ₄ +H ₂

* Wear of a-C:H on disk expressed as wear coefficients in mm³/(Nm)

Table 2.7 : Wear of a-C:H coated disks in nitrogen depending on the relative humidity, RH, data taken from references cited in this table

Erdemir et al. [269, 270] reported in various publications on a-C:H coatings with superlow friction and wear behavior obtained for dry nitrogen at high loads of 10 N and high velocities of 50 cm/s, depending on the selection of the precursor

gas at PECVD deposition. For the wear test the steel balls and the steel disks were coated with the a-C:H coatings.

The ball wear results, which can be observed in Figure 2.17, show a strong dependence on the type of the precursor gas and more specifically on its H/C ratio. High wear rates in the 10^{-7} mm³/(Nm)-range were observed for hydrogen free a-C and a-C:H which was produced using C₂H₂ (H/C=1) as precursor. Erdemir showed that for CH₄ (H/C=4) as precursor, low wear rates $< 10^{-8}$ mm³/(Nm) were achieved and that these wear rates can be further reduced to below 4×10^{-10} mm³/(Nm) using a mixture of 10% CH₄+ 90% H₂ (H/C=22) at coating deposition.

Under vacuum conditions it was shown that a-C:H needs high hydrogen content above 40 at.% in the coating in order to saturate the dangling bonds by forming stable C-H bonds. This results in a low surface contact energy between hydrogen atoms of 0.08 eV corresponding to the H-H binding energy as discussed by Donnet et al. [271] in order to finally achieve low friction and wear properties. The same mechanisms are expected for dry nitrogen atmosphere.

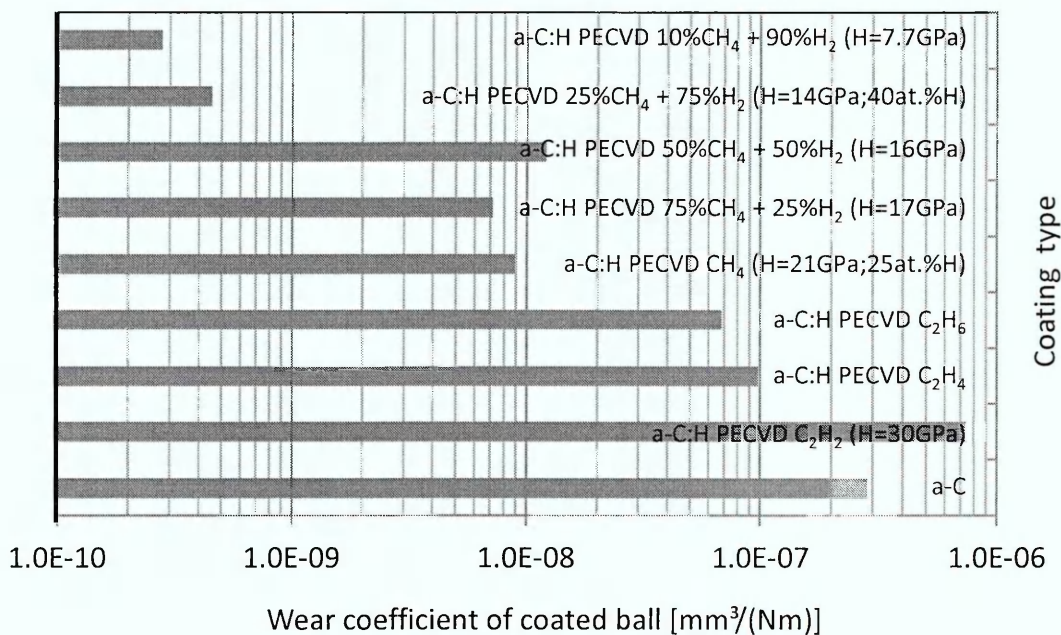


Figure 2.17 : Wear of a-C:H coated balls in dry nitrogen depending on the precursor gas, according to Erdemir et al. [269, 270]

Erdemir [272] discussed that at exposure of a-C:H films to higher temperatures the coatings may show increasing transformation to a graphitic phase and become more oxidized which results in a higher wear rate. The wear of a-C:H depending on the temperature is shown in Figure 2.18. The wear coefficient increases by four decades from $1.46 \times 10^{-10} \text{ mm}^3/(\text{Nm})$ at RT to $1.05 \times 10^{-7} \text{ mm}^3/(\text{Nm})$ at $150 \text{ }^\circ\text{C}$ and reaches $1.39 \times 10^{-6} \text{ mm}^3/(\text{Nm})$ at the maximum temperature of $250 \text{ }^\circ\text{C}$.

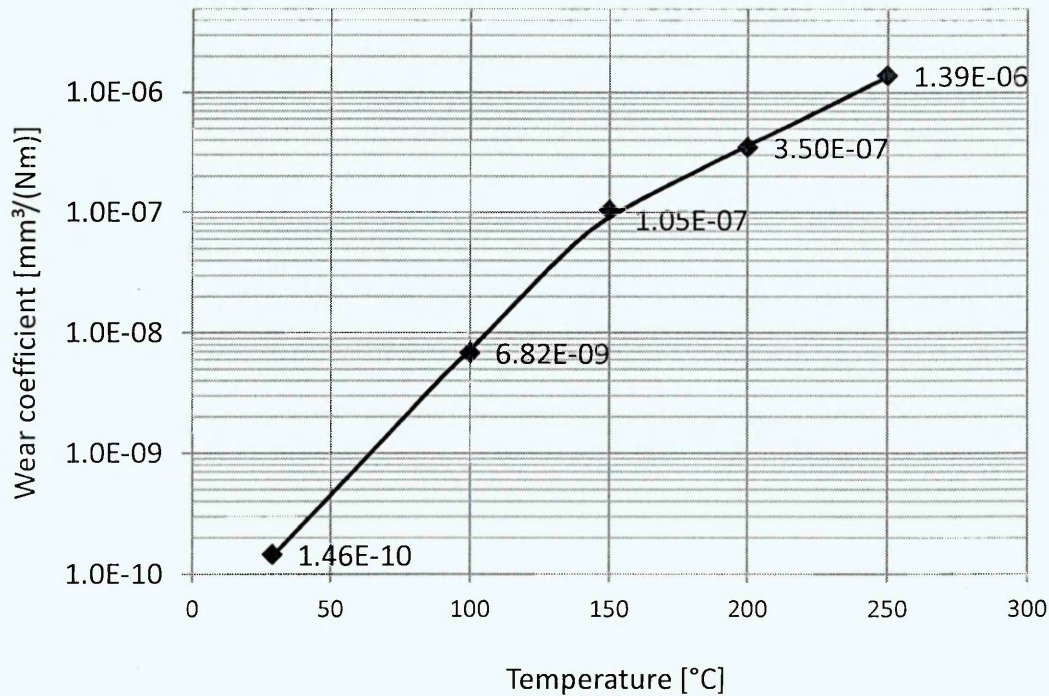


Figure 2.18 : Wear of a-C:H coatings depending on the temperature, according to Erdemir [272]

In order to achieve low wear rates the atmosphere where the a-C:H coating will be used and the wear conditions including the material of the wear counterpart have to be considered. The coating process and the process parameters, the coating properties and composition as well as the thickness of the coating have to be adapted to the application conditions and the required service life. The commercial requirements given by cost of ownership limitations also have to be fulfilled for industrial applications.

2.3.8 Friction and wear of a-C:H:Si (Si-DLC) coatings

The correct designation of silicon doped amorphous hydrogenated carbon according to the VDI 2840 guideline [273], is a-C:H:Si but the name Si-DLC is quite frequently used. Therefore the name Si-DLC is also used in this thesis. The principle friction and wear mechanisms have been already described in the a-C:H related section, therefore for the Si-DLC the specific friction and wear results and the related discussion explaining the friction and wear related effects as well as the production methods of the coatings are presented.

The characteristic behavior of friction and wear of Si-DLC was already widely discussed in publications of the late 1980s and early 1990s. The results from these early publications were primarily used in order to describe the tribological behavior of Si-DLC supplemented through selected results from later publications. During the following presentation of the coating process for a-C:H-based coatings and coating results in this thesis, specific literature references on Si-DLC will be provided and discussed.

Goranchev et al. [274] reported in 1986 on the deposition of Si-DLC by RF PECVD deposition using a silicon target that was covered with a layer from previous poisoning in an Ar-CH₄ gas mixture. Si-DLC coatings with low friction coefficients of 0.08 were deposited.

Sugimoto and Miyake [275] reported on highly lubricative Si-DLC films which were produced by electron cyclotron resonance (ECR) based deposition using ethylene and silane. A minimum friction coefficient of 0.007 was observed for a 4.9 N load and 13 cm/s sliding speed against a steel mating ball under high vacuum conditions. Well adhering oriented hydrocarbon layers were detected on the mating balls by using IR spectroscopy when low friction conditions were present. In a vacuum Miyake [276] found for Si-DLC at 10 at.% Si-content, produced by ECR using ethylene and silane, a minimum friction coefficient of below 0.01, which was almost constant after annealing at 400°C. Compared to this, at lower and higher silicon concentrations the friction coefficient increased after annealing. A high friction coefficient was observed after annealing at 600°C which was expected to originate from the change to a crystal-like Si-C structure. From micro IR-analyses a transfer layer of hydrogenated carbon was observed on the ball.

For PECVD deposition with SiCl_4 and CH_4 as precursors Oguri and Arai [277] achieved coatings of high Vickers hardness of more than HV 2000 with carbon contents of 55 to 85 at.% (ignoring hydrogen). By Raman spectroscopy diamond-like carbon was observed which indicates a Si-DLC deposition at these carbon contents. In their publication from 1991 [278] minimum friction coefficients of 0.03 to 0.05 were observed for Si-DLC at silicon contents of 15 to 25 at.% (ignoring hydrogen and chlorine). Figure 2.19 shows the initial and the steady-state friction coefficients using a steel ball depending on the load, according to Oguri and Arai. For the Si-DLC with Si-contents of 21 at.% (excluding hydrogen and chlorine) a large amount of wear debris was found on the steel mating ball which was combined with a higher wear rate of the coating above $10^{-7} \text{ mm}^3/(\text{Nm})$ compared to a-C:H. From Fourier transform infrared spectroscopy (FTIR) SiO_2 was detected on the wear debris. The formation of SiO_2 on the wear debris was considered to be combined with the creation of the low friction coefficient of the Si-DLC. In 1992 Oguri and Arai [279] showed for Si-DLC with 43 at.% C, 42 at.% H, 13 at.% Si and 2 at.% Cl in ambient air of 50% RH friction coefficients in the range of 0.06 to 0.09 and in dry nitrogen a friction coefficient of 0.03.

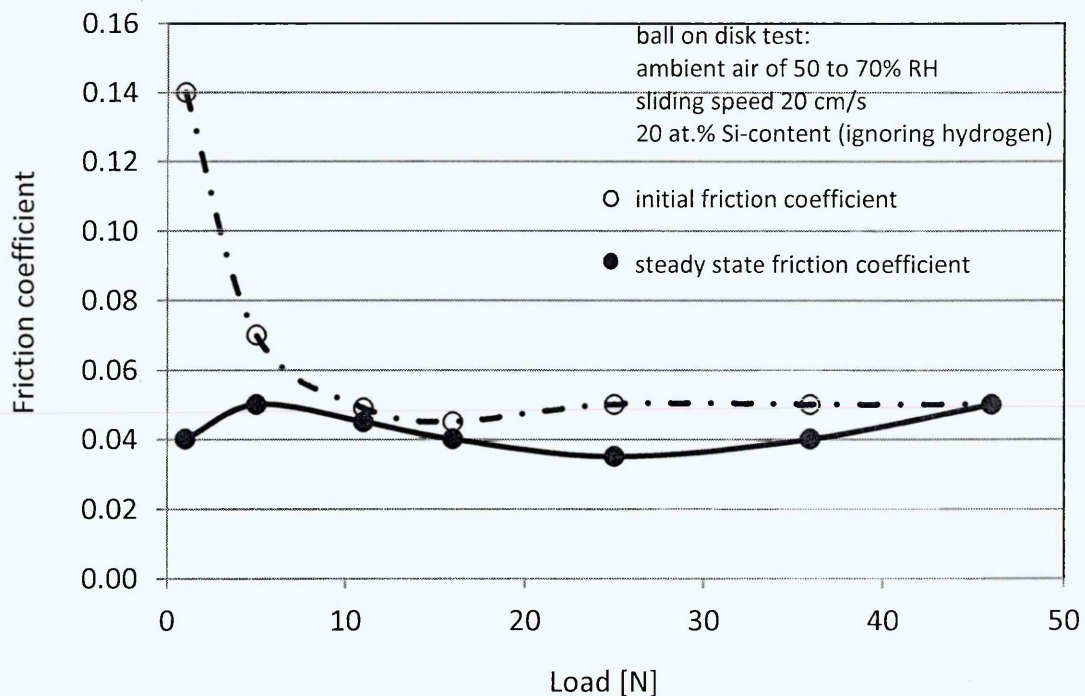


Figure 2.19 : Initial and steady state friction coefficients of Si-DLC depending on the load, redrawn according to Oguri and Arai [278]

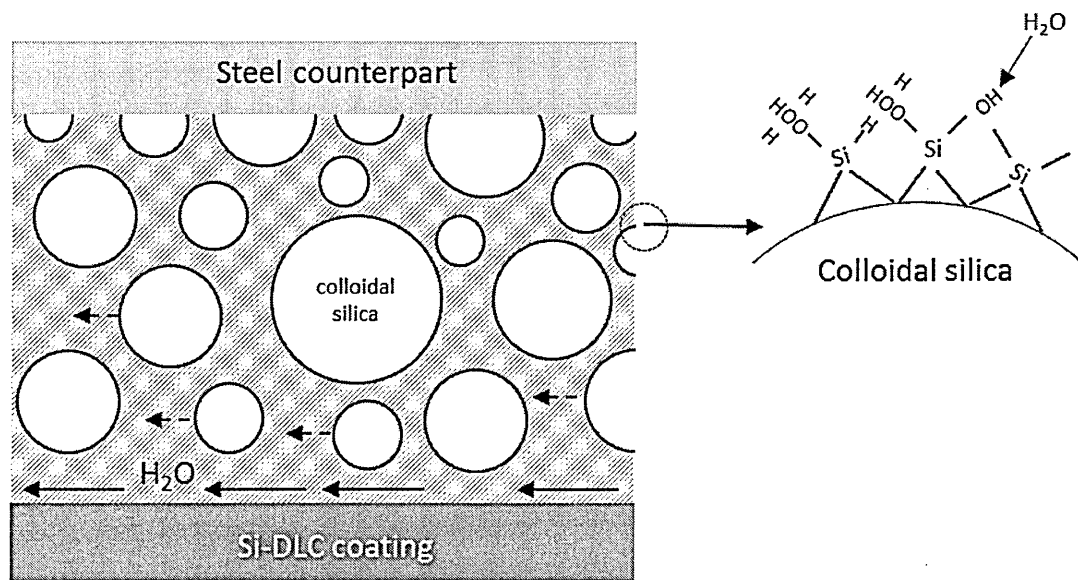


Figure 2.20 : Schematic to explain the low friction mechanism for Si-DLC in humid atmosphere, redrawn according to Oguri and Arai [279]

The low friction coefficient for the Si-DLC in contact with steel in humid air was explained by Oguri and Arai [279] by the formation of silica-sol which is expected to act as a lubricant. In Figure 2.20 this low friction mechanism for Si-DLC with the formation of silica-sol is shown.

In 1992 Oguri and Arai [280] reported on Si-DLC which has been transformed to graphite-like carbon with silicon after annealing for one hour under vacuum conditions at a temperature of 760°C. For the graphite-like carbon with silicon a high friction coefficient of about 0.2, which is similar to graphite, was observed.

Si-DLC coatings with low friction coefficients of about 0.05 (steel mating ball) in ambient air for the humidity range of 20 to 70% RH have been deposited by Hioki et al. [281] and Itoh et al. [282] by the ion beam assisted deposition (IBAD) method using heated silicone oil vapor as precursor and Ar for ion irradiation. Hioki expected that the moisture insensitivity originated from the hydrophobic behavior of remaining siloxane in the Si-DLC. In a dry nitrogen atmosphere the friction coefficient was reduced to below 0.02. A transfer layer containing carbon, silicon, oxygen and iron was observed on the steel ball by

electron probe micro-analysis (EPMA) after testing in air at 60% RH. Hioki presented in 1994 [283] for Si-DLC low friction coefficients as low as 0.05 for the range of silicon concentrations x of $0.05 \leq x \leq 0.35$.

Smeets et al. [284] presented for Si-DLC deposited by R.F. PECVD using silane and methane precursors minimum friction coefficients, in nitrogen of 50% RH, of 0.05 to 0.07 in the range of carbon concentrations of 75 to 80 at.% (neglecting hydrogen) using loads of 1, 5 and 10 N. For these Si-DLC coatings Meneve et al. [285] showed for the film stress a minimum of below 1.2 GPa for carbon contents of 65 to 80 at.%.

The wear of Si-DLC on the coated disk depending on the carbon content x , which is shown in Figure 2.21, decreases from $1 \times 10^{-5} \text{ mm}^3/(\text{Nm})$ at $x = 0.65$ to a wear rate of below $6 \times 10^{-7} \text{ mm}^3/(\text{Nm})$ at $x > 0.8$ using a steel mating ball with loads of 5 and 10 N applied in nitrogen atmosphere of 50% RH. The corresponding wear of the steel ball is given in Figure 2.22. Under the same test conditions ball wear coefficients of below $10^{-7} \text{ mm}^3/(\text{Nm})$ at $x = 0.65$ to below $5 \times 10^{-8} \text{ mm}^3/(\text{Nm})$ at $x = 1$ were determined.

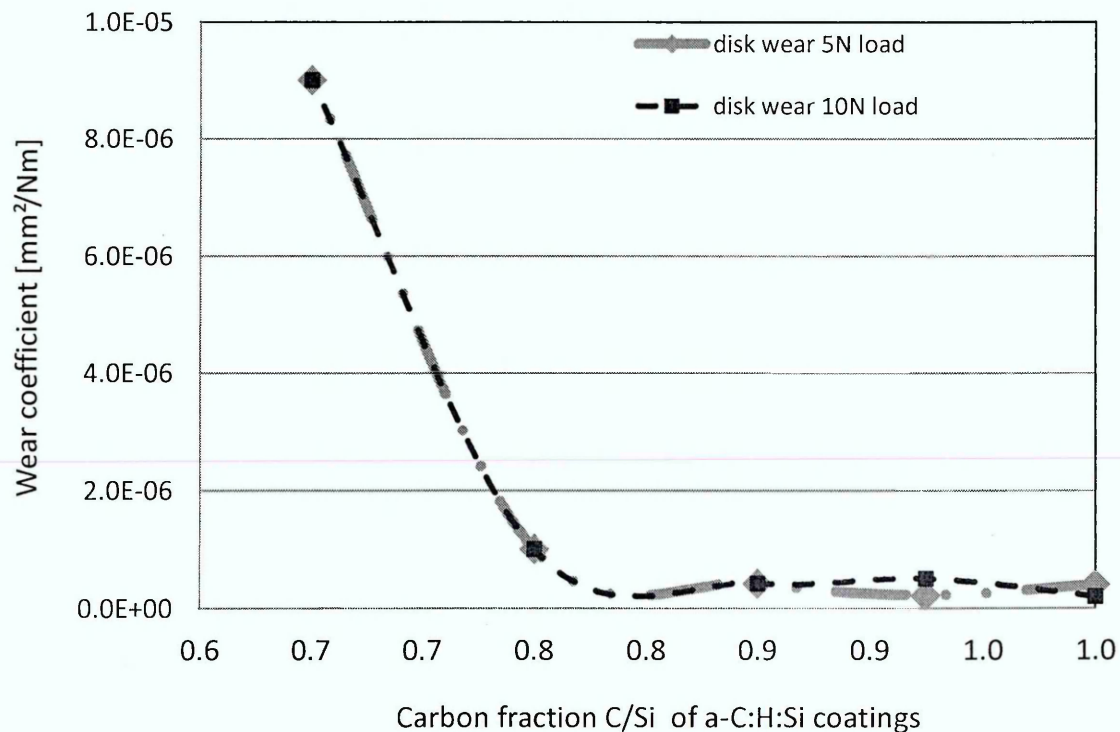


Figure 2.21 : Wear of the Si-DLC on coated steel disk depending on the carbon content x , redrawn according to Meneve et al. [285]

Gangopadhyay et al. [225] of the Ford Motor Company found for Si-DLC a low friction region at 5 to 18% atomic concentration of silicon, as detailed in Figure 2.23.

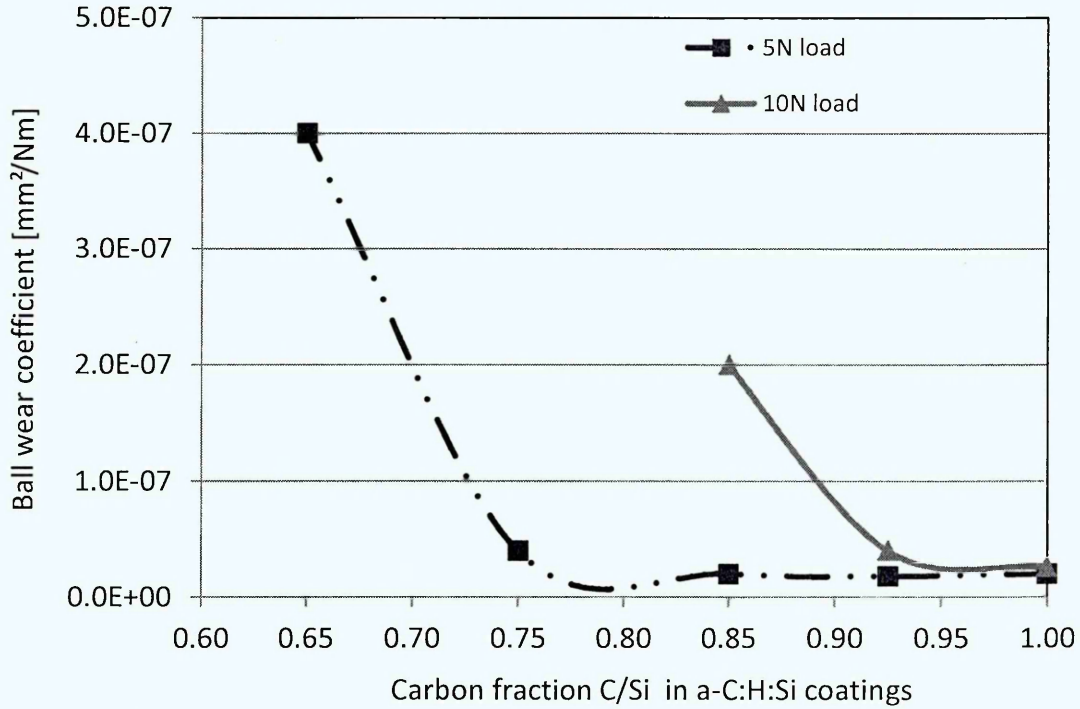


Figure 2.22 : Wear of steel mating ball sliding against Si-DLC coated steel disk depending on the carbon content x , redrawn according to Meneve et al. [285]

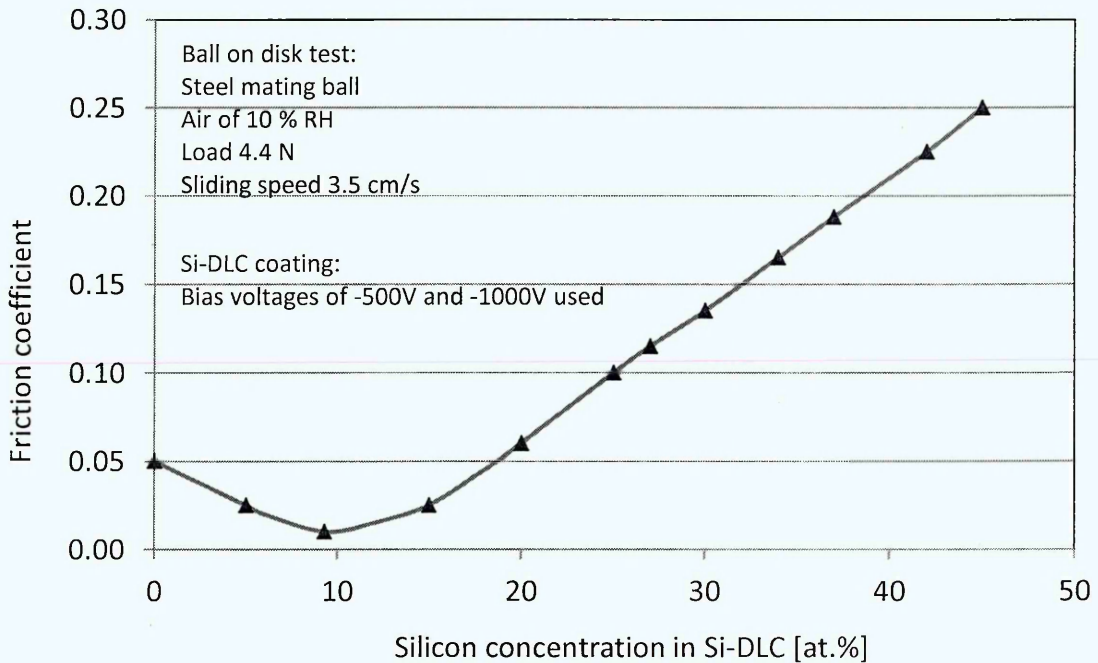


Figure 2.23 : Friction coefficient of a-C:H:Si depending on the atomic concentration of silicon, redrawn according to Gangopadhyay et al. [225]

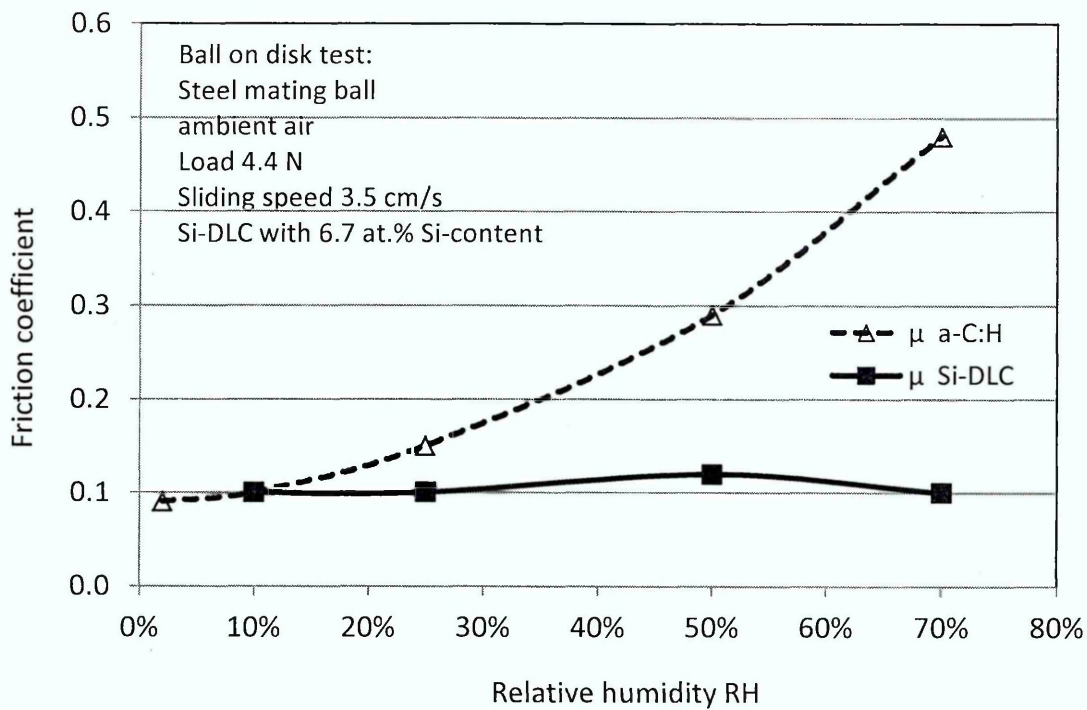


Figure 2.24 : Friction coefficient of a-C:H and a-C:H:Si depending on humidity, redrawn according to Gangopadhyay et al. [225]

It was also shown by Gangopadhyay et al. (see Figure 2.24) that the friction coefficient of a-C:H increases strongly as a function of humidity, whereas the friction coefficient of Si-DLC with 6.7 at.% Si was almost stable with about 0.1 in the humidity range of 2 to 70% RH. For the Si-DLC films transfer layers were observed for low as well as for high humidity conditions at almost equal ball wear rates. Compared to these results the a-C:H films showed at low humidity a transfer layer on the ball which almost disappeared at 70% humidity accompanied by the development of a wear scar. It was suggested that the silicon doping of a-C:H assists in the formation of a transfer layer under highly humid conditions. The wear rates of the Si-DLC coatings increased from $6 \times 10^{-7} \text{ mm}^3/(\text{Nm})$ at 3.5 cm/s to above $3.2 \times 10^{-6} \text{ mm}^3/(\text{Nm})$ at 37 cm/s sliding velocity. For the Si-DLC low wear rates comparable with a-C:H were achieved for silicon concentrations below 9.3 at.%.

Wear test results from Gilmore and Hauert [286] show for Si-DLC with 1 at.% Si an increase of the film wear rate by a factor of 2 which increased to a factor of 4

for 6 at.% silicon compared to the undoped a-C:H with wear rates in the range of 0.9 to $2.1 \times 10^{-7} \text{ mm}^3/(\text{Nm})$.

The frictional and wear characteristics of a-C:H and Si-DLC were compared by Kim et al. [287] for humidities of 5, 30 and 85% RH using a steel mating ball at 10 N load and 5 cm/s sliding speed under air atmosphere. For a-C:H the friction coefficient changed with humidity and was reduced from 0.23 at 5% RH to 0.12 at 30% RH and increased slightly to 0.16 at 85% RH, whereas the friction coefficient of Si-DLC was almost constant at about 0.08. It was found for both types of coatings that the wear rates increased with decreasing humidity.

Zhao et al. [288] deposited Si-DLC coatings with an silicon concentration of 3.9 at.% using a combination of unbalanced magnetron sputtering and RF PECVD. As a result of silicon doping Si, SiC and SiO₂ were found, whereby the diamond-like amorphous microstructure was not affected. Using a Si₃N₄ ball in water a superlow friction coefficient of about 0.005 was determined and as tribochemical products colloidal silica particles and layers which, together with hydrodynamic lubrication, were expected to allow the achieving of this very low friction coefficient.

Chouquet et al. [289] deposited Si-DLC using a low frequency PECVD process by adjusting the ratio of the TMS flow to the total gas flow in order to achieve different silicon contents of the coatings. The friction coefficients and the nanohardness of these coatings depending on the silicon concentration are shown in Figure 2.25. Very low friction coefficients below 0.05 and 19.5 to 15.5 GPa hardness were achieved for coatings with 6.4 and 14.5 at.% Si respectively. A visible wear track indicating a strong increase of the wear rate of the Si-DLC coatings can be observed with increasing TMS to the total gas flow ratio.

Yang et al. [290] used an Al₂O₃ ball in a ball-on-disk test at a load of 2 N and a sliding speed of 4.45 cm/s under ambient air of 30 to 40% RH. In contrast to a-C:H where the friction coefficient increased from 0.13 to 0.24, after annealing at 400 °C, the friction coefficient of Si-DLC with 16 at.% Si decreases from 0.17 to 0.15 and complete oxidation of the silicon to SiO₂ was observed. At a higher

Si content of 26 at.% the friction coefficient increases, after annealing to 400 °C, from 0.13 to 0.15 because of incomplete oxidation of the silicon which requires a higher temperature of 500 °C. The low friction behavior of Si-DLC was observed in combination with the existence of SiO₂ which protects the a-C:H.

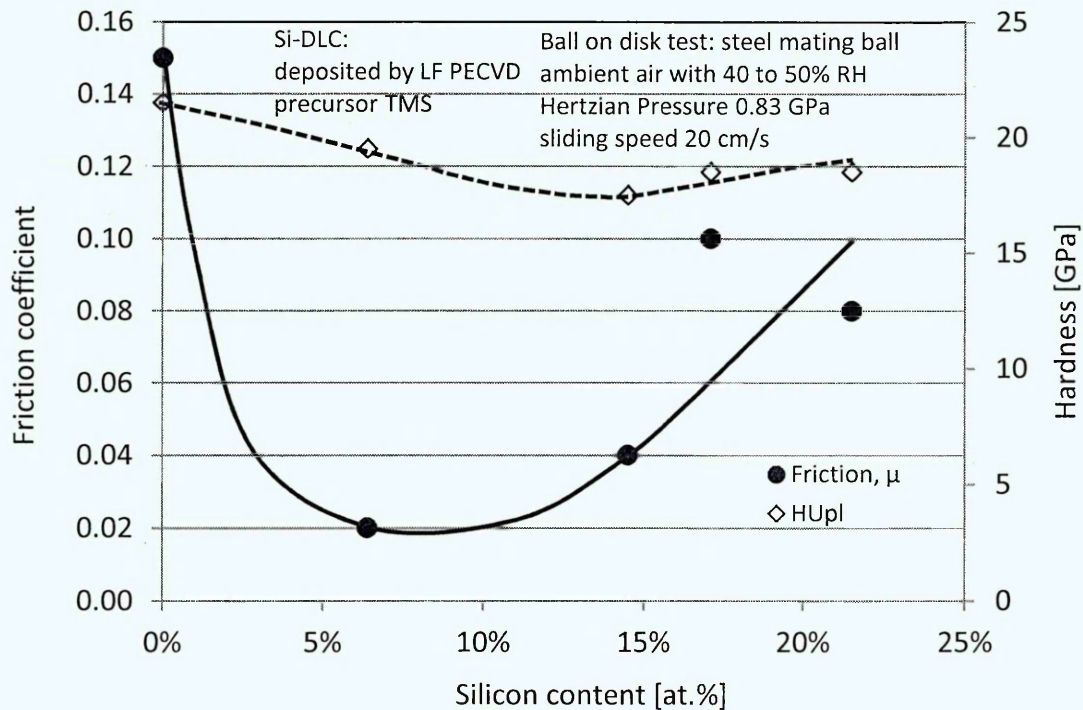


Figure 2.25 : Friction coefficient and hardness of Si-DLC coatings depending on the silicon content in the coating, according to Chouquet et al. [289]

The friction and wear of Si-DLC with silicon concentrations up to 17 at.% was investigated by Dohda et al. [291] using a ball-on-disk test with a steel ball and applying a load of 10 N together with a sliding speed of 20 cm/s in air of 30 to 50% RH. For a-C:H and Si-DLC with 2 at.% Si a friction coefficient of 0.23 and a depth of the wear track of about 0.3 μm were observed and by increasing the Si-content to 4 at.% the friction coefficient is reduced to 0.08 without a change of the wear depth. Through a further increase of the silicon concentration up to 11 at.% and 17 at.% the friction coefficient was slightly reduced to about 0.05 whereas the wear depth increased to 0.5 μm and 1.2 μm respectively. These results show, for the Si-DLC increasing wear rates with increasing Si contents even if at the same time, the friction coefficients are stable or become reduced.

Zhao et al. [292] discussed for Si-DLC the formation of a low shear strength interfacial layer through the transfer of SiO_2 to the wear counterpart, which reduces the friction coefficient, and the formation of the graphitic transfer layer from a-C:H by which superlow friction conditions can be achieved. In order to combine both effects, and to circumvent the difficulty that Si-DLC graphitizes at much higher temperatures compared to a-C:H, graphitic a-C:H:Si coatings were prepared directly by the use of special plasma conditions. Silicon doping up to a Si content of 8.2 at.% was achieved by magnetron sputtering of silicon at PECVD deposition of a-C:H, but the deposited coatings showed low nanohardness of 8.2 to 7.4 GPa [292].

Ultrasmooth Si-DLC coatings with silicon content of 9 to 10 at.% were prepared by an ion beam technique using TMS and toluene mixtures by Chen and Kato [293]. While the Si concentration was almost stable the hydrogen content of the coatings was reduced from 36.7 at.% at -250 V bias to 23.2 at.% at -1500 V bias and 17.3 at.% at -3500 V bias. The Raman spectra revealed for -250 V bias a low-disorder polymer-like type of coating that changed to diamond-like at -1500 V bias and finally to a high-disordering sp^2 bonded a-C at -3500 V bias. The ball-on-disk test was performed using Si-DLC coatings on the disk and the steel ball in dry nitrogen atmosphere under 2 N load at 20 cm/s sliding speed. For Si-DLC coatings with hydrogen content below 20 at.% friction coefficients in the range of 0.015 to 0.05 were observed while above 20 at.% H the friction coefficients were below 0.008 with a minimum of 0.001 at about 32 at.% H also be referred as superlow friction conditions.

Most of the Si-DLC coatings in the literature survey have been produced by PECVD. For these coatings high hydrogen contents, relatively low hardness and low wear resistance have been reported compared to a-C:H. The literature survey for the Si-DLC shows very low friction coefficients which are almost stable in the humidity range of 20 to 80% RH and a high temperature stability up to 500°C in oxidizing atmosphere.

3. Analytical and tribological methods for characterization of coatings

3.1 Adhesion evaluation using the scratch test

The scratch test is a quantitative method for evaluating the adhesion of coatings. The scratch test was applied using the CSM Revetest equipment. Fundamentals and details of the scratch adhesion test are found in the publications of Burnett and Rickerby [294] and Blau [295]. Quantitative scratch adhesion testing is described in the ASTM C1624 standard [296]. Additional information on the introduction of this standard is provided by Gonczy and Randall [297].

The tip of a diamond stylus is moved at constant scratch speed (scratch speed range 0 to 300 mm/min) and increasing normal load (loading rate range 0 to 300 N/min) over the surface of a coated flat sample. The tip of the stylus which has Rockwell C geometry with 120° angles has a spherical radius of 200 μm. The DLC-based coatings were tested using a sliding speed of 10.48 mm/min and a simultaneous load increase of 5 N/s. During scratching, stress waves are detected by an acoustic emission sensor. The output signal of the acoustical sensor is recorded as a function of the load and is used for the evaluation of the adhesion of coatings. The load which is needed to initiate a first cracking of the coating material is called “critical load”, L_{c1} , (Hertzian cracks). A further increase in load increases the initiated stresses and chipping and spalling of the coating material starts. The “critical load”, L_{c2} , is reached at the first appearance of local interfacial spallation or gross interfacial spallation of the coating. The first appearance of gross interfacial shell shaped spallation of the coating material is defined as “critical load” L_{c3} . The critical loads are influenced by various conditions such as the surface roughness, the type of layer material, the substrate material, the internal stress, the layer morphology etc.. Therefore the critical load should be compared only for the same types of coatings under similar contact conditions.

The use of the scratch test on real components is critical because these parts are mostly three-dimensional and the destructive character of testing. Therefore, flat highly polished test coupons are normally used for the scratch test.

The scratch test has to be carried out according to the standard ASTM C1624, ASTM G171 [298] or DIN EN 1071-3 [299].

Typical “critical load” values, L_{C2} , for DLC coatings on highly-polished steel coupons are:

10 - 20 N	(weak adhesion)
20 - 40 N	(good adhesion)
of above 40 N	(very good adhesion)

The adhesion of a-C:H characterized by the “critical load”, L_{C2} , obtained from the scratch test was discussed by Weber et al. [300] for the use of different interlayers.

3.2 Adhesion evaluation using the Rockwell C indentation test

The Rockwell C indentation test is a standard method for adhesion testing, which can be used on real components and on test coupons, that is described in the ISO 26443 standard [301]. The VDI guideline 3198 [302] was withdrawn but is still used in industry therefore this standard was selected for adhesion classification. After the Rockwell indentation, the adhesion of coatings is classified by the appearance of the indentation and the surrounding areas using optical microscopy. The standards define adhesion classes which are for ISO 26443 class 0 to class 3 and for VDI 3198 HF1 to HF6.

The applied load for the Rockwell C indenter, with 120° angles and a tip with a spherical radius of 200 μm , is 1372.9 N. The basic conditions of the Rockwell test are defined in ISO 6508 standard [303].

On the deposited a-C:H-based coatings the tests were carried out using a hardness tester type Testor H T2 001 RB of Amsler Otto Wolpert-Werke GmbH, Germany. Using optical microscopy the adhesion of the coatings was classified according to VDI 3198 as shown in Figure 3.1. The HF classification can be found at Heinke et al. [304] where different adhesion tests for PVD coatings,

including the scratch test, are compared. Vidakis et al. [305] describe the application of the scratch test to monolayers and multilayers using VDI 3198.

HF classification for the adhesion of coatings according to VDI 3198 [302]:

HF1 and HF2 very good adhesion – no or very small adhesion failures, crack network

HF3 and HF4 good and acceptable adhesion – some small adhesion failures, crack network

HF5 and HF6 not acceptable adhesion – significant adhesion failures, chipping of coating.

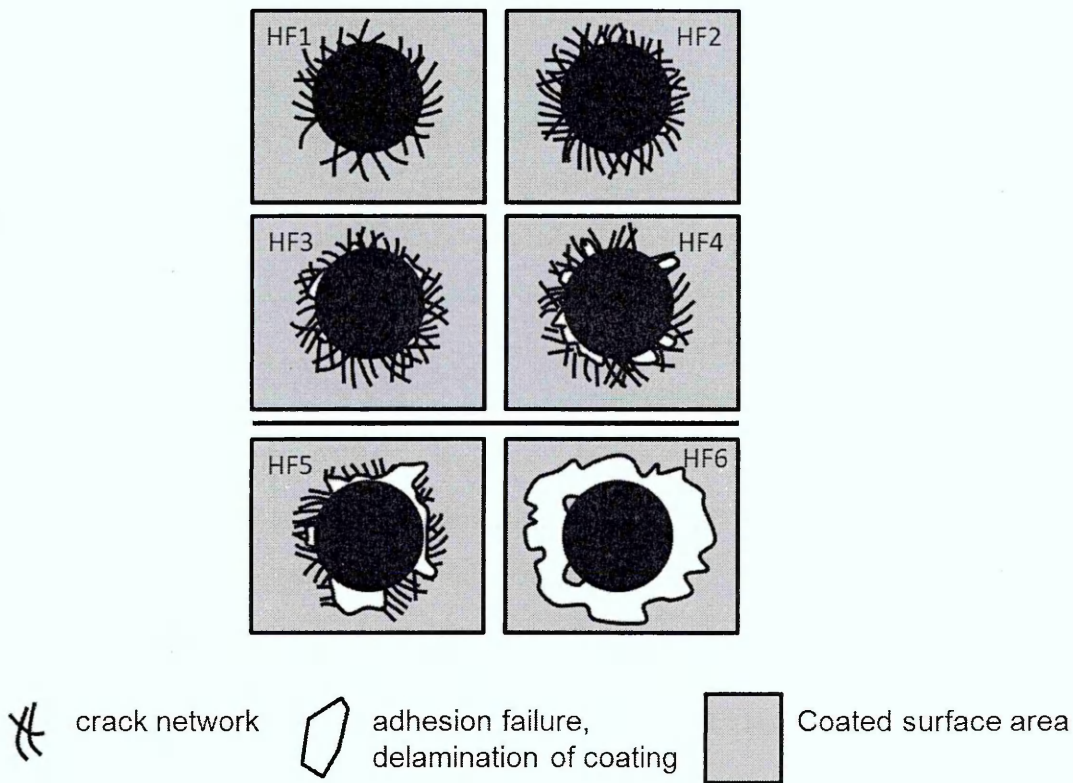


Figure 3.1 : Coating appearance and HF classification of coating adhesion after a Rockwell indentation test, redrawn according to VDI 3198 [302] guideline

3.3 Indentation hardness and reduced indentation modulus evaluation

Bhushan and Li [306] give a detailed description on the nanomechanical characterization of coatings, which includes the hardness evaluation by nanoindentation, an overview on nanoindentation apparatus, indentors and the analysis of indentation data. The first indentation hardness evaluation apparatus was presented by Martens [307] in 1898.

For the deposited a-C:H-based coatings the indentation hardness and the reduced elastic modulus (EIT) were determined by recording the load vs. displacement at linearly increasing and decreasing load using a commercial instrument, Fischerscope H 100 from Helmut Fischer, Germany. PVD coatings require the application of small loads in the mN range. This is to prevent that mechanical properties of the interlayers and/or the substrate influence the hardness results for the coatings because of a too deep penetration of the indenter. For tribological PVD coatings the indentation depths are in the 100 nm range with the limitation that the depth of penetration should not exceed 1/10 to 1/7 of the thickness of the tested coating.

For the evaluation of the plastic microhardness hereinafter also referred to as the “indentation hardness”, the instrumented indentation according to DIN EN ISO 14577 was used. It should be noted that more precise results can be achieved using the improved technique for determining hardness and elastic modulus of Oliver and Pharr [308] which is also known as depth-sensing indentation or nanoindentation.

The plastic microhardness (indentation hardness), was calculated according to equation (3.1):

$$H_{\text{Plast}} = F_{\text{max}}/A_c(h_c) \approx F_{\text{max}}/(26.43 * h_c^2) \quad (3.1)$$

with:

H_{Plast} = plastic microhardness (indentation hardness)

F_{max} = maximum applied load

$A_c(h_c)$ = contact area

F_{max} = F_{ax} = contact depth.

$A_c(h_c)$ =

h_{max} =

A Vickers diamond indenter and a standard load of 30 mN were used for testing the a-C:H-based coatings. For this load the maximum penetration depth was usually below 400 nm. The load, F , was reduced if the indentation depth exceeded 10% of the layer thickness.

The reduced indentation modulus (EIT) was used which is almost identical to the elastic modulus (Young's modulus), E , for a-C:H based coatings. The reduced indentation modulus (EIT) was calculated after determining of the reduced modulus (E_r) using the stiffness, S , and the contact area, A_c , from the indentation curve as described in Figure 3.2. The reduced indentation modulus (EIT) is defined as $E/(1-\nu^2)$ where ν is the Poisson's ratio of the tested material.

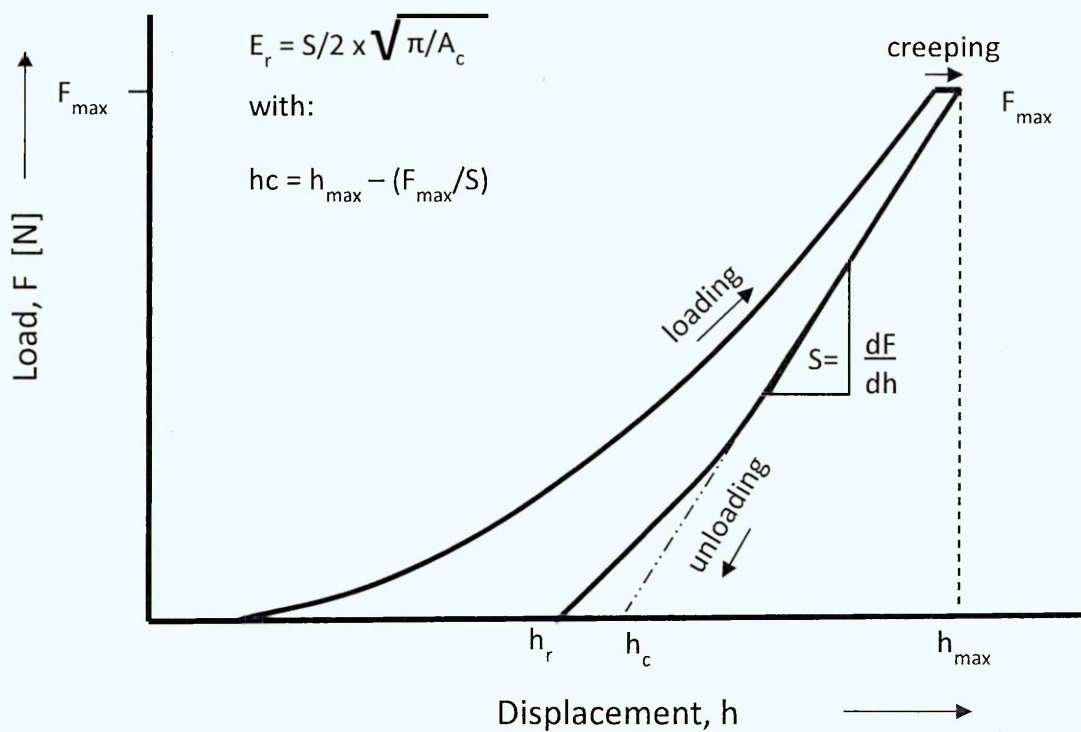


Figure 3.2 : Evaluation of the reduced modulus (E_r), according to Fraunhofer IST

Reviews on advanced indentation testing and measurement of hardness and elastic modulus were presented by Fischer-Cripps [309] and Oliver and Pharr [310].

3.4 Abrasive wear rate and film thickness evaluation using the ball cratering test

When using the ball cratering test, the coating thickness can be determined according to the DIN EN 1071-2 standard [311] and the abrasive wear resistance according to the DIN EN 1071-6 standard [312].

Details on the ball cratering test are discussed by Gee et al. [313] and for testing of plane and cylindrical DLC coated specimens by Michler and Siebert [314]. Taube [315] describes the testing of carbon-based coatings.

The principle of the ball cratering test is shown in Figure 3.3.

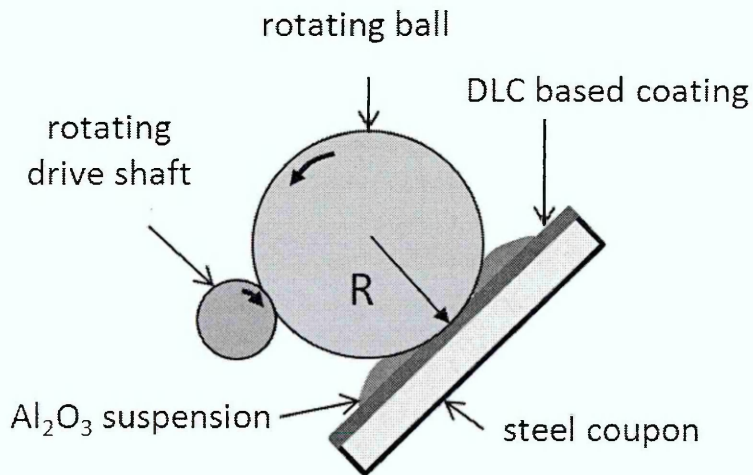
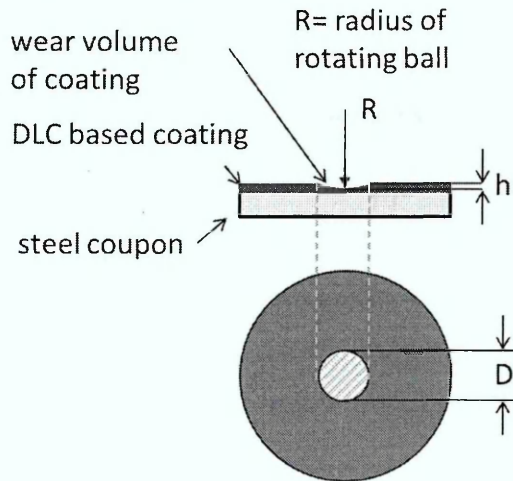


Figure 3.3 : Principle of ball cratering test to determine abrasive wear rates

Ball cratering was arranged using a Kalomax NT, equipment made by BAQ, with alumina suspension of a mean grain size of 1 μm as abrasive medium for testing the a-C:H-based coatings. A ball of a defined weight, which is rotated by a drive shaft, is positioned on a coated test coupon. The used ball, which is made of bearing steel (100Cr6), has a diameter of 30 mm. The tests were carried out at room temperature of about 20°C and at approximately 50% RH with a load of 0.54 N. After a wear duration of 3 to 9 minutes the diameter of the spherical wear calotte is measured using a light microscope and the wear volume is determined.

The evaluation methods for the wear rate of coatings and the layer thickness are shown in Figure 3.4. The unit used for abrasive wear rate, w_v , of coatings is $10^{-15} \text{ m}^3/(\text{Nm})$ which is equal to $10^{-6} \text{ mm}^3/(\text{Nm})$ required to directly compare the orders of magnitude with wear coefficients from the ball on disk test.

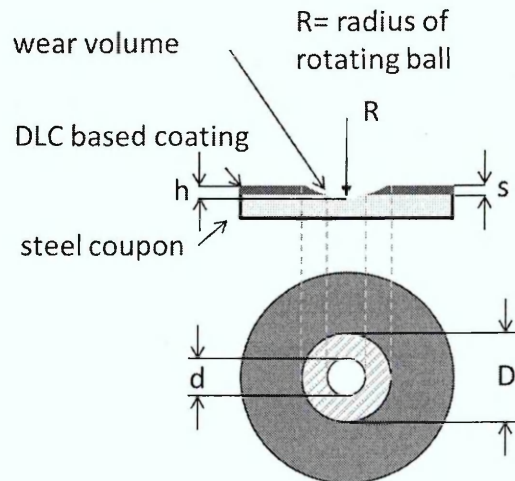
Evaluation of abrasive wear volume



$$h = R - (R^2 - D^2/4)^{1/2} \quad h = \text{penetration depth}$$

$$V = \frac{(h^2\pi)}{3} \times (3R-h) \quad V = \text{abrasive wear volume (spherical calotte)}$$

Layer thickness evaluation



$$s = (R^2 - d^2/4)^{1/2} - (R^2 - D^2/4)^{1/2}$$

$$s = \text{layer thickness}$$

Figure 3.4 : Evaluation of the abrasive wear volume and the layer thickness using the ball cratering test

3.5 Friction coefficient and adhesive wear coefficient determination using ball-on-disk test

For the evaluation of the wear rate of coatings, in the tribology, the ball-on-disk testing apparatus, according to the ASTM G99-04 standard [316], is more commonly used compared to the ball cratering test. The ball-on-disk test, which is known also as pin-on-disk test, allows determining of the friction coefficient according to the ASTM G99-95a [317] standard and the adhesive wear rate according to the ASTM G99 [318] or the DIN EN 1071-13 [319] standard. The friction and wear of a coating deposited on the disk and the wear of the mating ball are influenced by a number of additional conditions e.g. the ambient atmosphere, the material on the surface of the wear counterpart which may contain a coating, a transfer layer or wear debris etc. Very similar wear conditions exist in the reciprocating wear test according to the DIN EN 1071-12 standard [320] in which a linear oscillation movement is used.

The fundamentals of the ball-on-disk test have been studied in a multilaboratory tribotesting programme, details of which were discussed by Czichos et al. [321, 322].

Friction and wear results for a-C:H and a-C:H:W coatings achieved from ball-on-disk testing were presented by Taube et al. [323].

For the deposited a-C:H-based coatings friction and wear coefficients were determined using a ball-on-disk test apparatus which was self-built by Fraunhofer IST, Germany. The tested coatings were deposited on highly polished flat steel coupons of 35 mm diameter. The testing was carried out without additional lubrication, also known as dry conditions, mostly in air of about 50% RH. For the evaluation of friction coefficients, depending on the relative humidity, testing was performed in air within the range of 20 to 80% RH. A mating ball with a diameter of 4.8 mm was used, which was normally made of ball-bearing steel (100Cr6) but in some cases cemented carbide (WC with 6% Co binder) was used. Normally a load of 3 N but in some cases 1 N was used in combination with a sliding velocity of 4 cm/s. The corresponding Hertzian pressures were estimated to be in the range of 0.3 to 0.6 GPa. Figure 3.5 shows the schematics of the ball-on-disk test.

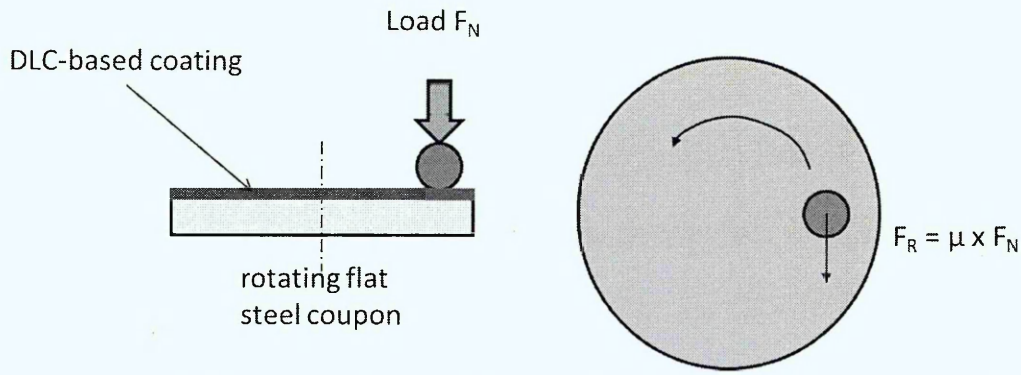


Figure 3.5 : Schematics of the ball-on-disk test

During the ball-on-disk test, which was performed under these conditions, the friction coefficient, μ , was determined from the measurement of the radial force, F_R , for a normal force, F_N , according to the formula: $\mu = F_R/F_N$.

The friction coefficients were continuously recorded in order to evaluate the running-in behavior and to define the friction coefficient at steady state conditions. After running the ball-on-disk test, the profile of the wear scar was determined using a contact profilometer on the circular wear track on the disk at four different positions and/or by an optical microscope observing the base area of the spherical wear calotte on the ball.

Four cross-sectional areas, S_1 , S_2 , S_3 and S_4 from the wear profiles were calculated. Using the radius, r , of the wear track the wear volume of the disk, V_{disk} , was evaluated according to the formula (3.2):

$$V_{\text{disk}} = \frac{1}{2} \times \pi \times r (S_1 + S_2 + S_3 + S_4) \quad (3.2)$$

For the ball the minimum diameter of the wear scar, A , and the diameter of the wear scar perpendicular to the minimum diameter, B , and the diameter of the ball, D , were used to calculate the wear volume of the ball according to formula (3.3):

$$V_{\text{ball}} = \pi \times A^3 \times B / (32D) \quad (3.3)$$

From the evaluation of the wear scars the wear volumes of the disk or the ball were calculated considering a material transfer, should one exist.

The specific wear rates of the disk, w_{disk} , and the ball, w_{ball} , were determined by dividing the wear volumes by the normal force (load), F_N , and the sliding distance, L , according to the formulas (3.4):

$$w_{\text{disk}} = V_{\text{disk}} / (F_N \times L) \text{ and } w_{\text{ball}} = V_{\text{ball}} / (F_N \times L) \quad (3.4)$$

3.6 Structural evaluation using X-Ray diffraction

X-ray diffraction (XRD) is used in order to investigate the structural properties of crystals and powders.

X-rays of defined wavelengths which are in the order of the atomic distances of 0.2 to 0.3 nm are used. Cu K α radiation with a wavelength of $\lambda = 0.154$ nm was used for structural evaluations of the a-C:H-based coatings by XRD and for the determination of the mass density by X-ray reflectometry (XRR).

An X'Pert MRD multipurpose instrument made by PANalytical B.V., The Netherlands, was used at a grazing angle incidence of 0.4° for structural evaluation on the a-C:H-based coatings in order to detect crystalline regions or an amorphous structure. The principle of the experimental setup is shown in Figure 3.6.

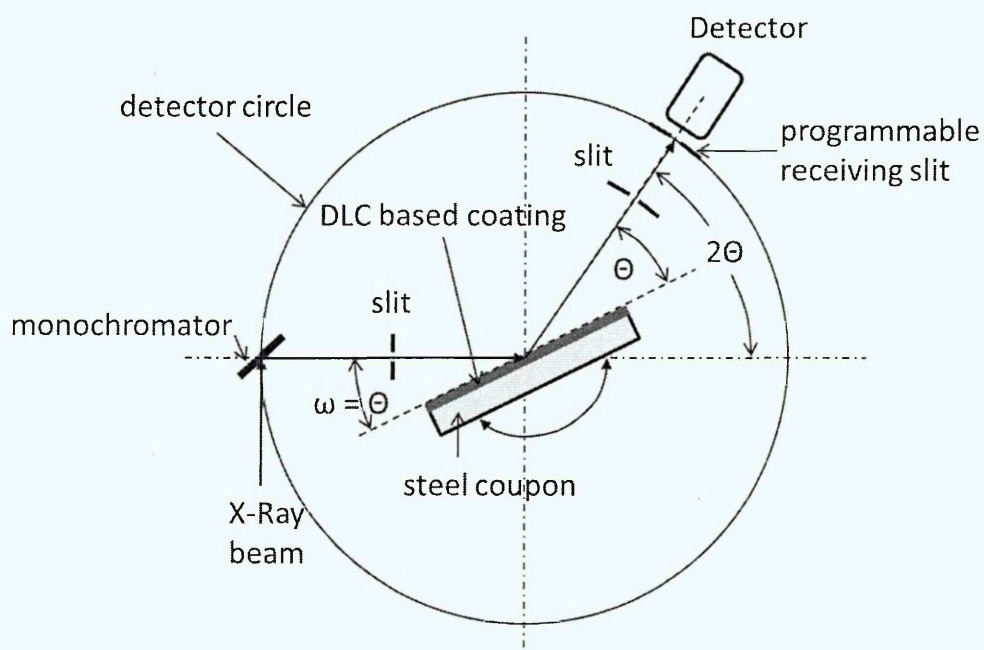


Figure 3.6 : Principle of the experimental setup for X-ray diffraction (XRD) and X-ray reflectometry (XRR)

Diffraction of the X-rays on the atomic planes of crystalline regions or crystallites of the materials from the deposited coatings occurs at an angle, Θ , for which a constructive interference exists.

The angle, Θ , for diffraction peaks can be calculated for the wavelength, λ , of 0.154 nm and the distance of lattice planes, d , of the investigated material by using Bragg's equation:

$$n * \lambda = 2d * \sin(\Theta) \quad (3.5)$$

$$n = 1, 2, 3, \dots$$

For an X-ray amorphous hydrogenated carbon based material the diffraction spectrum does not show diffraction lines.

3.7 Mass density evaluation using X-Ray reflectometry

X-ray reflectometry (XRR) was used for the evaluation of the mass density of coatings. The method can be also used to determine the layer thickness of thin coatings of up to about 200 nm and the surface or interface roughness. Details on the XRR method are discussed by Yasaka [324] and by Gibaud et al. [325]. Cu K α radiation was used for the XRR evaluations which were carried out using the X'Pert MRD multipurpose instrument with an experimental setup as described for XRD (see Figure 3.6).

The density of the a-C:H-based coatings was obtained from the critical angle, θ_c , for the incident radiation at the point when the X-rays start to penetrate the film.

The evaluation of the mass density for DLC-based coatings using XRR is described by Ferrari et al. [326]. Figure 3.7 shows an XRR spectrum for a carbon based coating redrawn according to Calliari et al. [327] in which the positions are marked from which the critical angle, θ_c , and the period of oscillation, $\Delta\theta$, can be taken. For the evaluation of the mass density the critical angle, θ_c , and for determining the layer thickness the period of oscillation, $\Delta\theta$, are used.

The mass density, ρ , can be determined using the equations (3.6) and (3.7):

$$\Theta_c = (2 * \delta)^{\frac{1}{2}} \quad (3.6)$$

Θ_c = critical angle

δ = dispersion

and

$$\delta = \frac{N_A}{2\pi} * r_0 * \lambda^2 * Z * \frac{\rho}{A} \quad (3.7)$$

ρ = mass density

N_A = Avogadro's number

Z = atomic number

r_0 = classical electron radius

λ = wavelength

A = atomic mass

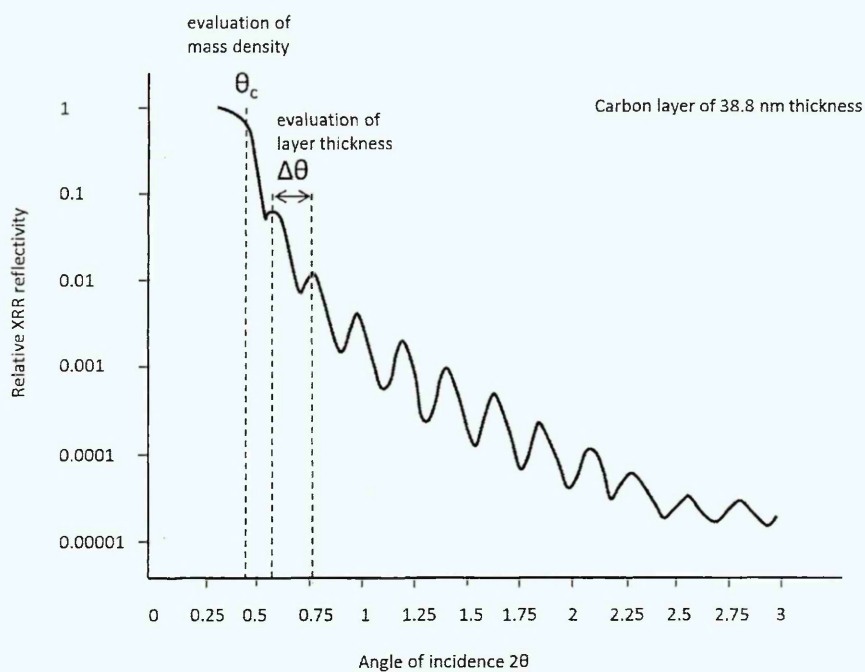


Figure 3.7 : XRR spectrum of a 38.8 nm carbon-based layer, redrawn according to Calliari et al. [327]

3.8 Secondary Ion Mass Spectroscopy (SIMS) for the analysis of the layer composition

Secondary Ion Mass Spectroscopy (SIMS) is a surface-sensitive microanalysis method with a typical information depth of <0.6 nm which allows lateral resolutions of <0.1 μm and minimum detectable trace concentrations of <1 ppm. The applications and the instrumental aspects of SIMS are discussed by Benninghoven et al. [328]. For analyzing the surface and near surface layers the static SIMS method [329], for which the removal time for a monolayer can be less than one hour, is used.

For depth profiling, which allows observing the elemental composition of a coating, depending on the depth or coating thickness, the dynamic SIMS method is used. The quantification of the elemental composition using dynamic SIMS is very complex and makes it necessary to use reference samples of a known composition for calibration. Details on dynamic SIMS are discussed by McPhail and Dowsett [330].

If Ar^+ ions are used in the primary beam, in a typical energy range of 1 to 30 keV, the emission of secondary ions depends on the detected element and on a matrix effect which is a combined effect of all components of the analyzed sample spot. In order to increase the detection sensitivity O_2^+ ions and oxidation of the surface are used. For Cs^+ , as primary ions, the secondary ion yield is very high which increases the sensitivity for detection and a reduced matrix effect can be observed.

Quantitative SIMS uses relative sensitivity factors, RSF, which need to be defined for a specific type of primary ion for the analyzed elements. Information about quantitative SIMS and RSF factors for Si and diamond are given by Wilson [331].

The elemental concentration of an element, E, in relation to a reference element, R, and the related RSF factor is calculated according to the following equation:

$$\frac{I_R}{C_R} = \text{RSF}_E * \frac{I_E}{C_E} \quad (3.8)$$

- RSF_E = relative sensitivity factor for element E
- I_E = secondary ion intensity for element E
- I_R = secondary ion intensity for reference element R
- C_E = concentration of E
- C_R = concentration of R

If the major or matrix element, M, is chosen as the reference element, R, the concentration of the element, E, can be calculated using the equation:

$$C_E = \text{RSF}_E * \frac{I_E * C_M}{I_M} \quad (3.9)$$

- C_M = concentration of matrix element M
- I_M = secondary ion intensity for matrix element M

The deposited a-C:H-based coatings were analyzed under UHV conditions using a primary ion beam of Cs⁺ ions using a SIMS instrument Cameca ims 5f made by Cameca SAS, France. The SIMS system is routinely used for quantitative depth profiling of a-C:H-based coatings.

Cs⁺ primary ions are used for the bombardment of the coating and MCs⁺ molecular secondary ions (M is the observed element) are analyzed with almost no matrix effect. Quantitative analysis of the composition, also of hydrogen, was discussed by Willich et al. [332, 333]. In [333] it was shown that hydrogen concentrations can be determined precisely for carbon-based materials with different matrix compositions like metal-containing and metal-free amorphous carbon.

3.9 Scanning Electron Microscope (SEM)

A scanning electron microscope (SEM) Leo 1530 of LEO Elektronenmikroskopie GmbH Oberkochen (Germany) was used to investigate the morphology and topography of the coatings. To image the morphology of the coatings fracture cross sections were used.

Typical operation data for the practical use of the SEM were:

Acceleration voltage:	0.5 to 30 kV
Beam current (max.):	20 nA
Beam current (operation):	Currents in the pA range
Resolution:	2 nm (the lateral dimension of the beam spot is smaller than the resolution)
Electron gun:	Tungsten filament (field emission)
Aperture inside beam:	10 to 120 μm
Magnification:	10x to 1000000x
Area at imaging:	10x \rightarrow 1 cm^2 ; 100x \rightarrow 1 mm^2 ; 1000x \rightarrow 100 μm^2
(for some magnifications)	10000x \rightarrow 10 μm^2 , 100000x \rightarrow 1 μm^2 , 1000000x \rightarrow 100 nm^2
Working distance (WD):	2 to 45 mm
4 Detectors:	Secondary electron detector (SE) In-lens detector for secondary electrons captured by the objective lens field (provides better surface imaging) Back scattered electron detector (BSE) for high-resolution compositional maps and for distinguishing different phases Energy dispersive X-ray detector (EDX) to investigate the elemental composition

3.10 Electron Probe Microanalysis (EPMA)

Electron Probe Micro Analysis (EPMA) was used for the analysis of the elemental composition of the coatings, with the exception of hydrogen using a commercial instrument, Cameca SX 100 of Cameca SAS (France).

Typical data for the operation of the EPMA instrument were:

Acceleration voltage:	5 to 30 kV
Beam current:	1 to 100 nA
Beam diameter:	1 to 2 μm
Electron gun:	Tungsten filament
SEM magnification:	150x to 20000x
Wavelength dispersive spectrometers (WDS):	5 spectrometers for monochromizing
3 Crystals:	Lithium fluoride (LIF) Pentaerythriol (PET) Thallium acid phthalate (TAP)
2 Pseudocrystals (PCs):	PC1 and PC2
Detectable elements	Boron and elements of higher atomic mass
Detection limit:	0.01 wt.%
Resolution:	$10^{-5} \sin \theta$
Calibration:	Using standards of defined elemental composition

4. Experimental

4.1 Ion assisted a-C:H deposition using industrial system concepts

The a-C:H-based coatings were produced by magnetron-based deposition under vacuum conditions by applying a combination of physical vapor deposition (PVD) and the plasma enhanced chemical vapor deposition (PECVD) method.

For the deposition of hard a-C:H-based coatings an intensive ion bombardment of the growing film, with ions in the 100 eV energy range, needs to be arranged in order to promote the generation of sp^3 hybridized carbon by the subplantation effect. The coating of three-dimensional parts with small distances between the parts requires a strong plasma support in order to achieve sufficient ion bombardment and ion plating conditions on all surface areas where coating occurs.

The a-C:H-based coatings have to be prepared under industrial conditions. This requires the capability to coat large substrate volumes which could be arranged using the Plasma Booster [334, 335, 64] concept (Figure 4.2) or the Closed Field concept (Figure 4.1). In the original Closed Field concept of Teer [61] only the magnetic fields of the magnetron cathodes were used for a-C:H deposition, as discussed by Monaghan [336]. The closed field with additional electromagnetic coils, which is shown in Figure 4.1, was presented by Donohue et al. [337] and Hurkmans et al. [338]. For small distances the closed field arrangement can be operated only by using the magnetic fields of the magnetron cathodes but at larger distances between the cathodes the operation of the electromagnetic coils is necessary in order to achieve closed field conditions.

In both industrial deposition concepts planar magnetron cathodes with targets of a rectangular shape are used. In order to achieve ion plating conditions the magnetron cathodes are operated in an unbalanced mode in both concepts. Typically the weakening of the inner pole of the magnetic field array is used in order to achieve unbalanced magnetron conditions. In the case of the use of electromagnetic coils at the cathodes the operation mode of the magnetron

cathodes can be changed from balanced operation to a strong unbalanced operation using the superposition of the magnetic field of the electromagnetic coil for which the magnetic field strength can be adjusted by the coil current. If the inner pole of the magnetic field array of the unbalanced magnetron cathode is weakened, magnetic field lines from the outer pole and the electromagnetic coil are directed into the space in front of the magnetron cathode. For the Closed Field arrangement the polarities of the outer magnetic poles of neighboring cathodes are changed which forms a magnetic bottle around the substrates as shown in Figure 4.1. For the Plasma Booster, which is shown in Figure 4.2, two magnetron cathode arrays which have different outer magnetic polarities are opposing each other. In order to become more independent from the electromagnetic coil operation used for unbalancing of the cathodes, the adjustment of the confinement by the magnetic bottle is arranged by using additional electromagnetic coils which surround the two cathode arrays. Using this arrangement an almost perfect magnetic bottle can be created.

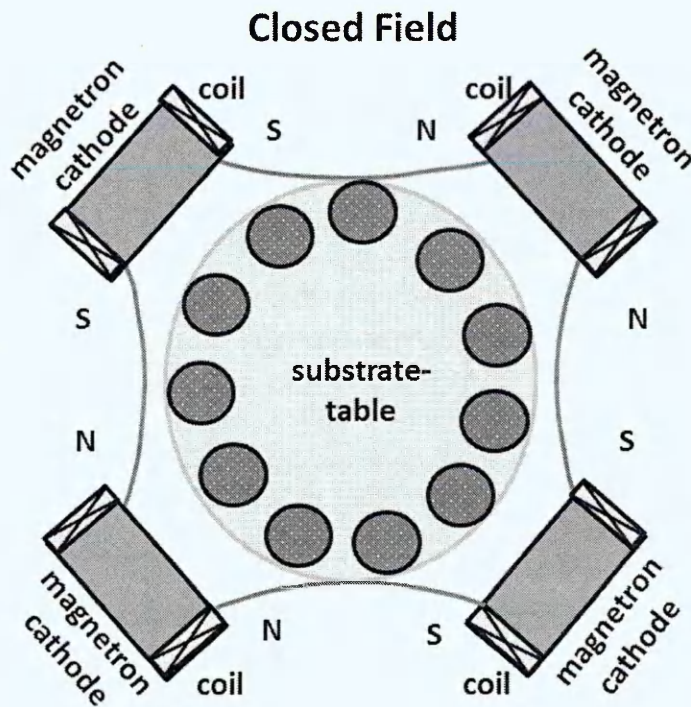


Figure 4.1 : Closed field arrangement for industrial coating of large substrate volumes with plasma assistance [61, 337, 338]

In the previously discussed unbalanced magnetron-based arrangements the magnetical confinement of the plasma in front of the magnetron cathodes is broken up and electrons are moved towards the substrate region. This, combined with electron impact ionization, moves the plasma to the substrates which are usually loaded on rotating planets. With both industrial deposition arrangements structure optimized and dense a-C:H-based coatings can be deposited at high substrate current densities of up to several mA/cm².

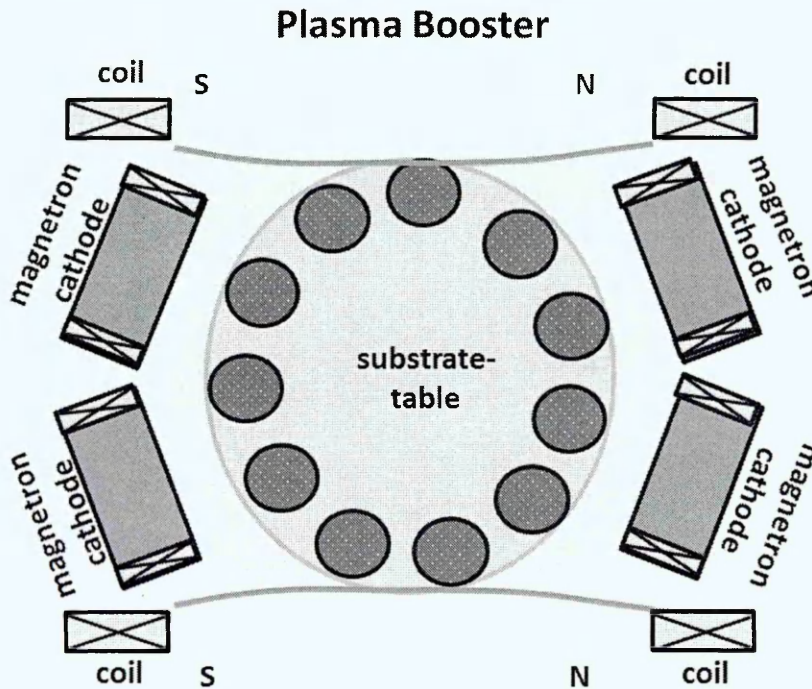


Figure 4.2 : Plasma Booster arrangement for industrial coating of large substrate volumes with plasma assistance [334, 335, 64]

4.2 Coating system, parts to be coated and basic process sequence

The coatings were deposited using an industrial PVD coating system Z1200 at the Fraunhofer Institute IST Braunschweig (manufacturer Systec GmbH Karlstadt, Germany) which is equipped with 4 large magnetron cathodes. A photograph of the vacuum chamber of the coating system Z1200 with magnetron cathodes on the opened chamber doors is shown in Figure 4.3.



Figure 4.3 : Coating system Z1200 with opened vacuum chamber doors at Fraunhofer IST

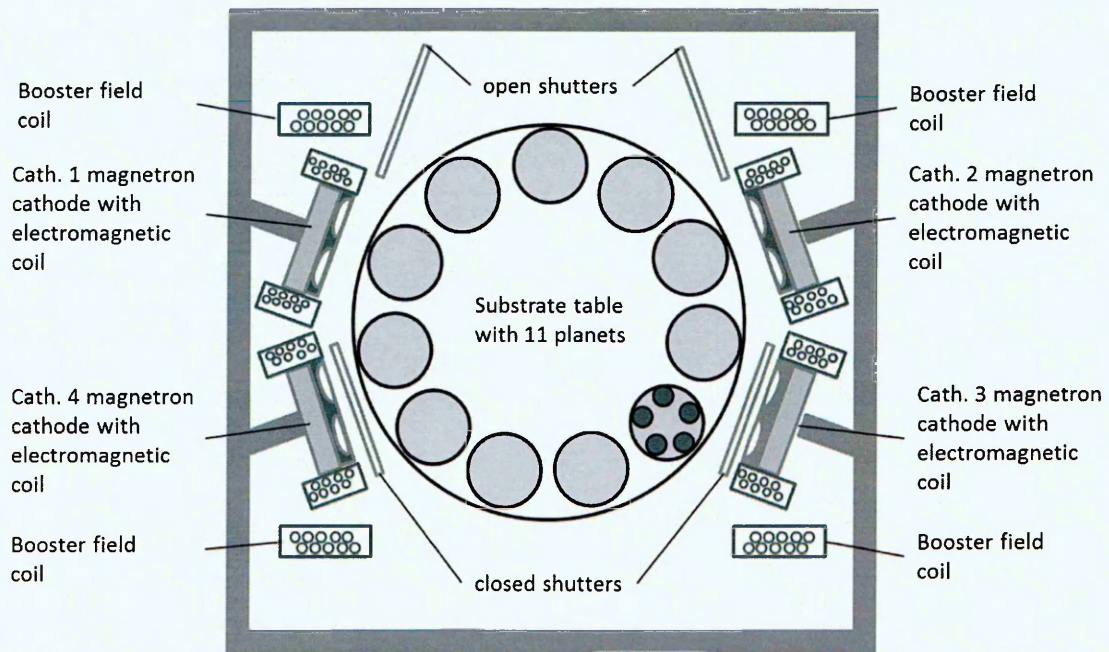


Figure 4.4 : Schematic cross-sectional view of the vacuum chamber of the Z1200 batch coater with Plasma Booster arrangement at Fraunhofer IST

The schematic cross-sectional view shows the substrate table with the substrates on 10 planet positions, planets of up to 150 mm diameter and about 600 mm length can be coated. The substrate table loaded with substrates can be completely removed from the coating chamber using a trolley mechanism. Shutters are positioned in front of the magnetron cathodes which are open during coating operation and closed during ion etching. During ion etching the shutters collect the target material from the magnetron cathodes which support the etching procedure with plasma from the magnetron discharges using the Plasma Booster.

The most important hardware elements of the Z1200 are described in Table 4.1.

Coating sources and Plasma Booster

- 4 magnetron cathodes, (length 1 m x width 0.25 m)
- 4 DC power supplies for magnetron cathodes with 20 KW output
- 6 electromagnetic Booster coils
- 3 DC power supplies for Booster coils
- 4 separately operated cathode shutters

Substrate table and electrical supply

- substrate table of Ø 800 mm (maximum load 800 kg)
- 10 substrate planets (length = 600 mm; Ø 150 mm)
- DC & pulsed-DC power supply for substrates (10KW, 5 – 350 KHz)
- (first) rotation of substrate table 0.5 to 6 RPM;
- (second) rotation of planets 0 to 20 RPM;
- (third) rotation of parts on planets arranged by latch mechanisms

Vacuum and Gases

- 2 turbomolecular pumps (nominal capacity 1000 l/s)
- 1 roots blower pump (nominal capacity 1000 m³/h)
- 1 rotary vane pump (nominal capacity 630 m³/h)
- 4 mass flow controllers for process gases (Ar, C₂H₂, N₂, O₂)

Automation

- 1 PLC control
- 1 visualization unit

Table 4.1 : Most important hardware elements of the Z1200 batch coater

Figure 4.5 shows two magnetron cathodes mounted on a chamber door of the Z1200 coating system.

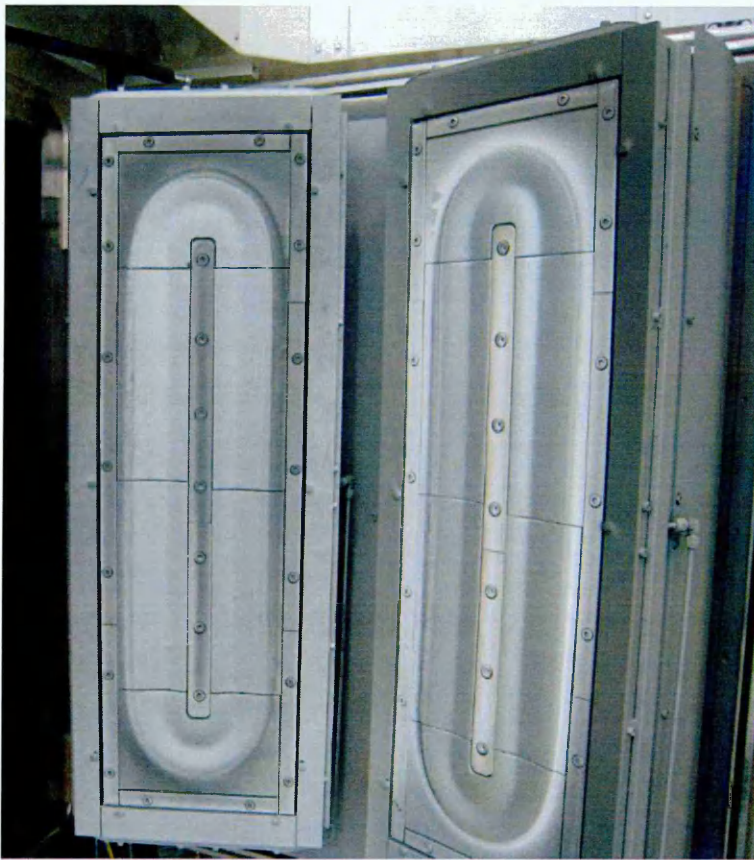


Figure 4.5 : Magnetron cathodes mounted on the door of the vacuum chamber of the Z1200 batch coater at Fraunhofer IST

A mixed load of test coupons, silicon wafers, dummy parts and/or components was used for coating. Test coupons with \varnothing 35 mm and a thickness of 4 mm are made of case-hardened (>62 HRC) 100Cr6 (SAE52100) steel and are polished on one plane surface ($R_a = 0.013 \mu\text{m} \pm 0.002 \mu\text{m}$ and $R_z = 0.062 \mu\text{m} \pm 0.012 \mu\text{m}$). These test coupons were coated then used for adhesion testing and evaluating the coating properties. The coupons must be coated at a temperature below the annealing temperature of 200°C in order to prevent a loss of surface hardness.

A load for coating with double rotation containing dummy pylons and one especially prepared pylon on which three test coupons and silicon wafers are mounted is shown in Figure 4.6.



Figure 4.6 : Substrate table of the batch coater Z1200 at Fraunhofer IST with dummy pylons and one especially prepared pylon with test coupons and silicon wafers

The process sequence with the main steps is shown in Table 4.2.

- I. Positioning of the movable substrate table loaded with uncoated substrates into the vacuum chamber of the coating system
- II. Closing of the chamber door and evacuation down to 2×10^{-5} mbar
- III. Cleaning of the substrates by ion etching using Plasma Booster support
- IV. Deposition of interlayers by magnetron sputtering
- V. Deposition of a-C:H-based layers by magnetron based PVD+PECVD
- VI. Cooling down of substrates, venting of vacuum chamber
- VII. Removing of the movable substrate table loaded with coated substrates from the vacuum chamber of the coating system

Table 4.2 : Process sequence with main steps

4.3 Process data for a-C:H and Si-DLC deposition

Targets which consist of tiles are mounted on the cathodes by using clamping bars. The target surface is 232 mm x 898 mm and the thickness of the targets is 18, 10 or 6 mm with the 10 and 6 mm targets being bonded on copper backing plates. Depending on the process type, 2 graphite targets, 1 metal target (Cr, Ti, Ta etc.) and one SiC/C target or alternatively one WC target which contains 6 weight% Co as binder material are mounted on the 4 cathodes of the system. The SiC/C target contains a mixture of SiC and graphitic carbon which makes the target electrically conductive (resistivity $\approx 1 \Omega\text{cm}$) and allows using a DC voltage for deposition. The composition of the SiC/C target was determined by EPMA analysis of a coating which was deposited in pure argon atmosphere. An elemental composition of 39 at.% silicon and 39 at.% carbon originating from SiC and 22 at.% free carbon was found by the EPMA analysis of the coating which corresponds with the composition given in the datasheet of the target manufacturer.

After evacuation of the coating system to a pressure of 2×10^{-5} mbar the ion etching procedure using pure argon and two-fold rotation was carried out with the use of two to four cathodes in Plasma Booster operation in order to support the etching procedure with plasma from these cathodes. During etching the shutters of the 4 cathodes are closed in order to collect the material which is deposited from the targets. The basic process parameters for the etching procedure are shown in Table 4.3.

Process gas	argon
Total pressure	2 to 15 $\times 10^{-3}$ mbar
Etching time	10 to 30 minutes
Substrate voltage	-300 to -1000 V pulse peak
Substrate current	2 to 8 A effective
Duty cycle	30 to 100%
Substrate current density	0.4 to 1 mA/cm ² (on active surface)
Magnetron cathode (2-4)	-500V to -750V / 10 to 30 A
Booster assistance	$\approx 80\%$

Table 4.3 : Process data for ion etching process

After finishing the etching process a pure metallic layer, typically chromium, with a thickness of 0.2 to 1 μm is deposited using pure argon as process gas and two-fold rotation. This layer serves to promote the adhesion of the functional top layer(s) by its good bonding properties to the substrate material and by releasing the stress which is introduced by the diamond-like functional coatings to the interface between the coating and substrate. The typical process data for the deposition of the metallic interlayer is shown in Table 4.4.

Metal target	Cr, Ti or Ta etc.
Process gas	argon
Deposition pressure	3 to 10 $\times 10^{-3}$ mbar
Deposition time	15 to 60 minutes
Cathode voltage	-500 to -750 V DC
Cathode current	10 to 30 A
Substrate voltage	-50 to -300 V pulse peak
Substrate current	1,5 to 3 A effective
Duty cycle	30 to 100%
Substrate current density	$\approx 1 \text{ mA/cm}^2$
Booster Assistance	$\approx 80\%$

Table 4.4 : Process data for the deposition of the metallic interlayer

In order to achieve a smooth transition from the metallic interlayer to the a-C:H-based layers a second interlayer is deposited onto the metallic interlayer. For pure a-C:H coatings a WC target is sputtered in an Ar/C₂H₂ gas mixture using an increasing acetylene mass flow with increasing deposition time. At similar deposition conditions, for Si-DLC and Si-DLC/a-C:H coating, a SiC/C target is used to produce the second interlayer. The basic process parameters for the deposition of the second interlayer are found in Table 4.5.

Target	WC or SiC/C
Process gases	argon and acetylene
Deposition pressure	3 to 10 x10 ⁻³ mbar
Deposition time	1 to 3 hours
Cathode voltage	-500 to -750 V DC
Cathode current	10 to 30 A
Substrate voltage	-50 to -300 V pulse peak
Substrate current	3 to 6 A effective
Duty cycle	30 to 100%
Substrate current density	≈ 1 mA/cm ²
Booster assistance	≈ 80%

Table 4.5 : Process data for the deposition of the second interlayer

By adjusting the acetylene mass flow, in the final part of the second interlayer, a-C:H:W or Si-DLC was deposited which offer perfect bonding conditions for the functional top layer of pure a-C:H and the Si-DLC.

In the final step of the deposition process the functional top layers of pure a-C:H and/or the Si-DLC are deposited in a dynamic mode again using two-fold rotation of the substrates. The basic parameters for these deposition processes are shown in Table 4.6.

Target(s)	graphite (one or two) and/or SiC/C
Process gases	argon and acetylene
Deposition pressure	3 to 10 x10 ⁻³ mbar
Deposition time	2 to 6 hours
Cathode voltage	-500 to -750 V DC
Cathode current	10 to 30 A
Substrate voltage	-200 to -400 V pulse peak
Substrate current	5 to 10 A effective
Duty cycle	70 to 80%
Substrate current density	1 to 2.5 mA/cm ²
Booster assistance	≈ 50%

Table 4.6 : Basic process parameters for the deposition of the functional top layers of pure a-C:H and/or the Si-DLC

5. Results and discussion

5.1 Reactive deposition using graphite, SiC/C and WC targets

For the reactive deposition of carbon-based coatings using metallic targets and C_2H_2 as reactive gas normally strong target poisoning and hysteresis effects are observed. In order to reduce the mass flow of C_2H_2 , as required for the deposition from metal targets, pure carbon or carbide targets were used.

The hystereses of the total pressure and the cathode voltage were taken at the deposition of a-C:H with two graphite targets. The cathodes were operated with a power of 10 kW on each cathode and the mass flow of acetylene was increased stepwise from 0 to 400 sccm followed by a stepwise decrease of the C_2H_2 flow back to 0 sccm. The hystereses of the total pressure and the cathode voltage which are achieved by changing the mass flow of acetylene are shown in Figure 5.1.

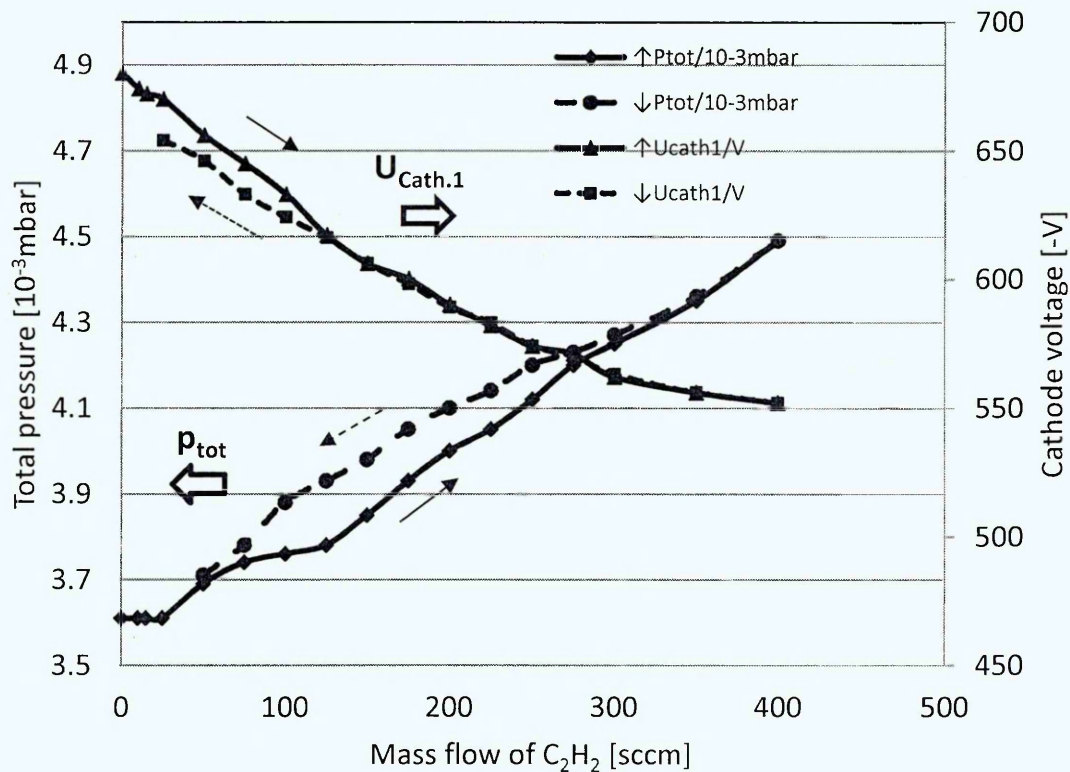


Figure 5.1 : Hystereses of one cathode voltage and the total pressure at reactive sputtering from two graphite targets depending on the acetylene gas flow (at 10 kW power on each cathode)

The hysteresis curves for the cathode voltage and the total pressure are very narrow. During sputtering of carbon from the graphite target it is expected that carbon of the graphite target reacts only slightly with the precursor gas.

The reduction of the cathode voltage with increasing mass flow of C_2H_2 can be explained by the increase of the total pressure.

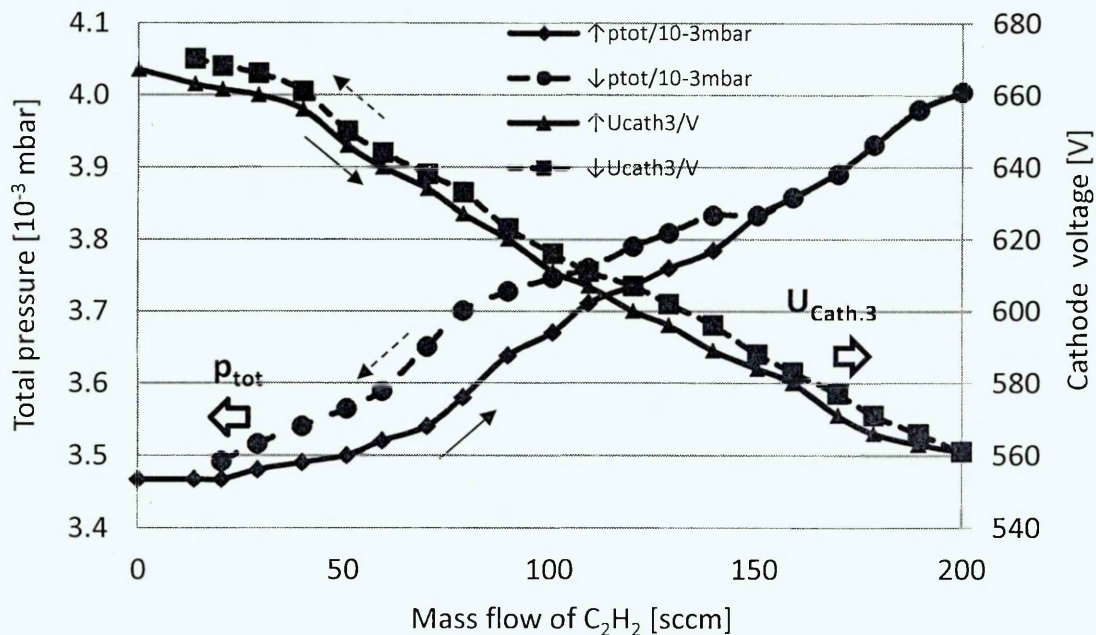


Figure 5.2 : Hystereses of the cathode voltage and the total pressure at reactive sputtering from an SiC/C target depending on the acetylene gas flow (one magnetron cathode operated at 10 kW power)

For one SiC/C target small hysteresis effects for the total pressure and the cathode voltage are again observed as shown in Figure 5.2. Caused by the one cathode operation, at 10 kW power, for acetylene only a maximum mass flow of 200 sccm is needed in order to complete the hysteresis curves. From the SiC/C target silicon and carbon are deposited and it is expected that the SiC/C target reacts only slightly with the precursor gas. Again the reduction of the cathode voltage with increasing mass flow of C_2H_2 could be explained by the increase of the total pressure.

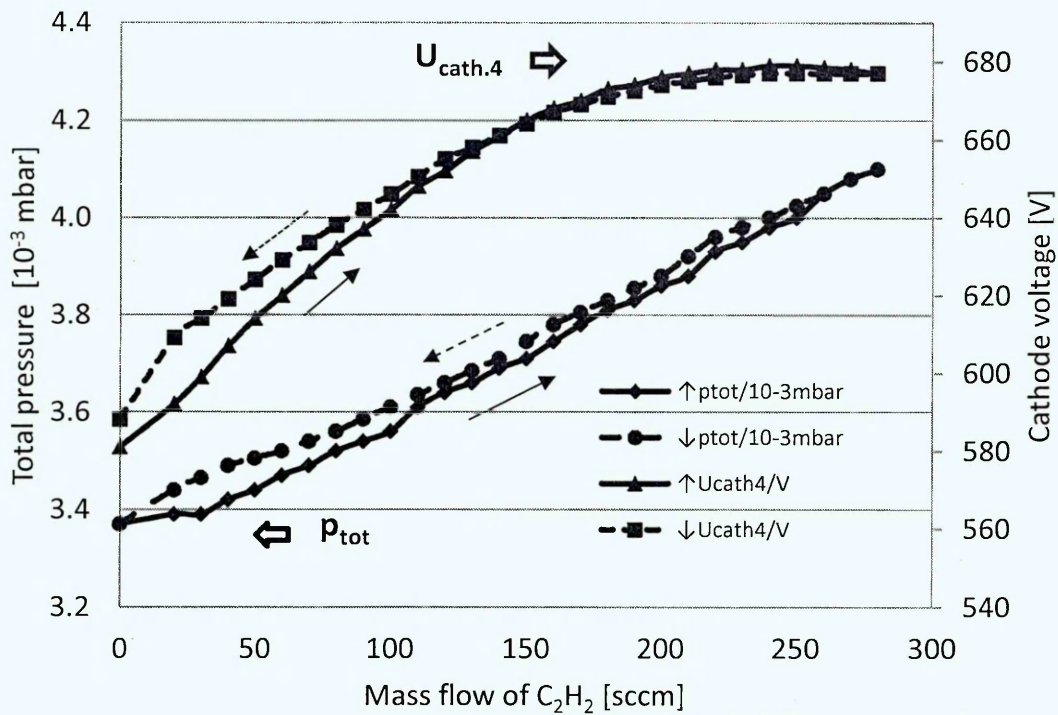


Figure 5.3 : Hystereses of the cathode voltage and the total pressure at reactive sputtering from an WC target depending on the acetylene gas flow (one magnetron cathode operated at 10 kW power)

The hysteresis curves of the total pressure and the cathode voltage for sputtering of WC are shown in Figure 5.3. For WC the cathode voltage increases with increasing mass flow of acetylene up to 240 sccm followed by a slight decrease with a further increase of the C_2H_2 flow up to 280 sccm. The increase of the cathode voltage could be explained by the reduction of the “secondary” electron emission from the target due to carbon deposition on parts of the target surface. The voltage reduction with a further increase of the C_2H_2 flow between 240 sccm and 280 sccm is expected to result from the change of the impedance of the glow discharge as the total pressure increases when having an almost stable target poisoning by carbon rich material on the magnetron target. In case of WC located on the erosion profile of the target, clear signs of target reactions were visible, whereas on the SiC/C target the erosion profile was clean. In spite of the availability of visible products of target reactions the hysteresis effects of the total pressure and the cathode voltage for the WC target were, once again, small.

5.2 Plasma Booster effect

The Plasma Booster was operated for the deposition of a-C:H using two cathodes at a power of 10 kW for each cathode in an argon/acetylene atmosphere at a total pressure of 4×10^{-3} mbar. The effect of the coil current on the substrate current is shown in Figure 5.4, according to Hofmann et al. [339].

For a substrate bias voltage of -100 V, the substrate current increases from 1 A without powering the electromagnetic coil to 7.2 A at a coil current of 180 A. For coil currents of above 100 A high substrate current densities of 1.5 to 2.5 mA/cm² were achieved.

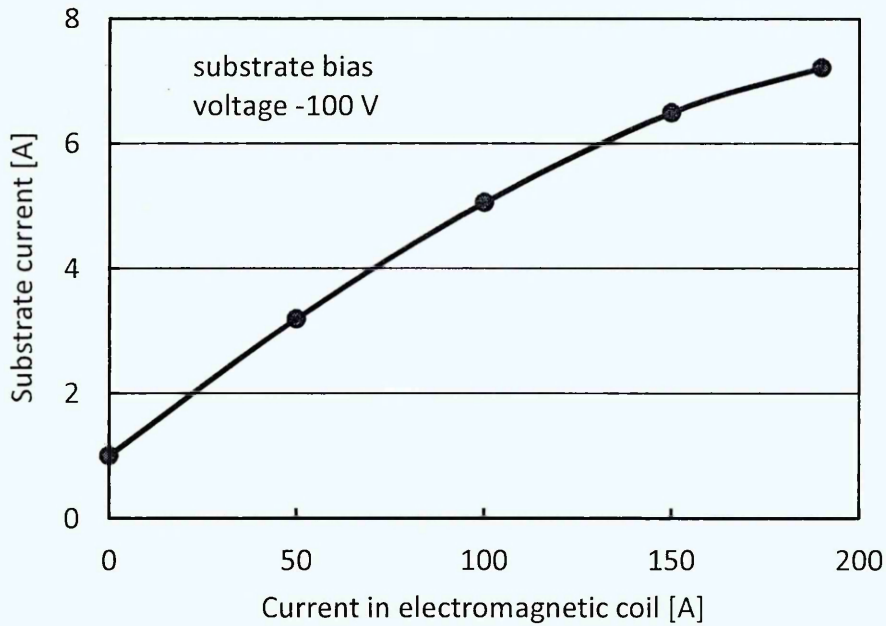


Figure 5.4 : Influence of current in the electromagnetic coils on the substrate current using the Plasma Booster arrangement, according to Hofmann et al. [339]

5.3 Layer systems and deposition rates for a-C:H and Si-DLC

For a-C:H-based coatings with high microhardness which is combined with high compressive stress of up to some GPa, the design of the layer system with specific interlayer coatings is very important in order to achieve a good adhesion for these coatings. In Figure 5.5 layer systems for a-C:H:W, a-C:H:Ti, a-C:H and Si-DLC are shown.

For the interlayers a layer thickness of up to some μm would be optimal in order to minimize the stress at the interface to the substrate. Industrially used a-C:H:Me coatings need only a metallic interlayer which is, in most cases, made of chromium or titanium, whereas for a-C:H coatings graded interlayers of $\text{WC}_x \rightarrow \text{a-C:H:W}$ or $\text{TiC}_x \rightarrow \text{a-C:H:Ti}$ are additionally used. In industrial applications, due to economic reasons, the thickness of the interlayers is often limited to less than $0.5 \mu\text{m}$.

Industrially used layer systems



New layer concepts including the HIPIMS Technology



Si-DLC layer systems

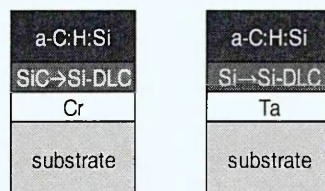


Figure 5.5 : Layer systems which are typically used for a-C:H:Me, a-C:H and a-C:H:Si (Si-DLC) as functional top layers

In order to increase adhesion new layer concepts are implemented using the High Power Impulse Magnetron Sputtering (HIPIMS) technology for etching and to improve the interface conditions by implanting titanium or chromium. By the HIPIMS process high quantities of metal ions are generated. This allows the combining of ion etching by metal ions [340, 341, 342] and metal implantation which offers the opportunity for creating wider interfacial zones allowing a better stress release.

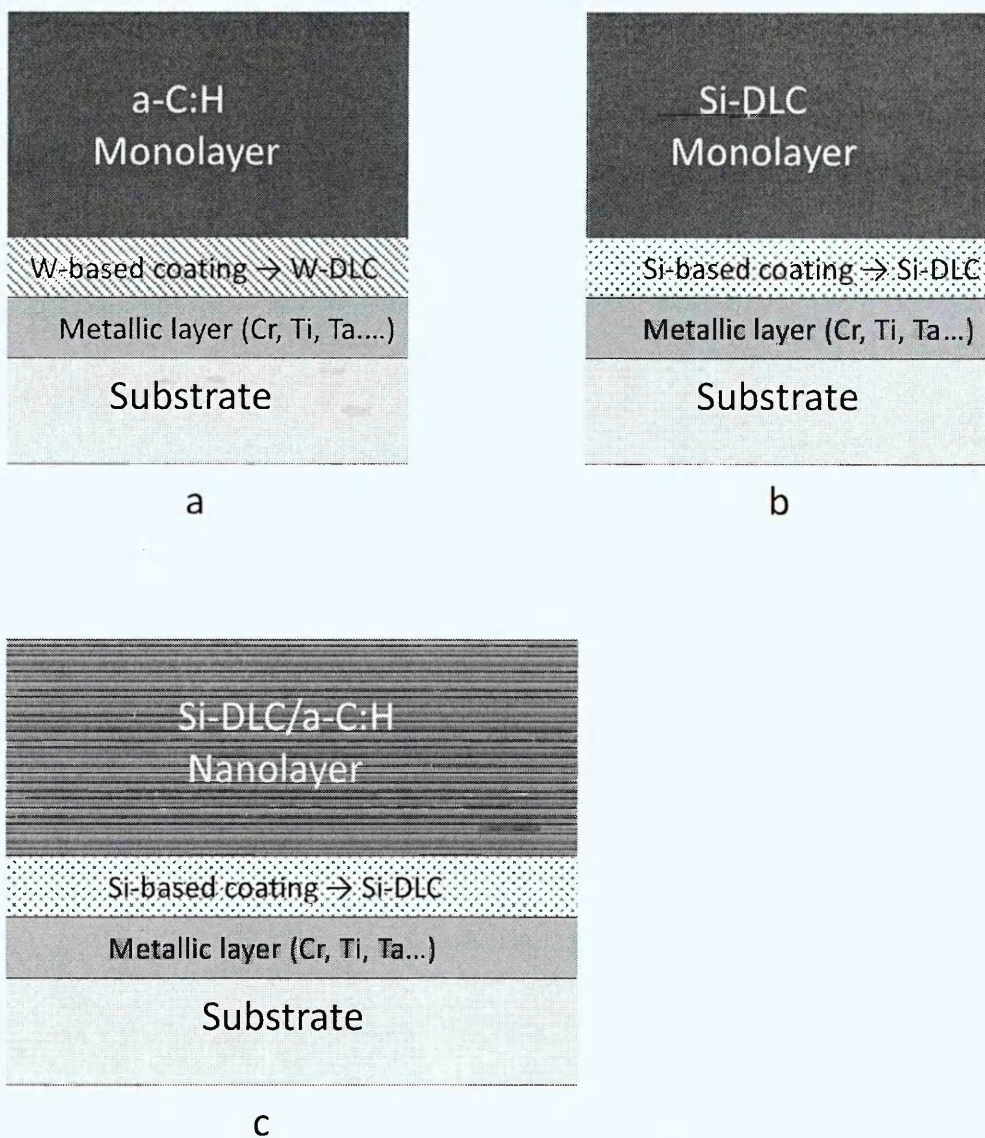


Figure 5.6 : Layer systems used for a-C:H, a-C:H:Si (Si-DLC) monolayers and Si-DLC/a-C:H nanolayers as functional top layers

For the Si-DLC coatings a graded $\text{SiC}_x \rightarrow \text{Si-DLC}$ layer is used on the metallic interlayers of chromium or tantalum. If the Si-DLC coatings need to be used in an extended temperature range of up to 500 °C the Cr layer has to be replaced by a layer of a refractory metal. The reason for this replacement is that chromium starts to form silicides at temperatures above 450 °C which was revealed by SIMS depth profiling after making tempering tests.

In Figure 5.6 the layer systems that have been used for the evaluation of layer properties are shown. For the Si-DLC/a-C:H nanolayer coatings the same interlayers were used as for the Si-DLC monolayer.

The nanolayer coatings were deposited by the Plasma Booster arrangement using magnetron cathodes with graphite target(s) for a-C:H and SiC/C target(s) for Si-DLC deposition in gas mixtures of argon and acetylene. The nanolayers were achieved by the rotation of the substrate table on which the substrates were coated at 2-fold rotation passing the different cathode regions periodically [339]. The individual layer thicknesses of the nanolayers are from 2 to 6 nm at 2-fold rotation for the process conditions used. The silicon content in the nanolayer coating was changed by adjusting different power ratios for the cathode with the SiC/C target and with the graphite target. For adjusting low Si contents one SiC/C target and two graphite targets were used, whereas for silicon concentrations of approximately 20 at.% and more only one cathode with a graphite target was used.

For dynamic deposition using two-fold rotation the average dynamic deposition rates for a-C:H, Si-DLC and Si-DLC/a-C:H nanolayer coatings, depending on the mass flow of acetylene, are shown in Figure 5.7. Only sputtering occurs if the mass flow of C_2H_2 is zero. Under this condition the deposition rate for SiC/C is about 50% higher than the deposition rate of graphite using only one cathode. The higher deposition rate of SiC/C is caused by the higher sputtering yield for SiC compared to carbon (graphite).

With increasing acetylene flow all deposition rates increase. This is caused by PECVD deposition of hydrogenated carbon-rich material in the extended plasma zone in front of the magnetron cathodes using the described Plasma

Booster operation by the decomposition of acetylene in the plasma of the discharge. The increase of the deposition rates at increasing flow of C_2H_2 results also from a good selection of target materials with high carbon content which show small target poisoning effects and therefore small reduction of the sputter deposition rates.

For the deposition processes where two cathodes were operated the deposition rate of hydrogenated carbon-rich material from the PECVD deposition is about twice as high as observed for only one cathode. This is expected to result from the generation of more plasma using two magnetron cathodes.

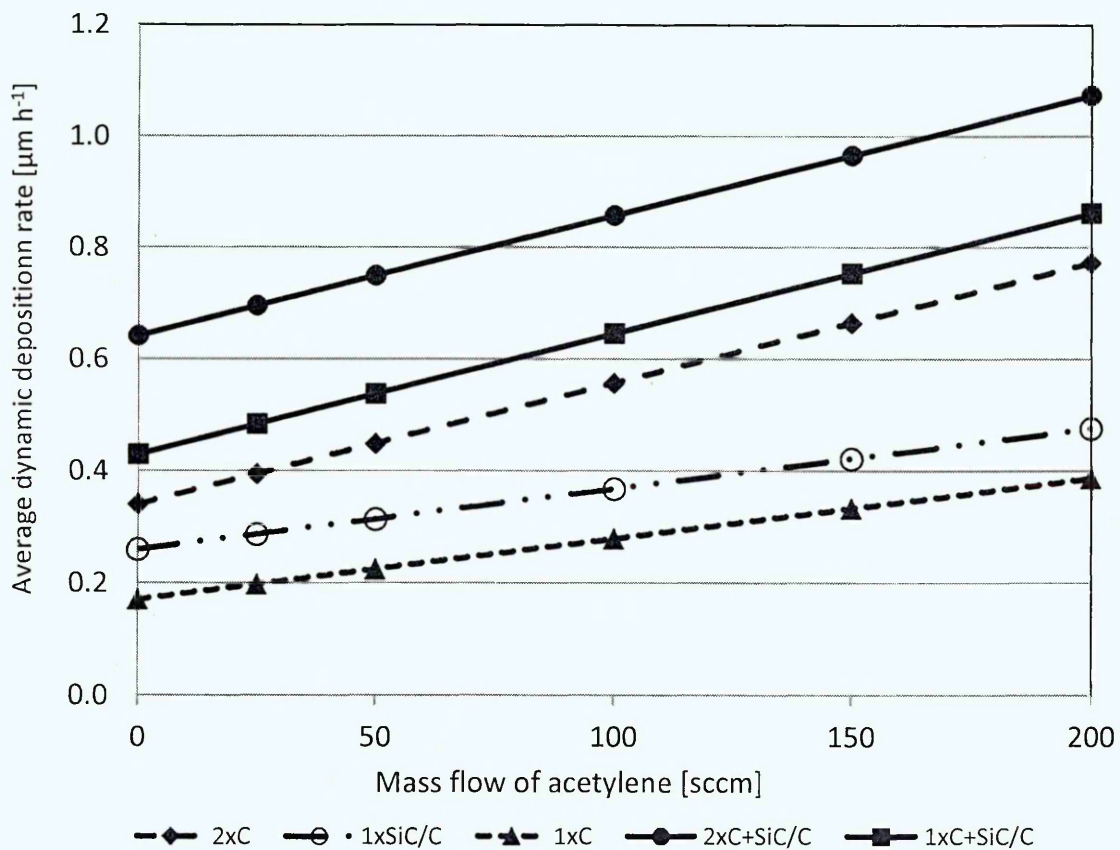


Figure 5.7 : Average dynamic deposition rates for deposition of a-C:H, Si-DLC and Si-DLC/a-C:H nanolayer coatings using two-fold rotation depending on the mass flow of acetylene for power densities at the targets of $5 W/cm^2$

If three cathodes are operated simultaneously no further increase of the PECVD related deposition rate was found compared to the operation of two cathodes. It is expected that, in the case of using three cathodes, the dissociation of

acetylene was not further increased compared to the conditions offered by the two cathode operation.

Under the described conditions the deposition of the coatings using acetylene as a reactive gas, or more precisely as a precursor, a hybrid process consisting of sputter deposition from the targets and of PECVD-based deposition occurs.

The deposition of silicon for the nanolayer coatings as well as for the Si-DLC is arranged only by sputtering from the SiC/C target which allows depositing thin Si-containing layers of one to some nanometer thickness by using the two-fold rotation at an appropriate setting of rotation and subrotation speeds.

State-of-the-art technique which is most frequently discussed in publications for the deposition of Si-DLC is a sole PECVD process with organic precursors, preferentially tetramethylsilane (TMS) is used. For the sole PECVD process the production of nanolayer coatings, which needs to change from Si-containing to undoped a-C:H, can be managed only very slowly and needs a change of the precursor gas which is linked with a large time constant. For industrial deposition of Si-DLC-based nanolayer coatings high deposition rates are needed and the time constant for the change of the precursor gas would be very high because of the large volume of the vacuum chamber and the limited pumping speed. Therefore the sole PECVD process offers unfavorable conditions for Si-DLC-based nanolayer deposition.

5.4 Results achieved for a-C:H coatings

The adhesion of a-C:H coatings with a thickness of 1.5 to 2.5 μm was investigated on the test coupons by the Rockwell Test according to the VDI 3198 guideline and by the scratch test according to DIN EN 1071-3, test details can be found in chapter 3.2 and chapter 3.1.

From the Rockwell adhesion test, very good and good adhesion was achieved by reaching the classification of HF1 to HF3 from the optical evaluation of the Rockwell indentation.

Using the scratch test critical loads L_{C2} of 25 to 40 N were achieved indicating good adhesion of the a-C:H coatings.

The hydrogen content of a-C:H-based material influences the tribological behavior of coatings significantly, as discussed previously in the literature survey. Therefore the conditions for hydrogen incorporation into the coating and the influence of the hydrogen content on various properties of a-C:H coatings will be discussed as follows.

The composition of coatings, including hydrogen, was analyzed by EPMA and SIMS using a quantitative calibration which includes hydrogen, as described in the chapter 3.8.

Figure 5.8 shows that the hydrogen concentration of a-C:H deposited at a substrate bias voltage of -200 V increases with the mass flow of acetylene as carbon-bearing gas. A strong increase of the hydrogen content in the a-C:H was observed for low C_2H_2 mass flows of up to 70 sccm followed by a slower increase in the range of 70 to 200 sccm. The explanation for this behavior is that at low acetylene flows the coating has a high capacity for binding hydrogen atoms that are released from the dissociation of C_2H_2 molecules in the plasma which then becomes reduced if the dangling bonds are more saturated with hydrogen at higher mass flows.

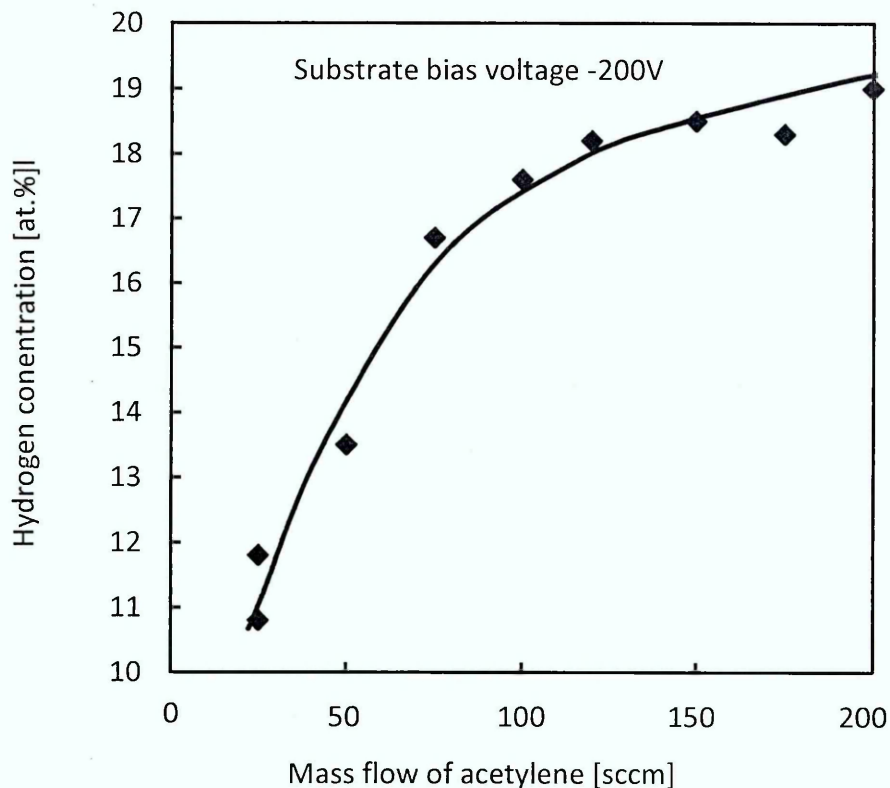


Figure 5.8 : Hydrogen content of a-C:H coatings depending on the mass flow of acetylene, according to Hofmann et al. [339]

The influence of the substrate bias potential on the hydrogen concentration of a-C:H is shown in Figure 5.9. Using a C₂H₂ flow of 25 sccm a high hydrogen content of 15 to 16 at.% is present at a substrate bias potential of -50 V which is reduced to 11 at.% at -200 V and further reduced to 10 at.% at the highest applied bias voltage of -300 V. If contoured substrates need to be coated with a-C:H the application of higher bias voltages of more than -300 V, which was often discussed in research papers, is not useful because the coatings become modified at the edges and the corners of the parts.

The subplantation of carbon atoms allows achieving a more diamond-like character of the coatings by increasing the mass density and creation of more sp³ hybridized C-C bondings. The subplantation is expected to be promoted as the bias voltages increase up to -300 V, whereas the hydrogen content in the coating is reduced. It was previously discussed that the incorporation of hydrogen, which is a light element, is expected to reduce the ridged network of carbon atoms and the mass density of a-C:H.

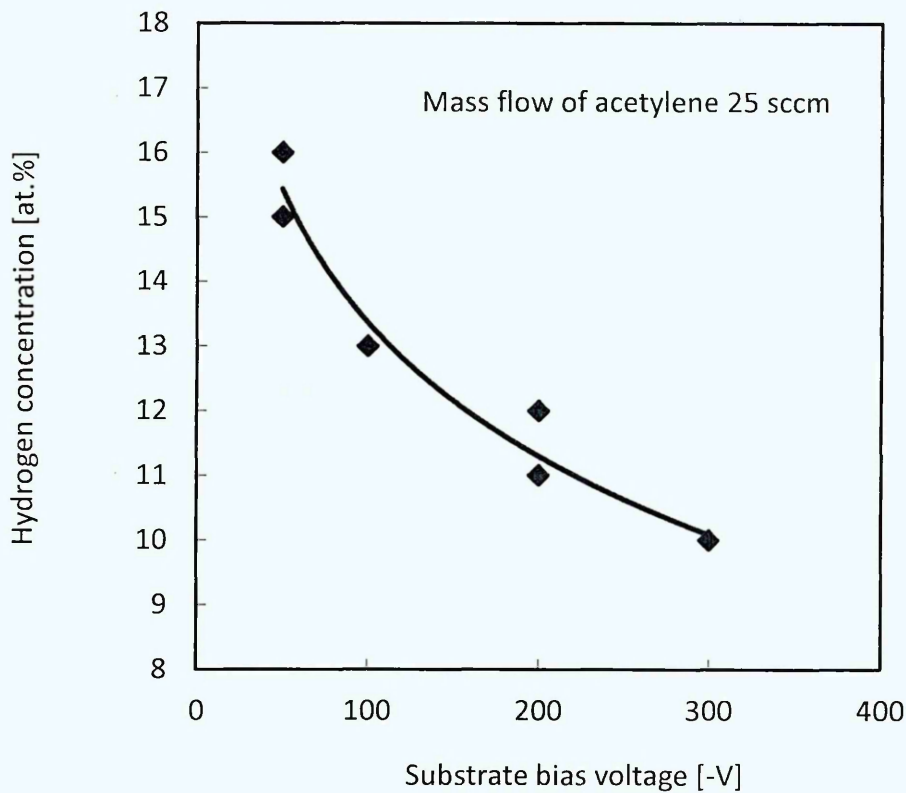


Figure 5.9 : Hydrogen content of a-C:H coatings depending on the substrate bias voltage, according to Hofmann et al. [339]

In order to characterize the coatings the mass densities of three different a-C:H-based coatings were evaluated by using XRR and plotted as a function of the hydrogen concentration as shown in Fig. 5.10. A relatively high mass density of 2.3 g/cm³ was achieved at the lowest hydrogen concentration of 11 at.% in the coatings. In various publications the relationship between density and sp³ content was discussed. A mass density of 2.3 g/cm³ would correspond to a sp³ fraction of approx. 40 % if the relationship given by Fallon et al. [343] for filtered ion beam deposited hydrogen-free diamond-like carbon will be applied. The relationship of Ferrari [344] for ta-C:H would correspond to a sp³ fraction of approximately 55% for the mass density of 2.3 g/cm³.

An almost linear relationship for the reduction of the mass density and the indentation hardness depending on an increasing hydrogen content of the coatings can be observed in Figure 5.10. The hardness reduction can be

explained by the reduction of the covalency [255] and the decrease of crosslinking in the a-C:H due to the replacement of C-C bonds by C-H bonds.

Hofmann et al. [339] found an empirical relationship between indentation hardness and hydrogen concentration $H(\text{GPa}) = 53.17 - 1.195 \times C_H$ (C_H : at.% hydrogen content). This relationship does not follow the empirical relationship for the indentation hardness and the hydrogen content $H(\text{GPa}) = 44.195 - 0.93 \times C_H$ (C_H : at.% hydrogen content) of Singha et al. [345] which was approved by Louro et al. [346].

Using additional data for the hardness of a-C:H from Fontaine et al. [347], Peter et al. [348] and Tillmann et al. [218] an increase of the hardness from 5 GPa at 38 at.% hydrogen to about 40 GPa at 11 at.% hydrogen can be observed as shown in Figure 5.11.

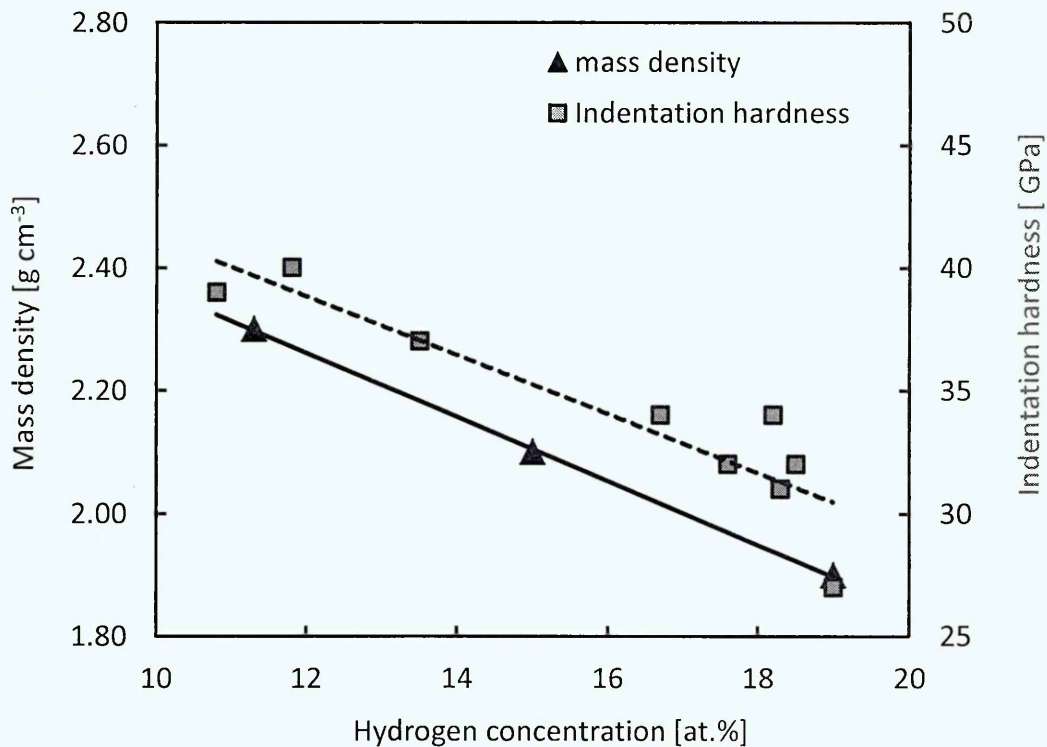


Figure 5.10 : Mass density and indentation hardness of a-C:H coatings depending on the hydrogen content, according to Hofmann et al. [339]

In Figure 5.12 it is shown that depending on the hydrogen content in the a-C:H a similar linear reduction is observed for the reduced indentation modulus (EIT). For a-C:H the EIT is almost the same as the Elastic modulus (Young's modulus). In Figure 5.12 the reduced indentation modulus (EIT) is shown together with the mass density as reference.

Ferrari et al. [344] showed a relationship for ta-C:H which was used to estimate the sp^3 content depending on the mass density of a-C:H. As discussed previously for the a-C:H with a high mass density of 2.3 g/cm^3 together with a high indentation hardness of about 40 GPa, a high EIT of about 225 GPa and 11 at.% hydrogen concentration, was estimated to have a high sp^3 fraction of about 55%. Whereas for a-C:H with a low mass density of 1.9 g/cm^3 together with an indentation hardness of 27 GPa, a EIT of about 175 GPa and 19 at.% hydrogen concentration, an sp^3 fraction of about 30% could be expected from the relationship of Ferrari et al. [344].

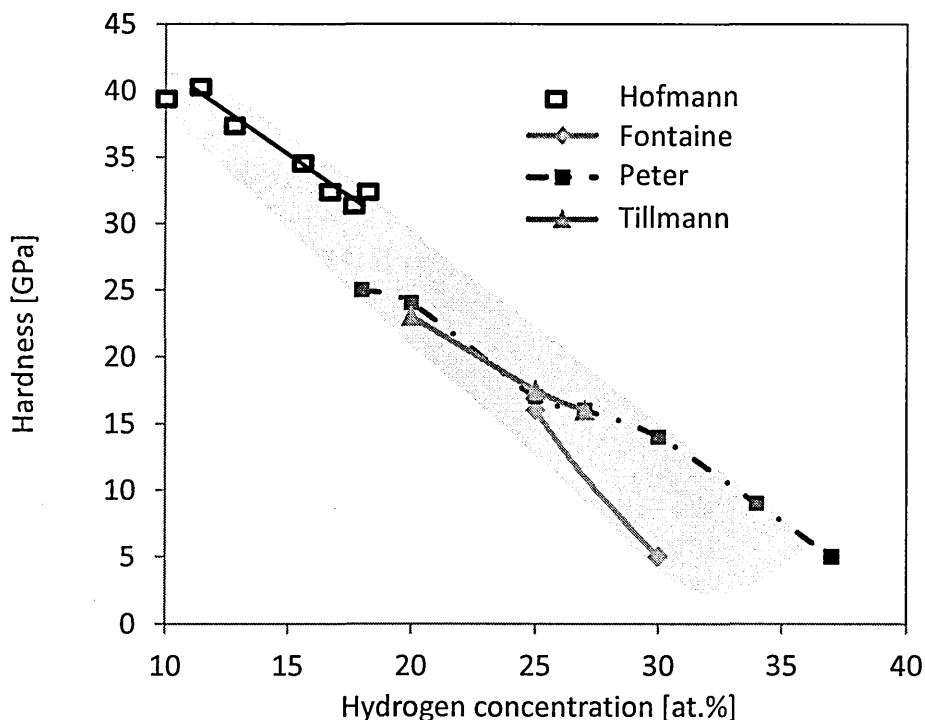


Figure 5.11 : Hardness of a-C:H coatings depending on the hydrogen content, according to Hofmann et al. [339], Fontaine et al. [347], Peter et al. [348] and Tillmann et al. [218]

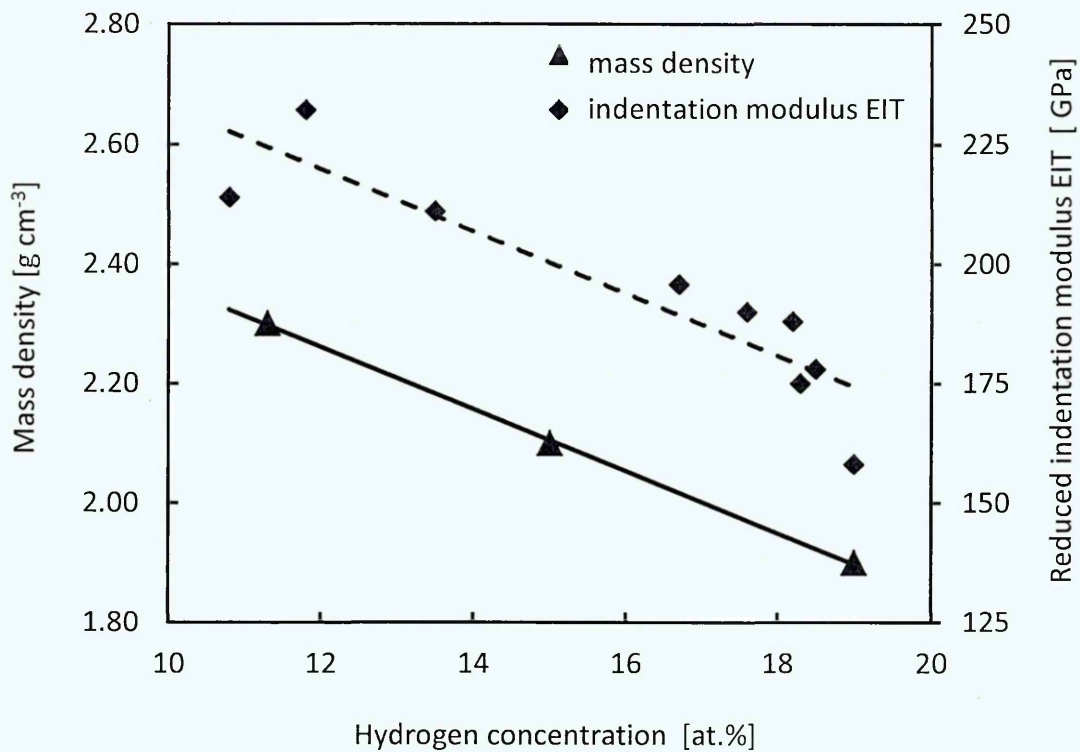


Figure 5.12 : Reduced indentation modulus (EIT) and mass density of a-C:H coatings depending on the hydrogen content, according to Hofmann et al. [339]

The dependency of the abrasive wear rate of a-C:H coatings on the hydrogen content is shown in Figure 5.13. The abrasive wear rate was determined by the ball cratering test, using a suspension of abrasive alumina particles of 1 μm diameter in glycerin. A very low wear rate of $0.6 \times 10^{-15} \text{ m}^3/(\text{Nm})$ was achieved for 11 at.% hydrogen in the a-C:H which increased to $0.9 \times 10^{-15} \text{ m}^3/(\text{Nm})$ as the hydrogen content increases to 19 at.%. A wider scattering of the abrasive wear rates was observed for a-C:H with hydrogen contents ≥ 17 at.%, which corresponds to mass flows of acetylene ≥ 90 sccm. At these high C_2H_2 mass flows the PECVD related deposition rate was $\geq 40\%$ of the total deposition rate and thus contributes significantly to the deposition of a-C:H. The high content of PECVD deposited a-C:H in the coating could be the reason for the scattering which was observed for the wear rates at high C_2H_2 mass flows.

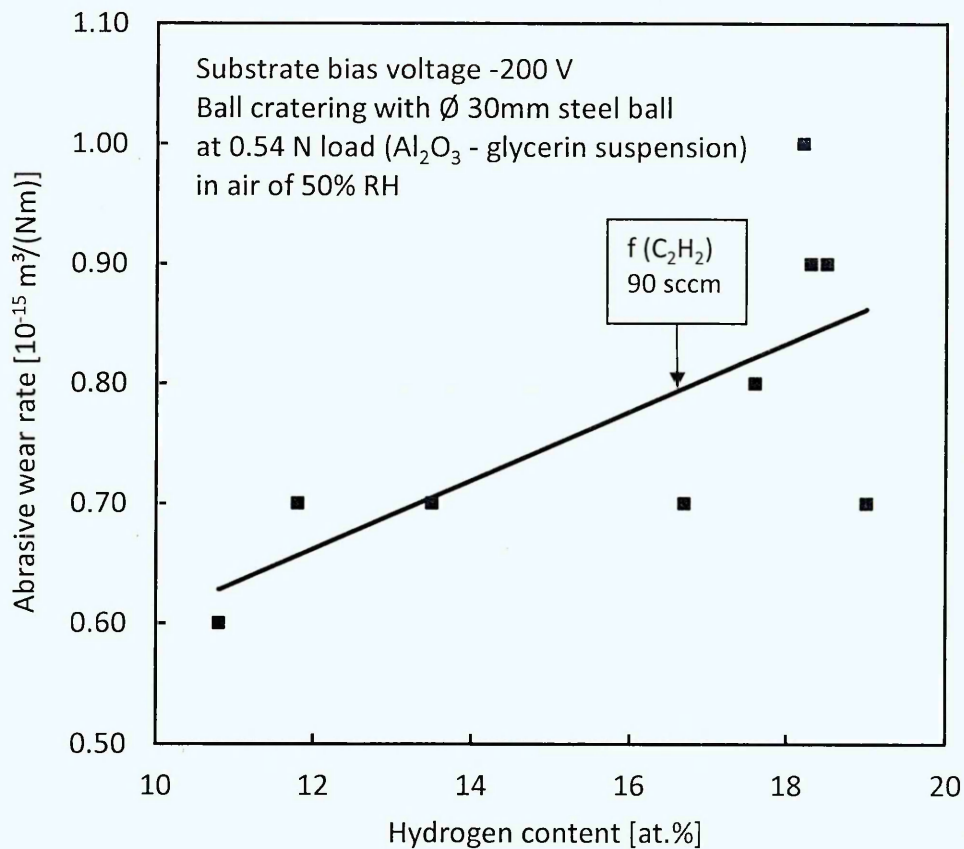


Figure 5.13 : Abrasive wear rate of a-C:H coatings depending on the hydrogen content, according to Hofmann et al. [339]

Low wear rates below $1 \times 10^{-15} \text{ m}^3/(\text{Nm})$ were only achieved by activating the Plasma Booster which allowed high ion current densities on the substrates of above $1 \text{ mA}/\text{cm}^2$.

If the Plasma Booster was not activated by powering the electromagnetic coils, higher wear rates of $10 \times 10^{-15} \text{ m}^3/(\text{Nm})$ and $6 \times 10^{-15} \text{ m}^3/(\text{Nm})$ were observed for substrate voltages of -100 V and -300 V respectively.

In Figure 5.14 the friction coefficient of a-C:H coatings depending on the atomic concentration of hydrogen in the film is shown. The coatings were produced using two cathodes which were equipped with graphite targets at a power of 10 kW on each cathode using a substrate bias voltage of -200 V. The friction coefficient was evaluated using the ball-on-disk test as described in chapter 3.5.

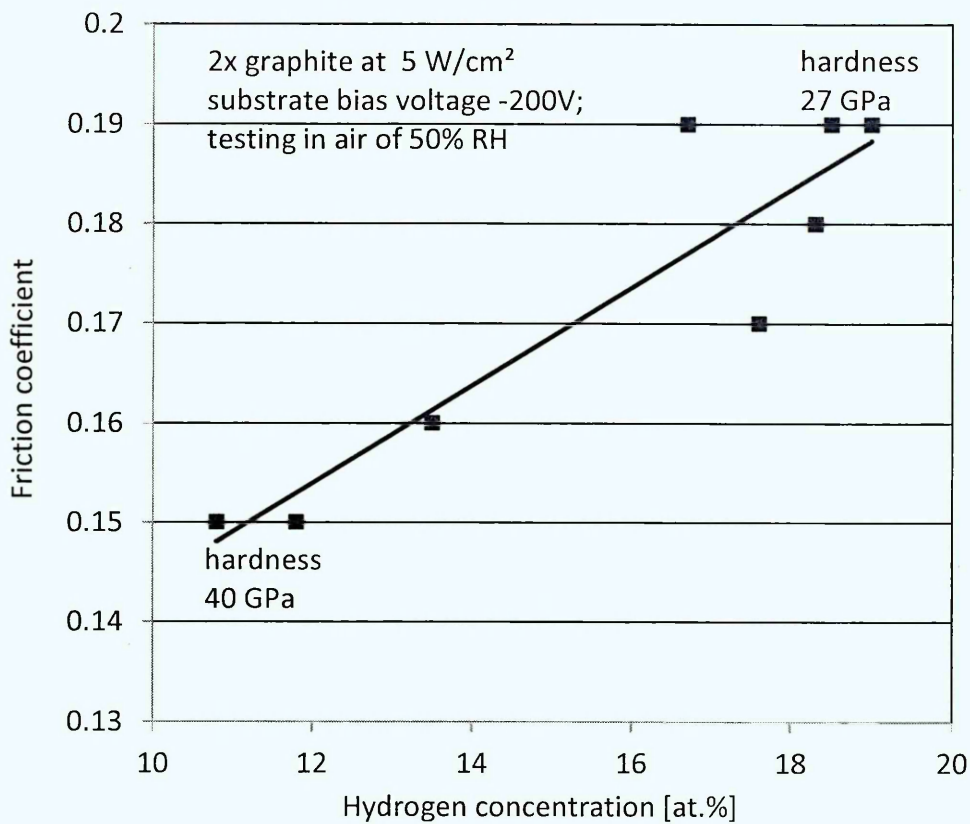


Figure 5.14 : Friction coefficient of a-C:H coatings depending on the hydrogen content

A low friction coefficient of about 0.15 was observed for a-C:H with 11 to 12 at.% hydrogen content in air of about 50% RH. The friction coefficient increased up to 0.19 as the hydrogen content increases to 19 at.%. Also for the friction coefficient a wide scattering was observed at high acetylene mass flows above 90 sccm and a high content of PECVD deposited a-C:H in the coating.

There is no simple explanation for the observed dependency of the friction coefficient in air, as oxidizing atmosphere, on the hydrogen content in the a-C:H at which carbon rich transfer layers are built-up and where its first layers are expected to be removed by oxidation as described by Donnet et al. [349, 233]. For a-C:H itself at a higher hydrogen content in the coating a better saturation of the dangling bonds of the a-C:H and therefore a lower friction coefficient should be expected. This means that the increase of the friction coefficient at a higher hydrogenation of the a-C:H has to result from other effects related to e.g. the

transfer layer or the formation of the coating with higher content of PECVD-deposited a-C:H.

A similar frictional behavior for a-C:H was observed by Donnet and Grill [350] who found for a-C:H with a hydrogen content of 20 to 42 at.% an increase of the friction coefficient from 0.12 to 0.18 if tested in ambient air of 40 to 60% RH. Donnet and Grill [350] reported for the same coatings tested under ultrahigh vacuum (UHV) conditions that the friction coefficient was higher than 0.5 up to a hydrogen concentration in the a-C:H of 34 at.% and for highly hydrogenated a-C:H with 42 at.% hydrogen content a very low friction coefficient of 0.02 was observed.

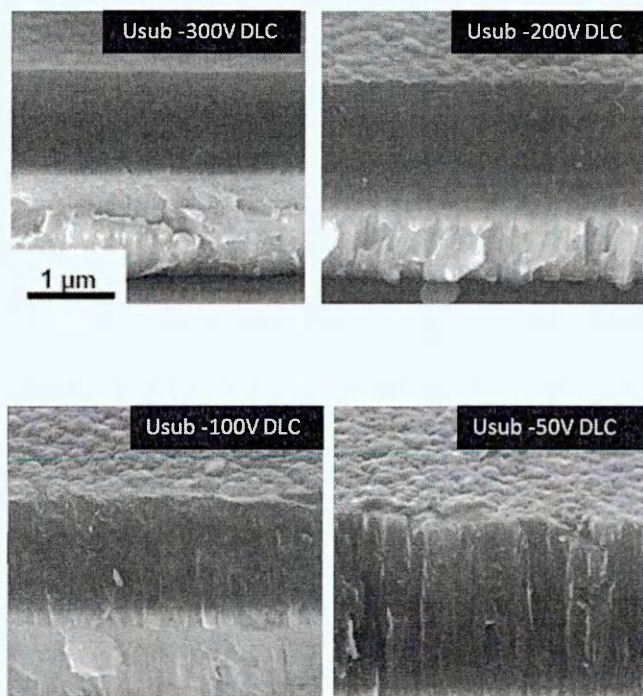


Figure 5.15 : Morphology of a-C:H coatings depending on the substrate bias voltage, fracture cross section according to Fraunhofer IST data

The dependence of the a-C:H morphology on the substrate bias voltage can be observed in Figure 5.15. At a bias voltage of -50 V the columnar growth is clearly visible and on the surface domes of the columns can be observed clearly. A slightly columnar structure can be observed for a bias voltage of -100 V which disappears completely if the substrate bias voltage is increased to -200 V. At substrate bias voltage of -200 V a dense, glassy and amorphous-like morphology with a slightly wavy surface topology can be observed. At a further

increase of the substrate bias voltage to -300 V the morphology becomes even more compact and glassy and the surface of the coating is very smooth and very slight dimples can be observed.

The observed dependency of the morphology of a-C:H coatings on the substrate bias voltage basically follows the classical structure zone models (SZM) of Thornton [71] of 1974 for sputtered coatings and the SZM of Messier [72] of 1984 which includes the influence of ion bombardment (see chapter 2.1.7).

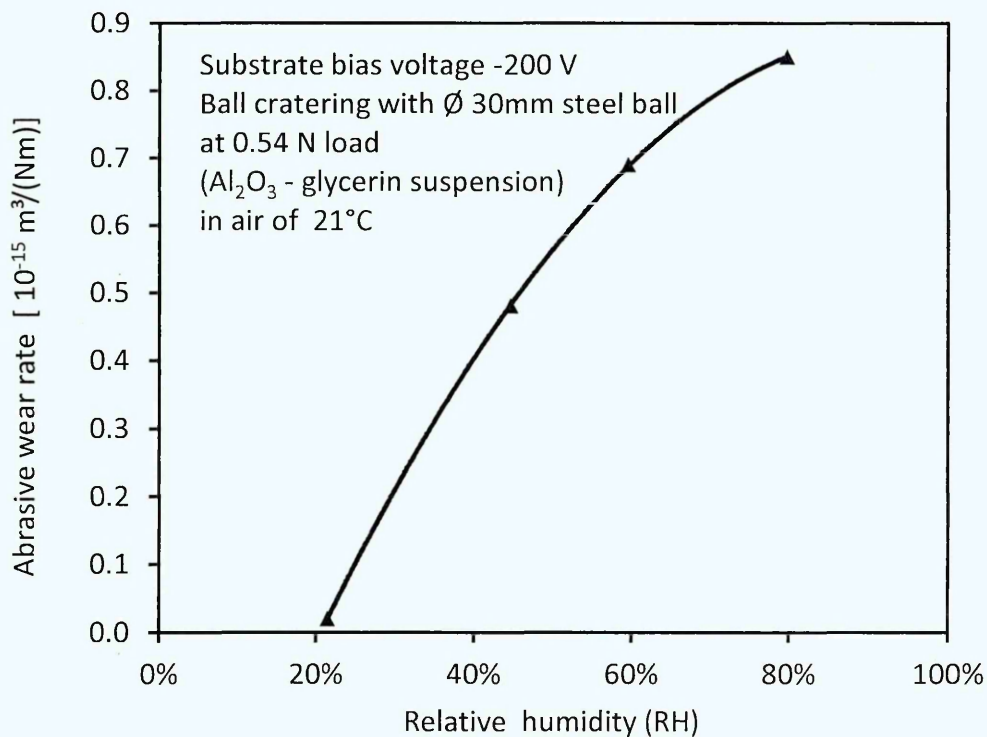


Figure 5.16 : Abrasive wear rate of a-C:H coatings depending on the relative humidity RH

For a-C:H with a high hardness of 40 GPa and 11 at.% hydrogen content the abrasive wear rate depending on the humidity of the ambient air is shown in Figure 5.16 using a ball cratering time of 9 minutes.

The wear rate of $0.02 \times 10^{-15} \text{ m}^3/(\text{Nm})$ for a-C:H at a low humidity of 21.5 % RH was extremely low and increased with a higher relative humidity up to $0.9 \times 10^{-15} \text{ m}^3/(\text{Nm})$ at 80 % RH.

Further research would be needed in order to explain the effect of the very low wear rate in air of low relative humidity by taking into account the influence of the Al_2O_3 glycerin suspension. Glycerin is hydrophilic and has a good solubility in water. In ambient air with humidity of 40 to 60 % RH glycerin is hygroscopic which enables the storing of water possibly influencing the humidity around the wear contact.

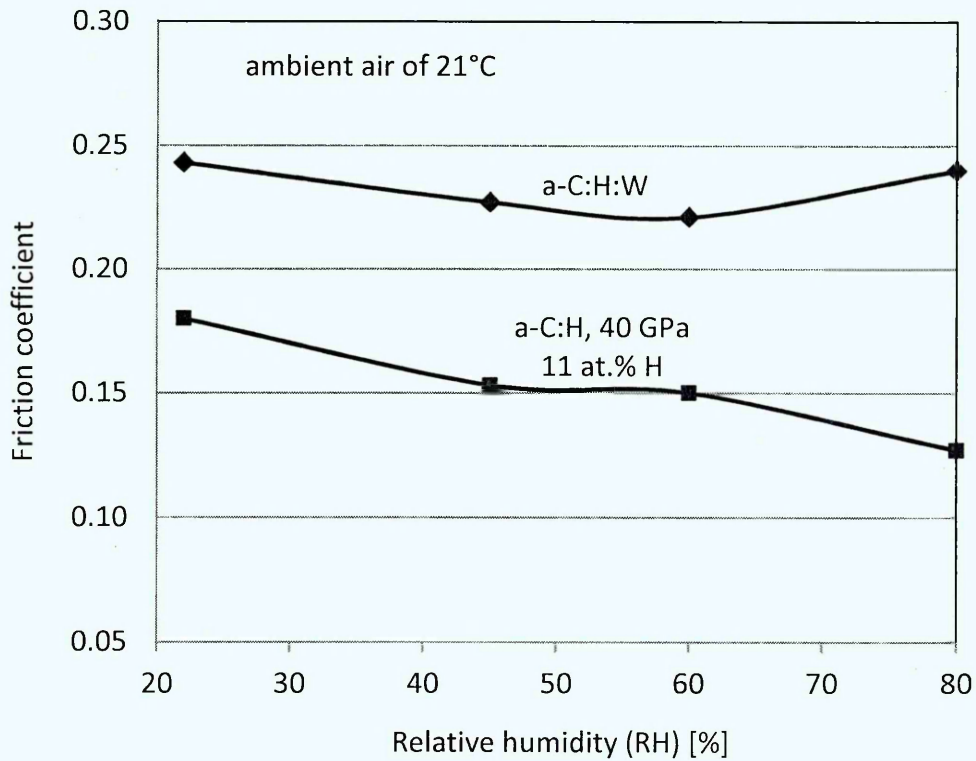


Figure 5.17 : Friction coefficient of a-C:H and a-C:H:W coatings depending on the relative humidity (RH) in air

A challenge was to stabilize the friction coefficient of a-C:H against the influence of increasing humidity in order to prevent an increase of the friction coefficient at a higher humidity of the ambient atmosphere.

A solution to overcome the increase in friction with higher humidity is the doping of the a-C:H with metal. In Figure 5.17 we can see that the friction coefficient of a-C:H:W is almost stable within the practically used humidity range of 20-80 % RH.

In chapter 2.3.6 of the literature survey it is shown that depending on the sliding conditions and the type of undoped a-C:H for the friction coefficient a strong

increase or almost no change or even a decrease was observed with increasing RH.

The hard a-C:H (40 GPa) coating with low hydrogen content shows friction coefficients which decrease from 0.18 to 0.13 in the humidity range of 20 to 80 % RH. The use of the 40 GPa a-C:H offers a solution for the stabilization of the friction coefficient against the influence of humidity.

The decrease of the friction coefficient at increasing humidity for a-C:H with a high hardness of 40 GPa and low hydrogen content of 11 at.% could be explained by the increase of the passivation of the dangling bonds by water molecules with increasing relative humidity.

5.5 Results achieved for Si-DLC/a-C:H nanolayer coatings

Si-DLC/a-C:H nanolayer coatings were deposited by dynamic deposition from SiC/C and graphite targets as described in chapter 4.3. The hydrogen content of these nanolayer coatings depending on the mass flow of acetylene is shown in Figure 5.18. At low mass flows of acetylene a very low hydrogen content below 10 at.% was achieved in the coatings. In the range of C_2H_2 mass flows of 0 to 60 sccm the hydrogen content strongly increased because of the high capability of the coating to incorporate hydrogen. At acetylene mass flows above 60 sccm the hydrogen incorporation into the coating was reduced and a saturation at about 16 at.% hydrogen concentration is expected, as indicated by the dotted trend line in Figure 5.18.

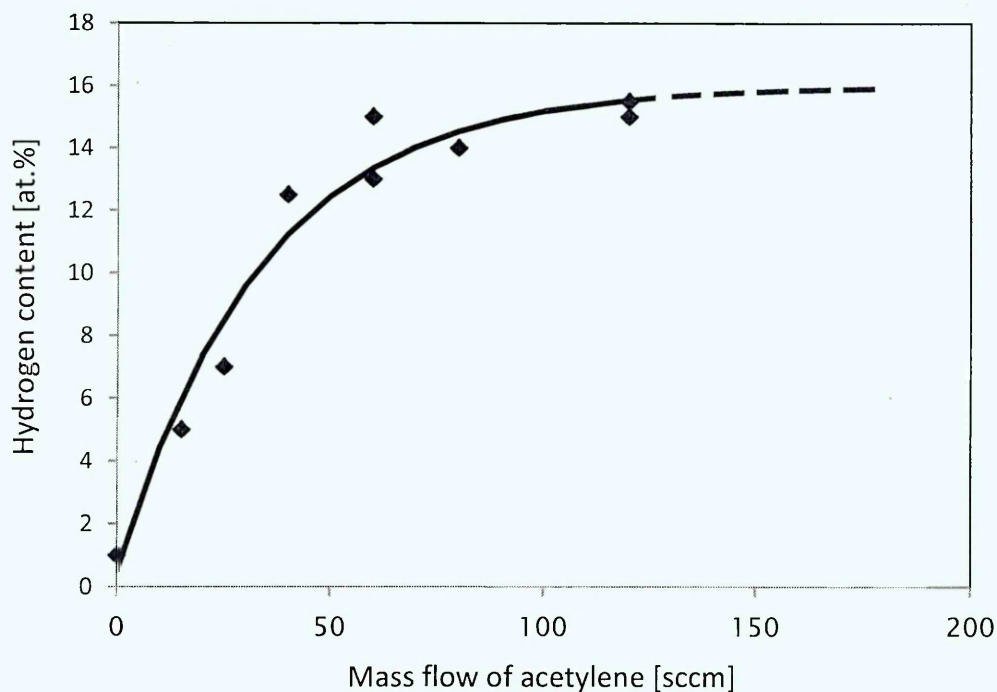


Figure 5.18 : Hydrogen content of Si-DLC/a-C:H nanolayer coatings depending on the mass flow of acetylene

The properties of a-C:H:Si/a-C:H nanolayer coatings strongly depend on the silicon content as discussed by Hofmann et al. [339]. Therefore the influence of the silicon incorporation has been investigated.

Figure 5.19 shows the dependency of the hydrogen content of Si-DLC/a-C:H nanolayer coatings on the silicon concentration in the coating according to

Hofmann et al. [339]. The data for this diagram have been taken from various target combinations which were used for the dynamic deposition process. It was found that the atomic concentration of hydrogen in the coating was reduced from 18 to about 7 at.% with an increase of the silicon concentration from 5 to 25 at.%. The adjustment of the silicon concentration was arranged by the setting of the power for the cathode with an SiC/C target compared to the power at the cathode(s) with a graphite target and the PECVD based deposition from the dissociation of acetylene. The dissociation of acetylene is the main process for the generation of hydrogen and ultimately the incorporation of hydrogen into the coating. Therefore the coating material deposited by sputtering from the SiC/C target and the graphite targets, which is almost hydrogen-free, reduces the hydrogen content in the film. At high silicon content more hydrogen-free material is deposited by sputtering from the SiC/C targets compared to the material originating from the PECVD process which lowers the hydrogen content in the film.

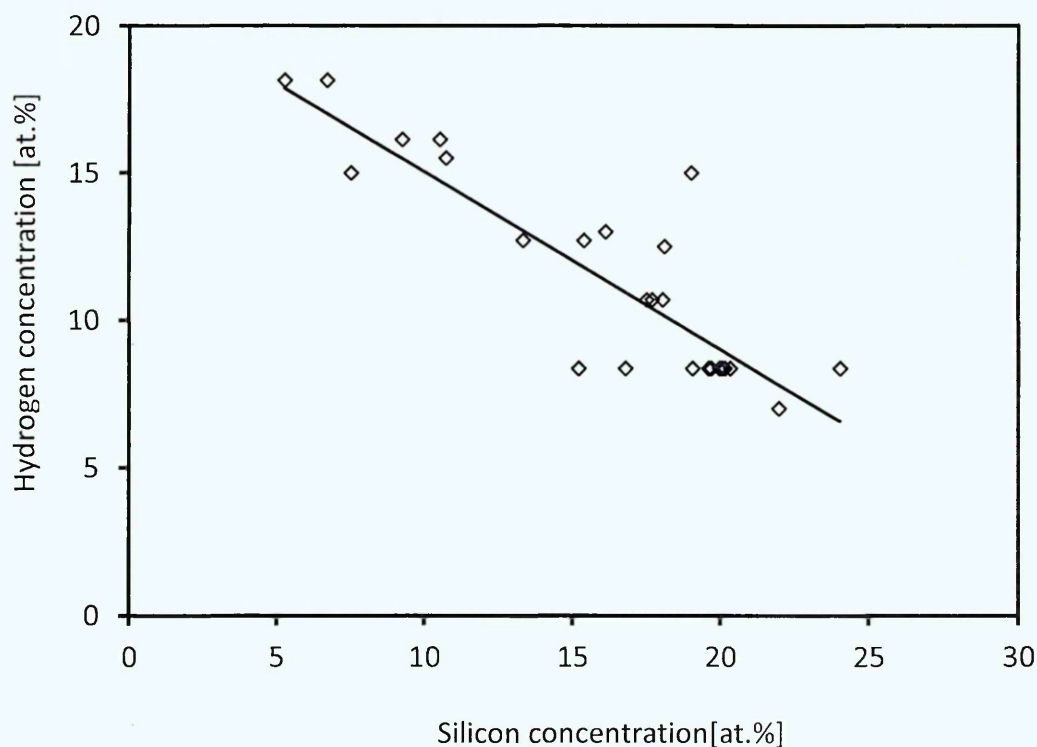


Figure 5.19 : Hydrogen concentration of Si-DLC/a-C:H nanolayer coatings depending on the silicon concentration, according to Hofmann et al. [339]

Figure 5.20 shows that for the Si-DLC/a-C:H nanolayer coatings high hardness values of 20 to 30 GPa were achieved using an SiC/C target as a silicon source according to the data from Hofmann et al. [339]. The silicon atoms in the Si-DLC are arranged only in fourfold-coordinated configuration and therefore increase the sp^3 to sp^2 ratio as discussed by Wu et al. [351].

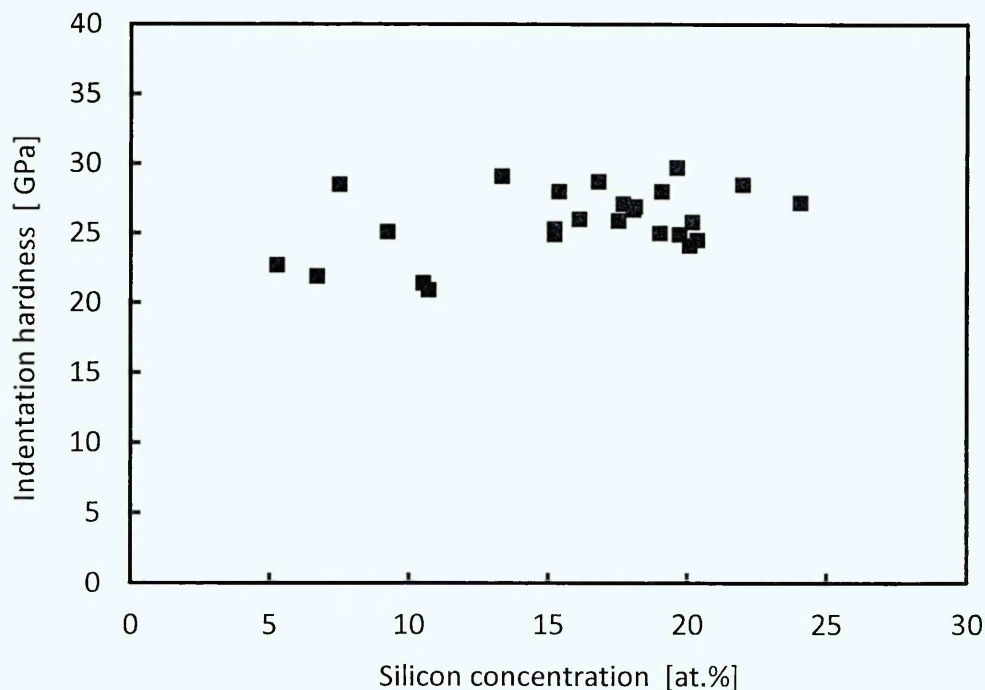


Figure 5.20 : Indentation hardness of Si-DLC/a-C:H nanolayer coatings depending on the silicon concentration, according to Hofmann et al. [339]

In the case of sputtering as a source of silicon for Si-DLC, the high hardness can be explained by a high sp^3 to sp^2 ratio which is not related to sp^3 coordinated polymeric material. Racine et al. [352] expected that the addition of silicon to a-C:H can promote sp^3 bonding by chemical means, which is not combined with additional compressive stress, by arranging the sp^3 hybridization using the subplantation effect. A structure model for the Si-DLC was presented by Palshin et al. [353] in which silicon is surrounded by four carbon atoms. For the Si-DLC Laidani et al. [354] observed that the Si incorporation produces Si-C bondings and forms carbide-like domains in a carbon matrix. The increasing number of Si-C bonds with an increase in silicon content can also promote the hardness.

In most cases silicon is deposited by PECVD deposition from hydrogen containing silicon precursors, like TMS. In this case the precursor acts as an additional source of hydrogen which increases the hydrogen content in the film to above 20 at.%. As a result of high hydrogen content of Si-DLC coatings, which are deposited using TMS, a low hardness of < 15 GPa, a reduction of stress and an improvement of the adhesion were reported for an increase in silicon content [355, 356, 357].

The abrasive wear rate of Si-DLC/a-C:H nanolayer coatings depending on the silicon concentration is shown in Figure 5.21 according to data of Hofmann et al. [339]. The wear rates were determined by carrying out the ball cratering test which is described in chapter 3.4. The wear rates of the Si-DLC/a-C:H nanolayer coatings increase with increasing silicon content of the coating at silicon concentrations above 10 at.% to $3.5 - 4.0 \times 10^{-15} \text{ m}^3/(\text{Nm})$ with a silicon content of 20 to 25 at.%. For a low silicon content of 5 to 10 at.% an almost constant wear rate of $1.4 \text{ to } 1.6 \times 10^{-15} \text{ m}^3/(\text{Nm})$ was observed.

Similar dependencies were observed by Meneve [285], Gangopadhyay [225] and Gilmore and Hauert [286] for the adhesive wear of Si-DLC (see chapter 2.3.6) using the ball-on-disk-test for wear testing.

In Figure 5.22 the hardness (H), the reduced indentation modulus (EIT) and the ratio of hardness to EIT are shown for the Si-DLC/a-C:H nanolayer coatings. The linear fit of EIT (almost equal to the elastic modulus, E) shows an increase from 170 GPa to 210 GPa as the Si content of the Si-DLC/a-C:H nanolayer coatings increases from 8 to 24.1 at.%. Therefore the linear trend line for the H/EIT-ratio shows a reduction from 0.17 to 0.12 as the silicon concentration of the Si-DLC/a-C:H nanolayer coatings increases from 8 to 24.1 at.%.

The reduction of the H/EIT-ratio by about 30% with an increasing silicon content of Si-DLC should correspond to a lower wear resistance according to Leyland and Matthews [253] (see chapter 2.3.5). Additionally, according to Laidani et al. [354], the number of Si-C bonds is expected to increase with increasing silicon content which should be combined with the formation of carbide-like domains in the carbon matrix. The increasing formation of such carbide-like domains is

expected to cause an additional reduction of the wear resistance of the Si-DLC/a-C:H nanolayer coatings as the silicon concentration increases. The increase of the wear rate could be explained if the carbide-like domains perform in the same way as silicon carbide, which has a significantly higher wear rate compared to a-C:H. For an SiC/C coating, which was prepared by non-reactive sputtering from an SiC/C target, a high wear rate of $9.4 \times 10^{-15} \text{ m}^3/(\text{Nm})$ was determined. The deposited SiC/C had a hardness of 27.4 GPa. Using the elastic modulus of 376 GPa, as taken from the material specifications of the SiC/C, a low H/EIT-ratio of 0.07 is calculated. At a silicon content of 39 at.% of the SiC/C the H/EIT-ratio of 0.07 would match the extrapolation of the linear fit of the H/EIT-ratio, as in Figure 5.22, and the wear rate of $9.4 \times 10^{-15} \text{ m}^3/(\text{Nm})$ would match the linear fit (for silicon contents above 15 at.%) of the wear rate, as in Figure 5.21.

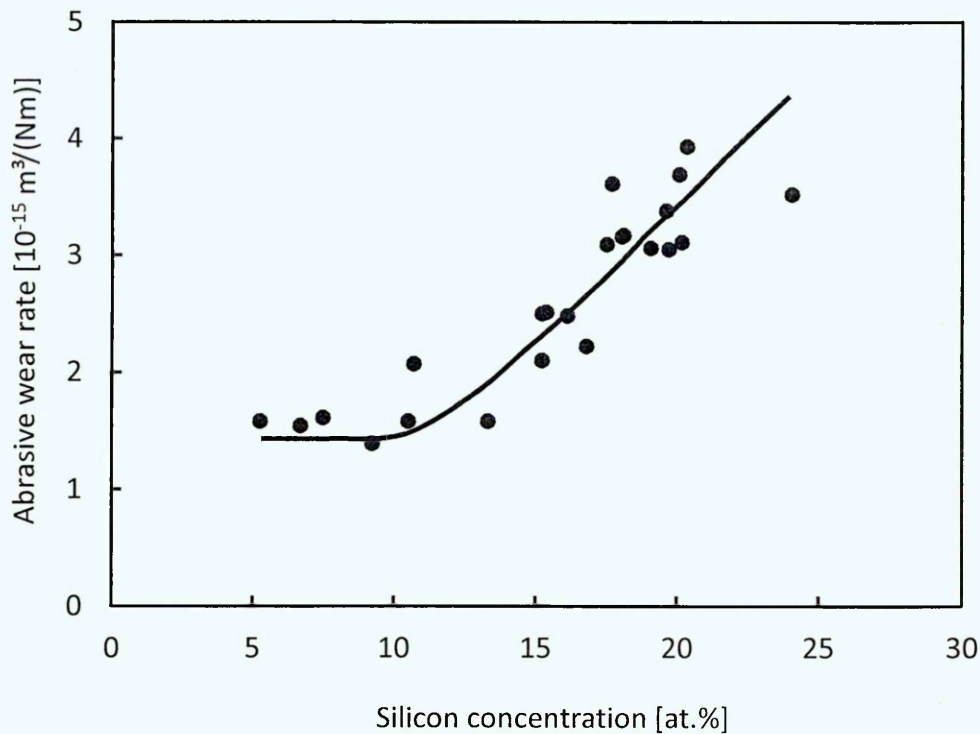


Figure 5.21 : Abrasive wear rate of Si-DLC/a-C:H nanolayer coatings depending on the silicon concentration, according to Hofmann et al. [339].

The friction coefficient of the coatings was evaluated by the ball-on-disk test using a case hardened 100Cr6 steel ball in air of 50% RH as described in chapter 3.5. In Figure 5.23 the friction coefficient of Si-DLC/a-C:H nanolayer

coatings depending on the silicon concentration is shown. In the range of a silicon concentration from 5.3 to 24 at.% the friction coefficient of Si-DLC/a-C:H nanolayer coatings decreases from 0.15 to 0.08 respectively. For the reduction of the friction coefficient by doping of a-C:H with silicon the formation of SiO₂ [278] and hydrated silica [279] was expected to play an important role.

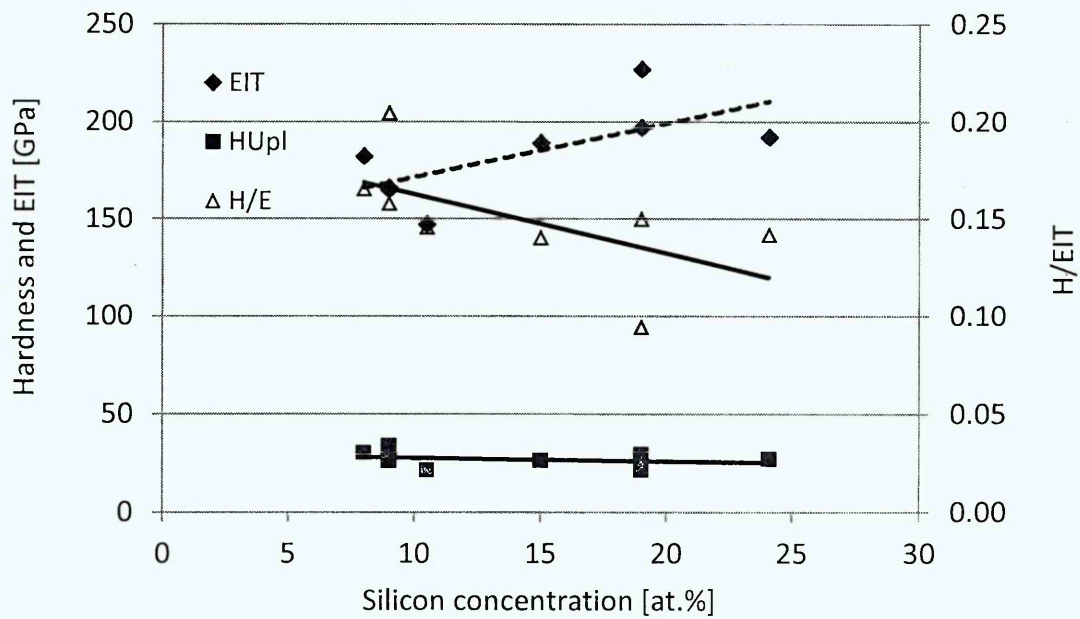


Figure 5.22 : Hardness, EIT and H/EIT-ratio of Si-DLC/a-C:H nanolayer coatings depending on the silicon concentration

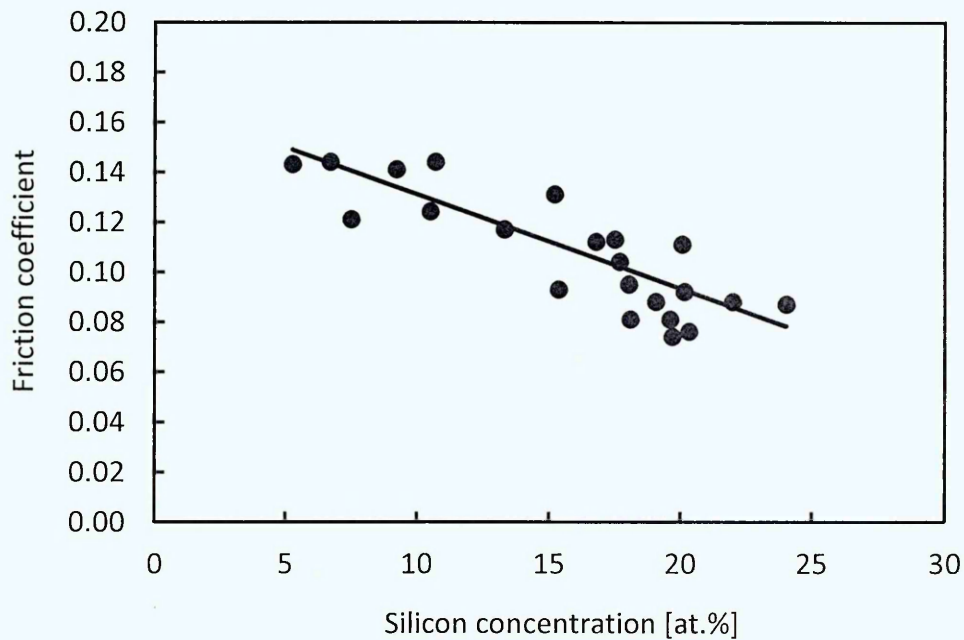


Figure 5.23 : Friction coefficient of Si-DLC/a-C:H nanolayer coatings depending on the silicon concentration, according to Hofmann et al. [339]

The mass density of Si-DLC/a-C:H nanolayer coatings, which was achieved from XRR spectrometry, and of SiC/C depending on the Si/C ratio of atomic concentrations is shown in Figure 5.24. The Si/C atomic concentration ratios for Si-DLC/a-C:H nanolayer coatings were calculated using atomic concentrations from EPMA, ignoring hydrogen. The carbon concentration of 56.4 at.% and silicon concentrations of 39 at.% for non-reactive sputtered SiC/C coating were achieved from a SIMS analysis. The density of 3 g/cm³ was taken from the materials datasheet of SiC/C. A linear dependency of the mass density was observed for Si/C atomic concentration ratios of 0.12 to 0.69 within which the mass density increases from 2.02 to 3 g/cm³.

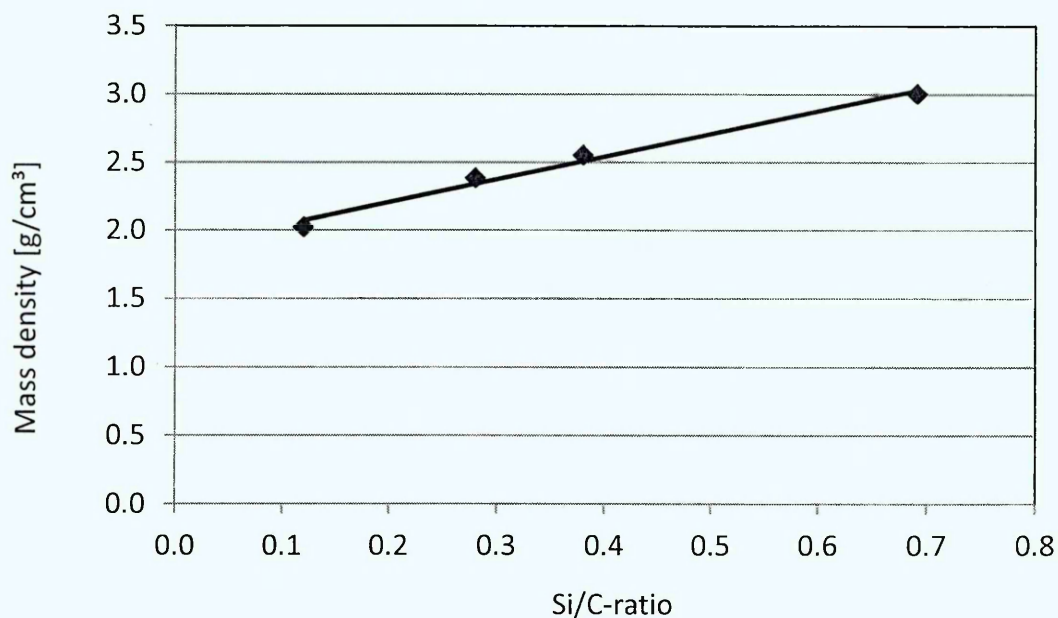


Figure 5.24 : Mass density of Si-DLC/a-C:H nanolayer coatings and SiC depending on the silicon to carbon atomic concentration ratios (Si/C)

The morphology of an Si-DLC/a-C:H nanolayer coating, which was produced by dynamic deposition using two-fold rotation, with a silicon content of 22 at.% is shown in Figure 5.25. The first interlayer of chromium was prepared by sputtering in a pure argon atmosphere. Onto this interlayer a second graded interlayer was deposited. This coating is started with sputtering of SiC/C in pure argon followed by ramping into a Si-DLC coating by using an increasing mass flow of acetylene. The Si-DLC/a-C:H nanolayer coating of about 2.5 μm layer thickness was deposited by dynamic sputtering from one graphite and one SiC/C target using a substrate bias voltage of -200 V and a mass flow of

acetylene of 25 sccm. For this Si-DLC/a-C:H nanolayer coating a hydrogen content of 7 at.%, a hardness of 26 GPa and a wear coefficient of $3.4 \times 10^{-15} \text{ m}^3/(\text{Nm})$ were determined. The fracture cross section image shows a very smooth fracture surface with no signs of a columnar growth for the Si-DLC/a-C:H nanolayer coating. Both the very smooth surface of the Si-DLC/a-C:H nanolayer coating and the smooth fracture surface indicate a dense, glassy amorphous-like microstructure. On the surface of this Si-DLC/a-C:H nanolayer coating small dimples are visible.

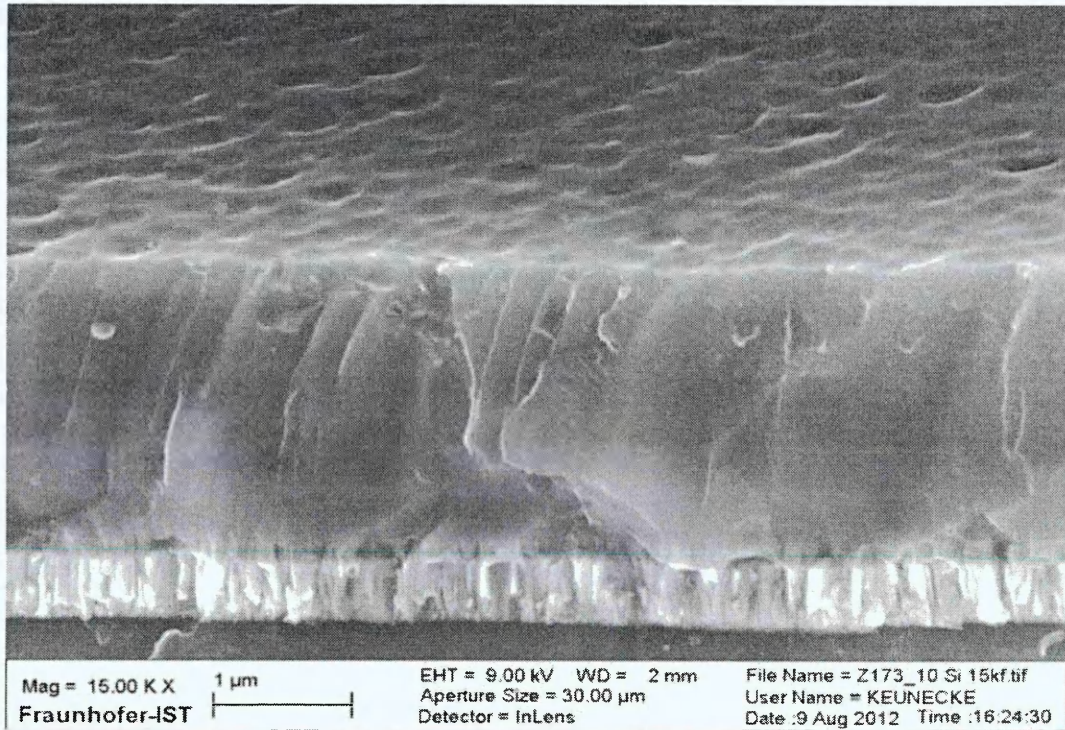


Figure 5.25 : Morphology of Si-DLC/a-C:H nanolayer coating with 22 at.% silicon content

In Figure 5.26 the SIMS depth profile of a Si-DLC/a-C:H nanolayer coating is plotted. This was produced using the same parameters as described for the coating which is shown in Figure 5.25. The atomic elemental compositions for chromium, argon, silicon, oxygen, nitrogen, carbon and hydrogen were quantitatively evaluated (details are discussed in chapter 3.8) and are shown as a function of the SIMS sputtering depth. Beginning with a sputtering depth of 0.2 μm an almost stable composition of 7 at.% hydrogen, 22 at.% silicon and 67 at.% carbon can be observed for the Si-DLC/a-C:H nanolayer coating. Starting

at a sputtering depth of 1.75 μm the silicon content increases and the carbon content decreases caused by the reduction of the C_2H_2 mass flow during the deposition of the second intermediate layer. They reach 39 at.% for the Si and 56.4 at.% for carbon at about 2 μm sputtering depth at pure SiC/C deposition. At a higher sputtering depth the Cr of the chromium layer followed by the Si from the silicon wafer, which was used as substrate, are found in the SIMS depth profile.

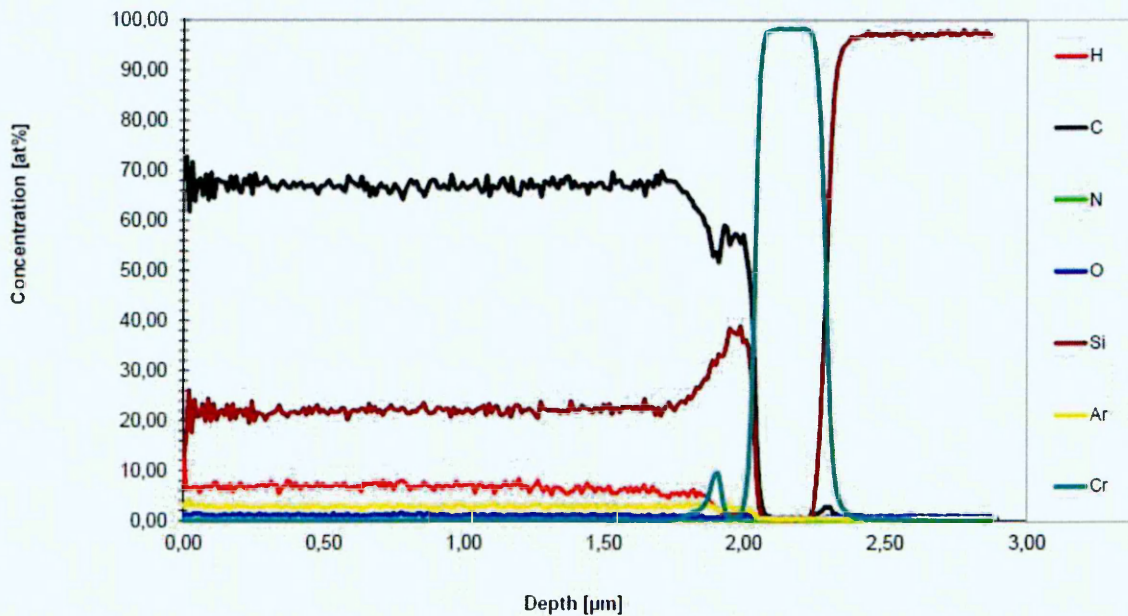


Figure 5.26 : SIMS depth profile of Si-DLC/a-C:H nanolayer coating with 22 at.% silicon content deposited on silicon wafer

In Figure 5.27 the X-ray diffraction spectrum an Si-DLC/a-C:H nanolayer coating with 19 at.% silicon content according to Hofmann et al. [339] is shown. The XRD spectrum of the Si-DLC/a-C:H nanolayer coating clearly reveals the amorphous-like morphology of the coating. No characteristic diffraction lines of crystalline SiC are visible in this spectrum.

In various publications (see chapter 2.3.6) it was postulated that the Si-DLC should not show an increase of the friction coefficient if tested under humid ambient air at increasing RH. This compares to an increase of the friction coefficient of pure a-C:H, which was commonly reported.

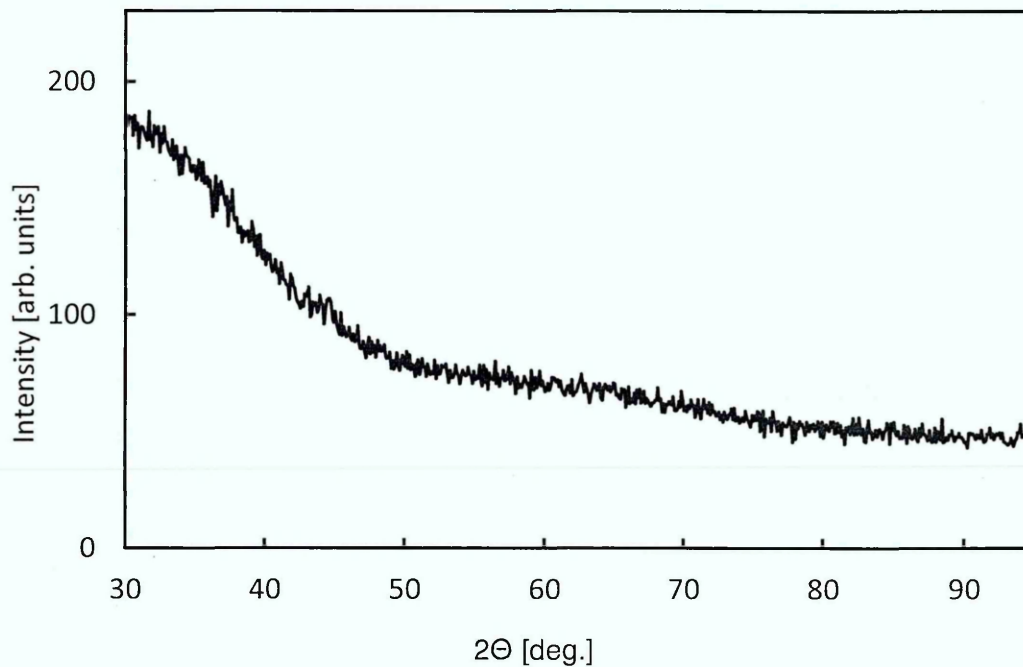


Figure 5.27 : XRD spectrum of Si-DLC/a-C:H nanolayer coating with 19 at.% silicon content (not including hydrogen), according to Hofmann et al. [339]

It was previously shown (see Figure 5.17) that pure a-C:H with a high hardness of 40 GPa and a low hydrogen content of 11 at.% performed even better under humid conditions than a tungsten doped a-C:H for which, in the humidity range relevant for most of the industrial applications of a-C:H-based coatings, an almost stable friction coefficient was observed.

Figure 5.28 shows the dependency of the friction coefficient on the relative humidity of the atmosphere. The Si-DLC/a-C:H nanolayer coating with a silicon content of 15 at.% and a hydrogen concentration of 12 at.% was produced by dynamic deposition using one graphite and one SiC/C target and two-fold rotation. A Si-DLC/a-C:H nanolayer coating with a layer thickness of 1.7 μm was deposited at a substrate bias voltage of -200 V and a mass flow of acetylene of 25 sccm. For the Si-DLC/a-C:H nanolayer a hardness of 26.5 GPa and a wear coefficient of $2.4 \times 10^{-15} \text{ m}^3/(\text{Nm})$ were determined.

The ball-on-disk test using a 100Cr6 steel mating ball was performed in a closed container. Using the ball-on-disk test in ambient air of 47% RH at 21 °C a friction coefficient of 0.1 was achieved.

Purging with dry nitrogen was used in order to reduce the relative humidity of the atmosphere in the container. When reaching a relative humidity of about

21% the ball-on-disk test was continued in the nitrogen-air atmosphere. In this air/nitrogen-mixture with 21% RH a friction coefficient of 0.092 was determined. In order to achieve high relative humidity in the container water vapor was produced by heating water therefore the temperature of the test atmosphere increased to 22 – 28 °C. Due to the presence of water vapor the humidity of the air in the container increased to 70 to 88% RH.

Under these humid air conditions a friction coefficient of 0.12 was determined. The friction coefficient of the Si-DLC/a-C:H nanolayer with 15 at.% silicon content was almost stable in the range of low and normal humidity and increased only slightly at high relative humidity of 70 to 88 % RH.

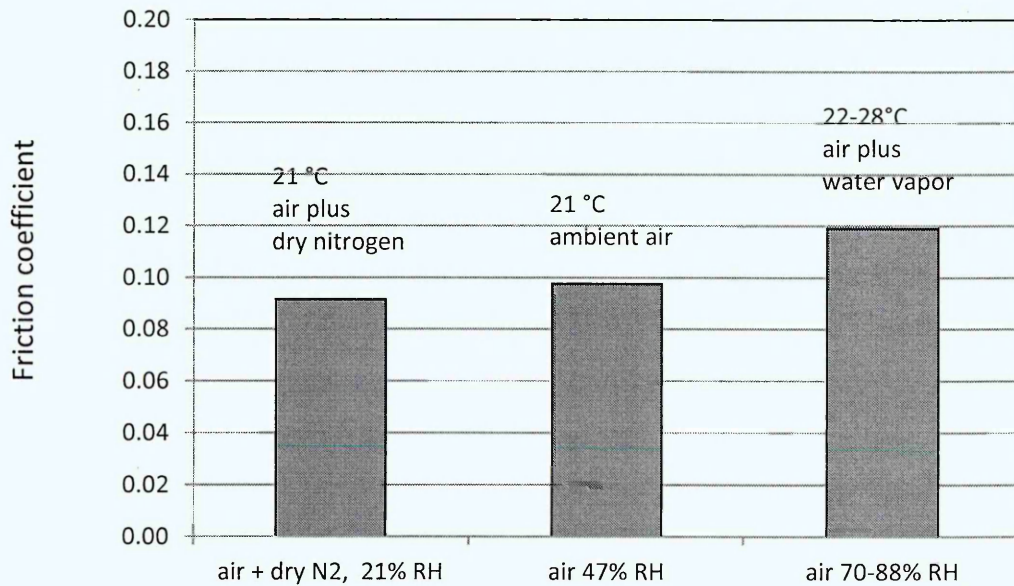


Figure 5.28 : Friction coefficient of Si-DLC/a-C:H nanolayer coating with 15 at.% silicon content depending on the relative humidity

5.6 Layer combinations combining low-wear and low-friction properties

From the wear results of Si-DLC/a-C:H nanolayer coatings, it was already shown that the combination of Si-DLC, for which high wear rates would have to be expected according to various publications, and highly wear resistant a-C:H allows to achieve low wear rates for the coating material. But the wear rate of Si-DLC/a-C:H nanolayer coatings increases strongly with increasing silicon content of the coatings even while the hydrogen content decreases. The previously discussed negative effects of the silicon doping on the wear resistance of the coating dominate the effect of having less hydrogen in the film which would, in pure a-C:H, lead to a decrease of the wear coefficient. On the other hand the silicon doping of the a-C:H reduces the friction coefficient in dry unlubricated contacts even in humid air atmosphere.

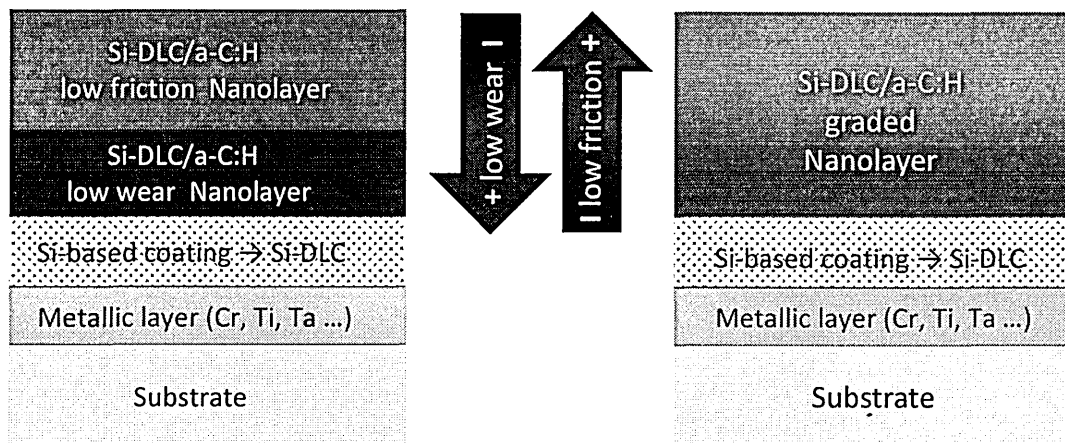


Figure 5.29 : Layer systems for Si-DLC/a-C:H nanolayer coatings in order to combine low-friction and low-wear properties, according to Hofmann et al. [339]

In order to combine the low wear and low friction properties a combination of a low-wear Si-DLC/a-C:H nanolayer coating with a silicon concentration of less than 10 at.% and an Si-DLC/a-C:H nanolayer coating with a silicon concentration of above 13 at.% which was discussed by Hofmann et al. [339] can be used. The low-friction and low-wear Si-DLC/a-C:H nanolayer combination is shown on the left side of Figure 5.29. In this layer combination a Si-DLC/a-C:H nanolayer coating with low silicon concentration is deposited first on the Si-based interlayer followed by an Si-DLC/a-C:H nanolayer coating with high silicon concentration. Another solution to achieve low wear and low friction

properties is the use of a graded Si-DLC/a-C:H nanolayer coating where the silicon concentration increases from less than 10 at.% to above 13 at.% with increasing layer thickness. The graded Si-DLC/a-C:H nanolayer coating is shown on the right side of Figure 5.29.

Si-DLC/a-C:H nanolayer coatings with silicon contents of 9 at.% and 19 at.% were prepared. Additionally, a combined Si-DLC/a-C:H nanolayer coating consisting of a first layer with 9 at.% Si and a second layer with 15 at.% Si on top was produced.

The wear results for these coatings from testing in air of about 50% RH at room temperature (RT) are discussed in this chapter, whereas all other properties and wear rates observed after tempering are presented in the following chapter. The wear results for the coatings obtained from the ball cratering test which was carried out at RT are shown in Figure 5.30.

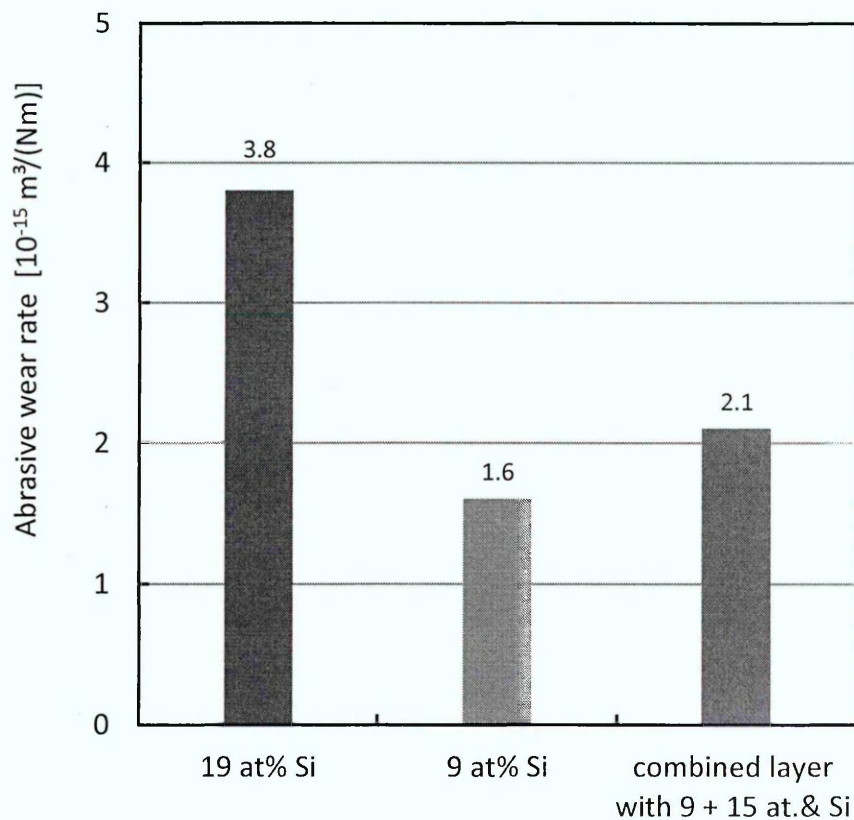


Figure 5.30 : Wear of Si-DLC/a-C:H nanolayer coatings with high Si content of 19 at.%, low Si content of 9 at.% and a combined layer with 9 at.% and 15 at.% Si (see Figure 5.29 left)

For the Si-DLC/a-C:H nanolayer coating with 19 at.% silicon concentration a high wear rate of $3.8 \times 10^{-15} \text{ m}^3/(\text{Nm})$ was determined. Whereas, for the Si-DLC/a-C:H nanolayer coating with low silicon concentration of 9 at.%, a low wear rate of $1.6 \times 10^{-15} \text{ m}^3/(\text{Nm})$ was achieved.

For the combined Si-DLC/a-C:H nanolayer coating with 9 at.% and 15 at.% Si a wear rate of $2.1 \times 10^{-15} \text{ m}^3/(\text{Nm})$ was determined.

Due to the principle of the ball cratering test, the wear of the top layer of the combined Si-DLC/a-C:H nanolayer, which has a low wear resistance, is, to a larger extent, responsible for the wear behavior while the layer with higher wear resistance to a minor extent.

This means the wear rate of a combined Si-DLC/a-C:H nanolayer depends on the thickness ratios of the layers with low friction and low wear properties.

If a low friction nanolayer with high layer thickness is used, at a standard measuring time for the ball cratering test of 9 minutes, the wear rate is high but becomes reduced if the wear testing time gets increased.

It can be summarized that for the tested combined Si-DLC/a-C:H nanolayer with almost equal individual layer thicknesses the layer with the high wear resistance clearly influenced the combined wear rate. This may be attributed to a lubricative effect of the nanolayer with low friction properties on the wear of the nanolayer with the high wear resistance on the point of contact.

5.7 Properties of a-C:H and Si-DLC/a-C:H nanolayer coatings after tempering

Various authors have discussed the thermal stability of a-C:H coatings. It was found that the effusion of hydrogen and the graphitization of the coatings start at a temperature of about 400 °C [276, 358, 359]. These changes which affect the microstructure allow a change of the a-C:H properties to be expected. At 400 °C a high weight loss was observed by Vassell et al. [360] and Louro et al. [346] caused by the chemical reaction of a-C:H with oxygen where carbon leaves the coating by forming CO₂ and at 500 °C the coating disappears [361].

The Si-DLC coatings also showed the start of hydrogen effusion at 400 °C as discussed by Camargo et al. [359] but only very slight graphitization was observed at this temperature as reported by Michler et al. [355]. For the Si-DLC Yang et al. [361] found that Si-DLC was oxidized at tempering in air in the temperature range 400 °C to 500 °C depending on the silicon content of the coating.

In order to check the temperature stability of Si-DLC/a-C:H nanolayer coatings a step-stress test was carried out in air. As temperature for the steps 200 °C, 300 °C, 400 °C and 500 °C, were selected using a heating duration of one hour followed by a waiting time of 2 hours without heating and opening of the oven door between temperature steps as shown in Figure 5.31. For the tempering tests polished high speed steel AISI M2 (HSS) coupons were used which have the same size and surface finish as the 100Cr6 coupons.

Si-DLC/a-C:H nanolayer coatings with silicon contents of 9 at.%, and 19 at.% and a combined Si-DLC/a-C:H nanolayer coating with 9 at.% and 15 at.% Si, as described in chapter 5.5, were used for the step-stress-test. A pure a-C:H coating with 40 GPa hardness and 11 at.% hydrogen content was used as reference in order to compare the step-stress results.

Figure 5.32 shows the indentation hardness of the a-C:H coatings and the Si-DLC/a-C:H nanolayer coatings with 9 and 19 at.% depending on the atomic concentration of silicon after undergoing the step-stress test as described above. The indentation hardness of the coatings decreases from 40 ±2 GPa to 22 ±2 GPa as the silicon concentration of these coatings increases from 0 to 19 at.% for room temperature and after tempering at 200 °C, 300°C and 400 °C.

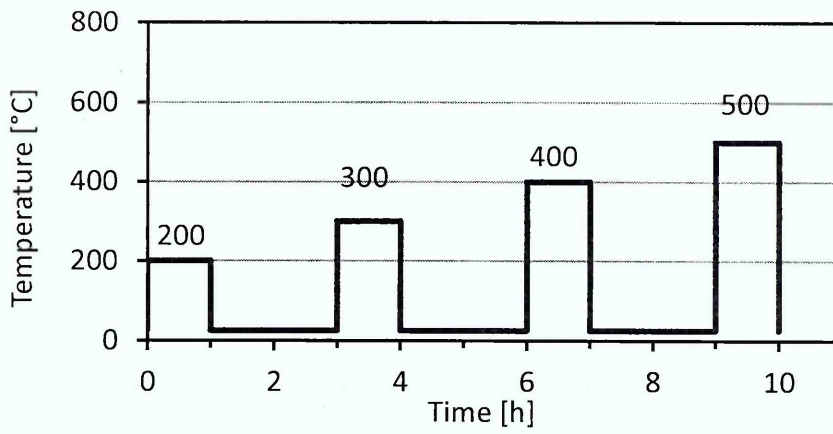


Figure 5.31 : Step-stress test temperature settings for tempering of Si-DLC/a-C:H nanolayer coatings and a 40 GP a-C:H coating

It can be also found that after tempering at the final temperature step of 500 °C, the hardness of the pure a-C:H coating was significantly reduced to 10 GPa whereas the hardness of the Si-DLC/a-C:H nanolayer coatings increased to 33.7 GPa at 9 at.% Si content and 29.5 GPa at 19 at.% Si concentration.

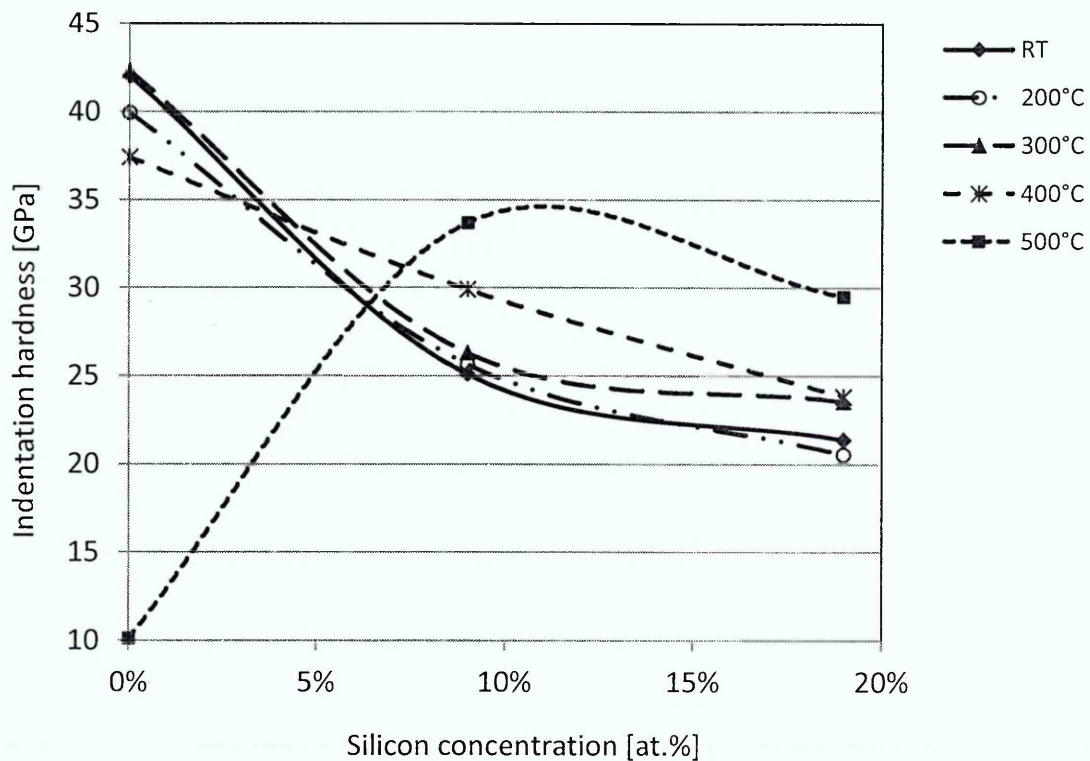


Figure 5.32 : Indentation hardness of Si-DLC/a-C:H nanolayer coatings and a 40 GP a-C:H coating depending on the atomic content of silicon at room temperature and after step-stress testing at 200°C, 300°C, 400°C and 500°C

The decrease of the hardness of the a-C:H coating at 500 °C can be explained by the beginning of graphitization of the coating whereas the increase of the hardness of the Si-DLC coatings could be explained by the effusion of hydrogen.

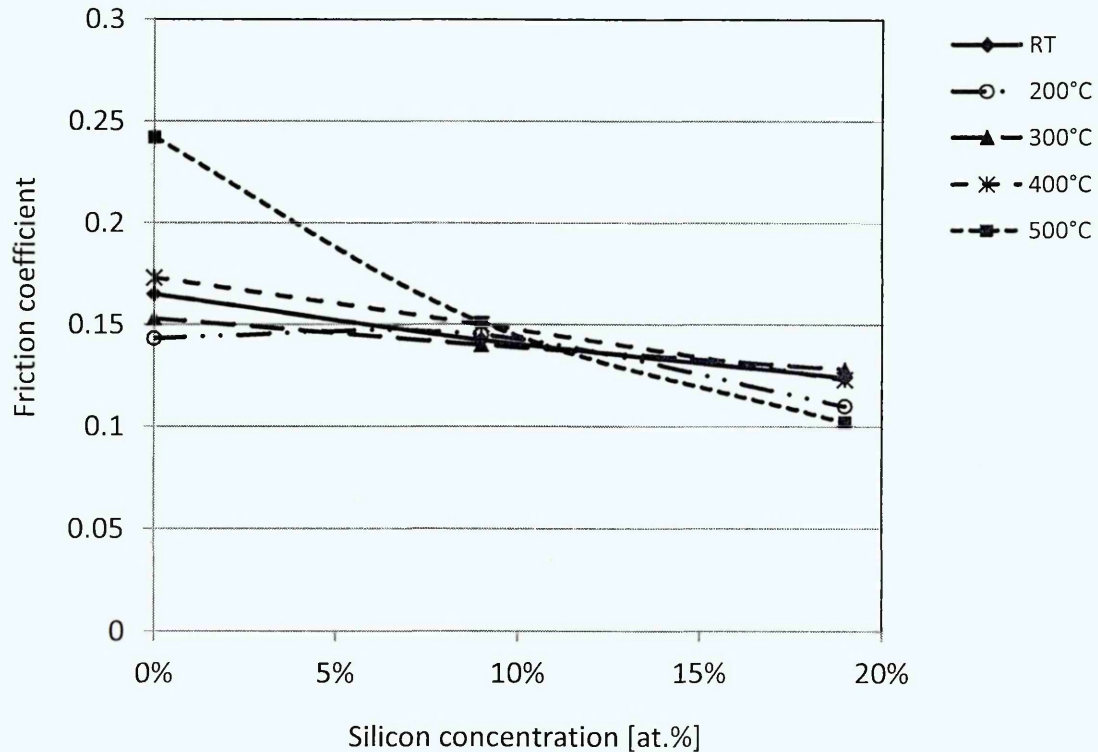


Figure 5.33 : Friction coefficient of Si-DLC/a-C:H nanolayer coatings and a 40 GPa a-C:H coating depending on the atomic content of silicon at room temperature and after step-stress testing at 200°C, 300°C, 400°C and 500°C

In Figure 5.33 the change of the friction coefficient of a-C:H coatings and Si-DLC/a-C:H nanolayer coatings with 9 and 19 at.% silicon is shown depending on the silicon concentration. For all coatings the friction coefficient is reduced if the Si content increases to 19 at.% for annealing temperatures from 200 °C to 500 °C. After the annealing of the coatings up to 500 °C the friction coefficients of the Si-DLC coatings are almost stable at 9 at.% Si and are slightly reduced at 19 at.% Si content. This could be explained by an increasing oxidation of silicon on the surface of the coatings at 500 °C. The SiO₂ is expected to reduce the friction coefficient when it is imbedded into the a-C:H matrix as discussed by Yang et al. [361]. For pure a-CH the friction coefficient

increases to 0.24 after heating up to 500 °C which can be explained by the graphitization of the coating.

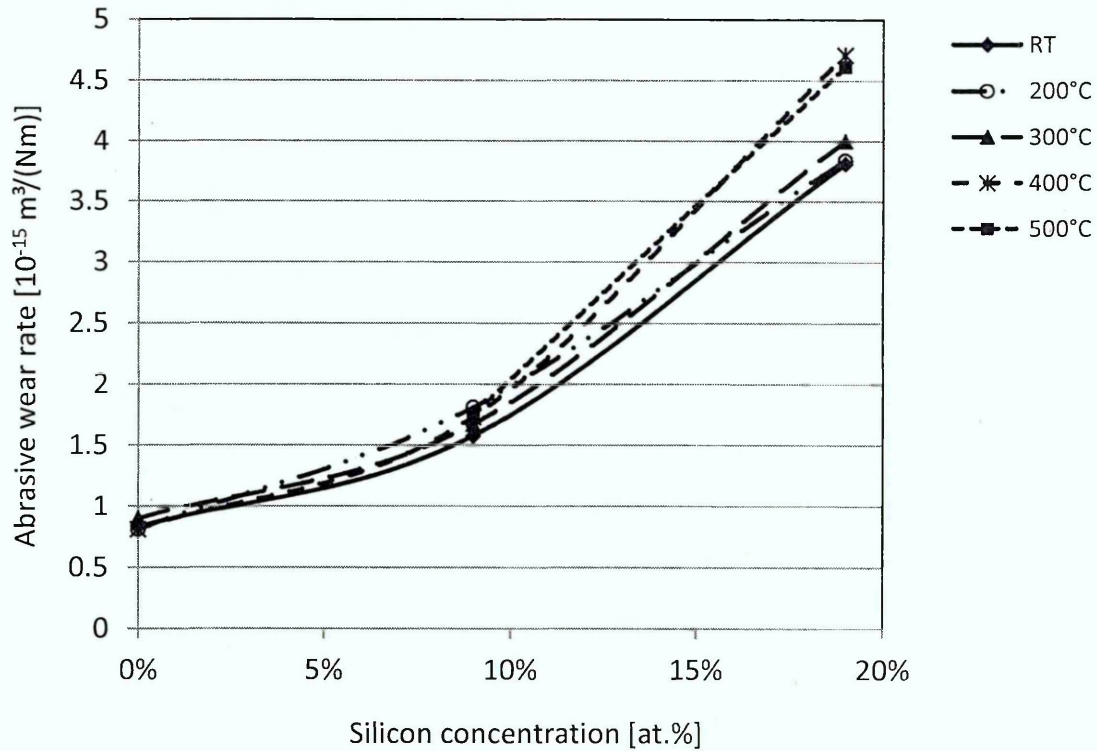


Figure 5.34 : Abrasive wear rate of Si-DLC/a-C:H nanolayer coatings and a 40 GPa a-C:H coating depending on the atomic content of silicon at room temperature and after step-stress testing at 200°C, 300°C, 400°C and 500°C

Figure 5.34 shows the abrasive wear rates, before and after tempering at temperatures of 200 °C to 500 °C, of a-C:H coatings and Si-DLC/a-C:H nanolayer coatings depending on the atomic concentration of silicon. The wear rates increase continuously from $0.8 - 0.9 \times 10^{-15} \text{ m}^3/(\text{Nm})$ for pure a-C:H and reach $3.8 - 4.7 \times 10^{-15} \text{ m}^3/(\text{Nm})$ for Si-DLC/a-C:H with 19 at.% Si. After heating the pure a-C:H at a temperature of 500 °C wear testing was not possible due to deterioration of the coating.

For pure a-C:H, Si-DLC/a-C:H nanolayer coatings with 9 and 19 at.% silicon and a combined Si-DLC/a-C:H nanolayer with 9 at.% Si and 15 at.% Si the indentation hardness depending on the temperature was discussed by Hofmann et al. [339]. The results are shown in Figure 5.35. The indentation hardness of the Si-DLC/a-C:H nanolayer coatings with 9 and 19 at.% silicon are almost stable after heating up to a temperature of 300 °C and increase almost linearly

in the range of 300 °C to 500°C. For the pure a-C:H the hardness is reduced at a temperature of 400 °C and drops to 10 GPa after tempering at 500 °C. For the combined Si-DLC/a-C:H nanolayer with 9 at.% Si and 15 at.% Si a higher hardness compared to the nanolayers which only contain 9 at.% Si and 19 at.% Si can be observed. In order to find the reason for the high layer hardness of the combined Si-DLC/a-C:H nanolayer additional investigations are necessary.

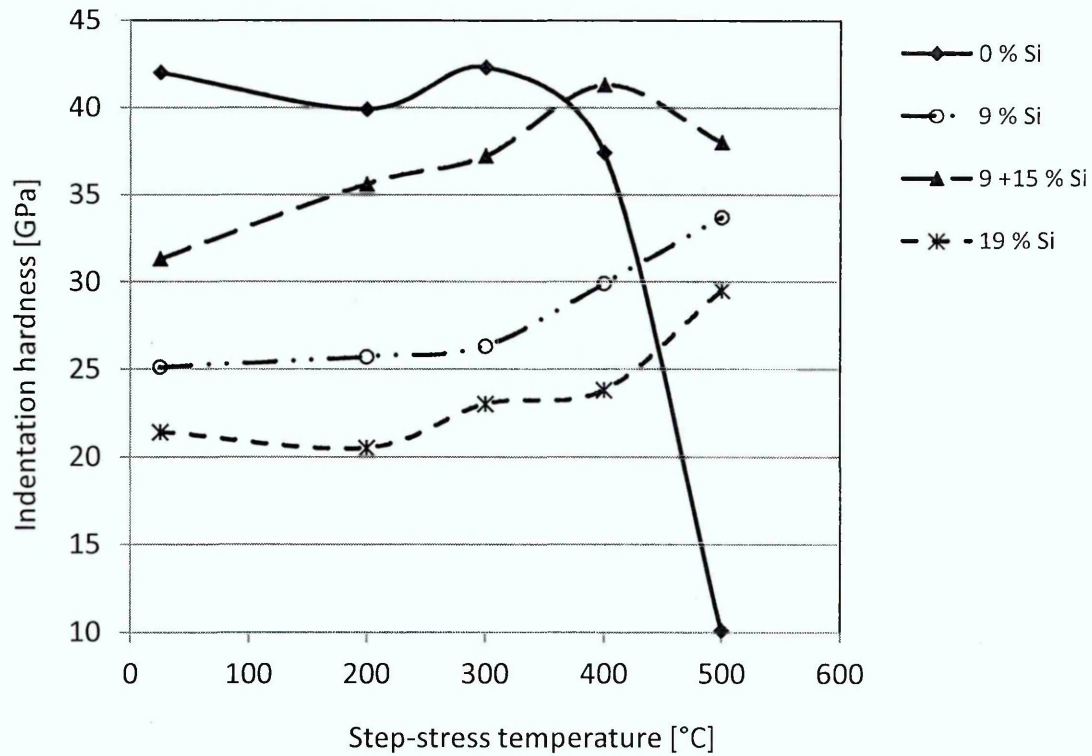


Figure 5.35 : Indentation hardness of Si-DLC/a-C:H nanolayer coatings and a 40 GPa a-C:H coating depending on the step-stress temperature, according to Hofmann et al. [339]

The friction coefficients for sliding against a 100Cr6 steel mating ball for pure a-C:H, for Si-DLC/a-C:H nanolayer coatings with 9 and 19 at.% silicon and for a combined Si-DLC/a-C:H nanolayer with 9 at.% Si and 15 at.% Si are shown in Figure 5.36 according to Hofmann et al. [339]. A high friction coefficient is observed for pure a-C:H after tempering at 500 °C but in the range of RT up to 400 °C friction coefficients of 0.14 to 0.17 are found. For the Si-DLC/a-C:H nanolayer coating with 9 at.% silicon an almost stable friction coefficient of 0.14 to 0.15 and for the nanolayer coating with 19 at.% silicon friction coefficients of 0.1 to 0.13 can be observed in the range of temperatures up to 500 °C.

A friction coefficient of 0.11 to 0.13 was determined for the combined Si-DLC/a-C:H nanolayer with 9 at.% Si and 15 at.% Si in the temperature range from RT to 300 °C. After tempering at 400 °C and 500 °C the friction coefficient was reduced to 0.08 and 0.09 respectively. The low friction coefficient of the combined layer is almost similar to the Si-DLC/a-C:H nanolayer with a high silicon content of 19 at.% and is noticeably lower than the friction coefficients of pure a-C:H and the Si-DLC/a-C:H nanolayer with low silicon content of 9 at.%. Another positive effect is that after tempering at 400 °C and 500 °C the combined layer has a very low friction coefficient which could be beneficial if high local temperatures in the tribocontact exist.

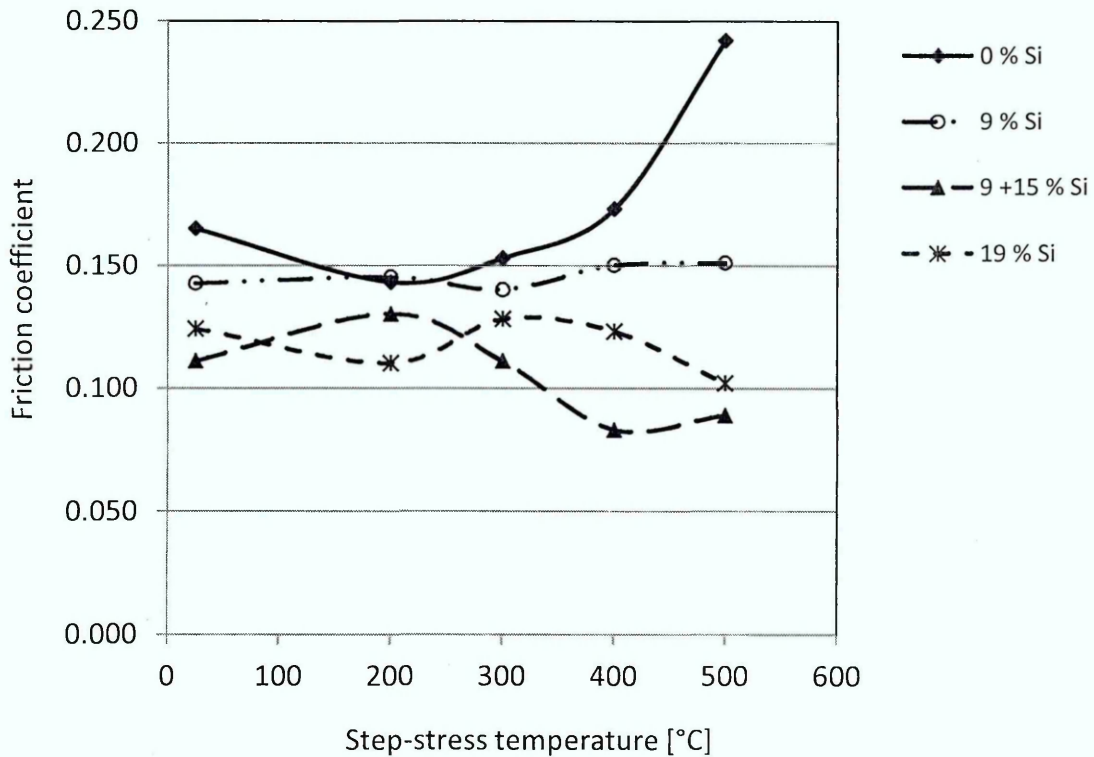


Figure 5.36 : Friction coefficient of Si-DLC/a-C:H nanolayer coatings and a 40 GPa a-C:H coating depending on the step-stress temperature, according to Hofmann et al. [339]

The abrasive wear rates of pure a-C:H, Si-DLC/a-C:H nanolayer coatings with 9 and 19 at.% silicon and a combined Si-DLC/a-C:H nanolayer with 9 at.% Si and 15 at.% Si depending on the temperature are shown in Figure 5.37. For pure a-C:H almost stable wear rates of 0.8 to $0.9 \times 10^{-15} \text{ m}^3/(\text{Nm})$ were

determined in the temperature range from RT to 400 °C but after tempering at 500 °C no wear testing was possible due to the deterioration of the coating. The wear rates of the Si-DLC/a-C:H nanolayer coatings with 9 at.% silicon and the combined Si-DLC/a-C:H nanolayer are almost constant and not very different within the temperature range from RT to 500 °C. This indicates that for the combined layer low wear rates were achieved as observed for coatings with low Si contents of less than 10 at.% and for industrially used a-C:H:Me coatings. As expected for the highly silicon doped Si-DLC/a-C:H nanolayer coatings with 19 at.% silicon high wear rates of 3.8 to 4.7 x 10⁻¹⁵ m³/(Nm) can be observed.

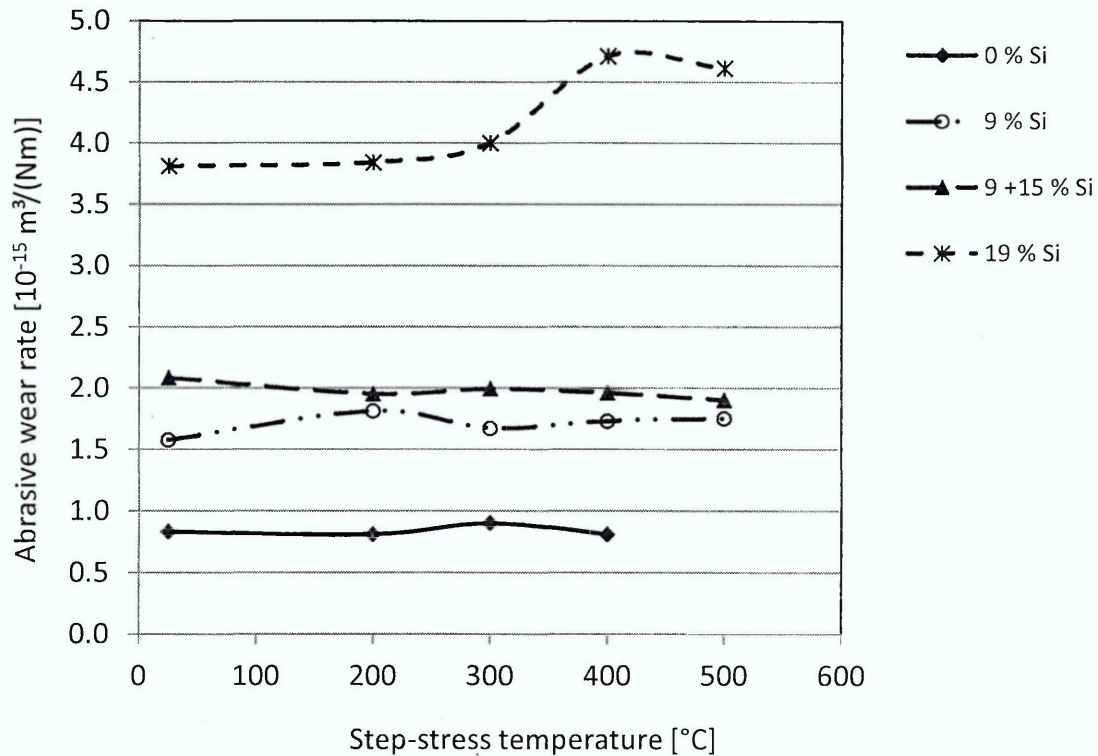


Figure 5.37 : Abrasive wear rate of Si-DLC/a-C:H nanolayer coatings and a 40 GPa a-C:H coating depending on the step-stress temperature

Both a low friction coefficient and a low abrasive wear rate of the combined layer at RT and after tempering at 200 to 500 °C show that it was possible to combine low friction and low wear properties with respect to applications under dry unlubricated conditions in an elevated temperature range.

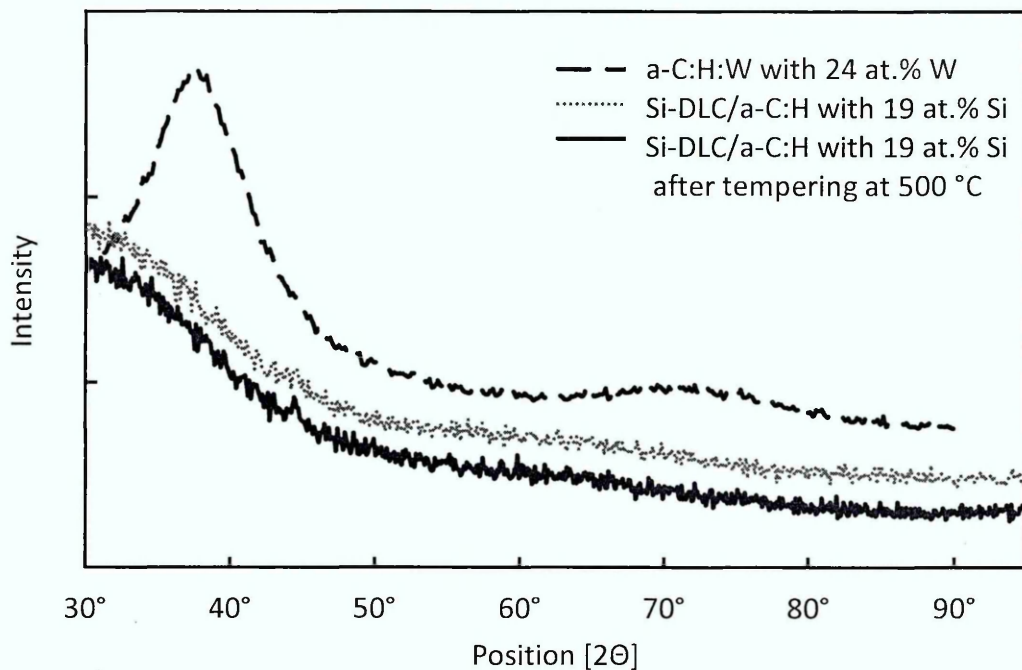


Figure 5.38 : XRD spectrum of Si-DLC/a-C:H nanolayer coating with 19 at.% silicon content (not including hydrogen) as deposited and after annealing in air at 500°C, according to Hofmann et al. [339]

It was previously shown (chapter 5.5) that in Si-DLC/a-C:H nanolayer coatings the amorphous-like morphology of a-C:H was not changed by a silicon incorporation for an as deposited coating with 19 at.% silicon content. Whereas for a-C:H:W coatings the formation of nanocrystallites of metal carbide, which was surrounded with sp^2 -rich a-C:H, has been reported by Grischke [362], Fryda [363] and Bewilogua et al. [364, 365]. In order to prove that tempering at 500 °C does not change the amorphous-like character of Si-DLC/a-C:H nanolayer coatings the structure was investigated by XRD spectroscopy. Figure 5.38 shows the XRD spectra of a Si-DLC/a-C:H nanolayer coating with 19 at.% Si before and after tempering at 500 °C and the XRD spectrum of an a-C:H:W coating with 24 at.% tungsten.

For the Si-DLC/a-C:H nanolayer coating the amorphous-like morphology of the coating remained after tempering at 500 °C which indicates that no crystalline SiC was formed. In contrast to this, for the a-C:H:W coating, a broadened diffraction peak which results from the nanocrystalline WC is visible.

5.8 Improvement of frictional and wear behavior under lubricated conditions

Under some lubricated conditions for the Si-DLC/a-C:H nanolayer coatings high friction coefficients and high wear rates can be observed. For example, at low sliding speeds using diesel fuel as lubricant the Si-DLC/a-C:H nanolayer coatings showed a high friction coefficient and a high wear rate. This is expected to result from insufficient wetting of the lubricant on silicon-doped a-C:H. For the wetting behavior the surface free energy of the coating material is important. In Table 5.1 the surface free energy and the contact angle for water are shown for selected a-C:H-based coatings and for PTFE using own data and data from Grischke et al. [366]. The surface free energy for Si-DLC of 30 to 35 mN/m is lower compared to the surface free energy of undoped a-C:H with 35 to 40 mN/m. This explains that wetting can become insufficient for silicon-doped a-C:H in critical applications where lubricants are used.

Material/ Coating	Precursor	Surface free energy [mN/m]	Contact angle for H ₂ O [deg.]
PTFE		18.5	110
a-C:H:F	C ₂ H ₂ +C ₂ F ₄	20-30	95-100
a-C:H:Si:O	C ₂ H ₂ +HMDSO and C ₂ H ₂ +HMDSO+O ₂	20-30	95-100
a-C:H:Si (Si-DLC)	C ₂ H ₂ +TMS	30-35	80-95
a-C:H:Si (Si-DLC)	C ₂ H ₂ +Si from SiC/C target	30-35	80-95
a-C:H	C ₂ H ₂	35-40	70-80
a-C:H:Me	C ₂ H ₂	40-50	70-60
a-C:H:N	C ₂ H ₂ + N ₂	40-120	70-40

Table 5.1 : Surface free energy and contact angles for H₂O for a-C:H-based coatings and PTFE, using own data and data from M. Grischke et al. [366]

Table 5.1 shows high surface free energies of 40 to 50 mN/m for metal-doped a-C:H (a-C:H:Me).

From the properties of the Si-DLC/a-C:H nanolayer coatings, which were previously discussed, it was observed that the combining of the properties of Si-DLC and the properties of a-C:H was possible. For example, the temperature stability of these layers was increased up to temperatures of 500 °C in air by the influence of the Si-DLC nanolayers on neighboring a-C:H nanolayers.

In order to optimize the nanolayer system with respect to the application of these coatings under lubrication, Hofmann [367] proposed a triple nanolayer system consisting of Si-DLC/a-C:H/a-C:H:Me.

Table 5.2 shows the properties of individual a-C:H-types of this triple nanolayer. These properties can be combined in Si-DLC/a-C:H/a-C:H:Me triple layer nanolayer concepts. As favorable properties of a-C:H one can see the high hardness and the low abrasive wear rates. For Si-DLC a very low friction coefficient and a high temperature stability up to 500°C is remarkable. For the combination of Si-DLC/a-C:H in some lubricated applications the low surface free energy of Si-DLC of 30-35 mN/m could create wetting problems which can be solved by adding a-C:H:Me with high surface free energy, high toughness and high electrical conductivity to the nanolayer system.

For the triple nanolayer new properties could be expected from the interaction of the nanolayer materials using specific optimization of the layer systems. The triple layer system allows combining the best properties of Si-DLC, a-C:H and Me-DLC within one coating for a specific application.

Using nanolayer coatings of the three different types of DLC for a given application the properties of nanolayer coatings can be specifically adapted. As basic selection criteria for the optimization of properties for triple layer combinations can be named the high wear resistance of the a-C:H, the low friction coefficient combined with a high temperature stability of the Si-DLC and the relatively high surface free energy of the a-C:H:Me to improve the wetting behavior under lubricated conditions.

The best coating for a specific application has to be found by optimizing nanolayer combinations in order to achieve the best performance under the light of the selection criterions given above and in more detail in Table 5.2.

a-C:H	Si-DLC (a-C:H:Si)	Me-DLC (a-C:H:Me)
Low abrasive wear rates of 0.5 to $1 \times 10^{-15} \text{ m}^3/(\text{Nm})$	Abrasive wear rates of 1.1 to $5 \times 10^{-15} \text{ m}^3/(\text{Nm})$	Abrasive wear rates of 2.0 to $10 \times 10^{-15} \text{ m}^3/(\text{Nm})$
High indentation hardness of 20 to 45 GPa	High indentation hardness of 20 to 30 GPa	Indentation hardness of 15 to 20 GPa
Low friction coefficients in normal air (dry unlubricated contact) 0.15 to 0.2	Very low friction coefficients in normal air (dry unlubricated contact) 0.06 to 0.15	Low friction coefficients in normal air (dry unlubricated contact) 0.2 to 0.3
Stable in air up to a temperature of about $350 \text{ }^\circ\text{C}$	Stable in air up to a temperature of about $500 \text{ }^\circ\text{C}$	Stable in air up to a temperature of about $350 \text{ }^\circ\text{C}$
Surface free energy of 35 to 40 mN/m	Low surface free energy of 30 to 35 mN/m	Surface free energy of 40 to 50 mN/m
		High toughness and good electrical conductivity

Table 5.2 : Overview of the characteristic properties of a-C:H, Si-DLC and a-C:H:Me coatings

6. Conclusions and summary

The reduction of friction and wear is the main target for the application of a-C:H-based coatings in the automotive industry. Due to continued increasing specific loads on automotive components a high wear resistance of these coatings is demanded. A further requirement is that a-C:H-based coatings can be used in oxidative atmosphere at higher temperatures of up to 500 °C compared to about 350 °C if pure a-C:H coatings are used.

From various publications it is known that doping of a-C:H with silicon allows an improvement of temperature resistance and a decrease in the friction coefficient of the coatings. Unfortunately these improvements are combined with a reduction of the wear resistance. Si-DLC coatings are usually deposited by the PECVD method. Precursors like tetramethylsilane (TMS) which contain a high atomic percentage of hydrogen are widely used as a source of silicon for the Si-DLC. Due to the deposition of Si-DLC in highly hydrogenous process atmospheres a high atomic content of hydrogen is incorporated in the coating. Using only PECVD deposition the high hydrogen content of the coatings from silicon doping of a-C:H, a low hardness and a low compressive stress of the coatings can be explained. In order to deposit thin alternating nanolayers of Si-DLC and a-C:H by using the "pure" PECVD method the gas atmosphere needs to be changed in order to produce silicon-free and silicon-containing coatings. The change of the process gas atmosphere is combined with high time constants which are determined by the volume of the recipient and the pumping speed. Therefore in a production system with large recipients and limited pumping speeds and under the requirement of high deposition rates the "pure" PECVD method is not practical in order to allow the industrial deposition of Si-DLC/a-C:H nanolayer coatings.

In order to circumvent the problems mentioned above for the deposition of Si-DLC/a-C:H nanolayer coatings, the silicon for the doping of a-C:H was deposited by sputtering from a silicon carbide target with some additional graphitic carbon (SiC/C). Si-DLC/a-C:H nanolayer coatings were deposited by dynamic deposition using two-fold rotation with strong plasma support from the Plasma Booster. For this deposition process PECVD deposition of carbon from acetylene and by sputtering from the SiC/C and graphite target(s) were used. The silicon sputter deposition from the SiC/C target for the doping of the a-C:H

is not accompanied by additional incorporation of hydrogen into the coating from a silicon source.

A literature survey on the basic processes for the layer deposition and properties of carbon-based and a-C:H-based coatings with a focus on the friction and wear properties of a-C:H and Si-DLC coatings was presented. This literature study includes information about mechanisms and models used to explain the friction and wear behavior of these coatings.

The layer sequence as well as the basic process conditions for a-C:H and Si-DLC monolayers and Si-DLC/a-C:H nanolayer coatings and the basic process parameter range for the deposition of such coatings are discussed.

The properties of a-C:H as part of the Si-DLC/a-C:H nanolayer coating were carefully studied. This included the influence on the properties depending on the hydrogen content of the coating.

For a-C:H a high indentation hardness of about 40 GPa, a high EIT modulus of 225 GPa and a low abrasive wear rate of $0.6 \times 10^{-15} \text{ m}^3/(\text{Nm})$ were achieved for coatings with a low hydrogen content of 11 at.%. Tribological properties of Si-DLC/a-C:H nanolayer coatings were discussed depending on the silicon content of the coatings. For these coatings a high indentation hardness of 20 to 30 GPa, low friction coefficients of 0.07 to 0.15 and high EIT moduli of 150 to 225 GPa were observed. The friction coefficients and the wear rates of the coatings were discussed for dry and humid atmospheres. It was observed that with increasing silicon content the wear resistance of the nanolayer coatings was reduced. For high silicon concentrations of 24 at.% high wear rates up to $4 \times 10^{-15} \text{ m}^3/(\text{Nm})$ with low friction coefficients of 0.07 to 0.09 were determined whereas for low silicon content low wear rates of around $1.5 \times 10^{-15} \text{ m}^3/(\text{Nm})$ and higher friction coefficients of 0.11 to 0.14 were achieved.

In order to combine low friction and low wear properties a combined Si-DLC/a-C:H nanolayer coating consisting of a first layer with 9 at.% Si and a second layer with 15 at.% Si on top was produced. For the combined layer a low wear rate of $2.1 \times 10^{-15} \text{ m}^3/(\text{Nm})$ and a low friction coefficient of 0.11 were determined.

The a-C:H and the Si-DLC/a-C:H nanolayer coatings were tempered in a step-stress test at temperatures up to 500°C. The indentation hardness, the friction coefficient, and the abrasive wear rate was determined after each tempering step for coatings with 0 to 19 at.% silicon content. It was found that the properties of a-C:H coatings changed at 400 °C and the coating deteriorated after tempering at 500 °C. The Si-DLC/a-C:H nanolayer coatings showed an increased hardness, slight changes of the friction coefficient and an almost stable wear resistance in the temperature region from RT to 500 °C.

The use of Si-DLC and the Si-DLC/a-C:H nanolayer coatings can become critical under certain lubricated applications at which high friction coefficients at low sliding speeds and high wear rates were observed. It can be expected that these critical conditions originate from insufficient wetting of lubricants caused by lower free surface energy of silicon-doped a-C:H of 30 to 35 mN/m compared to pure a-C:H with 35 to 40 mN/m. In order to improve the wetting behavior and to enable further optimization of the nanolayer for a specific application a triple-layer system of Si-DLC/a-C:H/a-C:H:Me was discussed. In the triple-layer system the a-C:H:Me (Me-DLC) nanolayer component with surface energies of 40 to 50 mN/m can be used to improve wetting under lubricated conditions.

The following summarized results for the coatings show that the aims and objectives (see chapter 1) were achieved.

- The coating properties were discussed depending on C₂H₂ massflow, bias voltage, hydrogen and silicon concentration in the coatings.
- a-C:H: High hardness >40 GPa, low wear rates of $0.6 \times 10^{-15} \text{ m}^3/(\text{Nm})$ and low hydrogen contents <11 at.%
- Si-DLC/a-C:H nanolayer coatings: High hardness of 20 to 30 GPa, high temperature stability up to 500 °C.

Low friction coefficients of 0.06 to 0.11 but high abrasive wear rates of $>2.5 \times 10^{-15} \text{ m}^3/(\text{Nm})$ were achieved at high silicon contents above 15 at.%.

For silicon contents <10 at.% low wear rates $<1.7 \times 10^{-15} \text{ m}^3/(\text{Nm})$ were combined with higher friction coefficients of 0.12 to 0.15.

- To combine low wear rates and low friction: A first Si-DLC/a-C:H nanolayer with low Si concentration followed by a second Si-DLC/a-C:H nanolayer with high Si concentration were deposited.

For a first layer with 9 at.% Si and a second layer with 15 at.% Si on top a low wear rate of $2.1 \times 10^{-15} \text{ m}^3/(\text{Nm})$ and a low friction coefficient of 0.11 were determined.

It was found that the layer with high wear resistance clearly influenced the combined wear rate which may be attributed to a lubricative effect of the low friction layer.

- Wetting behavior: By the low surface free energy of Si-DLC of 30 to 35 mN/m the wetting behavior for some lubricated applications may deteriorate. In this case a further optimization of the nanolayer system is required using a triple nanolayer with an additional Me-DLC nanolayer.

Further work needs to be done on optimization of the thickness ratios of combined low wear rate and low friction Si-DLC/a-C:H nanolayers in order to further increase the wear resistance.

For lubricated tribological applications the Si-DLC/a-C:H/a-C:H:Me triple layer nanolayers have to be optimized with respect to wear resistance, friction and wetting. The effects of the a-C:H:Me layer on the tribological properties need to be further investigated.

The work on the "triple layer" has to be continued with the optimization of combining the properties of the three DLC types for the nanolayer with respect to typical applications of the automotive sector.

For the combination of thin nanolayers a nonlinear behavior of the nanolayer system could be expected to occur. In order to identify such a nonlinear behavior very thin nanolayers with individual layer thicknesses of 1 nm or less have to be deposited to allow the materials of these thin nanolayers to interact on an atomic scale.

References

- [1] K. Holmberg, P. Andersson and A. Erdemir, Global energy consumption due to friction in passenger cars, *Trib. Int.* 47 (2012) 221-234
- [2] S.C. Tung and M. L. McMillan, Automotive tribology overview of current advances and challenges for the future, *Trib. Int.* 37 (2004) 517-536
- [3] J. Affenzeller, N.O. Owen, J.-F. Gruson, G. Lepperhoff, M. Blaich and W. Kriegler, Future road vehicle research a roadmap for 2020 and beyond, *Proc. 9th FUIRORE EAEC Int. Congress, Paris* (2003)
- [4] M. Baglione, M. Duty and G. Pannone, Vehicle system energy analysis methodology and tool for determining vehicle subsystem energy supply and demand, *SAE Technical Paper 2007-01-0398* (2007)
- [5] A. Bandivadekar, K. Bodek, L. Cheah, C. Evans, T. Groode, J. Heywood, E. Kasseris, M. Kromer and M. Weiss, On the road in 2035: Reducing transportation's petroleum consumption and GHG emissions, *MIT Report LFE 2008-05 RP* (2008)
- [6] C. Treutler, Industrial use of plasma-deposited coatings for components of automotive fuel injection systems, *Surf. Coat. Technol.* 200 (2005) 1969 – 1975
- [7] W.R. Grove, On the electro-chemical polarity of gases, *Phil. Trans. Roy. Soc. London* 142 (1852) 87-101
- [8] J.J. Thomson, Rays of positive electricity and their applications to chemical analyses, *Longmans Green & Co. Ltd. London* (1921) 1-237
- [9] A. Güntherschulze and K. Meyer, Kathodenzerstäubung bei sehr geringen Gasdrücken, *Z. Physik*, 62 (1930) 607-618
- [10] F.M. Penning, Die Glimmentladung bei niedrigem Druck zwischen koaxialen Zylindern in einem axialen Magnetfeld, *Physica* 3 (1936) 873-894
- [11] G.K. Wehner, Momentum transfer in sputtering by ion bombardment, *J. Appl. Phys.* 25 (1954) 270
- [12] G.K. Wehner, Sputtering of metal single crystals by ion bombardment, *J. Appl. Phys.* 26 (1955) 1056-1057
- [13] D. Mattox, Film deposition using accelerated ions, *Electrochem. Technol.* 2 (1964) 295
- [14] L. Maissel and P. Schaible, Thin films deposited by bias sputtering, *J. Appl. Phys.* 36 (1965) 237-242

-
- [15] D. Mattox, Apparatus for coating a cathodically biased substrate from plasma of ionized coating material, US Patent 3,329,601 (1967)
- [16] P. Clarke, Sputtering apparatus, US Patent 3,616,450 (1971)
- [17] J. Corbani, Cathode sputtering apparatus, US Patent 3,878,085 (1975)
- [18] J. Chapin, Sputtering process and apparatus, US Patent 4,166,018 (1979)
- [19] B. Window and N. Savvides, Charged particle fluxes from planar magnetron sputtering sources, *J. Vac. Sci. Technol. A4* (1986) 196-202
- [20] B. Window and N. Savvides, Unbalanced d.c. magnetrons as sources of high ion fluxes, *J. Vac. Sci. Technol. A4* (1986) 453-456
- [21] N. Savvides and B. Window, Unbalanced magnetron ion-assisted deposition and property modification of thin films, *J. Vac. Sci. Technol. A4* (1986) 504-508
- [22] P. Sigmund, Theory of sputtering I. sputtering yield of amorphous and polycrystalline targets, *Phys. Rev.* 184 (1969) 383-416
- [23] J. Lindhard, V. Nielsen and M. Scharff, *Kgl. Danske Videnskab., Mat.-Fys. Medd.* 36, No. 10 (1968)
- [24] P.C. Zalm, Energy dependence of the sputtering yield of silicon bombarded with neon, argon, krypton and xenon, *J. Appl. Phys.* 54 (1983) 2660-2666
- [25] N. Matsunami, Y. Yamamura, Y. Itikawa, N. Itoh, Y. Kazumata, S. Miyagawa, K. Morita, and R. Shimizu, A semi-empirical formula for the energy dependence of the sputtering yield, *Radiation Effects Letters* 57 (1980) 15-21
- [26] N. Matsunami, Y. Yamamura, Y. Itikawa, N. Itoh, Y. Kazumata, S. Miyagawa, K. Morita, R. Shimizu and H. Tawara, Energy dependence of the ion-induced sputtering yields of monoatomic solids, *Atomic Data and Nuclear Data Tables* 31 (1984) 1-80
- [27] Y. Yamamura, N. Matsunami, and N. Itoh, A new empirical formula for the sputtering yield, *Radiation Effects Letters* 68 (1982) 83-87
- [28] Y. Yamamura, H. Tawara, Energy dependence of ion-induced sputtering yields from monoatomic solids at normal incidence, *Atomic Data and Nuclear Data Tables* 62 (1996) 149-253
- [29] Y. Yamamura, Y. Itikawa, and N. Itoh, Angular dependence of sputtering yields of monoatomic solids, Institute of Plasma Physics IPPJ-AM-26, Nagoya University (1983) 1-118

- [30] T. Ono, K. Shibata, T. Kenmotsu, T. Muramoto, Z. Li and T. Kawamura, Extended incident-angle dependence formula of sputter yield, NIFS-DATA-097 (2006)
- [31] Q. Wei, K-D. Li, J. Lian and L. Wang, Angular dependence of sputtering yield of amorphous and polycrystalline materials, *J. Phys. D: Appl. Phys.* 41 (2008) 172002
- [32] J. Ziegler, J. Biersack and U. Littmark, *The stopping and range of ions in solids*, Pergamon Press, New York, NY, USA (1985)
- [33] J. Biersack and L. Haeggmark, A Monte Carlo computer program for the transport of energetic ions in amorphous targets, *Nucl. Instr. Meth.* 174 (1980) 257-269
- [34] J. Ziegler, M. Ziegler and J. Biersack, SRIM- the stopping and range of ions in matter, *Nucl. Instr. Meth. Phys. Res. B* 286 (2010) 1818-1823
- [35] N. Andersen, P. Sigmund, Energy dissipation by heavy ions in compound targets, *Mat. Fys. Medd. Dan. Vid. Selsk.* 39 (1974) 1-48
- [36] J. Comas and C. Cooper, Sputtering yields of several semiconducting compounds under argon ion bombardment, *J. Appl. Phys.* 37 (1966) 2820-2822
- [37] M.P. Seah and T.S. Nunnery, Sputtering yields of compounds using argon ions, *J. Phys. D: Appl. Phys.* 43 (2010) 253001
- [38] P. Sigmund, Fundamental processes in sputtering of atoms and molecules, *Mat. Fys. Medd. Dan. Vid. Selsk.* 43 (1992) 255-349
- [39] G. Betz and G.K. Wehner, Sputtering of multicomponent materials, in: R. Behrisch (Ed.), *Sputtering by Particle Bombardment*, Vol. 2. Springer, Heidelberg (1983) 11–90
- [40] F. Penning, Coating by cathode disintegration, US Patent 2,146,025 (1939)
- [41] R. Jepsen, Magnetically confined cold-cathode gas discharges at low pressures, *J. Appl. Phys.* 32 (1961) 2619-2626
- [42] J.S. Chapin, The planar magnetron, *Res. Dev.* 25 (1974) 37-40
- [43] G. Braeuer, B. Szyszka, M. Vergoehl and R. Bandorf, Magnetron sputtering – milestones of 30 years, *Vacuum* 84 (2010) 1354–1359
- [44] R. Kukla, T. Krug, R. Ludwig, and K. Wilmes, A highest rate self-sputtering magnetron source, *Vacuum* 41 (1990) 1968-1970
- [45] R. Adam, J. Krempel-Hesse and M. Baehr, Sputter cathode, US Patent 6,139,706 (2000)

-
- [46] H. McKelvey, Magnetron cathode sputtering apparatus, US Patent 4,356,073 (1982)
- [47] J.J. Hofmann, Dc reactive sputtering using a rotating cylindrical magnetron, Proc. Soc. Vac. Coaters Techcon. 32 (1989) 297-300
- [48] G. Veszi, The modern single-layer selenium photo-electric cell, J. Brit. Instn. Radio Eng. 13 (1953) 183-189
- [49] H.-O. Blom, S. Berg and T. Larson, Mass flow limitations in reactive sputtering, Thin Solid Films 130 (1985) 307-313
- [50] S. Berg, H.-O. Blom, T. Larsson and C. Nender, Modeling of reactive sputtering of compound materials, J. Vac. Sci. Technol. A 5 (2) (1987) 202-207
- [51] S. Berg, T. Larsson, C. Nender and H.-O. Blom, Predicting thin-film stoichiometry in reactive sputtering, J. Appl. Phys. 63 (1988) 887-891
- [52] T. Larsson, A model for reactive sputtering with magnetrons, Vacuum 39 (1989) 949-954
- [53] D. Depla and R. De Gryse, Target poisoning during reactive magnetron sputtering: part I: the influence of ion implantation, Surf. Coat. Technol. 183 (2004) 184-189
- [54] D. Depla and R. De Gryse, Target poisoning during reactive magnetron sputtering: part II: the influence of chemisorption and gettering, Surf. Coat. Technol. 183 (2004) 190-195
- [55] D. Depla, Z. Chen, A. Bogaerts, V. Ignatova, R. De Gryse and R. Gijbels, Modeling of the target surface modification by reactive ion implantation during magnetron sputtering, J. Vac. Sci. Technol. A22 (4) (2004) 1524-1529
- [56] S. Berg and T. Nyberg, Fundamental understanding and modeling of reactive sputtering processes, Thin Solid Films 476 (2005) 215-230
- [57] J. Musil, P. Baroch, J. Vlcek, K.H. Nam and J.G. Han, Reactive magnetron sputtering of thin films: present status and trends, Thin Solid Films 475 (2005) 208-218
- [58] T. Kubart, O. Kappertz, T. Nyberg and S. Berg, Dynamic behavior of the reactive sputtering process, Thin Solid Films 515 (2006) 421-424
- [59] D. Teer, A magnetron sputter ion-plating system, Surf. Coat. Technol. 36 (1988) 901-907
- [60] D. Teer, Technical note: a magnetron sputter ion-plating system, Surf. Coat. Technol. 39-40 (1989) 565-572

-
- [61] D. Teer, Magnetron Sputter ion plating, US Patent 5,556,519 (1996) filed 1994
- [62] W.D. Sproul, Multi-cathode unbalanced magnetron sputtering systems, Surf. Coat. Technol. 49 (1991) 284-289
- [63] D. Hofmann, P. Ballhause, A. Feuerstein and J. Snyder, Sputter ion plating with plasma boosters – a breakthrough in hard coating technology, Proc. SVC 35 (1992) 218-226
- [64] D. Hofmann, A. Feuerstein and H. Schuessler, System for coating substrates with magnetron cathodes, US Patent 5,196,105 (1993) filed 1991
- [65] W.D. Muenz, The unbalanced magnetron: current status of development, Surf. Coat. Technol. 48 (1991) 81-94
- [66] S. Kvasnica, P. Adamek and P. Spatenka, Imaging of unbalanced magnetron dc discharge, IEEE Transactions on Plasma Science 33 (2005) 364 - 365
- [67] I. Svadkovski, D. Golosov and S. Zavatskiy, Characterisation parameters for unbalanced magnetron sputtering systems, Vacuum 68 (2003) 283-290
- [68] G. Clarke, P. Kelly and J. Bradley, Cathode current distributions in an unbalanced magnetron, Surf. Coat. Technol. 200 (2005) 1341-1345
- [69] A. Solov'ev, N. Sochugov, K. Oskomov and S. Rabotkin, Investigation of plasma characteristics in an unbalanced magnetron sputtering system, Plasma Physics Reports 35 (2009) 399-408
- [70] B. Movchan and A. Demchishin, Study on the structure and properties to thick vacuum condensates of nickel, titanium, tungsten, aluminum oxide and zirconium dioxide, Fiz. Met. Metalloved 28 (1969) 653-660
- [71] J. Thornton, Influence of apparatus geometry and deposition conditions on the structure and topography of thick sputtered coatings, J. Vac. Sci. Technol. 11 (1974) 666-670
- [72] R. Messier, A. Giri and R. Roy, Revised structure zone model for thin film physical structure, J. Vac. Sci. Technol. A2 (1984) 500-503
- [73] A. Anders, A structure zone diagram including plasma based deposition and ion etching, Thin Solid Films 518 (2010) 4087-4090
- [74] L. Mond, C. Langer and F. Quincke, Action of carbon monoxide on nickel, J. Chem. Soc. Trans. 57 (1890) 749-753

- [75] W.C. Roberts-Austen, The extraction of nickel from its ores by the Mond process, Minutes of the Proc. (Institution of Civil Engineers) 135 (1898) 29-45
- [76] J. De Lodyguine, Illuminant for incandescent lamps, US patent 575002 (1893)
- [77] L. Atl, S. Ing and K. Laendle, Low-temperature deposition of silicon oxide films, J. Electrochem. Soc. 110 (1963) 465
- [78] S. Ing and W. Davern, Use of low-temperature deposited silicon dioxide films as diffusion masks in GaAs, J. Electrochem. Soc. 111 (1964) 120-122
- [79] S. Ing and W. Davern, Plasma-assisted deposition of dielectric films, J. Electrochem. Soc. 112 (1965) 285
- [80] W. Eversole, Synthesis of Diamond, U.S. Patents 3,030,187 and 3,030,188 (1958)
- [81] J. Angus, H. Will and W. Stanko, Growth of diamond seed crystals by vapor deposition, J. Appl. Phys. 39 (1968) 2915-2922
- [82] B. Derjaguin and D. Fedoseev, Growth of diamond and graphite from the gas phase, Nauka, Moscow (1977); published in:
B. Derjaguin and D. Fedoseev, Surf. Coat. Technol. 38 (1989) 131-248
- [83] S. Matsumoto, Y. Sato, M. Kamo and N. Setaka, Vapor deposition of diamond particles from methane, Jap. J. Appl. Phys. 21 (1982) L183-L185
- [84] M. Kamo, Y. Sato, S. Matsumoto and N. Setaka, Diamond synthesis from gas phase in microwave plasma, J. Cryst. Growth 62 (1983) 642-644
- [85] F. Celi and J. Butler, Diamond chemical vapor-deposition, Annu. Rev. Phys. Chem. 42 (1991) 643-684
- [86] J. Angus and C. Hayman, Low-pressure, metastable growth of diamond and "diamond-like" phases, Science 241 (1988) 913-921
- [87] D. Gruen, C₆₀ interactions with surfaces, gaseous species and photons: an overview, Nucl. Instr. Meth. Phys. Res. B 78 (1993) 118
- [88] R. Haubner and B. Lux, Diamond growth by hot-filament chemical vapor deposition: state of the art, Diam. Relat. Mater. 2 (1993) 1277-1294
- [89] D. Zhou, T. McCauley, L. Qin, A. Krauss and D. Gruen, Synthesis of nanocrystalline diamond thin films from an Ar-CH₄ microwave plasma, J. Appl. Phys. 83 (1998) 540-543

- [90] T. McCauley, D. Gruen and A. Krauss, Temperature dependence of the growth rate for nanocrystalline diamond films deposited from an Ar/CH₄ microwave plasma, *Appl. Phys. Lett.* 73 (1998) 1646-1648
- [91] A. Sumant, O. Auciello, H. Yuan, Z. Ma, R. Carpick and D. Mancini, Large-area low temperature ultrananocrystalline diamond (UNCD) films and integration with CMOS devices for monolithically integrated diamond MEMS/NEMS-CMOS systems, *Proc. SPIE* 7318 (2009) 731817
- [92] M. Meyyappan, L. Delzeit, A. Cassell and D. Hash, Carbon nanotube growth by PECVD: a review, *Plasma Sources Sci. Technol.* 12 (2003) 205
- [93] M. Meyyappan, A review of plasma enhanced chemical vapour deposition of carbon nanotubes, *J. Phys. D. Appl. Phys.* 42 (2009) 213001
- [94] S. Peter and I. Bialuch, Production relevant PECVD-methods with optimized precursors for a-C:H-deposition at high rate, AIF research report (2010), to be downloaded at:
http://www.efds.org/tl_files/efds/download/IGF/Richtlinien/Protokolle-Berichte/IGF%20Dateien%202010/15221BG-Schlussbericht.pdf
- [95] P. Awakowicz, R. Schwefel, P. Scheuber and G. Benstetter, Deposition of a-C:H films with an ECWR-reactor at 27 MHz: plasma diagnostics and film properties, *Surf. Coat. Technol.* 142-144 (2001) 342
- [96] C. Corbella, I. Bialuch, M. Kleinschmidt and K. Bewilogua, Modified DLC coatings prepared in a large-scale reactor by dual microwave/pulsed-DC plasma-activated chemical vapour deposition, *Thin Solid Films* 517 (2008) 1125
- [97] R.M. Dey, S.B. Singh, A. Biswas, R.B. Tokas, N. Chand, S. Venkateshwaran, D. Bhattacharya, N.K. Sahoo, S.W. Gosavi, S.K. Kulkarni and D.S. Patil, Substrate bias effects during diamond like carbon film deposition by microwave ECR plasma CVD, *Curr. Appl. Phys.* 8 (2008) 6
- [98] G. Fedosenko, A. Schwabedissen, J. Engemann, E. Braca, L. Valentini and J. Kenny, Pulsed PECVD deposition of diamond-like carbon films, *Diamond Relat. Mat.* 11 (2002) 1047
- [99] H.X. Li, T. Xu, J.M. Chen, H.D. Zhou and H.W. Liu, The effect of applied dc bias voltage on the properties of a-C:H films prepared in a dual dc-rf plasma system, *Appl. Surf. Sci.* 227 (2004) 364

-
- [100] B.H. Lung, M.J. Chiang, and M.H. Hon, Growth characterization and properties of diamond-like carbon films by electron cyclotron resonance chemical vapor deposition, *Thin Solid Films* 392 (2001) 16
- [101] T. Michler, M. Grischke, I. Traus, K. Bewilogua and H. Dimigen, Mechanical properties of DLC films prepared by bipolar pulsed DC PACVD, *Diamond Relat. Mat.* 7 (1998) 1333
- [102] S. Miyagawa, S. Nakao, M. Ikeyama, and Y. Miyagawa, Deposition of diamond-like carbon films using plasma based ion implantation with bipolar pulses, *Surf. Coat. Technol.* 156 (2002) 322
- [103] Z. Sun, X. Shi and E. Liu, High rate deposition of diamond-like carbon films by magnetically enhanced plasma CVD, *Thin Solid Films* 355-356 (1999) 146
- [104] T. Watanabe, M. Ishihara, K. Yamamoto, O. Tsuda, A. Tanaka, O. Takai and Y. Koga, Tribological properties of a-C:H films coated by the PBI method, *Diam. Relat. Mater.* 12 (2003) 105
- [105] M. Weiler, K. Lang, E. Li and J. Robertson, Deposition of tetrahedral hydrogenated amorphous carbon using a novel electron cyclotron wave resonance reactor, *Appl. Phys. Lett.* 72 (1998) 1314
- [106] S. F. Yoon, K. H. Tan, Rusli, J. Ahn and Q. F. Huang, Comparative study on the effects of ion density and ion energy on diamond-like carbon deposited by electron cyclotron resonance chemical vapor deposition, *J. Appl. Phys.* 89 (2001) 4830
- [107] J. W. Gielen, M. van de Sanden and D. C. Schram, Plasma beam deposited amorphous hydrogenated carbon: Improved film quality at higher growth rate, *Appl. Phys. Lett.* 69 (1996) 152
- [108] J. Szlufcik, K. De Clercq, P. De Schepper, J. Poortmans, A. Buczkowski, J. Nijs and R. Mertens, Improvement in multicrystalline silicon solar cells after thermal treatment of PECVD silicon nitride AR coating, *Proceedings of the 12th European Photovoltaic Solar Energy Conference, Amsterdam (1994)* 1018-1021
- [109] A. Aberle and R. Hezel, Progress in low-temperature surface passivation of silicon solar cells using remote-plasma silicon nitride, *Progress in Photovoltaics* 5 (1997) 29-50

- [110] N. Gherardi, S. Martin and F. Massines, A new approach to SiO₂ deposit using N₂-SiH₄-N₂O glow dielectric barrier-controlled discharge at atmospheric pressure, *J. Phys. D: Appl. Phys.* 33 (2000) L104
- [111] M. Gilliam, S. Gasworth, Characterization of the parameter space in expanding thermal plasma systems with organosiloxane and oxygen reagents, *Proc. Society of Vacuum Coaters Annual Conference, Chicago* (2008) 256-268
- [112] M. Fahland, High rate PECVD technology of Fraunhofer FEP, to be downloaded at: <http://www.fep.fraunhofer.de/en/Technologien/Hochrate-PECVD.html>
- [113] M. Ohring, *Materials Science of Thin Films, Deposition & structure*, Chapter 6: Chemical vapor deposition, Academic Press. (2001) 277-353
- [114] G. Braeuer, Report Photovoltaic Research (2009) available from; http://www.isfh.de/institut_solarforschung/files/04_braeuer.pdf
- [115] H. Habuka, Low temperature chemical vapour deposition of polycrystalline silicon carbide film using monomethylsilane gas, properties and applications of silicon carbide, Prof. Rosario Gerhardt (Ed.), ISBN: 978-953-307-201-2, InTech (2011) Available from: http://cdn.intechopen.com/pdfs/15085/InTech-low_temperature_chemical_vapour_deposition_of_polycrystalline_silicon_carbide_film_using_monomethylsilane_gas.pdf
- [116] H. Schmellenmeier, Die Beeinflussung von festen Oberflächen durch eine ionisierte Gasatmosphäre, *Experimentelle Technik der Physik* 1 (1953) 49-68
- [117] H. Schmellenmeier, Kohlenstoffschichten mit Diamantstruktur, *Z. Phys. Chem.* 205 (1956) 349-350
- [118] S. Aisenberg and R. Chabot, Ion-beam deposition of thin films of diamondlike carbon, *J. Appl. Phys.* 42 (1971) 2953-2958
- [119] D. Whitmell and R. Williamson, The deposition of hard surface layers by hydrocarbon cracking in a glow discharge, *Thin Solid Films* 35 (1976) 255-261
- [120] L. Holland and S.M. Ojha, Deposition of hard and insulating carbonaceous films on an r.f. target in a butane plasma, *Thin Solid Films* 38 (1976) L17-L19
- [121] C. Weissmantel, G. Reisse, H.-J. Erler, F. Henny, K. Bewilogua, U. Ebersbach and C. Schuerer, Preparation of hard coatings by ion beam methods, *Thin Solid Films* 63 (1979) 315-325
- [122] K. Enke, H. Dimigen and H. Huebsch, Frictional properties of diamondlike carbon layers, *Appl. Phys. Lett.* 36 (1980) 291-292

-
- [123] L. Andersson, A review of recent work on hard i-C films, *Thin Solid Films* 86 (1981) 193-200
- [124] L. Andersson, S. Berg, H. Norstrom, R. Olaison and S. Towta, Properties and coating rates of diamond-like carbon films produced by R.F. glow discharge of hydrocarbon gases, *Thin Solid Films* 63 (1979) 155-160
- [125] D. McKenzie and L. Briggs, Properties of hydrogenated carbon films produced by reactive magnetron sputtering, *Solar Energy Materials* 6 (1981) 97-106
- [126] S. Craig and G. Harding, Structure, optical properties and decomposition kinetics of sputtered hydrogenated carbon, *Thin Solid Films* 97 (1982) 345-361
- [127] D. Hofmann, H. Schuessler and W.-D. Muenz, Verfahren und Vorrichtung zum Herstellen harter Kohlenstoffschichten, German Patent DE 3442208 (1992) filed (1984)
- [128] D. Hofmann, W.D. Muenz, H. Schuessler and J. Goebel, Production and properties of hard carbon films prepared by magnetic field assisted deposition process, *Proc. IPAT Munich* (1985) 252-257
- [129] H. Dimigen, H. Huebsch and R. Memming, Tribological and electrical properties of metal-containing hydrogenated carbon films, *Appl. Phys. Lett.* 50 (1987) 1056-1058
- [130] D. Hofmann, S. Beisswenger and A. Feuerstein, Novel low temperature hard coatings for large parts, *Surf. Coat. Technol.* 49 (1991) 330-335
- [131] D. Hofmann, H. Schuessler, K. Bewilogua, H. Huebsch and J. Lemke, Plasma-Booster- assisted hydrogenated W-C coatings, *Surf. Coat. Technol.* 73 (1995) 137-141
- [132] D. Hofmann, DLC coating: 60 years history of R&D and applications to recent results, Plenary Presentation: Int. Conf. AEPSE Korea (2013)
- [133] K. Bewilogua and D. Hofmann, Diamond-like carbon films – from first experiments to worldwide applications, *Surf. Coat. Technol.* 242 (2014) 214-225
- [134] H.O. Pierson, *Handbook of carbon, graphite, diamond and fullerenes, Properties, processing and applications*, Noyes Publication (1993)
- [135] S. Neuville, Quantum electronic mechanisms of atomic rearrangements during growth of hard carbon films, *Surf. Coat. Technol.* 206 (2011) 703-726
- [136] M. Ashby and D. Jones, *Engineering Materials*, Pergamon Press, Oxford (1980) 58-78

-
- [137] B. Kelly, *Physics of Graphite*, Applied Science Publishers, London (1981)
- [138] J. Robertson, Amorphous carbon, *Adv. Phys.* 35 (1986) 317
- [139] P. Koidl, C. Wild, B. Dischler, J. Wagner and M. Ramsteiner, Plasma deposition, properties and structure of amorphous hydrogenated carbon films, *Mater. Sci. Forum* 52 (1989) 41
- [140] X. Jjiang, K. Reichelt, and B. Stritzker, The hardness and Young's modulus of amorphous hydrogenated carbon and silicon films measured with an ultralow load indenter, *J. Appl. Phys.* 66 (1989) 5805-5808
- [141] J. Angus, Diamond and diamond-like films, *Thin Solid Films* 216 (1992) 126-133
- [142] M. Weiler, S. Sattel, K. Jung, H. Eberhardt, V. Veerasamy and J. Robertson, Highly tetrahedral, diamond-like amorphous hydrogenated carbon prepared from a plasma beam source, *Appl. Phys. Lett.* 64 (1994) 2797
- [143] X. Jiang, J. Fassbender, and B. Hillebrands, Elastic constants of WC-a-C:H composite films studied by Brillouin spectroscopy, *Phys. Rev. B* 498 (1994) 13815-13819
- [144] C. Cooper, C. Beetz, B. Buchholtz, P. Wilbur and R. Wei, Spectroscopic and selected mechanical properties of diamond-like carbon films synthesized by broad-beam ion deposition from methane, *Diam. Relat. Mater.* 3 (1994) 534-541
- [145] C. Cooper, P. Holiday and A. Matthews, The effect of TiN interlayers on the indentation behavior of diamond-like carbon films on alloy and compound substrates, *Surf. Coat. Technol.* 63 (1994) 129-134
- [146] D.R. McKenzie, Tetrahedral bonding in amorphous carbon, *Rep. Prog. Phys.* 59 (1996) 1611
- [147] G. Pharr, D. Callahan, S. McAdams, T. Tsui, S. Anders, A. Anders, J. Ager, I. Brown, C. Bhatia, S. Silva and J. Robertson, Hardness, elastic modulus, and structure of very hard carbon films produced by cathodic-arc deposition with substrate pulse biasing, *Appl. Phys. Lett.* 68 (1996) 779-781
- [148] K. Lee, M. Kim, S. Cho, K. Eun and T. Seong, Structural dependence of mechanical properties of Si incorporated diamond-like carbon films deposited by RF plasma-assisted chemical vapour deposition, *Thin Solid Films* 308-309 (1997) 263-267

-
- [149] J. Wang, Y. Sugimura, A. Evans and W. Tredway, The mechanical performance of DLC films on steel substrates, *Thin Solid Films* 325 (1998) 163–174.
- [150] E. Harry, A. Rouzaud, M. Ignat and P. Juliet, Mechanical properties of W and W(C) thin films: Young's modulus, fracture toughness and adhesion, *Thin Solid Films* 332 (1998) 195–201
- [151] S. Cho, K. Lee, K. Eun, J. Han and D. Ko, Determination of elastic modulus and Poisson's ratio of diamond-like carbon films, *Thin Solid Films* 341 (1999) 207–210
- [152] J. Damasceno, S. Camargo, F. Freire and R. Carius, Deposition of Si-DLC films with high hardness, low stress and high deposition rates, *Surf. Coat. Technol.* 133–134 (2000) 247–252
- [153] A. Varma, V. Palshin and E. Meletis, Structure-property relationship of Si-DLC films, *Surf. Coat. Technol.* 148 (2001) 305–314
- [154] A. Ogwu, T. Coyle, T. Okpalugo, P. Kearney, P. Maguire and J. McLaughlin, The influence of biological fluids on crack spacing distribution in Si-DLC films on steel substrates, *Acta Mater.* 51 (2003) 3455–3465
- [155] J. C. Damasceno, S. Camargo and M. Cremona, Optical and mechanical properties of DLC-Si coatings on polycarbonate, *Thin Solid Films* 433 (2003) 199–204
- [156] G. Abbas, J. McLaughlin and E. Harkin-Jones, A study of ta-C, a-C:H and Si-a:C:H thin films on polymer substrates as a gas barrier, *Diam. Relat. Mater.* 13 (2004) 1342–1345
- [157] M. Kalin and J. Vizintin, A comparison of the tribological behavior of steel/steel, steel/DLC and DLC/DLC contacts when lubricated with mineral and biodegradable oils, *Wear* 261 (2006) 22–31
- [158] M. Michel, L. Muhlen, C. Achete and C. Lepienski, Fracture toughness hardness and elastic modulus of hydrogenated amorphous carbon films deposited by chemical vapour deposition, *Thin Solid Films* 496 (2006) 481–488
- [159] J. Robertson, Hard amorphous (diamond-like) carbons, *Prog. Solid St. Chem.* 21 (1991) 199–333
- [160] H. Ronkainen, Tribological properties of hydrogenated and hydrogen-free diamond-like carbon coatings, VTT Publications 434 (2001)

-
- [161] J. Robertson, Diamond-like amorphous carbon, *Mat. Sci. Eng. R* 37 (2002) 129-281
- [162] A. Erdemir and C. Donnet, Tribology of diamond and diamond-like carbon films: An overview, *Wear- Materials, Mechanisms and Practice*, edited by G. Stachowiak, Wiley (2005)
- [163] S. Hainsworth and N. Uhure, Diamond like carbon coatings for tribology: production techniques, characterization methods and applications, *Int. Mat. Rev.* 52 (2007) 153-174
- [164] C. Donnet and A. Erdemir editors, *Tribology of diamond-like carbon films: Fundamentals and applications*, Springer (2008)
- [165] P. Reinke, W. Jacob and W. Moeller, Influence of the ion energy on the growth and structure of thin hydrocarbon films, *J. Appl. Phys.* 74 (1993) 1354-1361
- [166] W. Jacob and W. Moeller, On the structure of thin hydrocarbon films, *Appl. Phys. Lett.* 63 (1993) 1771-1773
- [167] J. Robertson, Diamond-like carbon, *Pure & Appl. Chem.* 66 (1994) 1789-1796
- [168] A.C. Ferrari and J. Robertson, Interpretation of Raman spectra of disordered and amorphous carbon, *Phys. Rev. B* 61 (2000) 14095-14107
- [169] Carbon Films, Basic knowledge, film types and properties, VDI 2840 guideline (2012) 1-41
- [170] J.C. Phillips, Topology of covalent non-crystalline solids I: Short-range order in chalcogenide alloys, *J. Non-Cryst. Solids* 34 (1979) 153-181
- [171] J.C. Phillips, Topology of covalent non-crystalline solids II: Medium-range order in chalcogenide alloys and A-Si(Ge), *J. Non-Cryst. Solids* 43 (1981) 37-77
- [172] M.F. Thorpe, Continuous deformations in random networks, *J. Non-Cryst. Solids* 57 (1983) 355-370
- [173] K. Bewilogua, D. Dietrich, G. Holzhueter and C. Weissmantel, Structure of amorphous carbon films, *Phys. Status Solidi A* 71 (1982) K57-K59
- [174] D. Beeman, J. Silverman, R. Lynds and M.R. Anderson, Modeling studies of amorphous carbon, *Phys. Rev. B* 30 (1984) 870-875
- [175] J. Robertson and E.P. O'Reilly, Electronic and atomic structure of amorphous carbon, *Phys. Rev. B* 35 (1987) 2946-2957

- [176] J.C. Angus and F. Jansen, Dense 'diamond-like' hydrocarbons as random covalent networks, *J. Vac. Sci. Technol. A* 6 (1988) 1778-1782
- [177] J.C. Angus and Y. Wang, Diamond-like hydrocarbon and carbon films, in *Diamond-Like Films and Coatings*, R.E. Clausing and J.C. Angus (eds.), NATO ASI Series B 266, Plenum New York (1991) 173-192
- [178] Th. Frauenheim, G. Jungnickel, T. Koehler and U. Stephan, Structure and electronic properties of amorphous carbon: From semimetallic to insulating behaviour, *J. Non-Cryst. Solids* 182 (1995) 186-197
- [179] Y. Lifshitz, S.R. Kasi and J.W. Rabalais, Subplantation model for film growth from hyperthermal species: Application to diamond, *Phys. Rev. Lett.* 62 (1989) 1290-1293
- [180] J. Robertson, Deposition mechanisms for promoting sp^3 bonding in diamond-like carbon, *Diam. Relat. Mater.* 2 (1993) 984-989
- [181] J. Schwan, S. Ulrich, H. Roth, H. Ehrhardt, S.R.P. Silva, J. Robertson, R. Samlenski and R. Brenn, Tetrahedral amorphous carbon films prepared by magnetron sputtering and dc ion plating, *J. Appl. Phys.* 79 No. 3 (1996) 1416-1422
- [182] H. Hofsaess, H. Feldermann, R. Merk, M. Sebastian and C. Ronning, Cylindrical spike model for the formation of diamondlike thin films by ion deposition, *Appl. Phys. A* 66 (1998) 153-181
- [183] Y. Miyagawa, H. Nakadate, M. Ikeyama, N. Nakao and S. Miyagawa, Dynamic MC simulation for a-C:H deposition in methane plasma based on subplantation model, *Diam. Relat. Mater.* 12 (2003) 927-930
- [184] A. Erdemir and C. Donnet, Tribology of diamond-like carbon films: recent progress and future prospects, *J. Phys. D: Appl. Phys.* 39 (2006) R311-R327
- [185] K. Oguri and T. Arai, Tribological properties and characterization of diamond-like carbon coatings with silicon prepared by plasma-assisted chemical vapour deposition, *Surf. Coat. Technol.* 47 (1991) 710-721
- [186] K. Oguri and T. Arai, Two different low friction mechanisms of diamond-like carbon with silicon coatings formed by plasma-assisted chemical vapor deposition, *J. Mater. Res.* 7 (1992) 1313-1316
- [187] T. Hioki Y. Itoh, A. Itoh, S. Hibi and J. Kawamoto, Tribology of carbonaceous films formed by ion-beam assisted deposition of organic material, *Surf. Coat. Technol.* 46 233 (1991) 233-243

-
- [188] Y. Dong, Q. Li and A. Martini, Molecular dynamics simulation of atomic friction: A review and guide, *J. Vac. Sci. Technol. A* 31 (2013) 030801-1 - 030801-24
- [189] E. Lugscheider and K. Bobzin, The influence on surface free energy of PVD-coatings, *Surf. Coat. Technol.* 142-144 (2001) 755-760
- [190] B. Podgornik, B. Zajec, S. Strnad and K. Stana-Kleinschek, Influence of surface energy on the interactions between hard coatings and lubricants, *Wear* 262 (2007) 1199-1204
- [191] A. Zebda, H. Sabbah, S. Ababou-Girard, F. Solal and C. Godet, Surface energy and hybridization studies of amorphous carbon surfaces, *Appl. Surf. Sci.* 254 (2008) 4980-4991
- [192] M. Ban, M. Ryoji, S. Fujii and J. Fujioka, Tribological characteristics of Si-containing diamond-like carbon films under oil-lubrication, *Wear* 253 (2002) 331-338
- [193] M. Kalin, J. Vizintin, J. Barriga, K. Vercammen, K. van Acker and A. Arnsek, The effect of doping elements and oil additives on the tribological performance of boundary-lubricated DLC/DLC contacts, *Tribol. Letters* 17 (2004) 679-688
- [194] S. Miyake, T. Saito, Y. Yasuda, Y. Okamoto and M. Kano, Improvement of boundary lubrication properties of diamond-like carbon (DLC) films due to metal addition, *Tribol. Int.* 37 (2004) 751-761
- [195] K. Vercammen, K. van Acker, A. Vanhulsel, J. Barriga, A. Arnsek, M. Kalin and J. Meneve, Tribological behaviour of DLC coatings in combination with biodegradable lubricants, *Tribol. Int.* 37 (2004) 983-989
- [196] M.I. de Barros Bouchet, J.M. Martin, T. Le-Mogne and B. Vacher, Boundary lubrication mechanisms of carbon coatings by MoDTC and ZDDP additives, *Tribol. Int.* 38 (2005) 257-264
- [197] M. Kalin and J. Vizintin, The tribological performance of DLC coatings under oil-lubricated fretting conditions, *Tribol. Int.* 39 (2006) 1060-1067
- [198] M. Kalin and J. Vizintin, Differences in the tribological mechanisms when using non-doped, metal-doped (Ti, WC), and non-metal-doped (Si) diamond-like carbon against steel under boundary lubrication, with and without oil additives, *Thin Solid Films* 515 (2006) 2734-2747

-
- [199] I. Velkavrh, M. Kalin and J. Vizintin, The performance and mechanisms of DLC-coated surfaces in contact with steel in boundary-lubrication conditions – a review, *J. Mech. Eng.* 54 (2008) 189-206
- [200] M. Kalin, I. Velkavrh, J. Vizintin and L. Ozbolt, Review of boundary lubrication mechanisms of DLC coatings used in mechanical applications, *Meccanica* 43 (2008) 623-637
- [201] I. Velkavrh, M. Kalin and J. Vizintin, The influence of viscosity on the friction in lubricated DLC contacts at various sliding velocities, *Tribol. Int.* 42 (2009) 1752-1757
- [202] R.P. de Castro Costa, F.R. Marciano, D. A. Lima Oliveira and V.J. Trava-Airoldi, Enhanced DLC wear performance by the presence of lubricant additives, *Mater. Res.* 14 (2011) 222-226
- [203] A. Gangopadhyay, K. Sinha, D. Uy, D.G. McWatt, R. J. Zdrodowski, S. J. Simko, Friction, wear, and surface film formation characteristics of diamond-like carbon thin coating in valvetrain application, *Tribol. Transactions* 54 (2011) 104-114
- [204] J. Robertson, Properties of diamond-like carbon, *Surf. Coat. Technol.* 50 (1992) 185-203
- [205] A. Grill, Review of the tribology of diamond-like carbon, *Wear* 168 (1993) 143-153
- [206] S. Bull, Tribology of carbon coatings: DLC, diamond and beyond, *Diam. Relat. Mater.* 4 (1995) 827-836
- [207] H. Li, T. Xu, C. Wang, J. Chen, H. Zhou, H. Liu, Humidity dependence on the friction and wear behavior of diamond-like carbon films in air and nitrogen environments, *Diam. Relat. Mater.* 15 (2006) 1585-1592
- [208] M. Sedlacek, P. Podgornik and J. Vizintin, Tribological properties of DLC coatings and comparison test results: development of a database, *Mater. Charact.* 59 (2008) 151-161
- [209] J. Robertson, Comparison of diamond-like carbon to diamond for applications, *Phys. Status Solidi A* 205 (2008) 2233-2244
- [210] H. Ronkainen, A. Laukkanen, K. Holmberg, Modeling of friction and structural transformations in diamondlike carbon coatings, VTT Technical Research Centre of Finland (2013)

-
- [211] K.C. Ludema, Friction, Wear, Lubrication, A Textbook in Tribology, CRC Press (1996)
- [212] A. Caines, R. Haycock and J. Hillier, Automotive Lubricants Reference Book, Professional Engineering Publishing (2004)
- [213] L. R. Rudnick, Lubricant Additives Chemistry and Applications, Marcel Dekker (2003)
- [214] R. Memming and H.J. Tolle, Properties of polymeric layers of hydrogenated amorphous carbon produced by a plasma-activated chemical vapour deposition process II: Tribological and mechanical properties, Thin Solid Films 143 (1986) 31-41
- [215] J.-P. Hirvonen, R. Lappalainen, J. Koskinen, A. Anttila, T.R. Jervis and M. Trkula, Tribological characteristics of diamond-like films deposited with an arc-discharge method, J. Mater. Res. 5 (1990) 2524
- [216] A. Erdemir, C. Bindal, J. Pagan and P. Wilbur, Characterization of transfer layers forming on surfaces sliding against diamond-like carbon, Surf. Coat. Technol. 76-77 (1995) 559-563
- [217] Y. Liu, A. Erdemir and E.I. Meletis, Influence of environmental parameters on the frictional behavior of DLC coatings, Surf. Coat. Technol. 94-95 (1997) 463-468
- [218] W. Tillmann, F. Hoffmann, S. Momeni and R. Heller, Hydrogen quantification of magnetron sputtered hydrogenated amorphous carbon (a-C:H) coatings produced at various bias voltages and their tribological behavior under different humidity levels, Surf. Coat. Technol. 206 (2011) 1705-1710
- [219] S.J. Park, J.-K. Kim, K.-R. Lee and D.-H. Ko, Humidity dependence of the tribological behavior of diamond-like carbon films against steel ball, Diam. Relat. Mater. 12 (2003) 1517-1523
- [220] S.J. Park, K.-R. Lee and D.-H. Ko, Tribochemical reaction of hydrogenated diamond-like carbon films: a clue to understand the environmental dependence, Tribol. Int. 37 (2004) 913-921
- [221] H. Li, T. Xu, C. Wang, J. Chen, H. Zhou and H. Liu, Humidity dependence on the friction and wear behavior of diamond-like carbon film in air and nitrogen environments, Diam. Relat. Mater. 15 (2006) 1585-1592
- [222] C.A. Freyman, Y. Chen and Y.-W. Chung, Synthesis of carbon films with ultra-low friction in dry and humid air, Surf. Coat. Technol. 201 (2006) 164-167

-
- [223] J.C. Sanchez-Lopez, A. Erdemir, C. Donnet and T.C. Rojas, Friction-induced structural transformations of diamondlike carbon coatings under various atmospheres *Surf. Coat. Technol.* 163-164 (2003) 444-450
- [224] M. Suzuki, T. Ohana, and A. Tanaka, Tribological properties of DLC films produced with different hydrogen contents in water environment, *Diam. Relat. Mater.* 13 (2004) 2216-2220
- [225] A. K. Gangopadhyay, P. A. Willermet, M. A. Tamor and W. C. Vassell, Amorphous hydrogenated on films for tribological applications I: Development of moisture insensitive films having reduced compressive stress, *Tribol. Int.* 30 (1997) 9-18
- [226] A. Tanaka, T. Nishibori, M. Suzuki and K. Maekawa, Tribological properties of DLC films deposited using various precursors under different humidity conditions, *Diam. Relat. Mater.* 12 (2003) 2066-2071
- [227] A. Erdemir, G.R. Fenske, J. Terry and P. Wilbur, Effect of source gas and deposition method on friction and wear performance of diamondlike carbon films, *Surf. Coat. Technol.* 94-95 (1997) 525-530
- [228] R. Waesche and D. Klaffke, Tribology of DLC films under fretting conditions, in C. Donnet and A. Erdemir (eds.), *Tribology of diamond-like carbon films: Fundamentals and applications* (2008) 362-382
- [229] K. Miyoshi, J.J. Pouch and S.A. Alterovitz, Plasma deposited amorphous hydrogenated carbon films and their tribological properties, *NASA Technical Memorandum* 102379 (1989) 1-12
- [230] D.S. Kim, T.E. Fischer and B. Gallois, The effects of oxygen and humidity on friction and wear on diamond-like carbon films, *Surf. Coat. Technol.* 49 (1991) 537-542
- [231] A. Erdemir, M. Switala, R. Wei and P. Wilbur, A tribological investigation of the graphite-to-diamond-like behavior of amorphous carbon films ion beam deposited on ceramic substrates, *Surf. Coat. Technol.* 50 (1991) 17-23
- [232] D. Paulmier, H. Zaidi, H. Nery and T.L. Huu, Tribological behaviour of diamond-like coatings: effect of active gases in atomic and molecular states, *Surf. Coat. Technol.* 62 (1993) 570-576
- [233] C. Donnet, M. Belin, J.C. Auge, J.M. Martin, A. Grill and V. Patel, Tribochemistry of diamond-like carbon coatings in various environments, *Surf. Coat. Technol.* 68-69 (1994) 626-631

-
- [234] A.A. Voevodin, M.S. Donley, J.S. Zabinski and J.E. Bultman, Mechanical and tribological properties of diamond-like carbon coatings prepared by pulsed laser deposition, *Surf. Coat. Technol.* 76-77 (1995) 534-539
- [235] Y. Liu, A. Erdemir and E.I. Meletis, A study of the wear mechanism of diamond-like carbon films, *Surf. Coat. Technol.* 82 (1996) 48-56
- [236] Y. Liu, A. Erdemir and E.I. Meletis, An investigation of the relationship between graphitization and frictional behavior of DLC coatings, *Surf. Coat. Technol.* 86-87 (1996) 564-568
- [237] A. Erdemir, C. Bindal, G.R. Fenske, C. Zuiker and P. Wilbur, Characterization of transfer layers forming on surfaces sliding against diamond-like carbon, *Surf. Coat. Technol.* 86-87 (1996) 692-697
- [238] E.-S. Yoon, H. Kong and K.-R. Lee, Tribological behavior of sliding diamond-like carbon films under various environments, *Wear* 217 (1998) 262-270
- [239] J. Jiang and R.D. Arnell, On the running-in behaviour of diamond-like carbon coatings under the ball-on-disk contact geometry, *Wear* 217 (1998) 190-199
- [240] H. Ronkainen, S. Varjus and K. Holmberg, Tribological performance of different DLC coatings in water-lubricated conditions, *Wear* 249 (2001) 267-271
- [241] W. Zhang, A. Tanaka, K. Wazumi and Y. Koga, Effect of environment on friction and wear properties of diamond and diamond-like carbon film, *Thin Solid Films* 413 (2002) 104-109
- [242] K. Bewilogua and G. Braeuer, Kohlenstoffschichten gegen Reibung und Verschleiss, *Carolo-Wilhelmina* 1 (2002) 34-38
- [243] P. Gupta, Synthesis, structure and properties of nanolayered DLC/DLC films, PhD Thesis Panjab University (2003)
- [244] M. Suzuki, T. Watanabe, A. Tanaka and Y. Koga, Tribological properties of diamond-like carbon films produced by different deposition techniques, *Diam. Relat. Mater.* 12 (2003) 2061-2065
- [245] F. Bremond, P. Fournier and F. Platon, Test temperature effect on the tribological behavior of DLC-coated 100C6-steel couples in dry friction, *Wear* 254 (2003) 774-783

-
- [246] J.C. Sanchez-Lopez, A. Erdemir, C. Donnet and T.C. Rojas, Friction-induced structural transformations of diamondlike carbon coatings under various atmospheres, *Surf. Coat. Technol.* 163-164 (2003) 444-450
- [247] E. Liu, Y.F. Ding, L. Li, B. Blanpain and C.-P. Celis, Influence of the humidity on the friction of diamond and diamond-like carbon materials, *Tribol. Int.* 40 (2007) 216-219)
- [248] S. Lawes, M. Fitzpatrick and S.V. Hainsworth, Evaluation of the tribological properties of DLC for engine applications, *J. Phys. D: Appl. Phys.* 40 (2007) 5427-5437
- [249] A. Vanhulsel, F. Velasco, R. Jacobs, L. Ersels, D. Havermans, E.W. Roberts, I. Sherrington, M.J. Anderson and L. Gaillard, DLC solid lubricant coatings on ball bearings for space applications, *Tribol. Int.* 40 (2007) 1186-1194
- [250] H. Ronkainen, A. Laukkanen and K. Holmberg, Friction in a coated surface deformed by a sliding sphere, *Wear* 263 (2007) 1315-1323
- [251] A.J. Gant, M.G. Gee and L.P. Orkney, The wear and friction behaviour of engineering coatings in ambient air and dry nitrogen, *Wear* 271 (2011) 2164-2175
- [252] L.V. Santos, L.F. Bonetti, G.C. Rodrigues, P.A. Radi and V.J. Trava-Airoldi, The friction coefficients DLC films are dependent on the sliding environment and DLC hydrogen content, available at:
<http://mtc-m17.sid.inpe.br/col/sid.inpe.br/mtc-m17@80/2006/12.06.17.01/doc/The%20friction%20coeficients.pdf>
- [253] A. Leyland, A. Matthews, On the significance of the H/E ratio in wear control: a nanocomposite coating approach to optimised tribological behaviour, *Wear* 246 (2000) 1-11
- [254] J. A. Greenwood, J. B. P. Williamson, Contact of nominally flat surfaces, *Proceedings of the Royal Society of London. Series A, Mathematical and Physical Sciences* 295 (1966) 300-319
- [255] P.S. Kisly, in: E.A. Almond, C.A. Brookes, R. Warren (Eds.), *Proceedings of the International Conference on the Science of Hard Materials*, Adam Hilger Ltd., Bristol and Boston (1984)

- [256] C. Charitidis, S. Logothetidis and P. Douka, Nanoindentation and nanoscratching studies of amorphous carbon films, *Diam. Relat. Mater.* 8 (1999) 558–562
- [257] A. Matthews, S. Franklin, K. Holmberg, Tribological coatings: contact mechanisms and selection, *J. Phys. D: Appl. Phys.* 40 (2007) 5463–5475
- [258] D.B. Luo, V. Fridrici and Ph. Kapsa, A systematic approach for the selection of tribological coatings, *Wear* 271 (2011) 2132–2143
- [259] Y. Enomoto, Ceramic tribology in Japan, *Tribol. Int.* 28 (1995) 1-6
- [260] Y.-M. Gao, L. Fang, J.-Y. Su and X.-W. Xu, An investigation on component and formation of tribochemical film in Si_3N_4 -white iron sliding pair lubricated with distilled water, *Tribol. Int.* 30 No. 9 (1997) 693–700
- [261] Y.-M. Gao, L. Fang, J.-Y. Su and Z.-G. Xie, Investigation on the components and the formation of a tribochemical film in the Si_3N_4 -gray iron sliding pair lubricated with distilled water, *Wear* 206 (1997) 87-93
- [262] S. Sasaki, The effects of the surrounding atmosphere on the friction and wear of alumina, zirconia, silicon carbide and silicon nitride, *Wear* 134 (1989) 185-200
- [263] J. Jiang, S. Zhang and R.D. Arnell, The effect of relative humidity on wear of a diamond-like carbon coating, *Surf. Coat. Technol.* 167 (2003) 221–225
- [264] F. Tuinstra and J. L. Koenig, Raman spectrum of graphite, *J. Chem. Phys.* 53 (1970) 1126-1130
- [265] L.G. Cancado, K. Takai, T. Enoki, M. Endo, Y.A. Kim, H. Mizusaki, A. Jorio, L.N. Coelho, R. Magalhaes-Paniago and M.A. Pimenta, General equation for the determination of the crystallite size L_a of nanographite by Raman spectroscopy, *Appl. Phys. Lett.* 88 (2006) 163106-1 to 163106-3
- [266] D. Sheeja, B.K. Tay, S.M. Krishnan and L.N. Nung, Tribological characterization of diamond-like carbon (DLC) coatings sliding against DLC coatings, *Diam. Relat. Mater.* 12 (2003) 1389-1395
- [267] J. Jiang, S. Zhang and R.D. Arnell, The effect of relative humidity on wear of a diamond-like carbon coating, *Surf. Coat. Technol.* (2003) 221-225
- [268] H. Li, T. Xu, C. Wang, J. Chen, H. Zhou and H. Liu, Tribochemical effects on the friction and wear behavior of diamond-like carbon film under high relative humidity condition, *Tribol. Lett.* 19 (2005) 231-238

-
- [269] A. Erdemir, I.B. Nilufer, O.L. Eryilmaz, M. Beschliesser and G.R. Fenske, Friction and wear performance of diamond-like carbon films grown in various source gas plasmas, *Surf. Coat. Technol.* 120–121 (1999) 589–593
- [270] A. Erdemir, O.L. Eryilmaz, I.B. Nilufer, G.R. Fenske, Synthesis of superlow-friction carbon films from highly hydrogenated methane plasmas, *Surf. Coat. Technol.* 133-134 (2000) 448-454
- [271] C. Donnet, J. Fontaine, A. Grill and T. Le Mogne, The role of hydrogen on the friction mechanism of diamond-like carbon films, *Tribol. Lett.* 9 (2000) 137-142
- [272] A. Erdemir, Friction and wear of diamond and diamond-like carbon films, *Proc. Instn. Mech. Engrs.*, 216 *J. Eng. Tribol.* (2002) 387-400
- [273] Carbon films: Basic knowledge, film types and properties, VDI 2840 guideline (2008)
- [274] B. Goranchev, K. Reichelt, J. Chevallier, P. Hornshoj, H. Dimigen and H. Huebsch, R.F. reactive sputter deposition of hydrogenated amorphous silicon carbide films, *Thin Solid Films* 139 (1986) 275-285
- [275] I. Sugimoto and S. Miyake, Oriented hydrocarbons transferred from high performance lubricative amorphous C:H:Si film during sliding in a vacuum, *Appl. Phys. Lett.* 56 (1990) 1868-1870
- [276] S. Miyake, Tribological properties of hard carbon films: extremely low friction mechanism of amorphous hydrogenated carbon films and amorphous hydrogenated SiC films in vacuum, *Surf. Coat. Technol.* 54-55 (1992) 563-569
- [277] K. Oguri and T. Arai, Effect of excess carbon on the hardness of Si-C and Ti-C coatings formed by plasma-assisted chemical vapor deposition, *Thin Solid Films* 1986 (1990) L29-L31
- [278] K. Oguri and T. Arai, Tribological properties and characterization of diamondlike carbon coatings with silicon prepared by plasma-assisted chemical vapor deposition, *Surf. Coat. Technol.* 47 (1991) 710-721
- [279] K. Oguri and T. Arai, Two different low friction mechanisms of diamond-like carbon with silicon coatings formed by plasma-assisted chemical vapor deposition, *J. Mater. Res.* 7 (1992) 1313-1316
- [280] K. Oguri and T. Arai, Friction coefficient of Si-C, Ti-C and Ge-C coatings with excess carbon formed by plasma-assisted chemical vapour deposition, *Thin Solid Films* 208 (1992) 158-160

- [281] T. Hioki, Y. Itoh, A. Itoh, S. Hibi and J. Kawamoto, Tribology of carbonaceous films formed by ion-beam assisted deposition of organic material, *Surf. Coat. Technol.* 46 (1991) 233-243
- [282] Y. Itoh, S. Hibi, T. Hioki and J. Kawamoto, Tribological properties of metals modified by ion-beam deposition of silicone oil, *J. Mater. Res.* 6 (1991) 871-874
- [283] T. Hioki, K. Okamura, Y. Itoh, S. Hibi and S. Noda, Formation of carbon films by ion-beam-assisted deposition, *Surf. Coat. Technol.* 65 (1994) 106-111
- [284] J. Smeets, J. Meneve, R. Jacobs, L. Eersels, and E. Dekempeneer, Physical and tribological properties of a-Si_{1-x}C_x:H coatings prepared by r.f. plasma-assisted chemical vapour deposition, *Journal de Physique IV Vol. 3* (1993) 503-510
- [285] J. Meneve, R. Jacobs, L. Eersels, J. Smeets and E. Dekempeneer, Friction and wear behavior of amorphous hydrogenated Si_{1-x}C_x films, *Surf. Coat. Technol.* 62 (1993) 577-582
- [286] R. Gilmore and R. Hauert, Comparative study of the tribological moisture sensitivity of Si-free and Si-containing diamond-like carbon films, *Surf. Coat. Technol.* 133-134 (2000) 437-442
- [287] S.G. Kim, Y.K. Yong, W.S. Jang and S.W. Kim, Effects of humidity on the friction coefficient of diamond-like carbon (DLC) coating, *J. Korean Phys. Soc.* 54 No. 3 (2009) 1228-1236
- [288] F. Zhao, H.X. Li, L. Ji, Y.F. Mo, W.L. Quan, W. Du, H.D. Zhou and J.M. Chen, Superlow friction behavior of Si-doped hydrogenated amorphous carbon film in water environment, *Surf. Coat. Technol.* 203 (2009) 981-985
- [289] C. Chouquet, G. Gerbaud, M. Bardet, S. Barrat, A. Billard, F. Sanchette and C. Ducros, Structural and mechanical properties of a-C:H and Si doped a-C:H thin films grown by LF-PECVD, *Surf. Coat. Technol.* 204 (2010) 1339-1346
- [290] B. Yang, Y. Zheng, B. Zhang, L. Wei and J. Zhang, The high-temperature tribological properties of Si-DLC films, *Surf. Interface Anal.* 44 (2012) 1601-1605
- [291] K. Dohda, Y. Tsuchiya, K. Kitamura and H. Mori, Evaluation of tribo-characteristics of diamond-like-carbon containing Si by metal forming simulators, *Wear* 286-287 (2012) 84-91

-
- [292] F. Zhao, H.X. Li, L. Ji, Y.J. Wang, Y.F. Mo, W.L. Quan, Q.H. Kong, Y.X. Wang, J.M. Chen and H.D. Zhou,, Microstructure and mechanical properties of graphitic a-C:H:Si films, *Surf. Coat. Technol.* 206 (2012) 3467–3471
- [293] X. Chen and T. Kato, Growth mechanism and composition of ultrasMOOTH a-C:H:Si films grown from energetic ions for superlubricity, *J. Appl. Phys.* 115 (2014) 044908-1 to 044908-14
- [294] P.J. Burnett and D.S. Rickerby, The scratch adhesion test: An elastic-plastic indentation analysis, *Thin Solid Films* 157 (1988) 233-254
- [295] P.J. Blau, Scratch adhesion testing, in *Lab Handbook of Scratch Testing Chapter 7*, Blue Rock Technical Publ. Oak Ridge, TN (2002)
- [296] ASTM C1624, Standard test method for adhesion strength and mechanical failure modes of ceramic coatings by quantitative single point scratch testing (2010)
- [297] S.T. Gonczy and N. Randall, An ASTM Standard for quantitative scratch adhesion testing of thin, hard ceramic coatings, *Int. J. Appl. Ceram. Technol.* 2 (2005) 422-428
- [298] ASTM G171, Standard test method for scratch hardness of materials using a diamond stylus (2009)
- [299] DIN EN 1071-3, Advanced technical ceramics - Method of test for ceramic coatings - Part 3: Determination of adhesion and other mechanical failure modes by a scratch test (2005)
- [300] M. Weber, K. Bewilogua, H. Thomsen and R. Wittorf, Influence of different interlayers and bias voltage on the properties of a-C:H:Me coatings prepared by reactive d.c. magnetron sputtering, *Surf. Coat. Technol.* 201 (2006) 1576-1582
- [301] ISO 26443, Fine ceramics (advanced ceramics, advanced technical ceramics) – Rockwell indentation test for evaluation of adhesion of ceramic coatings (2008)
- [302] Coating (CVD, PVD) of cold forging tools, chapter 5.4 adhesion test of coating, VDI 3198 guideline (1992)
- [303] ISO 6508, Metallic materials – Rockwell hardness test (2005)
- [304] W. Heinke, A. Leyland, A. Matthews, G. Berg, C. Friedrich and E. Broszeit, Evaluation of PVD nitride coatings, using impact, scratch and Rockwell-C adhesion tests, *Thin Solid Films* (1995) 431-438

-
- [305] N. Vidakis, A. Antoniadis and N. Bilalis, The VDI 3198 indentation test evaluation of a reliable qualitative control for layered compounds, *J. Mater. Process. Technol.* 143-144 (2003) 481-485
- [306] B. Bhushan and X. Li, Nanomechanical characterization of solid surfaces and thin films, *Int. Mater. Rev.* 48 (2003) 125-164
- [307] A. Martens, *Handbuch der Materialkunde für den Maschinenbau*, Springer (1898) 234
- [308] W.C. Oliver and G.M. Pharr, An improved technique for determining hardness and elastic modulus using load and displacement sensing indentation experiments, *J. Mater. Res.* 7 (1992) 1564-1583
- [309] A.C. Fischer-Cripps, A review of analysis methods for sub-micron indentation testing, *Vacuum* (2000) 569-585
- [310] W.C. Oliver and G.M. Pharr, Measurement of hardness and elastic modulus by instrumented indentation: Advances in understanding and refinements to methodology, *J. Mater. Res.* 19 (2004) 3-20
- [311] DIN EN 1071-2, Advanced technical ceramics – Methods of test for ceramic coatings- Part 2: Determination of coating thickness by the crater grinding method (2002)
- [312] DIN EN 1071-6, Advanced technical ceramics – Methods of test for ceramic coatings- Part 6: Determination of the abrasion resistance of coatings by a micro-abrasion wear test (2007)
- [313] M.G. Gee, A. Gant, I. Hutchings, R. Bethke, K. Schiffmann, K. Van Acker, S. Poulat, Y. Gachon and J. von Stebut, Progress towards standardisation of ball cratering, *Wear* 255 (2003) 1–13
- [314] T. Michler and C. Siebert, Abrasive wear testing of DLC coatings deposited on plane and cylindrical parts, *Surf. Coat. Technol.* 163-164 (2003) 546-551
- [315] K. Taube, Carbon-based coatings for dry sheet-metal working, *Surf. Coat. Technol.* 98 (1998) 976-984
- [316] ASTM G99-04, Standard test method for wear testing with a Pin-on-Disk apparatus (2004)
- [317] ASTM G99-95a, Standard test method for wear testing with a Pin-on-Disk apparatus (2000)

-
- [318] ASTM G99, Standard test method for wear testing with a Pin-on-Disk apparatus (2010)
- [319] DIN EN 1071-13, Advanced technical ceramics – Methods of test for ceramic coatings – Part 13: Determination wear rate by the pin-on-disk method (2010)
- [320] DIN EN 1071-12, Advanced technical ceramics – Methods of test for ceramic coatings – Part 12: Reciprocating wear test (2010)
- [321] H. Czichos, S. Becker and J. Lexow, Multilaboratory tribotesting: Results from the Versailles advanced materials and standards programme on wear test methods, *Wear* 114 (1987) 109-130
- [322] H. Czichos, S. Becker and J. Lexow, International multilaboratory sliding wear tests with ceramics and steel, *Wear* 135 (1989) 171-191
- [323] K. Taube, M. Grischke and K. Bewilogua, Improvement of carbon-based coatings for use in the cold forming of non-ferrous metals, *Surf. Coat. Technol.* 68-69 (1994) 662-668
- [324] M. Yasaka, X-Ray thin-film measurement techniques: V X-ray reflectivity measurement, *The Rigaku Journal* 26 (2010) 1-9
- [325] A. Gibaud, M.S. Chebil and T. Beuvier, X-Ray reflectivity, in *Surface Science Techniques*, G. Bracco and B. Holst (eds.), Springer Series in Surface Science (2013) 191-216
- [326] A. C. Ferrari, A. Libassi, B. K. Tanner, V. Stolojan, J. Yuan, L. M. Brown, S. E. Rodil, B. Kleinsorge and J. Robertson, Density, sp^3 fraction, and cross-sectional structure of amorphous carbon films determined by x-ray reflectivity and electron energy-loss spectroscopy, *Phys. Rev. B* 62 (2000) 11089–11103
- [327] L. Calliari, A. Baranov, S. Fanchenko, A. Nefedov, A. Varfolomeev, X-ray reflectivity study of the early stages of a-C:H film growth, *Diam. Relat. Mater.* 14 (2005) 934– 941
- [328] A. Benninghoven, F.G. Rudenauer and H.W. Werner, *Secondary ion mass spectrometry: Basic concepts, instrumental aspects, applications and trends*, Wiley New York (1987)
- [329] A. Benninghoven, The history of static SIMS – A personal perspective, in *Tof-SIMS: Materials Analysis by Mass Spectrometry*, J.C. Vickerman and D. Briggs (eds.), IM Publications LLP and Surface Spectra Ltd. (2013)

- [330] D. McPhail and M. Dowsett, Dynamic SIMS, in Surface Analysis – The Principal Techniques, J. Vickerman and I. Gilmore (eds.), Wiley New York (2009)
- [331] R.G. Wilson, SIMS quantification in Si, GaAs, and diamond – an update, *Int. J. Mass Spectrometry and Ion Proc.* 143 (1995) 43-49
- [332] P. Willich and U. Wischmann, EPMA and quantitative MCs⁺-SIMS of metal-DLC coating materials, *Mikrochim. Acta* 132 (2000) 419-427
- [333] P. Willich, C. Steinberg, SIMS depth profile analysis of wear resistant coatings on cutting tools and technical components, *Appl. Surf. Sci.* 179 (2001) 263-268
- [334] D. Hofmann, S. Beisswenger and A. Feuerstein, Novel low temperature hard coating for large parts, *Surf. Coat. Technol.* 49 (1991) 330-335
- [335] D. Hofmann, H. Schuessler, K. Bewilogua, H. Huebsch and J. Lemke, Plasma-booster-assisted hydrogenated W-C coatings, *Surf. Coat. Technol.* 73 (1995) 137-141
- [336] D.P. Monaghan, D.G. Teer, P.A. Logan, I. Efeoglu and R.D. Arnell, Deposition of wear resistant coatings based on diamond like carbon by unbalanced magnetron sputtering, *Surf. Coat. Technol.* 60 (1993) 525-530
- [337] L.A. Donohue, J. Cawley, D.B. Lewis, J.S. Brooks and W.D. Muenz, Investigation of superlattice coatings deposited by a combined steered arc evaporation and unbalanced magnetron sputtering technique, *Surf. Coat. Technol.* 76-77 (1995) 149-158
- [338] T. Hurkmans, F. Hauzer, B. Buil, K. Engel and R. Tietema, A new large volume PVD coating system using advanced controlled arc and combined arc/unbalanced magnetron (ABSTM) deposition techniques, *Surf. Coat. Technol.* 92 (1997) 62-68
- [339] D. Hofmann, S. Kunkel, K. Bewilogua and R. Wittorf, From DLC to Si-DLC-based layer systems with optimized properties for tribological applications, *Surf. Coat. Technol.* 215 (2013) 357-363
- [340] M. Lattemann, A.P. Ehiasarian, J. Bohlmark, P. Persson, and U. Helmersson, Investigation of high power impulse magnetron sputtering pretreated interfaces for adhesion enhancement of hard coatings on steel, *Surf. Coat. Technol.* 200 (2006) 6495-6499

- [341] A.P. Ehiasarian, J. G. Wen and I. Petrov, Interface microstructure engineering by high power impulse magnetron sputtering for the enhancement of adhesion, *J. Appl. Phys.* 101 (2007) 054301-1 to 054301-10
- [342] W.D. Muenz and T. Zufrass, PVD-Verfahren und PVD-Vorrichtung zur Erzeugung von reibungsarmen, verschleissbestaendigen Funktionsschichten und damit hergestellte Beschichtungen (PVD-method and PVD-apparatus for the production of low friction, wear resistant functional coatings and coatings manufactured therewith), German patent application DE 102007058356A1 (2008)
- [343] P. J. Fallon, V. S. Veerasamy, C. A. Davis, J. Robertson, G. Amaratunga, W.I. Milne and J. Koskinen, Properties of filtered-ion-beam-deposited diamond-like carbon as a function of ion energy, *Phys. Rev. B* 48 (1993) 4777-4782
- [344] A.C. Ferrari, A. Libassi, B. K. Tanner, V. Stolojan, J. Yuan, L. M. Brown, S. E. Rodil, B. Kleinsorge and J. Robertson, Density, sp^3 fraction, and cross-sectional structure of amorphous carbon films determined by x-ray reflectivity and electron energy-loss spectroscopy, *Phys. Rev. B* 62, 16 (2000) 11089-11103
- [345] A. Singha, A. Ghosh, A. Roy and N. Ray, Quantitative analysis of hydrogenated diamondlike films by visible Raman spectroscopy, *J. Appl. Phys.* 100 (2006) 044910-1 to 044910-8
- [346] C. Louro, C. Wagner Moura, N. Carvalho, M. Stueber and A. Cavaleiro, Thermal stability in oxidative and protective environments of a-C:H cap layer on a functional gradient coating, *Diam. Relat. Mater.* 20 (2011) 57-63
- [347] J. Fontaine, J. Loubet, T. Le Mogne and A. Grill, Superlow friction of diamond-like carbon films: a relation to viscoplastic properties, *Tribol. Lett.* 17 (2004) 709-714
- [348] S. Peter, M. Guenther, D. Hauschild, D. Grambole, F. Richter, Mid-frequency deposition of a-C:H films using five different precursors, *Vacuum* 84 (2010) 958-961
- [349] C. Donnet, Tribology of solid lubricant coatings, *Condensed Mater. News* 4 (1995) 9-24
- [350] C. Donnet and A. Grill, Friction control of diamond-like carbon coatings, *Surf. Coat. Technol.* 94-95 (1997) 456-462

- [351] W.-J. Wu, T.-M. Pai, M.-H. Hon, Wear behavior of silicon-containing diamond-like carbon coatings, *Diam. Relat. Mater.* 7 (1998) 1478–1484
- [352] B. Racine, A.C. Ferrari, N.A. Morrison, I. Hutchings, W.I. Milne and J. Robertson, Properties of amorphous carbon–silicon alloys deposited by a high plasma density source, *J. Appl. Phys.* Vol. 90, No. 10 (2001) 5002-5012
- [353] V. Palshin, R. C. Tittsworth, C. G. Fountzoulas and E. I. Meletis, X-ray absorption spectroscopy, simulation and modeling of Si-DLC films, *J. Mater. Sci.* 37 (2002) 1535-1539
- [354] N. Laidani, G. Speranza, L. Calliari, V. Micheli and M. Anderle, Chemical and microstructural characterization of silicon-containing carbon films, *Surf. Coat. Technol.* 151–152 (2002) 138–143
- [355] J. Michler, M. Tobler and E. Blank, Thermal annealing behaviour of alloyed DLC films on steel: Determination and modelling of mechanical properties, *Diam. Relat. Mater.* 8 (1999) 510–516
- [356] I.L. Moskowitz and S.V. Babu, Surface morphology and quality of a-Si:C:H films, *Thin Solid Films* 385 (2001) 48-54
- [357] P. Papakonstantinou, J.F. Zhao, P. Lemoine, E.T. McAdams and J.A. McLaughlin, The effects of Si incorporation on the electrochemical and nanomechanical properties of DLC thin films, *Diam. Relat. Mater.* 11 (2002) 1074–1080
- [358] W. J. Wang, T.M. Wang and B.L. Chen, Hydrogen release from diamondlike carbon films due to thermal annealing in vacuum, *Nucl. Instr. and Meth. In Phys. Res. B* 117 (1996) 140-144
- [359] S.S. Camargo, R.A. Santos, A.L. Baia Neto, R. Carius and F. Finger, Structural modifications and temperature stability of silicon incorporated diamond-like films, *Thin Solid Films* 332 (1998) 130-135
- [360] W.C. Vassell, A.K. Gangopadhyay, T.J. Potter, M.A. Tamor and M.J. Rokosz, Characterization of silicon-stabilized amorphous hydrogenated carbon, *J. Mater. Eng. Perform.* 6 (1997) 426-432
- [361] B. Yang, Y. Zheng, B. Zhang, L. Wei and J. Zhang, The high-temperature tribological properties of Si-DLC films, *Surf. Interface Anal.* 44 (2012) 1601-1605
- [362] M. Grischke, *Fortschrittsberichte VDI-Serie 5* No. 179 (1989)
- [363] M. Fryda, *Fortschrittsberichte VDI-Serie 5* No. 303 (1993)

[364] K. Bewilogua, R. Wittorf, H. Thomsen and M. Weber, DLC based coatings prepared by reactive d.c. magnetron sputtering, Thin Solid Films 447-448 (2004) 142-147

[365] K. Bewilogua, J. Brand, H. Thomsen, M. Weber and R. Wittorf, Structure, properties and applications of diamond-like carbon coatings prepared by reactive magnetron sputtering, Z. Metallkd. 96 (2005) 998-1004

[366] M. Grischke, K. Bewilogua, K. Trojan and H. Dimigen, Application-oriented modifications of deposition processes for diamond-like-carbon-based coatings, Surf. Coat. Technol. 74-75 (1995) 739-745

[367] D. Hofmann, Coating containing Si-DLC, DLC, and Me-DLC, and a method for producing coatings, PCT patent application WO 2013/156107 A1 disclosure October (2013), priority April 2012